THOMAS RICHTER

SEDIMENTARY FLUXES AT THE MID-ATLANTIC RIDGE

SEDIMENT SOURCES, ACCUMULATION RATES, AND GEOCHEMICAL CHARACTERISATION

GEOMAR
Forschungszentrum
für marine Geowissenschaften
der Christian-Albrechts-Universität
zu Kiel

Kiel 1998

GEOMAR REPORT 73

GEOMAR
Research Center
for Marine Geosciences
Christian Albrechts University
in Kiel

Dissertation
zur Erlangung des Doktorgrades
der Mathematisch-Naturwissenschaftlichen Fakultät
der Christian-Albrechts-Universität zu Kiel
Zum Druck genehmigt am 18.12.1996

Redaktion der Serie: Gerhard Haass

Umschlag: GEOMAR Technologie GmbH

Managing Editor: Gerhard Haass

Cover: GEOMAR Technologie GmbH

GEOMAR REPORT
ISSN 0936 - 5788

GEOMAR REPORT
ISSN 0936 - 5788

GEOMAR
Forschungszentrum
für marine Geowissenschaften
D-24148 Kiel
Wischhofstr. 1-3
Telefon (0431) 600-2555, 600-2505

GEOMAR
Research Center
for Marine Geosciences
D-24148 Kiel / Germany
Wischhofstr. 1-3
Telephone (49) 431 / 600-2555, 600-2505

CONTENTS

Abstract
Zusammenfassung

1. Introduction 1

2. Background information 3

2.1 Hydrothermal activity and related tracers in pelagic sediments 3

2.2 Geological setting and hydrothermal activity in the Azores study area 6

3. Material and methods 10

3.1 Lithology, choice of cores for further study 10

3.2 Methods 12

3.2.1 Stratigraphy 12

3.2.2 Geochemistry 13

3.2.3 Mineralogy 15

4. Stable isotope stratigraphy, age control, and sedimentation rates 16

4.1 Introduction 16

4.2 Choice of foraminiferal species 16

4.3 Results and discussion 17

4.3.1 Oxygen isotope records and AMS age data 17

4.3.2 Epibenthic $\delta^{13}C$ minima: Reduction in deep water ventilation 23

4.3.3 Temporal and spatial variability of sedimentation rates 24

4.4 Conclusion 27

5. Sediment facies 28

5.1 Introduction 28

5.2 Results: Distribution of carbonate and organic carbon 28

5.3 Discussion: Ponded sediments in a restricted basin at the 38°05'N fracture zone (core GEOFAR KF16) 33

5.4 Conclusions 36

6. Factor analysis of sediment geochemical data: Element associations and relative importance of sediment sources 37

6.1 Introduction 37

6.2 Choice of elements and sample sets for factor analysis 38

6.3 Results 39

6.3.1 Entire data set, bulk composition 39

6.3.2 Entire data set, carbonate-free composition 41

6.3.3 Data from cores KF09 and KF13 42

6.3.4 Summary 45

6.4 Discussion: Volcaniclastic and detrital sediment sources 45

6.4.1 Compositional variability and sources of volcaniclastic input 45

6.4.2 Composition, temporal and spatial variability of detrital sources 48

6.5 Conclusions 53

7. Metal accumulation rates in Mid-Atlantic Ridge sediments: primary fluxes of potential hydrothermal tracers and secondary diagenetic modification 54

7.1 Introduction 54

7.2 Results 54

7.2.1 Metal accumulation rates 54

7.2.2 Metal distribution in oxidized surface layers 60

7.2.3 P, V, and As: scavenging from the water column by hydrothermal oxyhydroxides 61

7.2.4 Speciation of iron and manganese: information from selective leaching and Mössbauer spectroscopy 65

7.3 Discussion 75

7.3.1 Early diagenetic processes: modification of primary fluxes of metals 75

7.3.2 Spatial and temporal variability of metal accumulation rates 83

7.4 Conclusions 95

8. Barium in Mid-Atlantic Ridge sediments: Hydrothermal or biogenic origin and possible paleoceanographic implications 96

8.1 Introduction 96

8.2 Results 98

8.2.1 Relationship between Ba, Si and organic carbon 98

8.2.2 Stratigraphic distribution of Ba 102

8.2.3 Correction for detrital sources of barium 105

8.2.4 Mineralogy of gravity concentrates 108

8.2.5 Relationship between Sr, $CaCO_3$ and Ba 112

8.3 Discussion 113

8.3.1 Barium in proximal sediments at the Lucky Strike seamount: evidence for hydrothermal origin 113

8.3.2 Geochemical and paleoceanographic context of Ba peaks in distal pelagic sediments 116

8.4 Conclusions 127

9. A sedimentary serpentine layer: Alteration of marine ultramafic rocks at the 38°05'N fracture zone 128

9.1 Introduction 128

9.2 Core location and sedimentology 129

9.3 Results 130

9.3.1 Geochemistry 130
9.3.2 Mineralogy 131
9.4 Discussion 138
9.4.1 Serpentine in the mid-oceanic ridge environment 138
9.4.2 Estimation of chlorite composition 140
9.4.3 A normative model of mineral abundances 142
9.4.4 Cr/Ni-ratios as indicators of protolith composition 144
9.4.5 Conditions of formation as indicated by the mineral assemblage 148
9.5 Conclusions 153

10. General conclusion 154

References 157

Acknowledgments 174

APPENDIX

1) Selected core logs

2) Stable isotope data

3) X-ray fluorescence data

4) Carbonate and organic carbon

5) Selective leaching data

6) Metal accumulation rates

Abstract

Oxygen isotope stratigraphy was established, and various geochemical and mineralogical investigations were performed on Mid-Atlantic ridge crest sediments at 37-39°N in the vicinity of the Lucky Strike and Menez Gwen hydrothermal sites, in order to characterize sediment sources in time and space and to describe and quantify hydrothermal input in sediments.

Multivariate statistical analysis of geochemical data demonstrated that volcaniclastic, ultramafic, detrital and hydrothermal sediment sources are present in addition to biogenic carbonate, which dominates the chemical composition of most samples. The hydrothermal contribution includes metals derived from hydrothermal solutions (Fe, Mn, Cu) and elements scavenged from the water column by hydrothermal oxyhydroxides (P, V, As). The distribution of hydrothermal factor scores and the pattern of metal accumulation rates suggest maximum hydrothermal input at 37°N south of the Lucky Strike vent field, which may include contributions from other presently undiscovered vent fields south of the area of the present study. Metal accumulation rates are significantly higher than at abyssal plains remote from the ridge axis, and comparable to other hydrothermally influenced environments. While the downcore distribution of hydrothermal tracers was obviously modified by early diagenetic processes, time-integrated average fluxes clearly indicate continuous hydrothermal influence in the study area at least down to 55,000 years B.P. .

Barium appears to be dominantly of hydrothermal origin in sediments on the flanks of the Lucky Strike seamount, where it may be derived from redeposited hydrothermal precipitates containing abundant barite. A minor contribution of plume-derived fine-grained sulfides and possibly barite may be present in distal sediments based on the occurrence of a cubic phase, probably sphalerite, in gravity concentrates (>3.0g/cm^3). However, biogenic sources seem to predominate in these sediments. Ba maxima, particularly during early Termination I, were tentatively interpreted as indicators of productivity spikes which could result from a combination of incursions of cold surface water and enhanced terrigenous input.

An allochthonous chrysotile-dominated serpentine layer is intercalated within pelagic sediments in a basin in the central part of the 38°05'N fracture zone. This material was derived from alteration of ultramafic rocks and may represent a low-temperature hydrothermal deposit associated with this rock type. It was apparently transported down the walls of the fracture zone in this area of steep relief. Cr/Ni-ratios suggest an olivine-enriched protolith, which is in accord with the results of previous petrologic studies of peridotites at the Mid-Atlantic Ridge, and related to the proximity of the Azores hot spot. The predominance of chrysotile suggests that serpentinization took place at temperatures <200°C. Smectite/chlorite mixed layer phases and chlorite formed at the same or slightly higher temperatures. The accessory phases talc and tremolite indicate greenschist facies conditions, which may have occurred prior to serpentinization during a history of retrograde metamorphosis. Alternatively, talc and tremolite were derived from another source area on the walls of the fracture zone.

Zusammenfassung

Um die Herkunft der Sedimente in ihrer zeitlichen und räumlichen Variabilität zu charakterisieren und den hydrothermalen Eintrag zu beschreiben und zu quantifizieren, wurden geochemische und mineralogische Untersuchungen an Kernen vom Mittelatlantischen Rücken (37-39°N) nahe der Hydrothermalfelder Lucky Strike and Menez Gwen durchgeführt und eine detaillierte $\delta^{18}O$-Stratigraphie erstellt.

Die multivariate statistische Analyse geochemischer Daten zeigte das Vorkommen von vulkaniklastischen, ultramafischen, detritischen und hydrothermalen Sedimentquellen, neben biogenem Karbonat, welches die chemische Zusammensetzung der meisten Proben dominiert. Metalle aus hydrothermalen Lösungen (Fe, Mn, Cu) und Elemente, die in der Wassersäule an hydrothermalen Oxyhydroxiden adsorbiert wurden (P, V, As), bilden den hydrothermalen Eintrag im Sediment. Die Verteilung der hydrothermalen Faktorenwerte und der Metallakkumulationsraten zeigt maximalen hydrothermalen Einfluß bei 37°N südlich des Lucky Strike - Hydrothermalfeldes; dies könnte hydrothermalen Eintrag von anderen noch unentdeckten Quellen südlich des Arbeitsgebietes einschließen. Metallakkumulationsraten sind signifikant höher als in Tiefseebenen abseits des Rückens und vergleichbar mit anderen hydrothermal beeinflußten Gebieten. Die Verteilung der hydrothermalen Tracer im Kernprofil wurde durch frühdiagenetische Prozesse überprägt, Mittelwerte der Stoffflüsse zeigen jedoch andauernden hydrothermalen Eintrag zumindest während der letzten 55.000 Jahre.

Barium in Sedimenten am *Lucky Strike seamount* ist offenbar hydrothermalen Ursprungs und entstammt wahrscheinlich umgelagerten hydrothermalen Präzipitaten. Das Vorkommen einer kubischen Phase, vermutlich Sphalerit, in Schwermineralkonzentraten (>3.0g/cm^3) distaler Sedimente könnte auf Eintrag feinkörniger hydrothermaler Sulfide und möglicherweise Baryt aus *plumes* in der Wassersäule hinweisen. Barium ist in diesen Sedimenten jedoch offenbar überwiegend biogenen Ursprungs. Ba-Maxima, vor allem während der frühen Termination I, zeigen vermutlich Produktivitätsmaxima an, die durch Vorstöße kalter Oberflächenwassermassen und erhöhten terrigenen Eintrag bewirkt wurden.

Eine umgelagerte chrysotilreiche Serpentinlage kommt in Sedimenten in einem Becken im zentralen Bereich der 38°05'N *fracture zone* vor. Dieses Material ist ein Alterationsprodukt ultramafischer Gesteine, möglicherweise eine niedrigtemperierte hydrothermale Ablagerung, die später hangabwärts in den tiefsten Bereich des Beckens transportiert wurde. Cr/Ni-Verhältnisse deuten auf ein olivinreiches Ausgangsmaterial. Dies steht im Einklang mit petrologischen Untersuchungen an Peridotiten am Mittelatlantischen Rücken und ist auf den Einfluß des Azoren *hot spots* zurückzuführen. Das Vorkommen von Chrysotil als dominierende Serpentinphase zeigt Bildungstemperaturen <200°C an. Smektit/Chlorit-Wechsellagerungen und Chlorit wurden bei ähnlichen oder etwas höheren Temperaturen gebildet. Die akzessorischen Phasen Talk und Tremolit zeigen grünschieferfazielle Bedingungen an, die in einem früheren Stadium retrograder Metamorphose vorgelegen haben könnten. Talk und Tremolit könnten jedoch auch von einer anderen Lokation am Hang der *fracture zone* umgelagert worden sein.

1. Introduction

The objective of the GEOFAR cruise of RV Le Noroit (July/August 1993, Chief Scientist G.A. Auffret) was to sample pelagic sediments at and adjacent to the ridge axis, in order to investigate temporal and spatial variability of hydrothermal input. The main study area is situated at the Mid-Atlantic Ridge south of the Azores (37-39°N); the Lucky Strike and Menez Gwen hydrothermal sites have been recently discovered in this area (Langmuir et al. 1993, Fouquet et al. 1994, 1995). A second area of investigation is located in the vicinity of a seamount at the ridge axis at 20°30'N, hydrothermal nontronite deposits have been found here on top of the seamount (Auffret et al. 1991).

Sediments have the potential to provide a record of past and present hydrothermal activity which should leave an imprint on long-term sedimentation. Investigations of hydrothermal tracers in sediments can complement studies based on hydrothermal precipitates and hydrothermal particle plumes in the water column, notably because longer timescales (on the order of thousands to millions of years) are involved. Such studies require that sediments were continuously accumulated and that a detailed stratigraphy can be established.

The hydrothermal fraction in sediments should include metals primarily derived from hydrothermal solutions and elements scavenged from the water column (P, V, As). In distal sediments, hydrothermal input is superposed on background pelagic sedimentation with contributions from other sources. In the main study area, biogenic carbonate and opal, volcaniclastic input derived locally from the Mid-Atlantic Ridge and/or from the volcanic islands of the Azores, and detrital contributions from the Azores and the nearby continents may all be present. As some of the tracers may originate from several sources, these have to be separated in order to evaluate hydrothermal input in sediments. For example, iron may be derived from detrital or volcaniclastic sources in addition to Fe-oxyhydroxides in hydrothermal particle plume fallout and hydrothermal sulfides. While hydrothermal precipitates at the Lucky Strike and Menez Gwen fields contain abundant barite, barium has been used as a proxy for paleoproductivity in various off-axis sediments (e.g. Dymond et al. 1992) and must be at least partially of biogenic rather than hydrothermal origin in the area of the present study.

Accordingly, the entire sediment system with contributions from various sources has to be considered rather than discussing the hydrothermal fraction "in isolation". In addition, sediment geochemistry is likely to be affected by early diagenetic remobilization of metals and coprecipitated elements, and by environmental changes during the depositional history, e.g. the last glacial cycle. Paleoceanographic parameters affecting sediment geochemistry may include changing bottom current patterns diverting hydrothermal effluent and productivity fluctuations which, through changes in the supply of organic carbon, in turn drive early diagenetic processes.

Hence, the objectives of this study were to

- **characterize sediment sources in time and space**, based on multivariate statistical analysis of geochemical data, which allowed to determine **element associations of the hydrothermal sediment source**.
- **quantify fluxes of potential hydrothermal tracers**, based on **metal accumulation rates**, consider **spatial and temporal variability of hydrothermal tracers** in the framework of paleoceanography and early diagenetic processes.
- **investigate the origin of barium in ridge-crest sediments, hydrothermal vs. biogenic**, transport mechanisms for hydrothermal barite and possible paleoceanographic implications of fluctuations of the biogenic component.
- characterize the mineral assemblage, geochemistry and genesis of a **sedimentary serpentine layer** at the 38°05'N fracture zone, derived from hydrothermal alteration of ultramafic rocks.

These objectives were achieved based on a synthesis of stratigraphic, geochemical and mineralogical data. Stratigraphy and age control is based on oxygen isotopes of calcareous foraminifera, analogue ages of oxygen isotope events and some absolute ^{14}C-ages by accelerator mass spectrometry (AMS). Geochemical data include X-ray fluorescence (XRF) analysis of bulk sediments and **selective leaching** data (Robbins et al. 1983) which determine the abundance of operationally defined chemical and mineralogical fractions in the bulk sediments and which, through analysis of the leachates, provide information about element partitioning into various phases. Particularly, Fe- and Mn-oxyhydroxide phases can be detected with this method. Such phases may be derived from hydrothermal particle plumes and are susceptible to early diagenetic remobilization. Mineralogical data comprise X-ray diffraction (XRD) of carbonate-free bulk and clay-size fractions, transmission electron microscopy (TEM) of serpentine-bearing mineral assemblages, and Mössbauer spectroscopy on selected samples to characterize chemical forms of iron in sediments.

2. Background information

2.1 Hydrothermal activity in the oceans and related tracers in pelagic sediments

Since the discovery of hot springs on the ocean floor at the Galapagos Rise (Corliss et al. 1979) and the first observations of high-temperature "black smoker" activity on the East Pacific Rise (Spiess et al. 1980, Hékinian et al. 1983), **hydrothermal activity** was documented in a variety of geodynamic settings (see reviews by Rona 1988, Fornari & Embley 1995, German et al. 1995, and recent compilations edited by Humphris et al. 1995 and Parson et al. 1995). Initially, most studies concentrated on fast-spreading ridges such as the East Pacific Rise, and it was widely predicted that the heat flow on slow-spreading ridges would be insufficient to support high-temperature hydrothermal activity. However, it is now clear that hydrothermal activity is also common on slow-spreading ridges such as the Mid-Atlantic Ridge (MAR): After earlier observations at TAG (26°N) and Snake Pit (23°N) (e.g. Rona et al. 1984, 1986, Karson & Brown 1988, Thompson et al. 1988), the Broken Spur site at 29°N (Murton et al. 1994, 1995) and the Lucky Strike and Menez Gwen fields south of the Azores (Langmuir et al. 1993, Fouquet et al. 1994, 1995) were recently discovered. Other settings of hydrothermal activity include back-arc basins (e.g. Lau Basin; Fouquet et al. 1991 a, b) and intraplate volcanoes (Loihi Seamount; De Carlo et al. 1983, Karl et al. 1988; Teahitia and Macdonald seamounts; Hoffert et al. 1987, Puteanus et al. 1991).

Heated seawater reacts with basaltic rocks in hydrothermal convection cells at mid-ocean ridges under reducing conditions at low pH. Hydrothermal solutions subsequently rise to the seafloor and discharge both as diffuse flow and focused low- and high-temperature flow. High-temperature end member solutions have exit temperatures of up to 350°C, and show distinct chemical differences compared to average seawater. They are more acidic, enriched in dissolved metals and H_2S, and completely depleted in Mg and sulfate. Hydrothermal fluxes (injection into or removal from the oceans) for some elements are substantial compared to fluvial input. In particular, the ridge is a major sink for Mg and sulfate, a major source of Li, Rb and Mn and a significant source of Ca, Si and Ba for the oceans (Edmond et al. 1979, 1982, Von Damm et al. 1985).

While massive sulfide deposits on the seafloor and unusually dense biologic communities are restricted to the immediate vicinity of hydrothermal vent sites, hydrothermal input to the water column is dispersed laterally beyond its source. **Hydrothermal plumes** can be detected based on physical (temperature, light attenuation [Nelsen et al. 1986/87]) and chemical parameters (Mn, Fe, CH_4, ^3He, and others [e.g. Weiss et al. 1977, Lupton & Craig 1981, Klinkhammer et al. 1985, 1986]). Three phases of plume development can be differentiated (e.g. Rudnicki & Elderfield 1992): Plumes discharge at the vent site, rise through the water column (***buoyant plume***), and are subsequently dispersed laterally (***neutrally buoyant plume***). The initial rise of the plume is caused by its lower density compared to ambient bottom water (Converse et al. 1984, Little et al. 1987, Speer & Rona 1989). Turbulent entrainment of deep-ocean water into the buoyant plume occurs during this phase of plume development, diluting physical and chemical anomalies and changing the pH and other parameters (Lupton et al. 1985, Kadko et al. 1990). Density equilibrium with surrounding waters is attained about 100-400 m above the seafloor, and the plume becomes neutrally buoyant and spreads laterally (e.g. Rona & Speer 1989, Speer & Rona 1989). In the Pacific Ocean, hydrothermal manganese anomalies in the water column were detected as far away as 2000 km from the ridge axis (Klinkhammer & Hudson 1986). In contrast, plumes at the Mid-Atlantic Ridge generally remain trapped within the rift valley, as their maximum height is less than the depth of the axial valley (Klinkhammer et al. 1985, 1986). Consequently, water column surveys are an effective tool to prospect for new sites of hydrothermal activity at the MAR. Particle-rich plumes and elevated content of various hydrothermal tracers (Mn, He, CH_4) in the water column occur at various locations on the MAR where no active hydrothermal sites on the seafloor have yet been observed (Murton et al. 1994, Bougault et al. 1996, German et al. 1996). The Steinahóll vent-field at 63°N on the Reykjanes Ridge (German et al. 1994) and the Rainbow site at 36°18'N (German et al. 1996) were proposed based on the strongest water column signals.

Dispersal and changing composition of hydrothermal particles during all phases of plume development have been studied by means of theoretical calculations (Feely et al. 1987, Rudnicki & Elderfield 1993), sediment trap experiments (Dymond & Roth 1988), and water column sampling of buoyant and neutrally buoyant plumes (e.g. Baker & Massoth 1987, Trocine & Trefry 1988, Walker & Baker 1988, Mottl & McConachy 1990, Feely et al. 1990, 1992, German et al. 1991). These studies show that the particle composition is modified by

- **differential particle settling:** Coarse-grained sulfide and sulfate particles enriched in Fe, Zn, Cu and Cd settle rapidly within a few hundred meters of the vent, whereas fine-grained (<2μm) Fe- and Mn-oxyhydroxides and possibly some fine-grained sulfides are laterally dispersed in the neutrally buoyant plume (Feely et al. 1987, 1990). At the TAG site, 50% of total dissolved iron is rapidly removed as sulfides, and the remaining fraction precipitates as oxyhydroxides (Rudnicki & Elderfield 1993).
- **coprecipitation / scavenging of trace elements from seawater:** The strong correlation between Fe and P, As and V in hydrothermal particle plumes has been interpreted in terms of scavenging of these elements from seawater by hydrothermal Fe-oxyhydroxides in the buoyant plume (Trocine & Trefry 1988, Trefry & Metz 1989, German et al. 1991, Feely et al. 1991, 1992). The ratios of P, As and V to Fe remain constant during later phases of plume development, indicating that no further uptake on Fe-oxyhydroxides occurs in the neutrally buoyant plume. Therefore, Rudnicki & Elderfield (1993) suggested coprecipitation *during* rather than scavenging *after* particle formation as a more likely process. Coprecipitation or scavenging processes may be significant for the geochemical budget of P, V and As in the ocean (Trefry & Metz 1989, Kadko 1993, Rudnicki & Elderfield 1993).

- **differential precipitation of Fe-and Mn-oxyhydroxide phases:** Whereas Fe-oxyhydroxides precipitate almost quantitatively (>95%) at plume height, Mn remains in solution (Coale et al. 1991, German et al. 1991, Feely et al. 1992). There is growing evidence for microbial mediation of manganese scavenging (Cowen et al. 1986, 1990, Mandernack & Tebo 1993), and Cowen et al. (1990) proposed that elevated levels of dissolved Mn in proximal parts of the plume may be toxic for metal-depositing bacteria. Thus, bacterial Mn scavenging would only occur in more distal parts of the plume, with dissolved Mn levels sufficiently diluted by ambient seawater. On the other hand, manganese scavenging at the Juan de Fuca Ridge was not significantly affected by poisoning with sodium azide, suggesting that manganese scavenging occurs by an abiological mechanism, such as coprecipitation with iron oxyhydroxides (Mandernack & Tebo 1993).

  The net effect of differential precipitation of Mn vs. Fe is fractionation of these metals in both hydrothermal particle plumes and underlying metalliferous sediments, with Mn being deposited in more distal areas. Eventual Mn deposition in sediments may also be facilitated by metal-depositing bacteria, as manganate-coated bacteria tend to settle out from the vent plume and accumulate near the bottom (Mandernack & Tebo 1993) and bacterial macroaggregates with high settling velocities in the water column may form (Lavelle et al. 1992).

Fallout from hydrothermal particle plumes is subsequently deposited in underlying sediments (for a recent review of ridge-crest metalliferous sediment geochemistry, see Mills & Elderfield 1995). Early observations by Bostrøm and co-workers that sediments on active ridge crests are enriched in Fe and Mn and depleted in Al already suggested a genetic relationship between high heat flow, ocean-floor spreading, and metal-enriched sediments, predating the discovery of hot springs on the ocean floor. The ratio of Al/(Al+Fe+Mn) in surface sediments effectively delineates the ocean ridge system (Bostrøm & Peterson 1966, 1969, Bostrøm et al. 1969, Bostrøm 1973). These authors had proposed that Fe and Mn in ridge-crest sediments are derived from "mineralizing emanations" ultimately originating in the upper mantle. Further studies showed that a distinct hydrothermal fraction enriched in Mn, Fe, Zn, Cu, As, V, and P can be identified in pelagic sediments at and adjacent to the East Pacific Rise (Dymond 1981, Marchig & Gundlach 1982, Walter & Stoffers 1985, Marchig et al. 1986). At the Mid-Atlantic Ridge, similar investigations concentrated on the FAMOUS (37°N; Scott et al. 1979) and TAG (26°N; Shearme et al. 1983, Metz et al. 1988) areas. Later studies at TAG also identified a contribution from mass wasting of sulfide debris; both plume fallout and sulfide mound debris are superimposed on background biogenic and detrital sedimentation (German et al. 1993, Mills et al. 1993).

Sediments in the vicinity of active sites have the potential to record **temporal variability of hydrothermal activity**, based on the abundance variations or accumulation rates of hydrothermal tracers. This requires that sediment accumulation was continuous without perturbations by major slump events, and that their chronostratigraphy can be established. Furthermore, a suite of cores has to be investigated, as changes in hydrothermal input at a single site may simply be related to diversion of the hydrothermal effluent by changing bottom current patterns. On a time scale of millions of years, fluctuations of hydrothermal activity have been correlated to volcano-tectonic events at the East Pacific Rise (Lyle et al. 1986, 1987) and in the Lau back-arc basin (Hodkinson & Cronan 1994). Pulsed hydrothermal activity during the last 10,000 years has been observed on the East Pacific Rise (Shimmield & Price 1988). Radiometric dating of hydrothermal deposits at the TAG field revealed that hydrothermal activity has been episodic during the last 140,000 years (Lalou et al. 1990, 1993, 1995).

2.1 Geological setting and hydrothermal activity in the Azores study area

The main study area is located at the Mid-Atlantic Ridge south of the Azores in the vicinity of the triple junction separating the American, Eurasian and African plates (Fig. 2.1). Detailed multibeam bathymetry data of the Mid-Atlantic Ridge in the study area, collected during the SIGMA cruise of RV *l'Atalante* (Needham et al. 1992), are presented in Fig. 2.2. The generally shallow depth of the ridge axis, with topographic highs in the center of segments rising up to 700 m water depth, is an effect of the proximity of the Azores hot spot (Detrick et al. 1995). Second-order ridge segments trending NNE-SSW are separated by right-stepping non-transform discontinuities forming depressions with maximum water depths exceeding 3000 m. This pattern results in an overall NE-SW orientation of the ridge (Fig. 2.2).

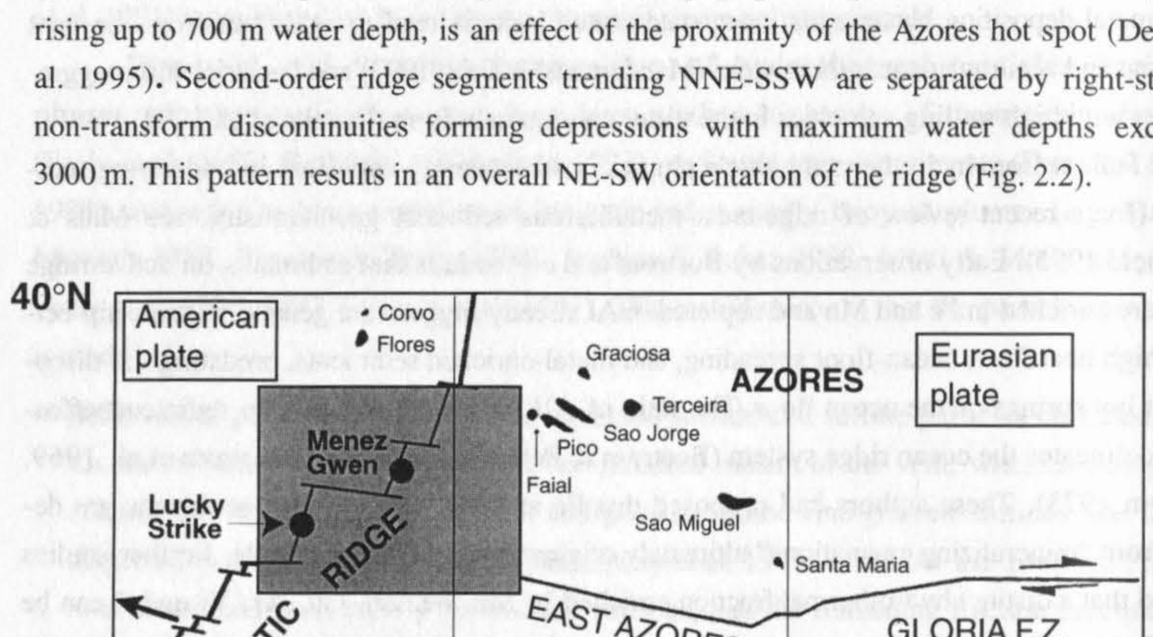
40°N
American plate
Corvo
Flores
Graciosa
AZORES
Eurasian plate
Terceira
Sao Jorge
Pico
Menez Gwen
Faial
Lucky Strike
Sao Miguel
Santa Maria
RIDGE
EAST AZORES F.Z.
GLORIA F.Z.
MID ATLANTIC
African plate
35°N
30°W
25°W

Fig. 2.1: Plate tectonic setting of study area south of the Azores (redrawn after Fouquet et al. 1994). Shaded rectangle represents area shown in bathymetric maps (Figs. 2.2 and 2.3). Black dots show location of hydrothermal sites.

Fig. 2.2 *(following page)*: Bathymetry of the Mid-Atlantic Ridge in the Azores study area (data obtained by D. Needham, IFREMER Brest, during SIGMA cruise of RV *l'Atalante*)

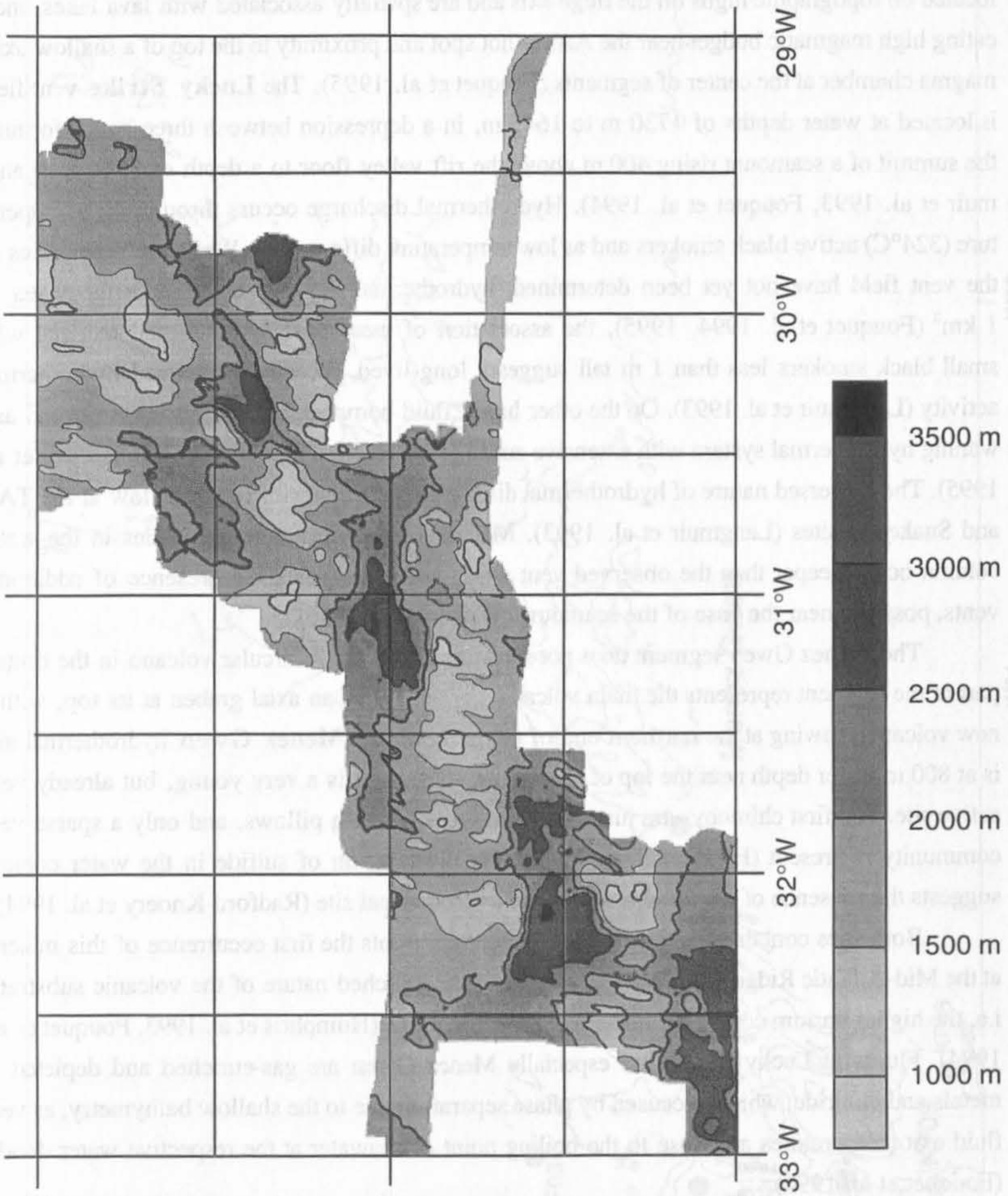
29°W
30°W
31°W
32°W
33°W
39°N
38°N
37°N
3500 m
3000 m
2500 m
2000 m
1500 m
1000 m

Hydrothermal venting was recently discovered in the study area at the **Lucky Strike** and **Menez Gwen** sites (Langmuir et al. 1993, Fouquet et al. 1994, 1995). Both sites are located on topographic highs on the ridge axis and are spatially associated with lava lakes, indicating high magmatic budget near the Azores hot spot and proximity to the top of a shallow axial magma chamber at the center of segments (Fouquet et al. 1995). The **Lucky Strike** vent field is located at water depths of 1730 m to 1645 m, in a depression between three cones forming the summit of a seamount rising 400 m above the rift valley floor to a depth of 1570 m (Langmuir et al. 1993, Fouquet et al. 1994). Hydrothermal discharge occurs through high-temperature (324°C) active black smokers and as low temperature diffuse flow. While the boundaries of the vent field have not yet been determined, hydrothermal deposits cover a surface area of 1 km^2 (Fouquet et al. 1994, 1995), the association of weathered hydrothermal material with small black smokers less than 1 m tall suggests long-lived, recently reactivated hydrothermal activity (Langmuir et al. 1993). On the other hand, fluid compositional data suggest an old and waning hydrothermal system with extensive zones of subseafloor alteration (Klinkhammer et al. 1995). The dispersed nature of hydrothermal discharge contrasts with focused flow at the TAG and Snake Pit sites (Langmuir et al. 1993). Methane and temperature anomalies in the water column occur deeper than the observed vent sites, which suggests the presence of additional vents, possibly near the base of the seamount (Wilson et al. 1996).

The Menez Gwen segment does not show a central rift. A circular volcano in the central part of the segment represents the main volcanic center. It has an axial graben at its top, with a new volcano growing at the northern end of the graben. The **Menez Gwen** hydrothermal site is at 800 m water depth near the top of this young volcano. It is a very young, but already very active site. The first chimneys are just starting to grow on fresh pillows, and only a sparse vent community is present (Fouquet et al. 1994). The distribution of sulfide in the water column suggests the presence of a second unidentified hydrothermal site (Radford-Knoery et al. 1994).

Both sites contain abundant **barite**, which represents the first occurrence of this mineral at the Mid-Atlantic Ridge. This may be related to the enriched nature of the volcanic substrate, i.e. the higher barium content of underlying basaltic rocks (Humphris et al. 1993, Fouquet et al. 1994). Fluids at Lucky Strike and especially Menez Gwen are gas-enriched and depleted in metals and chloride, which is caused by phase separation due to the shallow bathymetry, as vent fluid exit temperatures are close to the boiling point of seawater at the respective water depths (Fouquet et al. 1994).

During the GEOFAR cruise, gravity cores were retrieved along three E-W transects across the ridge axis, complemented by cores Ac.KS04 and -KS05 obtained by the hydrographic service of the French Navy (EPSHOM) (Fig. 2.3). Other gravity cores and box cores have been obtained in the vicinity of the Lucky Strike seamount (not shown in Fig. 2.3)

Fig. 2.3 *(following page)* : Location of GEOFAR sediment cores in the study area south of the Azores. Bathymetry obtained by D. Needham during SIGMA cruise of RV*l'Atalante*. Ridge axis segments and non-transform discontinuities schematically shown by continuous and broken lines, respectively. For geographic location of study area, refer to Fig. 2.1.

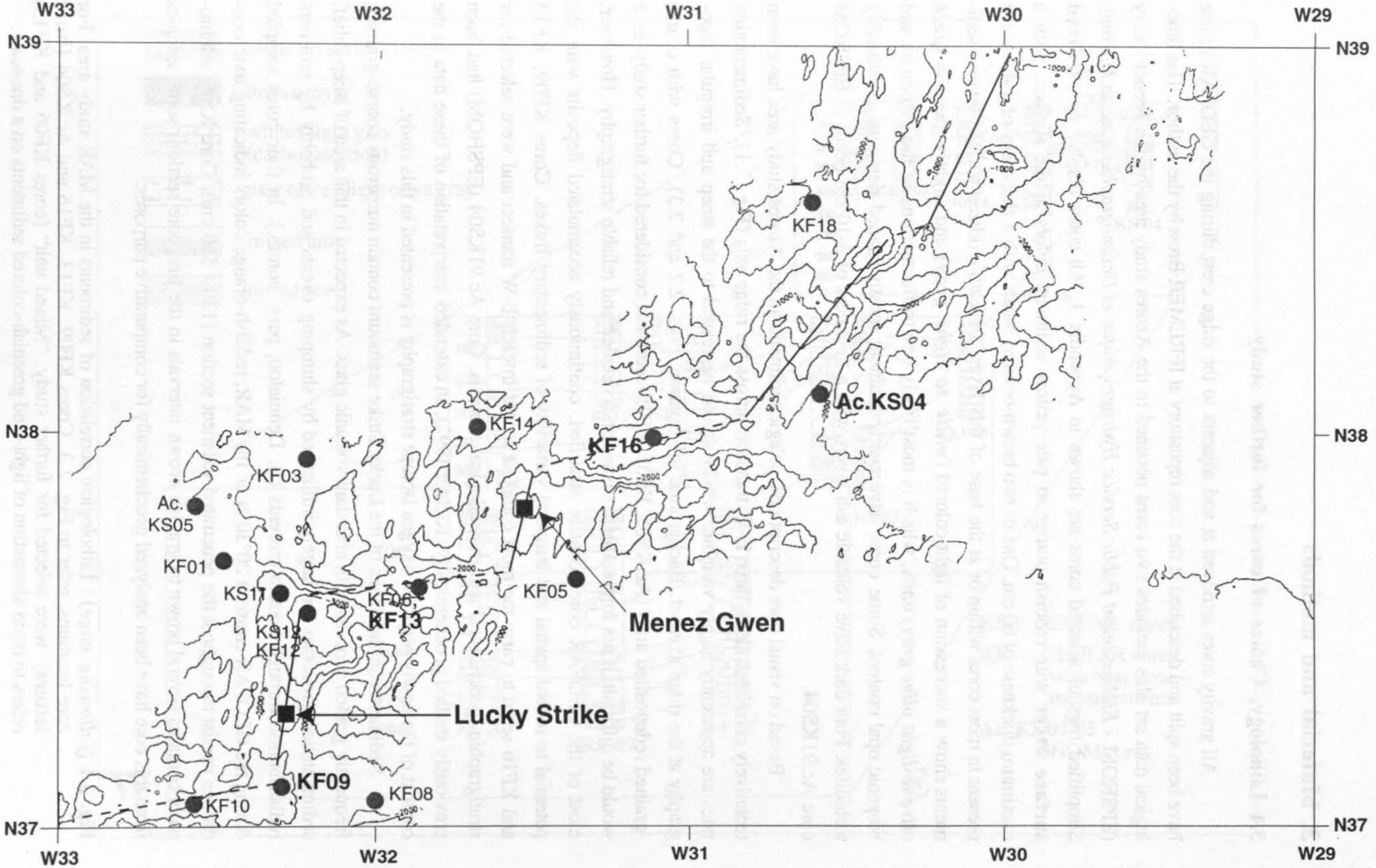
W33
W32
W31
W30
W29
N39
N38
N37
-1000
-2000
KF18
Ac.KS04
KF14
KF16
KF03
Ac.
KS05
KF01
KS17
KF06
KF13
KS12
KF12
KF05
Menez Gwen
Lucky Strike
KF09
KF10
KF08

3. Material and methods

3.1 Lithology, Choice of cores for further study

All gravity cores retrieved at and adjacent to the ridge crest during the GEOFAR cruise have been split and described at the core repository at IFREMER Brest by the author. The lithological data set also includes two cores obtained in the Azores study area by the French Navy (EPSHOM - *Etablissement Public Service Hydrographique et Océanographique de la Marine*). Simplified logs of selected cores are shown in Appendix 1. All cores display an **oxidized surface layer** with reddish orange to pale yellow sediment colors at the surface, with a maximum thickness of 60 cm. One or two brown-colored bands with a thickness of 1-5 cm are present in most cores within or at the base of this layer. Beneath oxidized surface layers, sediments show a succession of light-colored (***white to light gray***) and slightly greenish (***pale olive to light olive gray***) units, which is most likely due to fluctuations of the carbonate and biogenic opal content. Some cores have coarse-grained, mostly graded deposits, presumably turbidites. Four dark olive volcanic ash layers with a thickness of 3-10 cm occur in EPSHOM core Ac.91KS04.

Based on visual core descriptions, pelagic sediments in the Azores study area have been tentatively correlated along three E-W transects across the ridge axis (Fig. 3.1). Sedimentation rates are apparently highly variable, which should be related to the steep and irregular topography at the ridge axis (cf. Background information, Figs. 2.2 and 2.3). Cores with coarse -grained redeposited units (Ac.KS05, KF03, KF05) were not considered for further study, as it would be difficult, if not impossible, to establish a detailed and reliable stratigraphy. However, most of the GEOFAR cores contain stratified, continuously accumulated deposits with the potential to record spatial and temporal variability of sedimentary fluxes. Cores KF09, KF13 and KF16 seem to carry the most complete record in each E-W transect and were selected for stratigraphic, geochemical and mineralogical analysis. Core Ac.91KS04 (EPSHOM) had been previously studied geochemically (Richter 1992), an extended interpretation of these data in the context of the newly acquired oxygen isotope stratigraphy is presented in this study.

Sediments on the flanks of the Lucky Strike seamount contain numerous coarse-grained, frequently graded deposits with abundant volcanic glass. As expected in this area of steep relief, sedimentation processes are largely influenced by slumping events and probably by sediment redistribution through bottom currents (B. Dennielou, pers. comm.). In four cores sampled during the GEOFAR cruise at 20°30'N on the MAR, reddish-orange colors indicating oxic conditions persist throughout the penetrated sediment section (130 - 500 cm). Core KS03 additionally contains several brown to grayish brown intervals in the first core section; some samples from this core have been analyzed geochemically for comparative purposes.

Fig. 3.1 *(following page)* : Lithological correlation of sediments in the MAR study area. For core locations, refer to Fig. 2.3. Cores KF09, KF13, KF16 and Ac.KS04 **(bold letters)** were selected for further study. "Mixed unit" (cores KF06 and KF13) refers to rapid alternation of light- and greenish-colored sediments on a dm-scale.

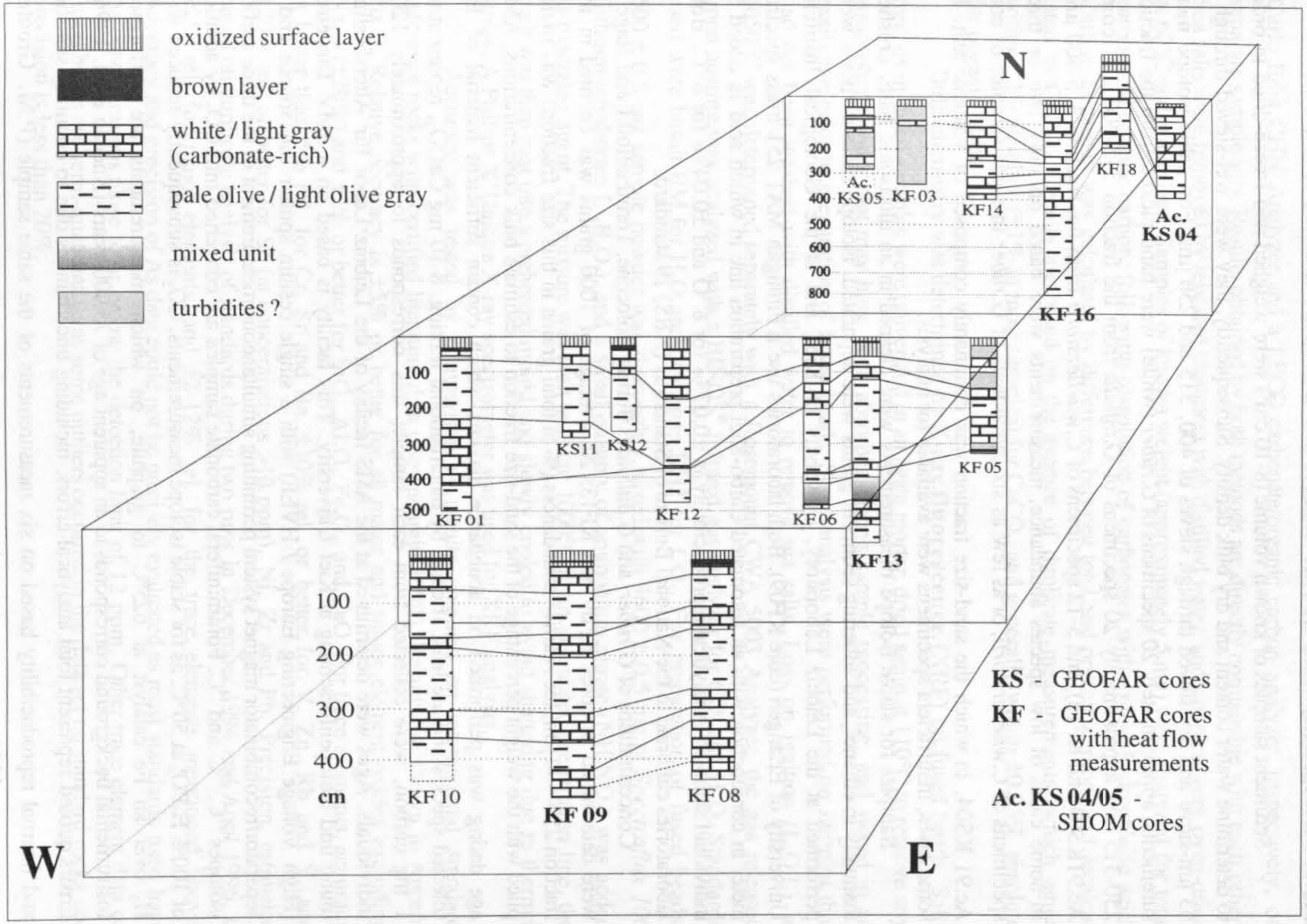
oxidized surface layer
brown layer
white / light gray (carbonate-rich)
pale olive / light olive gray
mixed unit
turbidites ?
N
100
200
300
400
500
600
700
800
Ac. KS 05
KF 03
KF14
KF 16
KF18
Ac. KS 04
100
200
300
400
500
KF 01
KS11
KS12
KF 12
KF 06
KF13
KF 05
100
200
300
400
cm
KF 10
KF 09
KF 08
W
E
KS - GEOFAR cores
KF - GEOFAR cores with heat flow measurements
Ac. KS 04/05 - SHOM cores

3.2 Methods

3.2.1 Stratigraphy

Sediment samples of known volume (8-10 cm^3) were weighed and freeze-dried in order to determine water content and dry bulk density. Subsequently, they were wet-sieved through a 63 µm-sieve and dry-sieved through sieves of 400, 315 and 250 µm. For stable isotope measurements, approximately 20 specimens of *G.ruber* (white) were hand-picked from the fraction 250-315 µm, approximately 20 specimens of *G.inflata* from the fraction 315-400 µm (cores Ac.91KS04 and KF16), and 5-12 specimens of *C.wuellerstorfi* from the fraction 315-400 µm. In some cases of low species abundance, measurements were based on only two or three specimens of *C.wuellerstorfi*, or as few as six individuals of *G.ruber* in some samples of core Ac.91 KS04, in which the sand-size fraction was dominantly composed of volcanic ash. In some cases, insufficient specimens were available for analysis.

Samples for stable isotope measurements were cleaned in an ultrasonic bath, crushed manually in ethanol, and adhering sediment grains were separated. Isotope measurements were performed at the Leibniz Laboratory, University of Kiel, and at the Geological Institute, University of Erlangen (core KF09). Both laboratories use a Finnigan MAT 251 mass spectrometer in conjunction with an automated Carbo-Kiel preparation line in which acid is added to individual samples. Analytical reproducibility is ±0.07‰ for $\delta^{18}O$ and ±0.04‰ for $\delta^{13}C$. Both laboratories calibrate to the National Bureau of Standards (NBS) 19 standard.

Concentrations of *G.ruber* and *G.bulloides* during Holocene, Termination I and stage 2 were determined in cores KF09 and KF13. An average of 1000 grains was counted in the fraction 250-400 µm; the *relative* abundances (% of total grains in this size fraction) was multiplied with the weight percentage of the sand-size fraction to estimate bulk concentrations. AMS age dating was performed on abundance maxima which contain sufficient material of the selected species and are least affected by bioturbational mixing. 8-10 mg $CaCO_3$, representing 1 mg carbon, were collected from each sample; this corresponds to approximately 1200 individuals. Ages were determined at the AMS facility of the Leibniz Labor für Altersbestimmung und Isotopenforschung at Kiel University. This facility is based on a 3MV Tandetron (High Voltage Engineering Europe / HVEE) with a single cesium sputter ion source and a separator/recombinator magnet system permitting simultaneous measurement of the three carbon isotopes ^{12}C, ^{13}C and ^{14}C. Foraminiferal carbonate samples are converted into CO_2 by addition of 100% H_3PO_4 at 50°C, as for stable isotope measurements. CO_2 is subsequently reduced with H_2 over an Fe catalyst at 625°C to graphite, on which measurements are performed. Instrumental background corresponds to an apparent age of 75,000 years (Nadeau et al. 1996). Errors quoted represent total analytical errors, including uncertainties due to counting statistics and internal reproducibility based on six measurements of the same sample (P.M. Grootes, pers. comm. 1996).

3.2.2 Geochemistry

Two sets of **calcium carbonate** and **organic carbon** determinations were run on a Carlo Erba CHN Analyzer and a LECO carbonate/organic carbon analyzer, respectively, on separate sample sets. Results obtained by both methods are directly comparable with each other. Sea salts were removed by repeated treatment with distilled water, and samples were oven-dried at 60°C and pulverized. Samples of known weight (approximately 5 mg) were analyzed for total carbon and organic carbon, following dissolution of carbonates with excess hydrochloric acid. Carbonate carbon was calculated by difference between total and organic carbon, and recalculated as $CaCO_3$. Results are based on the average of duplicate measurements, which agree within ±2% absolute (±1% in most samples) for $CaCO_3$, and generally within ±0.05% absolute for organic carbon.

Bulk chemistry was determined by **X-ray fluorescence** (XRF) on fused beads. Salt-free, oven-dried samples were pulverized in an agate mortar, dried again at 110°C to remove any atmospheric water that may have been absorbed during sample processing, and stored in an exsiccator prior to preparation of fused beads. Some analysis were performed on samples that had not been washed with distilled water to remove sea salts. Loss on ignition (L.O.I.) at 1050°C was determined separately with a Rosemount CWA 5003 Analyzer, the gas released upon heating was analyzed with a BINOS$^{®}$ infrared gas analyzer for CO_2 and H_2O. Standards used were basalt BM for H_2O and limestone KH2 for CO_2. For preparation of fused beads, 600 ± 0.5 mg sample powder was thoroughly mixed with 3600 ± 0.5 mg of *Spectroflux 100* (lithium-tetraborate $Li_2B_4O_7$), and a small quantity of ammonium nitrate (NH_4NO_3) was added as oxidizing agent. The mixture was melt at about 1000°C in an automated preparation line, the melt was then cast into a preheated mould and slowly cooled to avoid shattering due to thermal stress. A Philips X'Unique X-ray spectrometer was used for XRF analysis.

Accuracy was tested by comparison of results obtained on international standard reference rocks with certified literature data (Govindaraju 1994). Results are shown in Appendix 3. Relative accuracy is ±5% or better for all major and minor element oxides excluding Na_2O (±20%) and ±2% or better for SiO_2, Al_2O_3, Fe_2O_3, and CaO. For trace elements, accuracy is better than 5% rel. for Cr, Sr and Ba, ±10% rel. or better for V, Zn, Rb and Y, and ±20% rel. or better for Sc (at concentrations >10 ppm), Ni, Zr and Pb. Precision, estimated based on duplicate analysis of standards during two runs in December 1994 and April 1996, is ±2% rel. for major elements, and ±2-12% rel. for the trace elements mentioned above. Accuracy and precision of As data could not be precisely evaluated as most standards used have As concentrations close to or below the detection limit of 12 ppm. Other trace element data on fused beads are semi-quantitative as some outliers occurred in the data set on standard rocks and precision is less than 20%.

Various **selective leaching** techniques were applied to determine element partitioning between operationally defined chemical and mineralogical fractions in sediments (e.g. Chester & Hughes 1967, Tessier et al. 1979, Robbins et al. 1984, Fitzgerald et al. 1987). The method of Robbins et al. (1984) used in the present study accounts for carbonate/sorbed, organic-bound, and oxhydroxide fractions in marine sediments, and a residual fraction insoluble in three successive leaches:

- **Carbonate, sorbed cations, and sea salts** are dissolved with acetic acid buffered with sodium acetate to a pH of 5.0.
- **"Labile" organic matter and organic-bound cations** are extracted with sodium dodecyl sulfate (1%W/V) buffered with sodium bicarbonate ($NaHCO_3$) at pH=8.8 and T=80°C.
- **Fe- and Mn- oxyhydroxides** are removed with hydroxylamine-hydrochloride ($NH_2OH \bullet HCl$) buffered with Na-citrate at pH=5.0.

The **residual fraction** should be dominantly composed of clay minerals and detrital and volcanic aluminosilicate phases.

All leach solutions are strongly buffered at the respective pH values, as the leaching behavior of trace metals may vary as a function of pH (Trefry & Metz 1984). 0.5xxx g of freeze-dried sediment were transferred into 50 ml centrifuge tubes, grinding was avoided as it may affect mineral structures and thus change the leaching behavior. Each extraction was repeated five times to ensure complete dissolution of the respective fraction, individual extraction steps consisted of

(1) addition of 20 ml of the respective leach solution
(2) vortex mixing of sample and leach (10 min.)
(3) disaggregation of sample in an ultrasonic bath (10 min.)
(4) centrifugation (10 min. at 4,000 G) to separate sample and leach
(5) pipetting off the supernate, and transferring it to 100 ml plastic bottles. Supernates from five repeated treatments were combined to yield 100 ml of leach solution.

Between leaching steps, samples were washed with deionized (Milli-Q) water to minimize carry-over of the leachant, dried overnight at 60°C and weighed to determine the weight loss associated with each leaching step.

Iron and manganese were analyzed spectrophotometrically in the carbonate and oxyhydroxide leach solutions. Iron was determined with *Merck Spectroquant® Eisen* as a violet bipyridine complex at 565 nm, manganese with *Merck Spectroquant®14770* as reddish-brown formaldoxime complex at 445 nm. Standard solutions to obtain calibration lines were prepared from the respective leach solutions. As the manganese analysis by the formaldoxime method may be affected by iron interferences (Chiswell et al. 1990, McArthur & Osborn 1989), such interferences were largely eliminated by masking of iron at alkalic pH and selective destruction of iron complexes with a reducing Titriplex® solution, and separate calibration lines for Mn determinations were established at 0, 1, 2, and 3 mg/l Fe. Leach solutions were diluted by 1:10

or 1:50, as required to obtain concentrations in the range of linear extinction (0.05 - 2.5 mg/l Fe and 0.06 - 6 mg/l Mn). Reproducibility based on duplicate measurements is ±10% for iron in the carbonate leach, ±3% (mostly ±1%) for Fe in the oxyhydroxide leach, and ±6% (mostly ±3%) and ±4% for manganese in the carbonate and oxyhydroxide leach, respectively. Chloride in the carbonate leach was determined on selected samples by titration with $AgNO_3$.

3.2.3 Mineralogy

Bulk and carbonate-free mineralogy were determined by **X-ray diffraction (XRD)**. A Phillips diffractometer with Co radiation was used, pulverized samples were scanned from 2-75° 2Θ with a scanning speed of 0.05° 2Θ/s. Carbonate was removed with 20% acetic acid. The MacDiff 3.0 software written by R. Petschick (University of Frankfurt/Main) installed on a Macintosh Power PC was used for graphic presentation, determination of peak positions and mineral identification.

For determination of **clay mineralogy**, the fraction <2µm was separated in a settling tube (Atterberg method) in a room held at constant temperature. 10 ml 25% ammonia per 100 l deionized water were used as a dispersing agent, resulting in a pH of 9-10. Magnesium chloride ($MgCl_2 \bullet 2H_2O$) was added to allow for settling of the separated clay fraction in plastic beakers. Briefly, subsequent treatment of the clay fraction included removal of $MgCl_2 \bullet 2H_2O$ by repeated washing with distilled water followed by centrifugation, dissolution of carbonate with acetic acid, removal of organic matter with 30% H_2O_2, removal of biogenic opal with Na_2CO_3, and Mg-saturation of clay minerals by adding a 50% $MgCl_2 \bullet 2H_2O$ solution. Subsequently, excess chloride was removed by repeated washing with distilled water followed by centrifugation. Finally, 3 ml of a freshly dispersed 15 ml-suspension were pipetted onto a cellulose filter and filtrated to obtain an oriented sample of the clay fraction. Both untreated and ethylene-glycol solvated oriented samples were analyzed by XRD. Ethylene-glycol solvation was used to identify expandable (smectite) components, samples were exposed to an ethylene-glycol saturated atmosphere in an exsiccator for 24h. Randomly oriented powder samples were scanned from 70-75° 2Θ for identification of 060 reflections.

Selected samples of the clay-size fraction of a serpentine-bearing mineral assemblage were studied by **transmission electron microscopy (TEM)** to identify the serpentine polytype present. EDAX qualitative chemical analysis was used to estimate the chemical composition of amphiboles. The transmission electron microscope at the Institute of Mineralogy and Petrography, Kiel University, was operated by M. Czank. A suspension in ethanol was pipetted onto object trays, the liquid subsequently evaporated.

Selected samples were studied by **Mössbauer spectroscopy** by M. Drodt (Institute of Nuclear Physics, University of Lübeck) to give clues on chemical forms of iron. Oven-dried, pulverized samples were investigated at 77K in transmission geometry with a sample thickness of approximately 1-2 mm; one sample was also analyzed at 4.2K for a more detailed study of the magnetic component.

4. Stable isotope stratigraphy, age control, and sedimentation rates

4.1 Introduction

The alternation of light-colored and greenish-gray units in MAR sediments (cf. Chapter 3.1) indicates fluctuations in biogenic and detrital input and suggests variable sedimentation rates during the last glacial cycle. Determination of metal accumulation rates and hence quantification of fluxes of potential hydrothermal tracers has to be based on a detailed chronostratigraphy, which was primarily derived from planktonic and benthic oxygen isotope records, supported by carbon isotope data. **Oxygen isotopes of calcareous foraminifera** are now well established as the standard stratigraphic tool in carbonate-rich marine sediments; the global sequence of oxygen isotope events has been defined in the 1980's (Imbrie et al. 1984, Pisias et al. 1984, Prell et al. 1986, Martinson et al. 1987).

Age control is based on

- **analogue ages** of oxygen isotope events during the last 30,000 years, according to the $\delta^{18}O$ stratigraphy and chronology of Winn et al. (1991)
- the **chronostratigraphy** of Martinson et al. (1987) obtained by **orbital tuning of oxygen isotope records** (prior to 30,000 years)
- **absolute ages** obtained by **^{14}C accelerator mass spectrometry (AMS)** in cores KF13 and KF09. A detailed age profile in core KF13 allows to test the age interpretations of oxygen isotope data and helps investigating short-term variability of sedimentation rates during the last glacial stage and across Termination I.

Sedimentation rates were calculated by linear interpolation between stratigraphic datums, after conversion of ^{14}C years into calendar years (Table 1).

4.2 Choice of foraminiferal species for $\delta^{18}O$ stratigraphy and AMS ages

The planktonic species *Globigerinoides ruber* (white) and *Globorotalia inflata* and the benthic species *Cibicidoides wuellerstorfi* were selected for oxygen and carbon isotopic analyses; AMS ages were obtained from *G. ruber* (for Holocene samples) and *Globigerina bulloides* (in glacial sections).

The isotopic composition of planktonic foraminifera is affected by their depth habitat in the surface ocean. Planktonic foraminifera are vertically stratified according to temperature preferences (Deuser et al. 1981, Fairbanks et al. 1980, 1982, Curry et al. 1983). *Globigerinoides ruber* was selected for isotopic analysis because it calcifies in the surface mixed layer, and therefore its isotope values are most representative of surface water conditions. A systematic study of various planktonic foraminifera in surface sediments and plankton tows at the Northeast African margin demonstrated that $\delta^{18}O$ values of *G.ruber* delineate patterns of sea-surface temperature (SST) during summer (Ganssen & Sarnthein 1983). The carbon isotopic composition of this species can be interpreted in terms of the nutrient content in surface waters. In this study, the white variety was analyzed, because pink tests show up to 0.5‰ lighter $\delta^{18}O$

and up to 1‰ heavier carbon isotope values than white ones (Deuser et al. 1981, Ganssen & Sarnthein 1983). *Globorotalia inflata* is living throughout the upper 200 m of the water column above the thermocline and documenting SST of the winter season (lit. cit.). This species was analyzed in addition to *G. ruber* in cores Ac.91 KS04 and KF16, where specimens of *G. ruber* were insufficient for isotope analysis in some samples.

Since *G.ruber* calcifies near the surface of the mixed layer, analysis of this species would also yield the most authentic absolute ages, since no "old" carbon was used at calcification. However, sufficient quantities of *G.ruber* were present only in Holocene samples. For samples from Termination I and Isotope Stage 2, *G. bulloides* was analyzed; this species was found to be present in sufficient and fairly constant amounts throughout the sections investigated, hence minimizing the effects of bioturbational mixing. This species occupies a deeper depth habitat; therefore, absolute ages could be biased towards slightly older values.

The benthic foraminifera *C.wuellerstorfi* was chosen for isotope analysis, because this species colonizes an **epibenthic** habitat up to 14 cm above the seafloor (Corliss 1985, Lutze & Thiel 1989, Linke & Lutze 1993); the carbon isotope composition of its tests reliably records ambient bottom water chemistry. In contrast, many other benthic species such as *Uvigerina peregrina* live in (mostly) infaunal and epifaunal habitats, depending on food supply. Their carbon isotopic composition is thus influenced, to a varying extent, by the local pore water composition and closely, but not linearly, correlated with the accumulation rate of organic carbon (e.g. Graham et al. 1981, Zahn et al. 1986, McCorkle et al. 1990).

4.3 Results and Discussion

4.3.1 Oxygen isotope records and AMS age data

Stable isotope records and AMS age data are shown in Figs. 4.1-4.4, numerical data are tabulated in the appendix. If possible, the definition of oxygen isotopic events is based on epibenthic records of *C.wuellerstorfi* . However, this species was frequently rare or absent, particularly during glacial times. No continuous benthic record is available for core KF16, and only few benthic isotope data are available for core KF09, so that the stratigraphy was entirely based on the planktonic record.

Core **Ac.91 KS04** best displays the standard sequence of oxygen isotope events down to isotope stage 5.1, also used to age calibrate the other isotope records. Stratigraphy of the benthic record is almost continuous, excluding Termination I that is defined by just a few data points. In the lower portion of Termination I, the planktonic record seems to be affected by downcore bioturbation. While no detailed abundance counts were performed on this core, *G.ruber* is more abundant in the Holocene. The core top has an apparent age of 9,800 years (oxygen isotope event 1.1); however, the oxidized surface layer is preserved. It is therefore improbable that a sizable Holocene sediment section had originally been present and was completely lost by coring. It seems more reasonable that little or no material was deposited at this site during the Holocene.

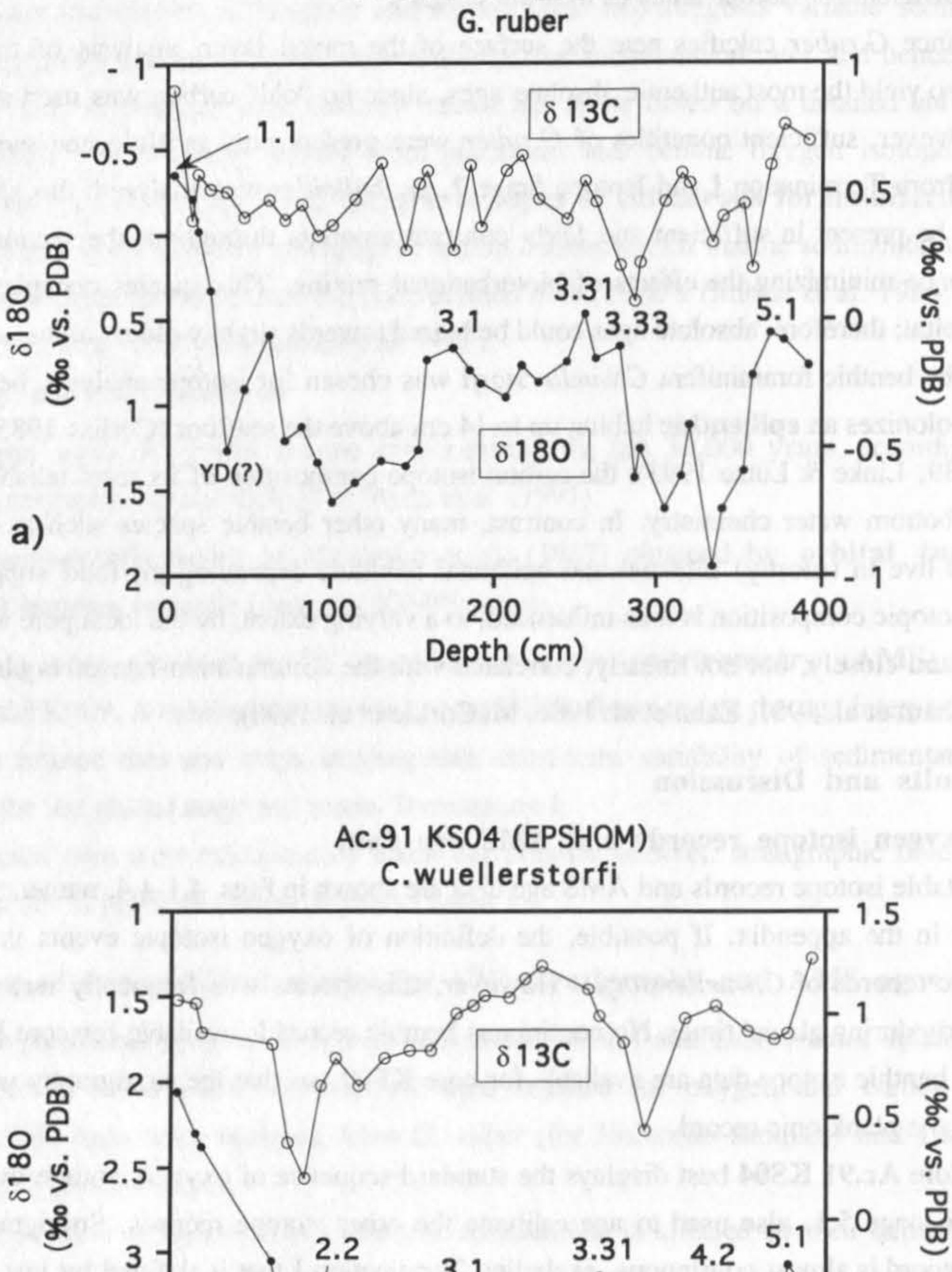

Fig. 4.1: a) planktonic, **b)** benthic stable isotope records of core Ac.91 KS04 (EPSHOM) (38°05.45 N 30°35.84 W / 2184 m water depth)

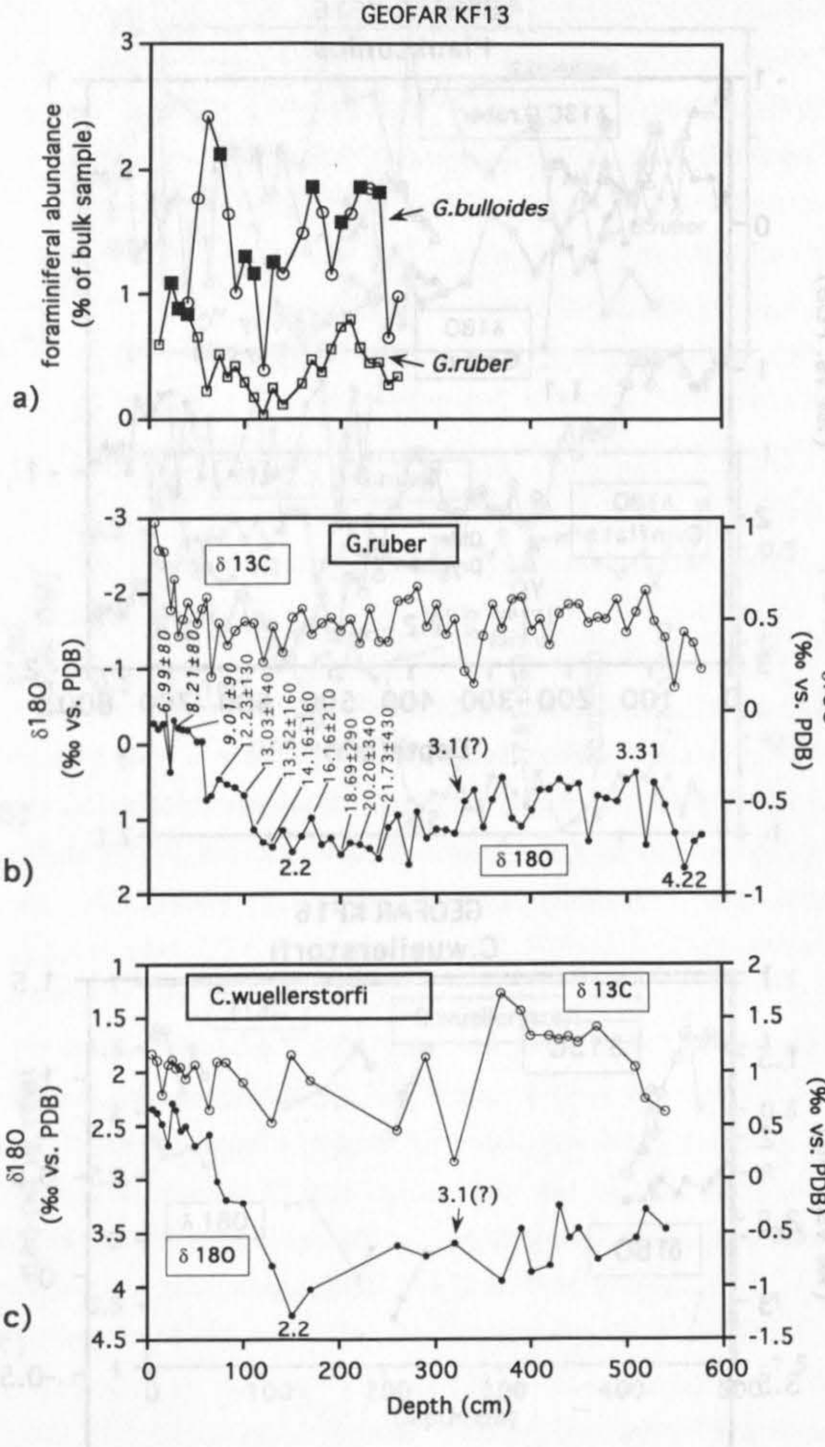

Fig. 4.2: a) concentrations of G.bulloides and G.ruber in core GEOFAR KF13 (37°34.698 N 31°50.53 W / 2690 m water depth). Filled squares indicate samples selected for AMS ^{14}C age dating.

b) planktonic, **c)** benthic stable isotope records. Holocene AMS ages (***bold italic***) based on *G.ruber*, other ages based on *G.bulloides*. All ages are in conventional ^{14}C kyears corrected for the reservoir effect of the ocean (-400 years).

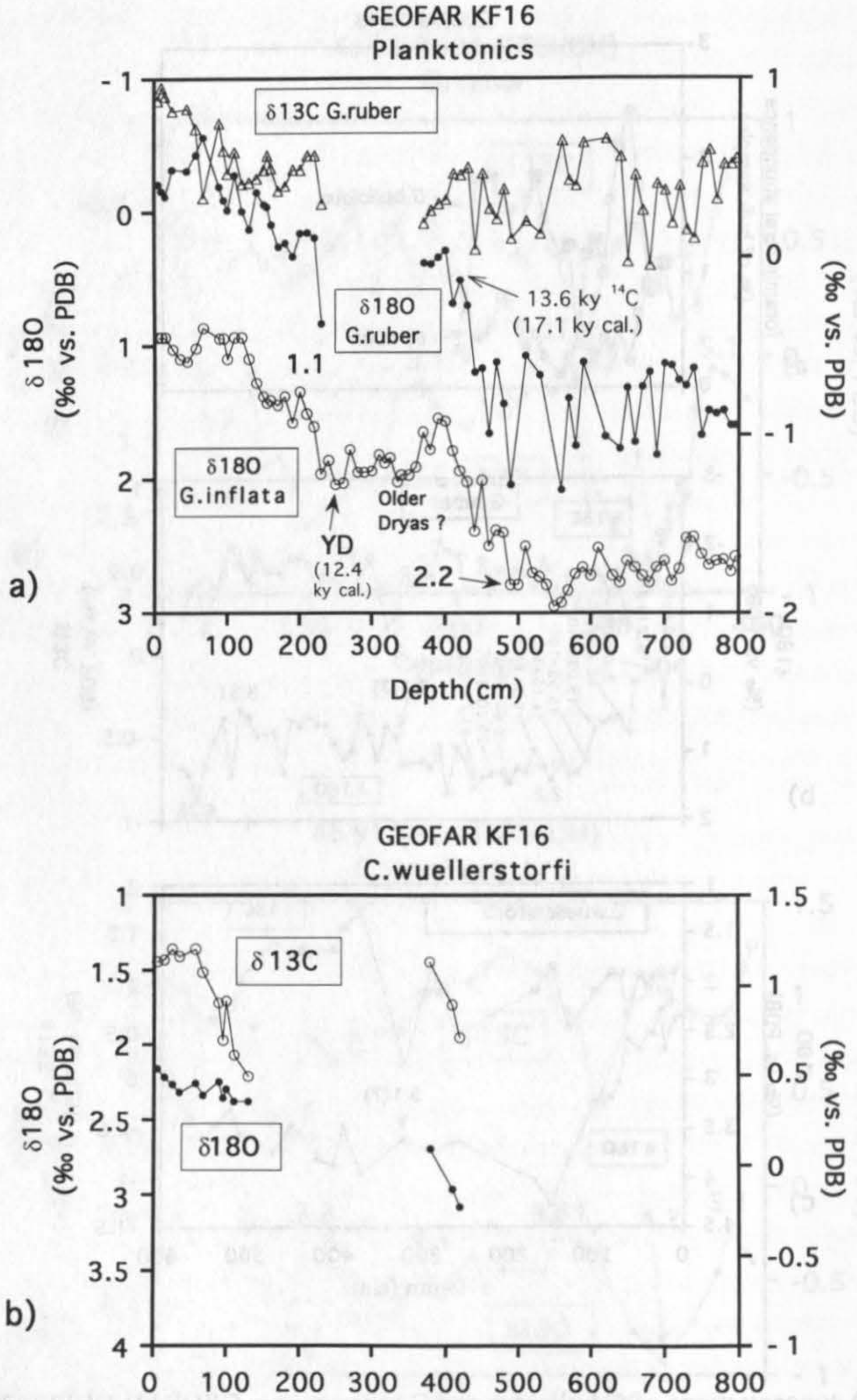

Fig. 4.3: a) planktonic, **b)** benthic stable isotope records of core GEOFAR KF16 (37°59.94 N 31°07.70 W / 3050 m water depth). *(Ages assigned by analogy)*

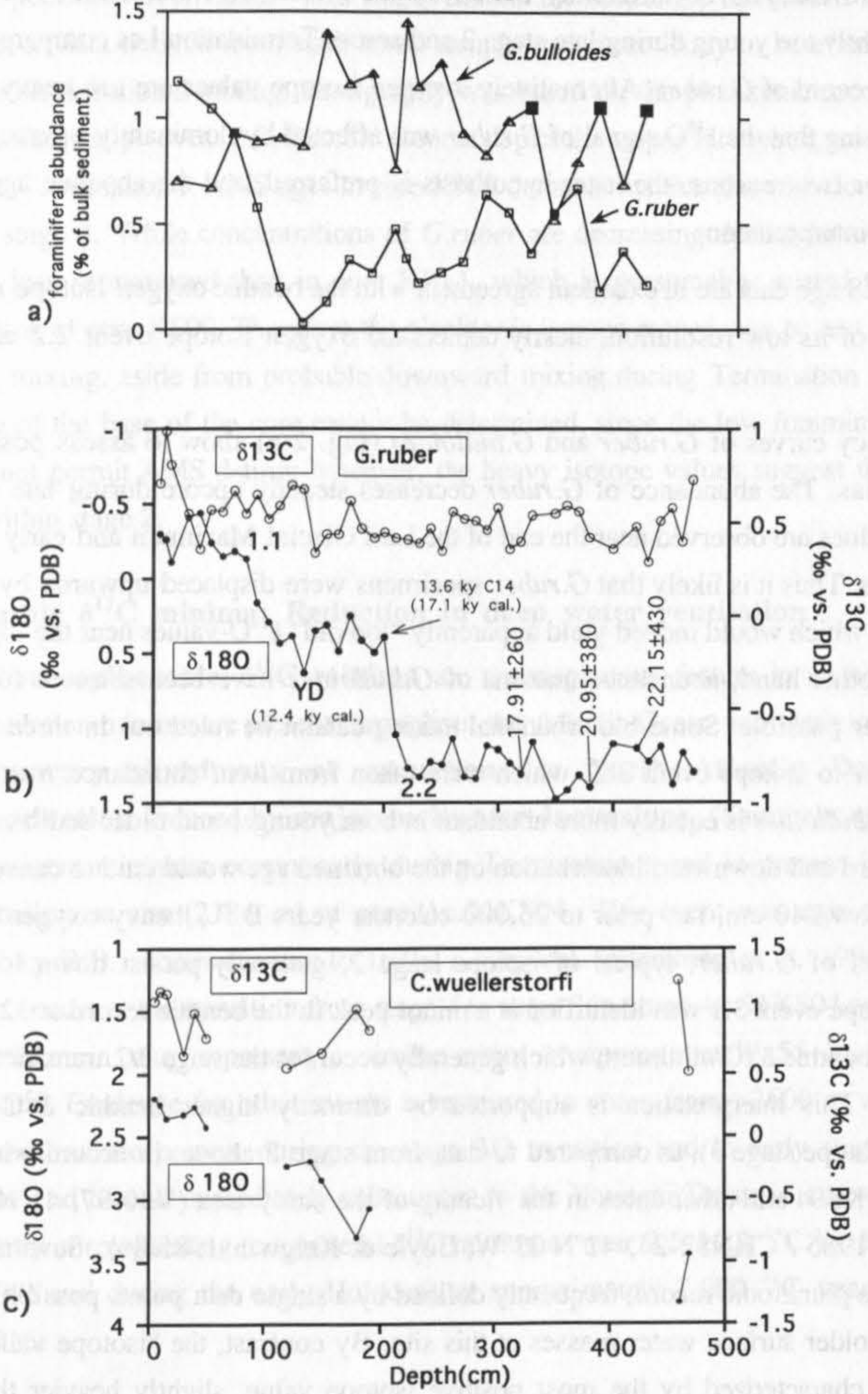

Fig. 4.4: **a)** concentrations of *G.bulloides* and *G.ruber* in core GEOFAR KF09 (37°06.680 N 32° 17.208 W / 2655 m water depth). Filled squares indicate samples selected for AMS ^{14}C age dating.
b) planktonic, **c)** benthic stable isotope records. AMS ^{14}C ages (based on *G. bulloides)* in conventional kyears corrected for the reservoir effect of the ocean (-400 years). Other ages assigned by analogy.

In core **KF13**, detailed AMS ages are available down to 240 cm. While the planktonic isotope record is based on *G.ruber*, most ^{14}C ages were obtained on *G.bulloides* because of insufficient specimens of *G.ruber* during Isotope Stage 2 and Termination I. Hence, the two data sets are likely to be differently biased by the effects of bioturbation: All absolute ages appear slightly too young during late stage 2 and across Termination I as compared to the planktonic $\delta^{18}O$ record of *G.ruber*. Alternatively, oxygen isotope values are too heavy and thus "too old", implying that the $\delta^{18}O$ signal of *G.ruber* was affected by dominantly upcore bioturbational mixing. For two reasons, the latter hypothesis is preferred, and the absolute ages are retained for the age interpretation

- The AMS age data are in excellent agreement with the benthic oxygen isotope record, which, in spite of its low resolution, clearly depicts the oxygen isotope event 2.2 at 150 cm core depth.
- Frequency curves of *G.ruber* and *G.bulloides* (Fig. 2 a) allow to assess possible bioturbational bias. The abundance of *G.ruber* decreases steadily upcore during late stage 2, minimum values are observed near the end of the Last Glacial Maximum and early during Termination Ia. Thus it is likely that *G.ruber* specimens were displaced upwards by bioturbational mixing, which would indeed yield apparently "too old" $\delta^{18}O$-values near the top of the LGM. On the other hand, abundance maxima of *G.bulloides* have been selected for AMS dating wherever possible. Some bioturbational mixing cannot be ruled out in three AMS samples just prior to isotope event 2.2, which were taken from *local* abundance maxima; however, since *G.bulloides* is equally more abundant in both younger and older sediments, the effects of upward and downward bioturbation on the obtained age would tend to cancel each other.

Below 240 cm, i.e. prior to 25,000 calendar years B.P., heavy oxygen isotope values ($\delta^{18}O$ >1‰) of *G.ruber*, typical of isotope stage 2, generally persist down to 320 cm core depth. Isotope event 3.1 was identified at a minor peak in the benthic record at 320 cm, coinciding with a benthic $\delta^{13}C$ minimum which generally occurs at the stage 3/2 transition (Sarnthein et al. 1994). This interpretation is supported by distinctly higher benthic $\delta^{13}C$-values below 320 cm (isotope stage 3), as compared to data from stage 2 above, in accord with results from core Ac.91KS04 and other cores in the vicinity of the study area (V30-97, 41°N 33°W; Mix & Fairbanks 1985 / CHN82-24, 42°N 33°W; Boyle & Keigwin 1985/86). Several $\delta^{18}O$-maxima occur in the planktonic record, frequently defined by a single data point, possibly indicating the arrival of colder surface water masses at this site. By contrast, the "isotope valley" centered at 560 cm is characterized by the most positive isotope value, slightly heavier than at the Last Glacial Maximum, and clearly defined by several data points. This should correspond to isotope event 4.22 (60.4 ky). Accordingly, isotope event 3.31 was fixed at the lightest $\delta^{18}O$-values in the planktonic record, just subsequent to the ascent from heavy values of stage 4, and coinciding with a $\delta^{18}O$-minimum in the benthic record. *C.wuellerstorfi* specimens are absent near the base of the core, hence isotope stage 4 is not depicted in the benthic record.

The other two cores, **KF09** and **KF16**, have only fragmentary benthic $\delta^{18}O$ records. In core KF16, *G.ruber* is also practically absent during the Younger/Older Dryas interval, and rare in the vicinity of the Last Glacial Maximum (LGM). In some cases, analysis had to be based on as few as six specimens of *G.ruber*. This might explain the seemingly disordered nature of its isotope record, as data derived from such small samples are more likely to be affected by analytical error or bioturbational mixing. Stratigraphy was based on the planktonic records in both cores down to the isotope event 2.2. Benthic records depict the upper Holocene, and some data points indicate Termination I. AMS ages in core KF09 demonstrate that the core does not penetrate down to stage 3. While concentrations of *G.ruber* are decreasing during Isotope Stage 2, this pattern is less pronounced than in core KF13, which is presumably related to the more southern location of core KF09. Therefore the planktonic isotope record may be less affected by bioturbational mixing, aside from probable downward mixing during Termination Ib. In core KF16, the age of the base of the core cannot be determined, since the low foraminiferal abundance would not permit AMS dating; however, the heavy isotope values suggest that the base may still lie within stage 2.

4.3.2 Epibenthic $\delta^{13}C$ minima: Reduction in deep water ventilation

Short-lived **epibenthic $\delta^{13}C$ minima** are a conspicuous feature in all cores. These deepwater ventilation minima are present throughout the Atlantic Ocean and were interpreted in terms of **temporary shutdowns or reductions in North Atlantic Deep Water (NADW) production** induced by **major meltwater incursions** (Sarnthein et al. 1994). The most prominent minimum occurs early during Termination I and is present in all cores, even at the shallowest site (2184 m) of core Ac.91KS04. This event was age calibrated at 13.4-13.6 ^{14}C ky B.P., corresponding to 16.9-17.1 ky cal. (Sarnthein et al. 1994). Another $\delta^{13}C$ minimum occurs at the transition from stage 4 to stage 3 in cores Ac.91KS04 and probably KF13; this minimum may represent a similar event at approximately 55 ky (Sarnthein, unpublished data). Evidence for other events is restricted to cores from >2600 m water depth. Further $\delta^{13}C$ minima are present during the stage 3/2 transition and in early stage 2 in core KF13, near the end of and immediately subsequent to the Younger Dryas in cores KF09 and KF13, apparently corresponding to a general $\delta^{13}C$ minimum near 9.5-10.2 ^{14}C ky B.P. (Sarnthein et al. 1994) and during the early Holocene at approximately 7,000 ^{14}C years in KF09, KF13 and KF16.

4.3.3 Temporal and spatial variability of sedimentation rates

Sedimentation rates in all cores are based on analogue ages of oxygen isotope events and available AMS ages, as presented in Table 4.1. During the last 30,000 years, ^{14}C ages do not correspond to true (calendar) ages, which is demonstrated by discrepancies between radiocarbon ages and ages obtained by other methods including annual chronologies, based on tree-rings (e.g. Stuiver et al. 1986, Becker & Kromer 1993) or varved sediments (e.g. Lotter et al. 1992), and U-Th ages (Bard et al. 1990). Mostly, ^{14}C ages are systematically younger, with a maximum difference of 3,500 years prior to 13,200 ^{14}C yrs. B.P. (Bard et al. 1990). Changes in the production of ^{14}C in the atmosphere caused by variations of the geomagnetic field strength appear to be the dominant controlling factor to account for these differences (Stuiver et al. 1991, Mazaud et al. 1992), besides changes in the CO_2 exchange between the ocean and the atmosphere (Sarnthein et al. 1994). The relationship between ^{14}C ages and calendar years is telescopic and partly non-linear due to the presence of major "^{14}C plateaus"; therefore sedimentation rates were calculated in the domain of calendar years only. ^{14}C ages were converted into calendar years according to Stuiver & Braziunas (1993), following the tree-ring chronology of Stuiver et al. (1991) and Becker & Kromer (1993) for the Holocene and the U/Th datings of Bard et al. (1990, 1993) for Termination I and oxygen isotope stage 2.

Sedimentation rates are consistently high (3-30 cm/ky) in the studied cores close to the ridge axis, compared to a regional average of 1.6 cm/ky (G.A. Auffret, written comm. 1995). This may be due to local sediment ponding and may also include the effects of enhanced biogenic productivity and/or preservation and of higher detrital input derived locally from the ridge axis. Among the four cores studied, lowest rates occur in core Ac.91KS04, which is situated in a small basin just outside the MAR rift valley. Higher rates occur inside the rift valley in cores KF13 and KF09, more elevated rates in the latter core are consistent with the regional pattern of higher rates in the southern part of the study area (B.Dennielou, pers. comm.). Very high sedimentation rates in core KF16, which are an order of magnitude higher than in the other cores, are related to the particular core location in the deepest part of a basin in the central area of the 38°05'N fracture zone. This basin appears to act as a sediment trap, implying significant lateral sediment supply at this core site, e.g. including a fine-grained layer with abundant serpentine, which is inferred to be of allochthonous origin (cf. Chapter 9).

Sedimentation rates are higher during isotope stage 2 and the early Termination I than in the Holocene. This assumption may be valid even though some loss of surface sediment is typical of box cores and has certainly occurred in cores KF13 and Ac.91KS04. However, it is rather improbable that a substantial Holocene sediment section has been entirely lost during the coring process in core Ac.91KS04, since the oxidized surface layer is well preserved. For calculation of accumulation rates near the surface of core KF13, constant sedimentation rates of 6.6 cm/ky were assumed for the late Holocene in core KF13. This would imply a loss of 27 cm at the core surface, which is still reasonable for box cores.

Ac.91 KS04 (38°05.45N 30°35.84W / 2183 m water depth)			
Event	**Depth (cm)**	**Age (ky cal.)**	**Sed.rate (cm/ky)**
1.1	4	9.8	
2.2 (LGM)	82	18.3	9.2
3.1	175	29.5	8.3
3.31	263	50.2	4.3 (3.8*)
3.33	278	55.5	2.8
4.2	334	65.2	5.9 (5.2*)
5.1	377	79.25	3.0 (2.4*)

* excluding volcanic ash layers

GEOFAR KF13 (37°34.698N 31°50.53W / 2690 m water depth)					
Event	**foraminiferal species**	**Depth (cm)**	**^{14}C-Age (ky)**	**Age (ky cal.)**	**Sed.rate (cm/ky)**
AMS-Age	*G.ruber*	22	6.99±80	7.43	
AMS-Age	*G.ruber*	30	8.21±80	8.64	6.6±1.0
1.1 + AMS-Age	*G.ruber*	40	9.01±90	9.62	10.2±3.4
Younger Dryas		60	10.4	12.4	7.7±1.1
AMS-Age	*G.bulloides*	73	12.23±130	14.2	7.2±0.5
AMS-Age	*G.bulloides*	100	13.03±140	15.0	33.8±8.6
AMS-Age	*G.bulloides*	110	13.52±160	16.75	5.7±0.9
AMS-Age	*G.bulloides*	130	14.16±160	17.66	31.3±10.5
2.2 (LGM)		150	14.8	18.3	31.3±6.3
AMS-Age	*G.bulloides*	170	16.16±210	19.66	14.7±2.7
AMS-Age	*G.bulloides*	200	18.69±290	22.19	11.9±2.9
AMS-Age	*G.bulloides*	220	20.20±340	23.7	13.2±3.9
AMS-Age	*G.bulloides*	240	21.73±430	25.3	13.1±4.4
3.1		320 ?	26.00	29.5	19.0±1.7
3.3		510		50.2	9.2
4.22		560		60.4	4.9

GEOFAR KF16 (37°59.94N 31°07.70W / 3050 m water depth)

Event	**Depth (cm)**	**Age (ky cal.)**	**Sed.rate (cm/ky)**
1.1	200	9.8	20.4 (18.7 *)
YD	250	12.4	19.2
End Term. Ia	420	17.1	36.2
2.2	490	18.3	58.3
3.1	>800	29.5	>28.6

* excluding allochthonous serpentine layer

GEOFAR KF09 (37°06.680N 32°17.208W / 2655 m water depth)

Event	**foraminiferal species**	**Depth (cm)**	**^{14}C-Age (ky)**	**Age (ky cal.)**	**Sed.rate (cm/ky)**
1.1		80	9.0	9.8	8.9
YD		130	10.3	12.4	19.2
End Term. Ia		200	13.6	17.1	14.9
2.2		230	14.8	18.3	25.0
AMS-Age	*G.bulloides*	320	17.91±260	21.41	28.9±2.2
AMS-Age	*G.bulloides*	380	20.95±380	24.45	19.7±3.4
AMS-Age	*G.bulloides*	420	22.15±430	25.65	33.3±13.4
3.1		>470	26.00	29.5	>13.0

Table 4.1: Summary of age data for cores GEOFAR KF13, Ac.91 KS04, GEOFAR KF16 and GEOFAR KF09. Age control based on analogue ages of oxygen isotope events, and AMS ^{14}C ages in cores KF13 and KF09. Surface sedimentation rates in cores Ac.91KS04 and KF13 not indicated, as some surface sediment was certainly lost during the coring process.

The detailed AMS age profile in core KF13 allows to deduce **short-term variability of sedimentation rates during Termination I**. Between 13.0 and 13.5 ^{14}C kyrs. B.P., the capacity of such investigations is limited by potential artifacts of the conversion from ^{14}C years into calendar years, because the non-linear relationship between the two timescales is particularly pronounced in this time interval, and the extent of ^{14}C plateaus is yet unknown. A pulse of very high sedimentation rates occurs immediately subsequent to the Last Glacial Maximum. AMS ages of 13,520 and 14,160 ^{14}C yrs. B.P. indicate that this interval is coeval to **Heinrich layer 1**, which was AMS-dated at 13,490-14,590 ^{14}C yrs. B.P. at DSDP Site 609 (Bond et al. 1992). No ice-rafted detritus was observed in the coarse fraction, which is not surprising because this core is located slightly south of the main IRD belt from 40-55°N in the Atlantic Ocean (Ruddiman 1977, Grousset et al. 1993). Based on geochemical data it is suggested that this interval was characterized by enhanced continentally-derived detrital input and possibly by higher productivity (cf. Chapter 8). The rapid drop in sedimentation rates above (100-110 cm) may be at least partially an artifact of the conversion from ^{14}C- into calendar years. Therefore, the „amplitude" of a second sedimentation pulse which apparently occurred between 12.2 and 13.0 ^{14}C yrs. B.P. cannot be ascertained. For Isotope Stage 2, sedimentation rates are remarkably constant in core KF13, aside from higher rates in the early part of this stage; on the other hand, the AMS age data indicate highly variable rates in core KF09. Prior to stage 2, sedimentation rates drop in cores Ac.91KS04 and KF13 and rise slightly during stage 4 in the first core.

4.4 Conclusion

Generally, the nature of the isotope records indicates that **continuous accumulation of pelagic sediments** was perturbed by major turbidites and/or hiatuses. Thus the cores selected for geochemical analysis should provide a reliable record of **sedimentary fluxes during the last 30,000 to 80,000 years.**

5. Sediment facies

5.1 Introduction

As discussed above (Chapter 3.1), most box cores in the study area are characterized by a succession of white to light gray and pale olive to light olive gray oozes; this pattern was used to tentatively correlate cores (cf. Fig. 3.1). Based on the oxygen isotope data discussed in Chapter 4, light-colored units generally correspond to Holocene, moderately warm isotope stage 3 and interglacial stage 5 periods, whereas pale olive to light olive gray units correspond to the Younger Dryas cold event and glacial stages 2 and 4. This demonstrates that correlations solely based on visual core descriptions contain at least preliminary stratigraphic information.

In the following section, distributions of calcium carbonate and organic carbon are presented in order to provide background information about the sediment material on which geochemical and mineralogical analysis, discussed in later sections, were performed. It will be demonstrated that sediments in the study area are dominantly carbonate-rich pelagic oozes; hydrothermal input would thus be superimposed on continuous pelagic sedimentation. The lithology of rapidly accumulating sediments in core GEOFAR KF16 will be discussed in more detail, and related to its location in a restricted basin in the central part of the 38°05'N fracture zone.

5.2 Results: Distribution of carbonate and organic carbon

Plots of $CaCO_3$ and organic carbon vs. depth are shown in Figs. 5.1 and 5.2. The depth distribution of $CaCO_3$ generally follows the well-known "Atlantic-type" pattern with higher values in interglacial and lower values in glacial periods (e.g. Kennett 1982).

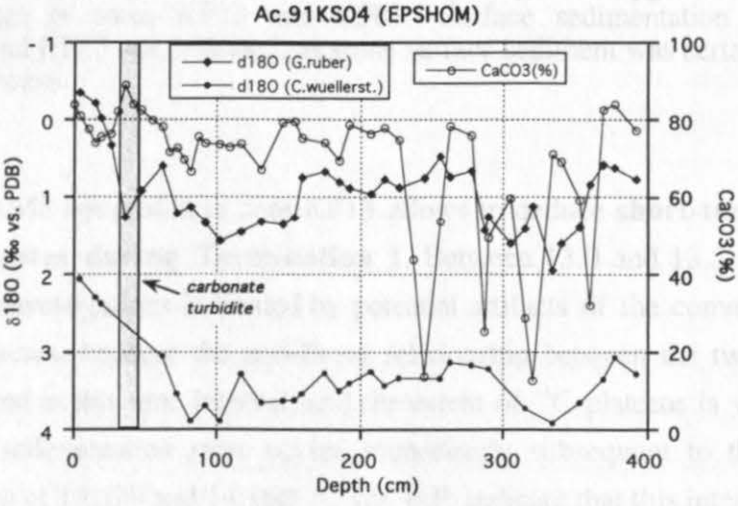

Fig. 5.1: Distribution of $CaCO_3$ vs. depth. Data for core Ac.91 KS04 (*above*) measured by A. Boelaert (IFREMER Brest, France).

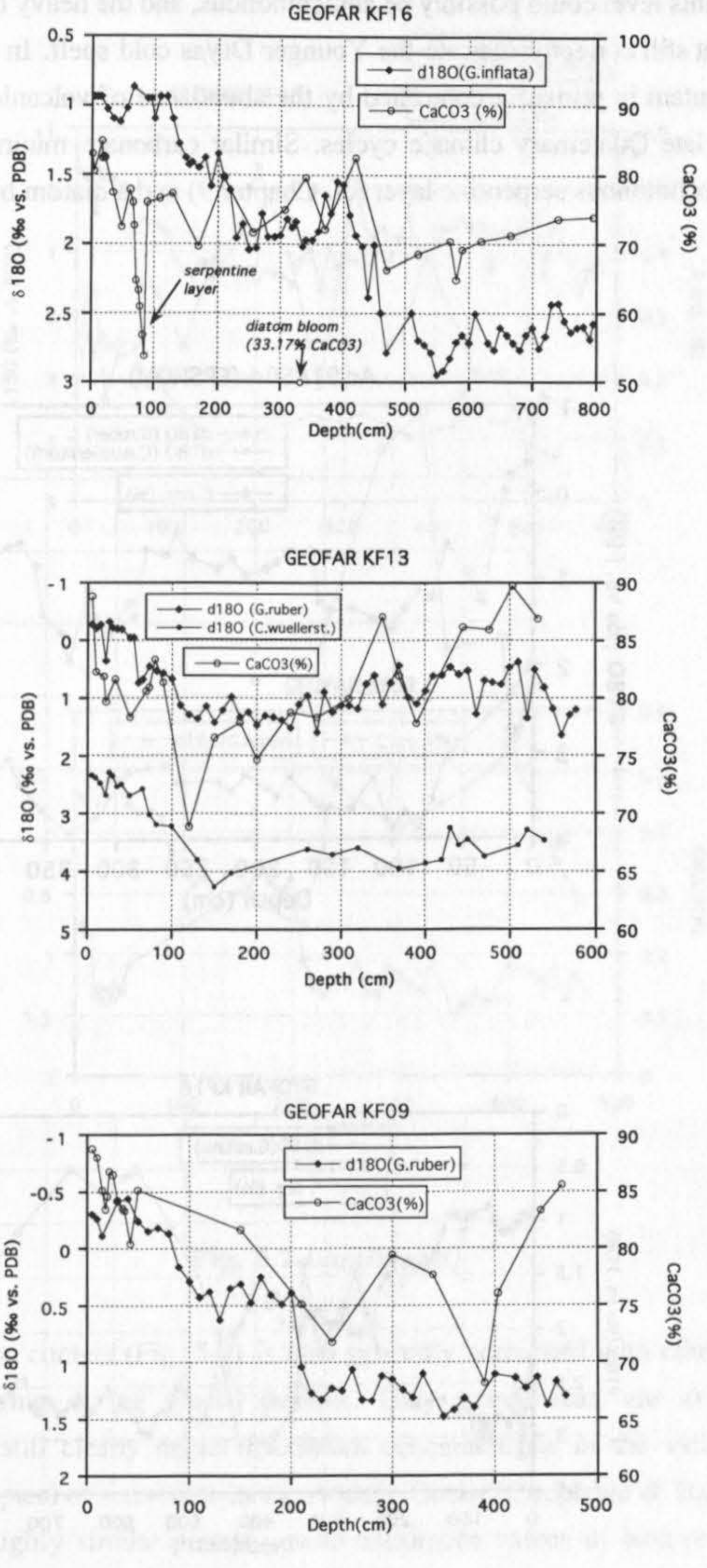

Fig. 5.1 *(continued)*

In core Ac.91KS04, a carbonate maximum around 60 cm occurs in a sandy layer interpreted as a calcareous turbidite. As the sand-size fraction in this layer dominantly contains shallow-water carbonate, mostly shell debris, presumably derived from the Azores platform, the foraminifera at this level could possibly be autochthonous, and the heavy oxygen isotope values of *G.ruber* might still correctly indicate the Younger Dryas cold spell. In the lower part of this core, $CaCO_3$-content is primarily controlled by the abundance of volcanic glass and no longer correlated with late Quaternary climatic cycles. Similar carbonate minima in core KF16 are related to an allochthonous serpentine layer (cf. Chapter 9) and a diatom bloom (cf. below).

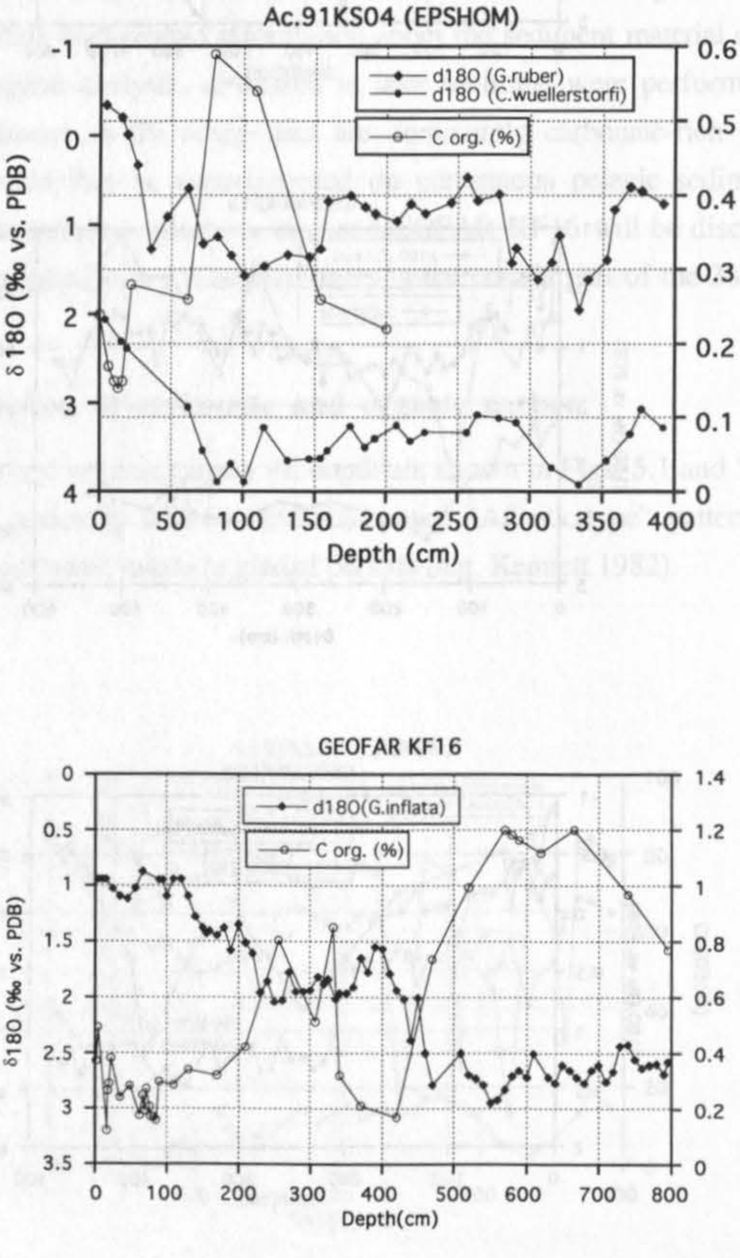

Fig. 5.2: Distribution of organic carbon vs. depth

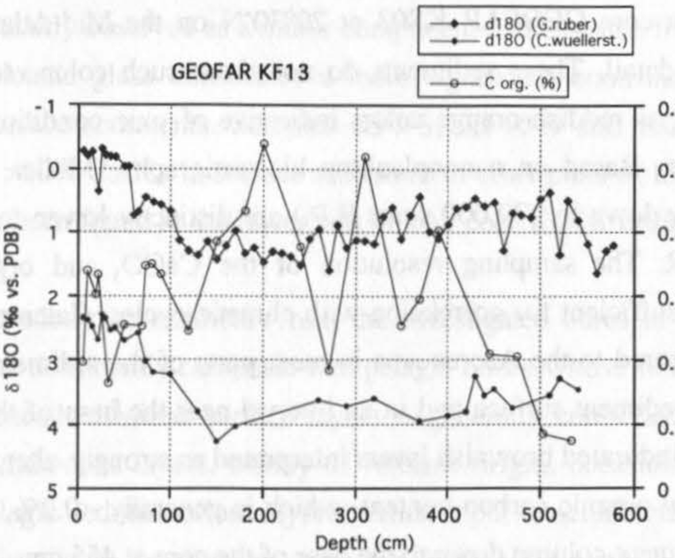

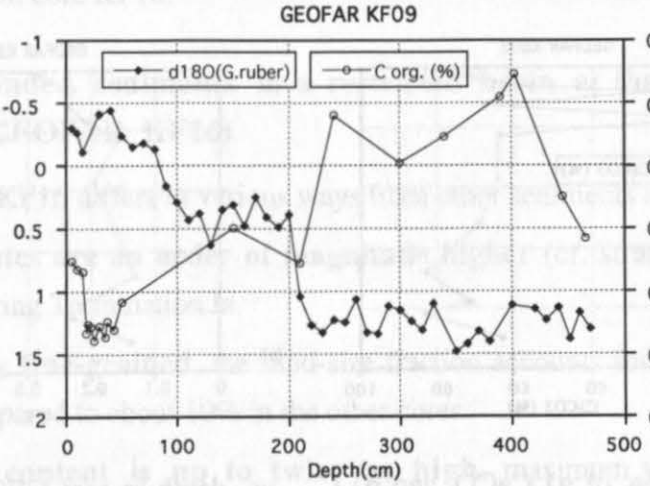

Fig. 5.2 *(continued)*

Organic carbon content (Fig. 5.2) is also generally correlated with climatic cycles, with higher values occurring during glacial periods. Only scarce data are available for core Ac.91KS04, which still clearly depict maximum concentrations in the vicinity of the Last Glacial Maximum, typical of sediments in the Atlantic Ocean (Coppedge & Balsam 1992). The other cores show roughly similar patterns, with maximum values in Isotope Stage 2. Slight earlier maxima occur during the Younger Dryas event. In core KF13, organic carbon is highly variable, but concentrations are again generally lower in Stage 3 and decrease to very low values <0.1% near the base of the core.

On a carbonate-free basis, the mineralogy of most samples is dominated by varying amounts of quartz and plagioclase and generally minor pyroxene. Quartz is likely to be of continental, presumably eolian origin, whereas plagioclase and pyroxene are derived from volcanic rocks at the Azores and/or the Mid-Atlantic Ridge.

Sediments in core GEOFAR KS03 at 20°30'N on the Mid-Atlantic Ridge have been investigated in less detail. These sediments do not show such color variations between light gray and pale olive, as reddish-orange colors indicative of oxic conditions prevail throughout the sediment section. Based on nannoplankton biostratigraphy (Müller 1996), sedimentation rates (0.5-0.9 cm/ky down to 270,000 years B.P.) are distinctly lower compared to the Azores region of the MAR. The sampling resolution of the $CaCO_3$ and organic carbon profiles (Fig. 5.3) is thus insufficient for correlation with climatic cycles. Calcium carbonate content is lower (<70%) compared to the Azores area in most parts of the sediment section, with maximum values at the sediment surface and in an interval near the base of the core. Minima at 42 and 85 cm occur in indurated brownish layers interpreted as strongly altered volcanic ash layers (cf. below). The low organic carbon content, which is generally <0.2%, may explain the oxic character of the sediment column down to the base of the core at 455 cm.

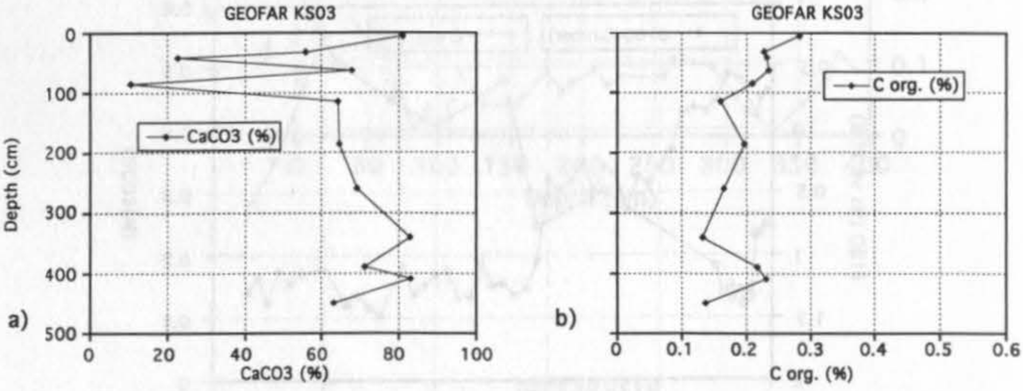

Fig. 5.3: Distribution of **a)** $CaCO_3$ and **b)** $C_{org.}$ vs. depth in core GEOFAR KS03 (20°30'N region at the Mid-Atlantic Ridge)

In several cores, background pelagic sedimentation is disrupted by allochthonous layers with low calcium carbonate content. A greenish-gray fine-grained, poorly consolidated serpentine-bearing layer with a sharp base and gradational contact at the top is present from 69-85 cm in core GEOFAR KF16 (discussed in detail in Chapter 9). Dark olive coarse-grained volcanic ash layers with sharp top and basal contacts are intercalated within pelagic sediments in core Ac.91KS04. Brown to grayish brown indurated layers in core GEOFAR KS03 are interpreted as strongly altered volcanic ash layers, based on the abundance of smectite and plagioclase, and the chemical composition, notably the high Mg content. Coarse-grained black to dark olive volcanic ash layers in core Ac.92KS04 (EPSHOM) studied for comparative purposes are frequently normally graded and represent turbidites derived from the island of Flores or from a nearby seamount (B.Dennielou, written comm. 1995). They are overlain by olive to dark gray fine-grained indurated levels interpreted as alteration products of volcanic ash, similar to those observed at 20°30'N.

Major volcanic input is restricted to discrete layers in most parts of the study area, but volcanic glass is frequently observed as a minor component in the coarse fraction. At the Lucky Strike seamount, volcanic glass constitutes a more significant contribution, decreasing the $CaCO_3$ content of surface sediments. Samples KF7-S, KF10-S and KG18-S have 55-65% $CaCO_3$, compared to >80% $CaCO_3$ in surface sediments in other parts of the study area. Nearly pure volcanic ash has been found in the lower part of box core KG18 retrieved on the southern flank of the seamount.

It can be concluded that sediments from the investigated cores in the main study area south of the Azores are dominantly carbonate-rich pelagic oozes whose lithology and variations of sediment color beneath oxidized surface layers is generally controlled by late Quaternary climatic cycles. Allochthonous layers, mostly of volcanic origin, occasionally disrupt this pattern of continuous pelagic sedimentation. Hydrothermal input in sediments generally cannot be discerned based on visual core descriptions, it should represent a minor contribution compared to background pelagic sedimentation of carbonate oozes. A notable exception is the allochthonous serpentine layer in core KF16.

5.3 Discussion: Ponded sediments in a restricted basin at the 38°05'N fracture zone (core GEOFAR KF16)

The lithology of core KF16 differs in various ways from other sediments in the study area:

- **Sedimentation rates are an order of magnitude higher** (cf. stratigraphy section) and reach 58 cm/ky during Termination Ia.
- Sediments are very **fine-grained**, the sand-size fraction accounts for approximately 3% of total sediment compared to about 10% in the other cores.
- **Organic carbon content is up to twice as high**, maximum values during Oxygen Isotope Stage 2 reach 1.2%.
- **Carbonate content is generally lower** than in the other cores (mostly less than 70% during Stage 2).
- Two **diatom layers** occur at 324-327 cm and 330-336 cm, which possibly corresponds to the Older Dryas event (cf. stratigraphy section). These layers have an olive to olive gray color, a low $CaCO_3$ content (33.17%), a strong odor of H_2S, and a matted texture.
- **Hydrogen sulfide is present in porewaters** in the lower part of the core below 400 cm, as indicated by the yellowish-brownish color of extracted porewaters. X-ray diffraction reveals abundant opal and pyrite in these sediments.
- Various bluish green and olive **laminations** are present in sediments from these sections, olive laminations have a particularly strong smell of H_2S.

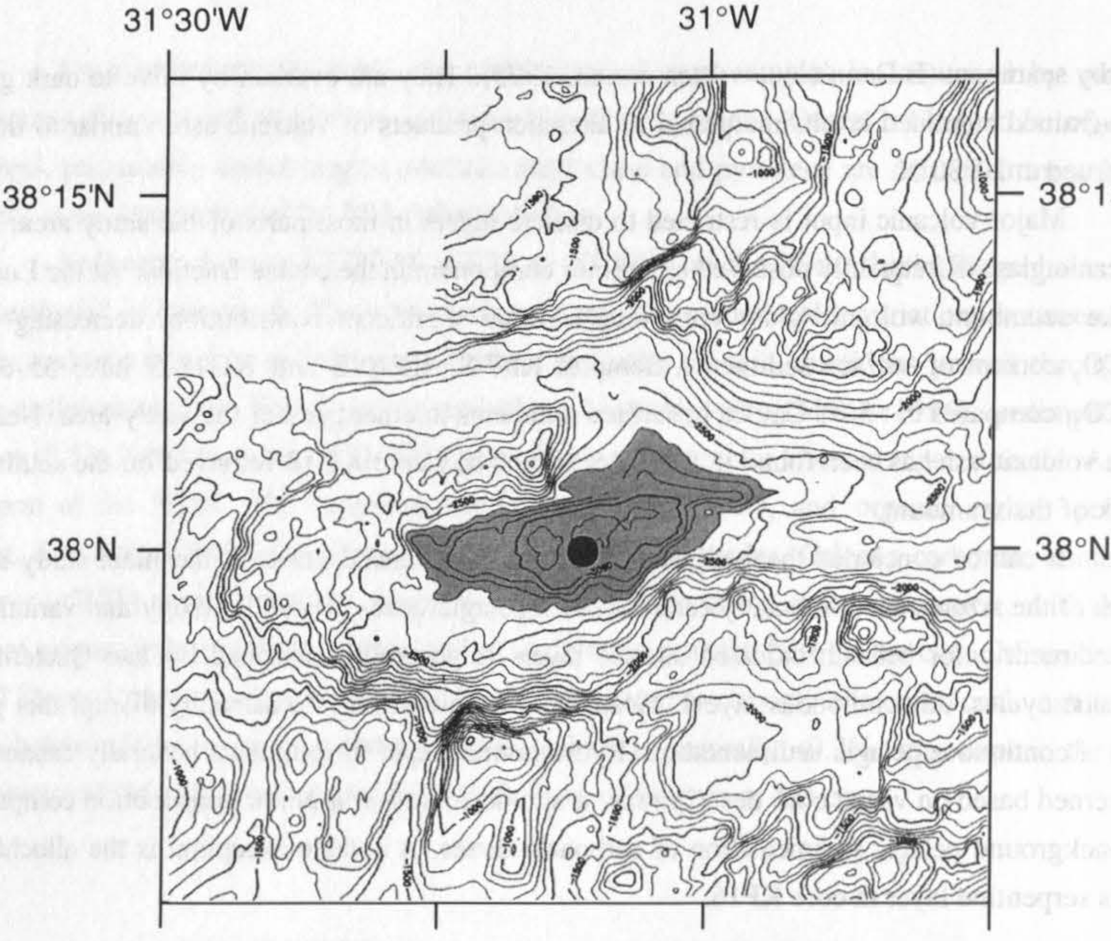

Fig. 5.4: Location of core GEOFAR KF16 (black dot) in the deepest part of a small basin in the central area of the 38°05'N fracture zone. Gray shading marks deepest area of the basin, which is elongated WSW-ENE parallel to the trend of the fracture zone.

These observations can be related to the particular location of this core (Fig. 5.4). It was retrieved in the deepest part of a small basin in the central area of the 38°05'N fracture zone, in 3050 m water depth. This basin apparently acted as a **sediment trap**, so that high accumulation rates of fine-grained sediments are found here. In this restricted setting, enhanced supply of organic carbon during glacial periods at high sedimentation rates could have resulted in complete oxygen consumption at shallow depths below the sediment surface and thus explain the presence of hydrogen sulfide and the preservation of sedimentary laminations.

DSDP Site 520 drilled near the axis of a small narrow basin in the South Atlantic Ocean (Leg 73 Scientific Party 1984) represents another example of ponded sediments in a silled basin generated at the Mid-Atlantic Ridge. An interval with extremely high sedimentation rates (44 cm/ky) at this site was attributed to slumping from the flanks of the basin. While such resedimented oozes could not always be distinguished from pelagic oozes, slumping was confirmed by the presence of exotic basaltic pebbles within nannofossil oozes. Laminated diatom oozes and diatomites have also been observed at this site, which is unusual for the open ocean environment distant from high-productivity areas. Preservation of diatom-rich sediments was ascribed to stagnant, CO_2-rich and oxygen-depleted bottom waters, and was further enhanced by rapid burial at the prevailing high sedimentation rates of redeposited sediments. Evidence for stagnant bottom water conditions is also based on the absence of burrows and benthic fossils and the abundance of pyrite in diatom-rich sediments (Gombos 1984). While organic carbon content of diatomites and associated sediments is fairly low (0.14-0.36%), indicating oxidization of most of the organic material in the water column, it is still an order of magnitude higher than in oxic sediments at other sites of DSDP Leg 73 (0.026-0.052%), which suggests that organic material reaching the ocean floor has largely been preserved (Leg 73 Scientific Party 1984).

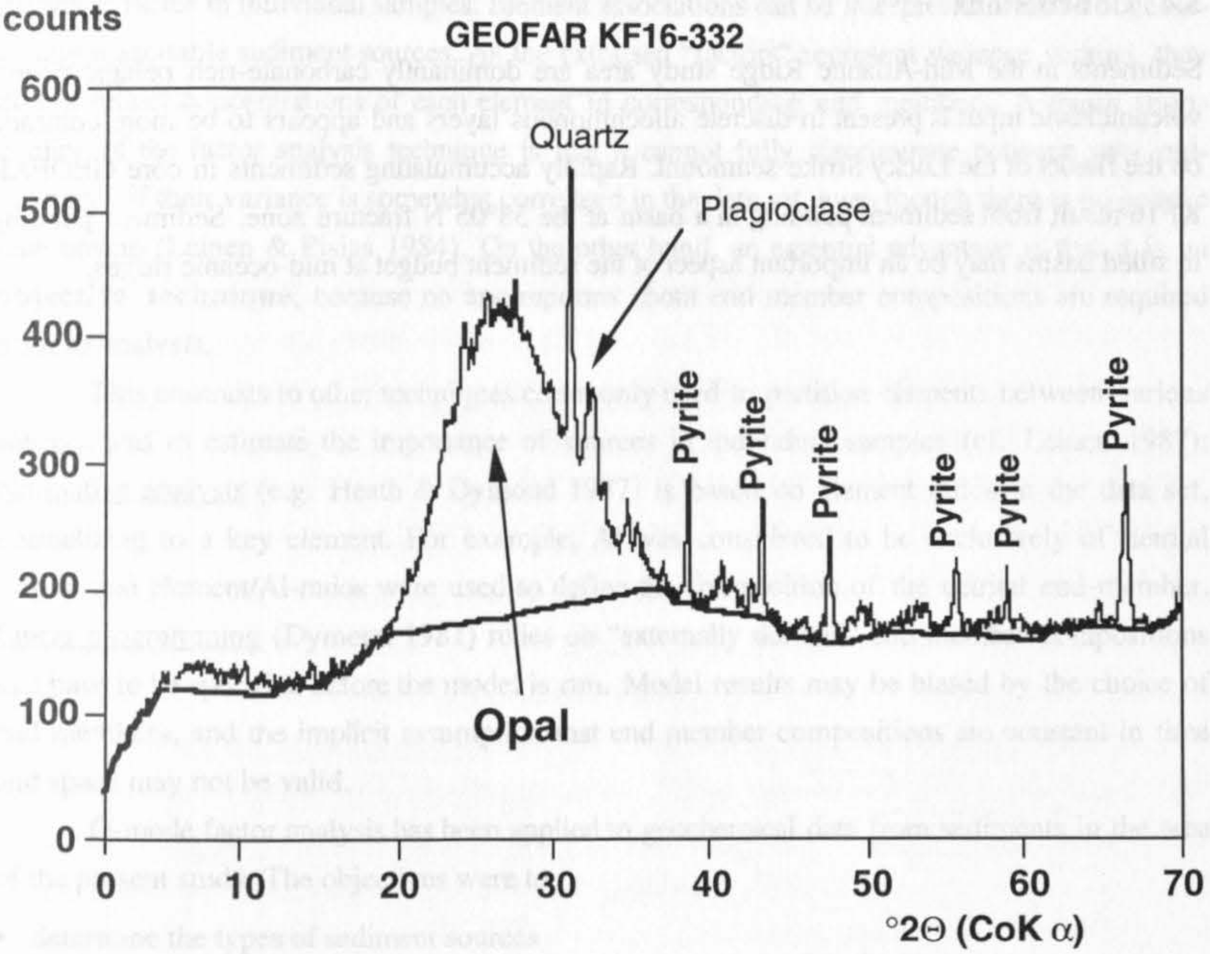

Fig. 5.5: X-ray diffractogram of diatom layer KF16-332 (carbonate dissolved with acetic acid)

Laminated diatom oozes composed of near monospecific assemblages of *Thalassiotrix* have also been observed in Neogene sediments during ODP Leg 138 in the equatorial Pacific Ocean (Kemp & Baldauf 1993, Kemp et al. 1995). Diatom mats occurred in packets 10-20m thick, were rapidly deposited at rates exceeding 10 cm/ky, and could be correlated for distances of more than 2,000 km. In this case, diatom laminae were preserved in oxic sediments. This was related to the vast scale of the deposits and the strength of the mats, such that the benthic community could not penetrate into the diatom meshwork, and laminations were preserved by physical means.

In the study area, diatom layers are a unique feature in core KF16. This would either imply that diatom blooms only occurred on a local scale, or that diatom layers have not been preserved at other locations. As the scale of the deposits is much smaller compared to the Neogene Pacific Ocean, preservation of diatom laminae by physical means may not have occurred. Accordingly, preservation at the site of core KF16 may be related to suppression of benthic activity by oxygen deficiency in bottom waters. This is suggested by the presence of H_2S and pyrite (Fig. 5.5) in diatom-rich sediments.

5.4 Conclusions

Sediments in the Mid-Atlantic Ridge study area are dominantly carbonate-rich pelagic oozes; volcaniclastic input is present in discrete allochthonous layers and appears to be more common on the flanks of the Lucky Strike seamount. Rapidly accumulating sediments in core GEOFAR KF16 result from sediment ponding in a basin at the 38°05'N fracture zone. Sediment ponding in silled basins may be an important aspect of the sediment budget at mid-oceanic ridges.

6. Factor analysis of sediment geochemical data: Element associations and relative importance of sediment sources

6.1 Introduction

Pelagic sediments represent a mixture of various sources, which may include detrital, biogenic, hydrothermal and other contributions. **Factor analysis** is a **multivariate statistical technique** commonly used to resolve complex associations between variables in large data sets. Various studies have applied this technique to geochemical data of marine sediments, including hydrothermally influenced environments (e.g. Leinen & Pisias 1984, Hodkinson & Cronan 1991, McMurtry et al. 1991, Lackschewitz et al. 1994). Factor loadings indicate the elements associated with each factor, and factor scores the relative importance of each "end member" factor in individual samples. Element associations can be interpreted in terms of geologically reasonable sediment sources. As the extracted "factors" represent variance vectors, they do not reflect concentrations of each element in corresponding end members. A major shortcoming of the factor analysis technique is that it cannot fully discriminate between two end-members, if their variance is somewhat correlated in the data set, even though there is no genetic relationship (Leinen & Pisias 1984). On the other hand, an essential advantage is that it is an **objective technique**, because no assumptions about end member compositions are required prior to analysis.

This contrasts to other techniques commonly used to partition elements between various sources and to estimate the importance of sources in individual samples (cf. Leinen 1987): Normative analysis (e.g. Heath & Dymond 1977) is based on element ratios in the data set, normalizing to a key element. For example, Al was considered to be exclusively of detrital origin, and element/Al-ratios were used to define the composition of the detrital end-member. Linear programming (Dymond 1981) relies on "externally defined" end member compositions that have to be specified before the model is run. Model results may be biased by the choice of end members, and the implicit assumption that end member compositions are constant in time and space may not be valid.

Q-mode factor analysis has been applied to geochemical data from sediments in the area of the present study. The objectives were to

- determine the types of sediment sources
- identify the elements associated with each source, and to
- investigate downcore variability of sediment sources.

More specifically, the aim was to test for the presence of a hydrothermal contribution, and to determine the corresponding element association which may include elements primarily supplied from hydrothermal sources and elements scavenged by hydrothermal oxyhydroxide particles from the water column. Subsequent to the presentation and interpretation of the results of factor analysis, volcanic and detrital contributions are compared to the composition of potential sources including MORB-type basalts, volcanic rocks of the Azores Islands, and average continental crust, in order to substantiate previous conclusions. In later chapters, other element associations and corresponding sediment sources will be related to stratigraphical and mineralogical data, including

- **quantification of hydrothermal fluxes** based on **metal accumulation rates**, comparison to literature data from other hydrothermally influenced environments, and a discussion of the diagenetic modification of primary fluxes (Chapter 7)
- description of the **barium distribution in ridge-crest sediments**, and implications on the **hydrothermal and/or biogenic origin of Ba** (Chapter 8)
- detailed mineralogical investigations on an allochthonous **serpentine layer** (core KF16, 38°05'N fracture zone), and interpretation in terms of the **genesis and conditions of formation** of this layer (Chapter 9).

Accordingly, this section serves as a general introduction to topics adressed subsequently in more detail.

6.2 Choice of elements and sample sets for factor analysis

Biogenic carbonate is the dominant sediment source in time and space (most of the samples contain >60% [biogenic] $CaCO_3$). Figure 6.1 shows scatter plots of $CaCO_3$ vs. Ca and Sr, respectively (this does not include data from core Ac.91KS04, because no independent $CaCO_3$ measurements are available on these samples). While the non-zero y-axis intercepts of regression lines indicate that other sources of Ca and Sr do exist, these are certainly of minor importance. The "excess" Ca content of samples from the vicinity of the Lucky Strike seamount suggests a volcaniclastic Ca contribution.

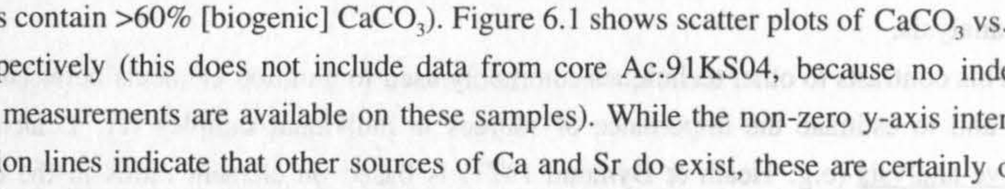

Fig. 6.1: Scatter plots of $CaCO_3$ vs. Ca and Sr. The excellent correlations indicate that these elements are dominantly associated with a biogenic carbonate source. Excess Ca in sediments from the vicinity of the Lucky Strike seamount is probably derived from volcaniclastic sources.

Preliminary factor analysis calculations showed that this biogenic contribution explains only a small proportion of total variance, as only two elements are associated with this source. As the $CaCO_3$ content can be directly determined, total Ca and Sr have been omitted from the factor analysis data set, which facilitated the identification of sediment sources that cannot be discerned and quantified with other methods, and the assessment of their element associations and relative importance. This ignores a possible contribution of non-carbonate Ca.

Twenty-one elements (Si, Al, K, Ti, Mg, Fe, Mn, P, Rb, Cr, Ni, Co, Ba, Zn, Cu, Nb, Pb, V, Y, As) were included in the data set for factor analysis. Analysis were done on bulk geochemical data of the entire data set (157 samples) to assess the importance of various sediment sources on the entire sediment budget and the bulk chemical composition. Subsequently, data recalculated on a carbonate-free basis (CFB) were used as input to factor analysis to eliminate the variable diluting effect of biogenic carbonate. The entire data set was found to be strongly influenced by few samples of volcaniclastic origin or derived from alteration of ultramafic rocks. A second set of analysis on a bulk and carbonate-free basis was performed based on data from cores KF13 and KF09 (43 samples), which do not include such samples with extreme chemical composition.

6.3 Results

6.3.1 Entire data set, bulk composition

Results of factor analysis on the entire bulk geochemical data set are shown in Fig. 6.2. **Factor 1** (44.3 % of the variance) has high loadings on Si, Al, Fe and V, and slightly lower loadings on Zn, Nb, Sc and Cr. These elements are commonly associated with a **volcanic** sediment source. This interpretation is confirmed by highest factor scores occurring on volcanic ash layers of core Ac.91 KS04 (EPSHOM), smectite-rich layers in cores GEOFAR KS03 and Ac.92 KS04 (EPSHOM) inferred to be alteration products of volcanic ashes, and samples from the Lucky Strike seamount containing abundant volcanic glass. Positive loadings occur on most elements of the data set, because samples with major volcanic input have little or no biogenic carbonate, which dilutes bulk concentrations of all "lithogenic" elements in surrounding pelagic sediments. Distinctly lower factor loadings on Ti and especially K are compatible with a mid-ocean ridge basalt composition of the associated volcanic rocks.

Factor 2, explaining 16.5% of the variance, has highest loadings on Mn and P, and lower loadings on As, V, Fe and Cu. This element association suggests a **hydrothermal** sediment source, including metals which may be derived from hydrothermal solutions (Mn, Fe, Cu) and elements scavenged by hydrothermal oxyhydroxides in the water column (As, P, V). The fairly low loading on Fe can be explained by the fact that iron is also derived from volcanic sources and therefore primarily associated with Factor 1. Highest scores on Factor 2 occur for samples from oxidized surface layers, indicating downcore diagenetic remobilization of metals and coprecipitated elements and reprecipitation under oxidizing conditions. Highest scores for core KF09 suggest maximum hydrothermal influence to the south of the Lucky Strike segment.

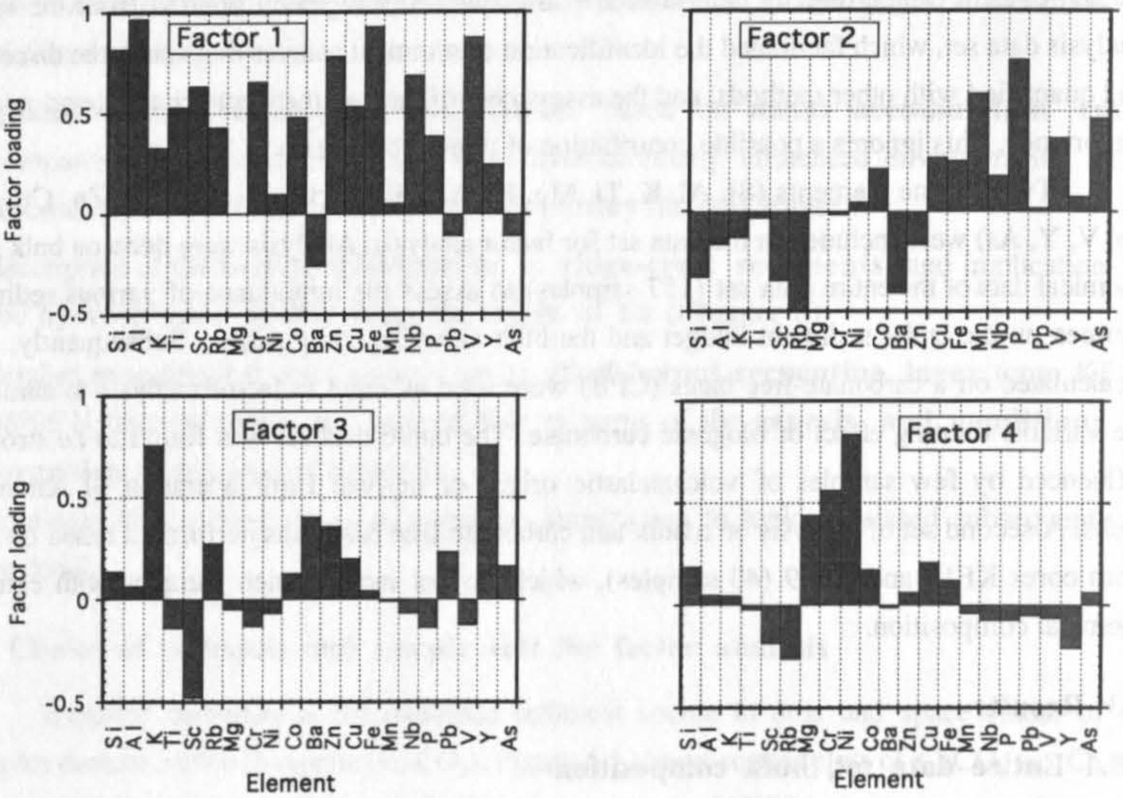

Fig.6.2: Factor analysis (entire data set, bulk concentrations)

A high score occurs also for the surface sample of core KG18, located in the immediate vicinity of the Lucky Strike seamount, indicating some hydrothermal influence at this site, which is superposed on predominating volcanic input.

Factor 3 explains 11.6% of the total variance. It has high loadings on K and Y, and lower loadings on Ba, Zn, Rb and Pb. Generally, samples from glacial periods have higher scores on this factor; highest scores occur consistently during Termination I and are associated with carbonate minima. This factor is interpreted to represent **continentally-derived detrital input**, since detritus derived from local basalt alteration is characterized by low K. Rb is primarily adsorbed on K-bearing detrital phases such as illite and orthoclase (Wedepohl 1969). For sediments of the North Atlantic and the Norwegian-Greenland Sea, various authors showed that an "acidic" lithogenic component enriched in Si, K, Rb and Y can be distinguished from a basic component enriched in Fe, Ti and Mg (Grousset et al. 1982, Lackschewitz 1991, Paetsch 1991, Lackschewitz et al. 1994). Mineralogically, the acidic component is characterized by quartz and the clay minerals illite, kaolinite and chlorite, and the basic component by plagioclase, pyroxenes, amphiboles and montmorillionite (Grousset et al. 1982).

Factor 4 (9.3% variance) is characterized by high loadings on Mg, Cr and Ni. These are elements typical of **ultramafic** rocks; highest scores occur for samples from the serpentine layer of core KF16 derived from alteration of a marine ultramafic protolith (discussed in detail in Chapter 9). Lower, but still significantly positive scores also occur for samples with high scores on Factor 1; while volcanic ash layers also have elevated contents of Mg and Cr, concentrations of these elements are an order of magnitude lower than for serpentine layer samples.

6.3.2 Entire data set, carbonate-free composition

A second factor analysis has been performed on the entire data set recalculated on a **carbonate-free basis**, in order to eliminate the effects of variable dilution by biogenic carbonate (Fig. 6.3). The inferred sediment sources and the distribution of factor scores corresponding to each source are fairly similar; however, the amount of variance explained by each factor and some of the element associations have changed:

The **hydrothermal/diagenetic** factor now explains 38.5% of the total variance; it is characterized by high loadings on Fe, P, As, V and Cu. Notably, Fe and V are dominantly associated with this factor after recalculation on a carbonate-free basis. In oxidized surface layers, carbonate-free element abundances of 11-22% Fe, 1-8% Mn and 200-500 ppm As represent significant enrichments compared to average pelagic clay (6.5% Fe, 0.67% Mn, 13 ppm As; Turekian & Wedepohl 1961). While this evidently includes the effects of diagenetic remobilization, a hydrothermal origin for the element association of this factor is further substantiated by metal accumulation rates comparable to values observed in other hydrothermally influenced mid-ocean ridge and back-arc basin environments (cf. Chapter 7), and by documented hydrothermal activity in the study area. The distribution of factor scores is similar to the distribution described above for bulk Factor 2; furthermore, positive scores occur close to the base of core GEOFAR KF13 suggesting slightly higher relative hydrothermal influence.

The **ultramafic** factor explains 19.3% of the total variance, it has yet higher loadings on Mg, Cr and Ni with a factor score distribution as described above (bulk Factor 4). The third factor (13.4% var.) has high loadings on Nb and Y, and somewhat lower loadings on Pb, Zn and Co. This may represent a **detrital** component enriched in these trace elements. Highest scores occur during the Holocene; high scores also occur during Isotope Stage 3 in core KF13. Only Al and Ti have high loadings on the fourth factor (8.5% var.) considered to represent a **detrital/volcanic** contribution. In addition to high scores on samples with obvious volcanic influence (cf. above), elevated scores on all samples from core GEOFAR KS03 and on some samples of Holocene age in cores KF16 and KF09 suggest that this source is sporadically but repeatedly present in carbonate-rich "background" sediments; this is in accord with minor amounts of volcanic glass fragments frequently observed in the coarse fraction.

Finally, the **terrigenous** factor explains 7.4% of the total variance. It has a high loading on K and lower loadings on Si and Ba. Factor loadings are generally elevated during Termination I and Isotopic Stage 2 compared to Holocene values; no distinct peaks occur during Termination I in the carbonate-free data set. This suggests that the composition of detritus

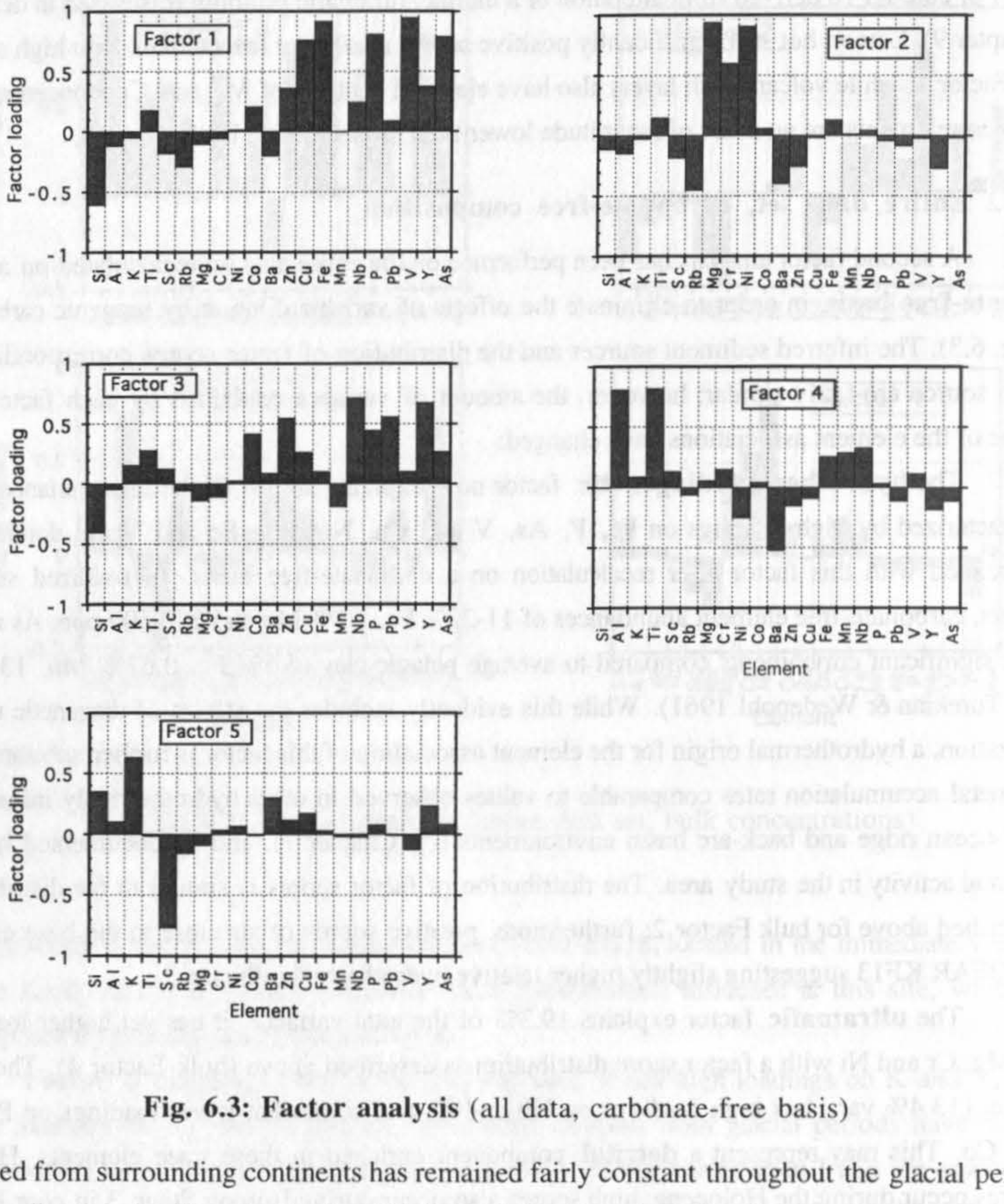

Fig. 6.3: Factor analysis (all data, carbonate-free basis)

derived from surrounding continents has remained fairly constant throughout the glacial period. The „spikes" during Termination I visible in the bulk data set might rather represent a change in the *amount* of detritus diluting the prevailing input of biogenic carbonate. The presence of Si and Ba in this factor could represent **enhanced biogenic productivity** during glacial periods.

6.3.3 Data from cores KF09 and KF13

In the entire data set (bulk and carbonate-free), comparatively few samples with major volcanic or ultramafic input account for a large proportion of total variance. One consequence is that a number of elements have fairly low communalities, since their variance is not linked to the principal factors that have been extracted. In order to further elucidate the variability that is associated with detrital input and diagenetic processes, separate factor analysis (bulk and carbonate-free) have been performed on samples from cores **KF13 and KF09** (total of 43 samples), which lack lithologic layers strongly influenced by volcanic or ultramafic input (Figs. 6.4 and 6.5).

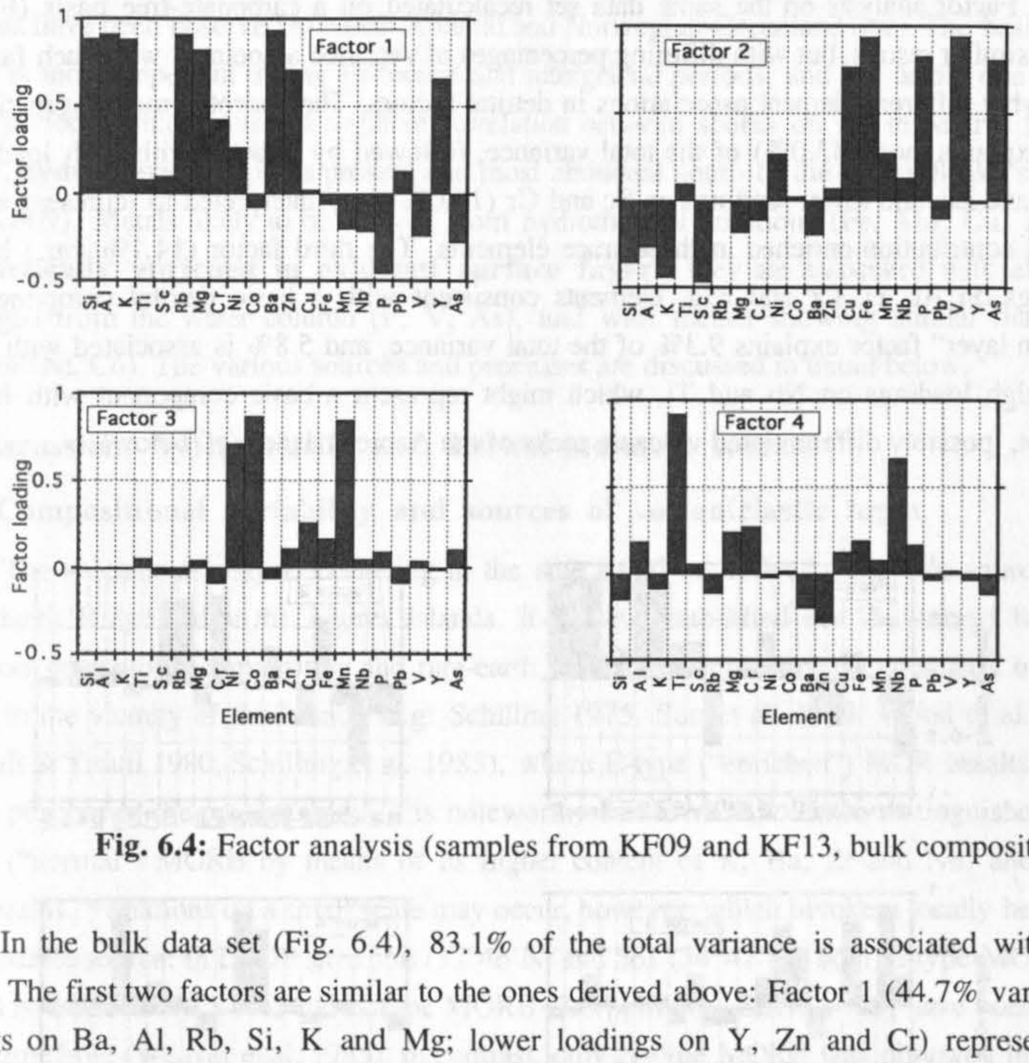

Fig. 6.4: Factor analysis (samples from KF09 and KF13, bulk composition)

In the bulk data set (Fig. 6.4), 83.1% of the total variance is associated with four factors. The first two factors are similar to the ones derived above: Factor 1 (44.7% var., high loadings on Ba, Al, Rb, Si, K and Mg; lower loadings on Y, Zn and Cr) represents an **"acidic" terrigenous detrital** component, with highest scores occurring during Termination I. In the absence of volcanic and ultramafic input, Mg and Cr are also primarily associated with this source, since their concentrations are elevated compared to "average" pelagic sediment with higher $CaCO_3$ content. The second factor (19.4% var.) has high loadings on metals presumably derived from a hydrothermal source (Fe, Cu) and coprecipitated elements (V, P, As), and distinctly lower loadings on Mn and Ni. As described above, high factor scores for samples from the oxic surface layer indicate diagenetic remobilization of metals and coprecipitated elements. Factor scores are two- to three times higher for samples from core KF09, indicating that the influence of this **hydrothermal-diagenetic** source is more important south of the Lucky Strike segment. Factor 3 (10.0% var.) has high loadings on Mn, Ni and Co, and lower loadings on Cu and Fe. High scores on this factor are restricted to samples from **dark brown layers** within the surficial reddish-orange to yellow oxidized zone. The differing diagenetic behavior of Mn, Ni and Co will be discussed in detail in the section on metal accumulation rates (Chapter 7). The fourth factor has high loadings on Nb and Ti and lower loadings on Cr and Mg. It is considered to represent a **basic detrital** component. Highest factor scores occur for Holocene samples beneath the oxidized surface layer; factor scores are inversely correlated with scores on Factor 1.

Factor analysis on the same data set recalculated on a carbonate-free basis (Fig. 6.5) yields similar results, but with differing percentages of variance associated with each factor and somewhat different element associations in detrital factors. The hydrothermal-diagenetic factor now explains most (43.0%) of the total variance, followed by a factor with high loadings on Pb, Y and Zn, and lower loadings on Sc and Cr (16.0% var.) interpreted to represent an acidic detrital contribution enriched in these trace elements. The third factor (14.1% var.) has high loadings on Al, Ti, Cr and Mg, elements consistent with a basic detrital component. The "brown layer" factor explains 9.3% of the total variance, and 5.8% is associated with a factor with high loadings on Nb and Ti, which might represent a basic component with high Nb content, possibly differentiated volcanic rocks of the Azores islands (cf. below).

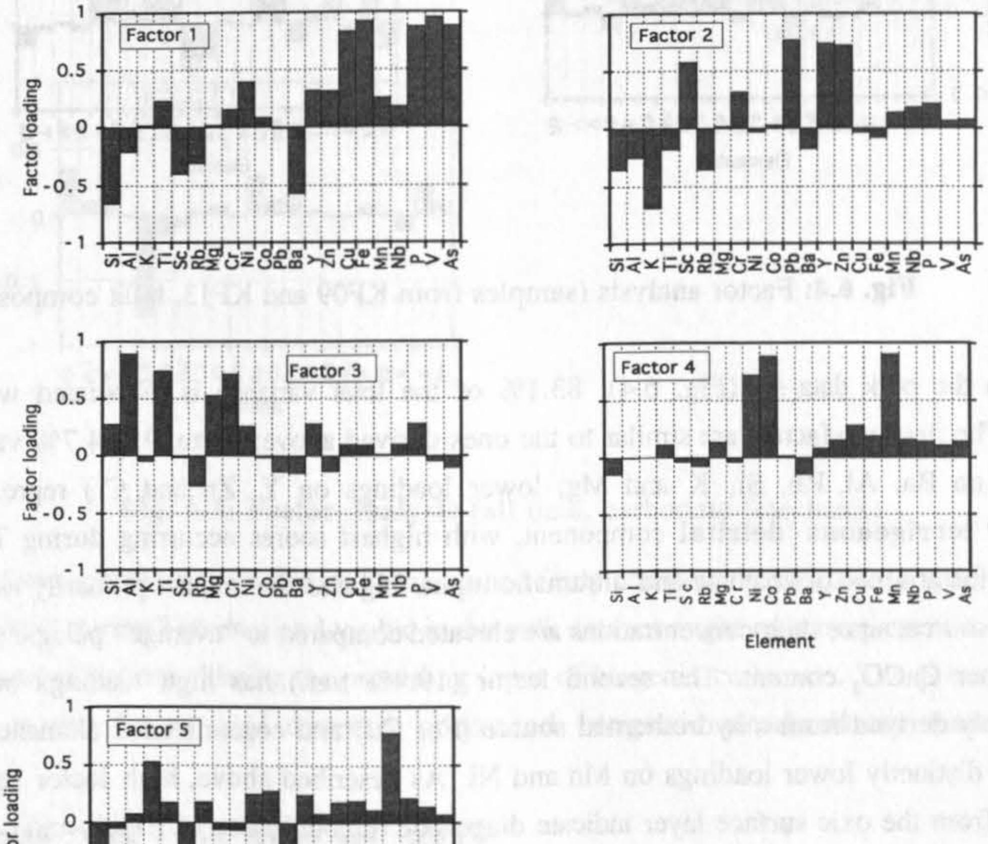

Fig. 6.5: Factor analysis (cores KF09 and KF13, carbonate-free composition)

6.3.4 Summary

In summary, factor analysis reveals that the following sources and processes influence sediment geochemistry: **Volcanic** and **ultramafic** input is significant in some samples from allochthonous layers intercalated within pelagic sediments. **Detrital** sources are more widespread, it is possible to distinguish at least one **basic** and one **acidic** component (similar to the ones that have been observed in North Atlantic and Norwegian-Greenland Sea). The basic component is more important during Holocene and interglacial periods, and the acidic one during glacial periods, which causes a negative correlation between scores on the respective factors. Finally, **hydrothermal** input is present and most abundant south of the Lucky Strike segment (core KF09). Metals likely to be derived from hydrothermal solutions (Fe, Mn, Cu, Zn) are **diagenetically enriched in oxidized surface layers**; they are associated with elements scavenged from the water column (P, V, As), and with metals showing similar diagenetic behavior (Ni, Co). The various sources and processes are discussed in detail below.

6.4 Discussion: Volcaniclastic and detrital sediment sources

6.4.1 Compositional variability and sources of volcaniclastic input

The volcanic ash layers occurring in the area could be derived from two sources: the Mid-Atlantic Ridge and/or the Azores islands. It is well established that the Azores hot spot influences the isotopic composition and rare-earth and incompatible element chemistry of MAR basalts in the vicinity of the islands (e.g. Schilling 1975, Sun et al. 1979, Wood et al. 1979, Bougault & Treuil 1980, Schilling et al. 1983), where E-type ("enriched") MOR basalts occur. For the purpose of the present study, it is noteworthy that E-MORB can be distinguished from N-type ("normal") MORB by means of its higher content of K, Ba, Zr and Nb, and lower Zr/Nb-ratios. Variations on a small scale may occur, however, which invoke a locally heterogeneous mantle source: In DSDP sites 558 (37°46'N) and 561 (34°47'N), both E-type MORB (7-21 ppm Nb, Zr/Nb = 4.5-9.6) and N-type MORB (2-3 ppm Nb, Zr/Nb > 20) have been found in the same hole (Weaver et al. 1985). In contrast, only N-type MORB was observed in DSDP sites 562, 563 and 564 at 33°N, south of the Hayes Fracture zone (Weaver et al. 1985).

The Azores Islands are characterized by mafic-felsic bimodal volcanism, i.e. alkali basalts and trachytic and peralkaline rhyolitic rocks (comendites and pantellerites), with only few volcanic rocks falling in a compositional gap between 54-65% SiO_2 (White et al. 1979, Davies et al. 1989, Storey et al. 1989, Widom et al. 1992, Mungall & Martin 1995). Compared to tholeiitic MAR basalts, alkali basalts from the Azores are characterized by higher contents of Ti, K and of the trace elements Zr, Ba and Nb. Major differences exist both between islands and within individual islands; for example, Sao Miguel is more "potassic" than the other Azores islands (Schmincke 1973, White et al. 1979). A detailed discussion of these variations is beyond the scope of this study.

Locations of cores containing volcaniclastic layers are summarized in Table 6.1. Sample Noratlante KS12-S, included for comparison, was taken from the surface of a sediment core in a basin just to the west of the island of Sao Miguel, remote from the MAR axis; the other cores are located close to the ridge axis at various distances from the Azores islands. Two of the normally graded ash turbidites in core Ac.92KS04 are overlain by indurated fine-grained layers with elevated H_2O^+ content (1.8-2.7%) which contain abundant smectite-like clay minerals (cf. Chapter 9); a third fine-grained layer (Ac.92KS04-237) of similar chemical and mineralogical composition has an erosive base (B.Dennielou, written comm. 1994). These fine-grained layers most probably represent alteration products of volcanic material; the direct spatial association with their supposed precursor rocks allows to investigate the effects of alteration on chemical composition. Samples from core GEOFAR KS03 also show evidence of alteration, namely elevated H_2O^+ content (4-5%) and abundant smectite-like clay minerals.

Sediment core	Core location	Water depth	Remarks
Ac.91KS04	38°05N 30°36W	2183 m	basinal setting immediately E of ridge axis
Ac.91KS06	38°20N 29°58W	2500 m	
Ac.92KS04	38°31N 30°54W	1820 m	NE-trending slope, 20 km NNW of a seamount culminating at 500 m water depth at the ridge axis, with documented submarine explosive volcanism (Ondréas et al. 1995)
GEOFAR KG18	37°17N 32°16W	1690 m	flank of Lucky Strike seamount
GEOFAR KS03	20°26N 45°40W	3940 m	vicinity of 20°30'N seamount
Noratlante KS12	38°N 26°W	2500 m	basinal setting, W of the island of Sao Miguel (remote from Mid-Atlantic Ridge axis)

Table 6.1: Locations of cores with volcaniclastic layers

Table 6.2 compares diagnostic elements in volcaniclastic sediments at the MAR with representative data on volcanic rocks from the Mid-Atlantic Ridge (28-45°N) and the Azores islands. The following discussion is based on bulk data recalculated on a carbonate-free basis; sediment samples contain between 0 and 40% biogenic $CaCO_3$. The composition of volcaniclastic sediments may be influenced by minor amounts of contaminating phases such as biogenic opal or detrital quartz. Furthermore, submarine alteration (seafloor weathering) may increase the concentrations of K, Ba and possibly Ti, which is obvious from a comparison between ashes from core Ac.92KS04 and their overlying alteration products.

Compared to all other sedimentary samples, sample Noratlante KS12-S has a distinctly higher SiO_2, TiO_2 and K_2O and lower MgO content. Since the other major element data also indicate an evolved volcanic rock, the higher SiO_2 concentrations cannot be explained simply as a result of contamination by biogenic opal or detrital quartz. Aside from a lower K_2O content, the composition of this particular sample is similar to basalt hybrids (cf. Table 6.2) that occur in the Agua de Pau magmatic system on the island of Sao Miguel (Storey et al. 1989).

	SiO_2	TiO_2	MgO	K_2O	Zr	Ba	Nb	*Ref.*
	(%)	(%)	(%)	(%)	(ppm)	(ppm)	(ppm)	
Volcaniclastic sediments:								
Noratlante KS12-S	**56.90**	**2.47**	**4.23**	**2.28**	**---**	**---**	**---**	*2*
Ac.91KS04-280	51.48	1.52	5.90	0.60	180	---	36	*1*
Ac.91KS04-238	49.20	1.59	7.18	0.67	130	230	34	*1*
Ac.91KS04-310	50.69	1.62	6.43	0.65	146		35	*1*
Ac.91KS04-353	50.48	1.69	6.80	0.61	154	323	34	*1*
Ac. 91KS06-S	50.48	1.55	8.34	0.64	150	310	26	2
Average	**49.92**	**1.61**	**7.19**	**0.64**	**145**	**288**	**32**	
Ac.92 KS04-115 *	48.48	1.64	6.29	0.99	71	473	33	*1*
Ac.92 KS04-237 *	49.12	1.97	5.81	1.21	94	395	42	*1*
Ac.92 KS04-254 *	47.64	1.99	5.33	1.06	118	487	41	*1*
Average *	**48.41**	**1.87**	**5.81**	**1.09**	**94**	**452**	**39**	
Ac.92 KS04-122	48.29	1.56	6.28	0.72	96	263	28	*1*
Ac.92 KS04-180	48.90	1.67	6.47	0.64	111	235	24	*1*
Ac.92 KS04-265	47.63	1.86	5.76	0.90	132	301	33	*1*
Average	**48.27**	**1.70**	**6.17**	**0.75**	**113**	**266**	**28**	
GEOFAR KG18-13	48.10	1.14	8.03	0.41	71	144	19 #	*1*
GEOFAR KS03-42 *	47.67	1.22	8.11	0.86	79	168	10 #	*1*
GEOFAR KS03-85 *	48.63	1.20	8.47	0.65	97	80	13 #	*1*
Azores volcanic rocks:								
Alkali basalts	46.63	3.51	8.06	1.45	234	462	59	*3,4,6*
Mugearites	52.80	2.71	3.38	1.88	414	566	75	*5*
Basalt hybrids	55.67	2.01	3.73	4.86	319	1073	72	*4*
Trachytes	62.16	0.71	0.66	5.87	1015	228	196	*5,6*
Comenditic trachytes	65.87	0.58	0.24	3.86	764	1444	127	*6*
Comendites	67.90	0.40	0.06	4.51	1197	426	186	*6*
Pantellerites	66.47	0.54	0.13	4.64	1488	185	267	*6*
MAR basalts:								
Plume MORB (Azores)	49.72	1.46	7.90	0.50	---	150	---	*7*
Trans. MORB (34-38°N)	50.30	1.21	7.79	0.20	---	40	---	*7*
Normal MORB (28-34°N)	48.77	1.15	9.67	0.08	---	4.2	---	*7*
DSDP Site 558 E-MORB	49.33	1.38	7.83	0.41	90	55	14.4	*8*
DSDP Site 561 N-MORB	48.08	0.94	7.39	0.28	52	8	2.1	*8*

Table 6.2: Diagnostic element abundances in volcaniclastic sediments [corrected for minor biogenic carbonate] compared to Mid-Atlantic Ridge basalts and representative volcanic rocks of the Azores islands (averages of published analytical data).
Sediment samples with evidence of major alteration (elevated $H2O^+$ content, abundant smectite) marked by an asterisk (*).
# semi-quantitative X-ray fluorescence (fused beads) data
Data from: 1)this study, 2)Richter 1992, 3) Davies et al. 1989, 4) Storey et al. 1989, 5) Widom et al. 1992, 6)Mungall & Martin 1995, 7) Schilling et al. 1983, 8) Weaver et al. 1985.

All the other samples have a basaltic composition. The volcanic ash layers east of the ridge axis at **38°N** all have a fairly uniform composition, even though sample Ac.91 KS04-280 has a higher SiO_2 and Zr, and lower MgO content. Unaltered samples from core Ac.92 KS04 are compositionally similar, but have lower SiO_2, Zr and Ba. All samples have slightly higher SiO_2, higher TiO_2, K_2O, Zr, Ba and Nb and generally lower MgO than samples farther from the south. The higher K_2O content is not entirely related to alteration, because all of these samples contain abundant fresh volcanic glass. The trace element content may indicate that these layers are derived from the Azores islands, the TiO_2 and K_2O content suggests a local enriched MORB material. In any case, the composition of the 38°N samples indicates that they are derived from evolved volcanic rocks, whose source is supposedly related to the influence of the Azores hot spot. Sample KG18-13 taken on **Lucky Strike seamount** definitively has an E-MORB type composition. The very fresh appearance of this sample and a low H_2O^+ content preclude that the K_2O content is influenced by alteration. - The Nb data on this sample and on two samples from core KS03 located close to the 20°30'N seamount have to be considered with caution, since a comparison of Nb data obtained on rock standards with their certified reference composition reveals that analytical errors of Nb can reach 40% of the absolute certified value at low Nb-concentrations (<20ppm) for X-ray fluorescence data on fused beads. If the Nb content of sample KG18-13 were overestimated by 40%, its actual Nb content would be 13.6 ppm, which is a value typical of E-type MORB (Weaver et al. 1985). While this interpretation is evidently speculative, it would be consistent with the other trace element data.

At the **20°30'N seamount** location, a N-MORB type source would be expected. The high K_2O- and Ba-content is probably due to alteration. The Zr content appears elevated compared to "typical" N-MORB (Table 1); however, Weaver et al. (1985) have classified some samples with ≥90 ppm Zr as N-type MORB based on high Zr/Nb ratios and other criteria such as isotopic composition and REE patterns.

It can be concluded that the chemical composition of the studied samples reflects an increasing influence of the Azores hot spot with proximity to the Azores islands. The N-S gradient in Nb concentrations, with decreasing concentrations reflecting decreasing influence of the Azores hot spot, should be correct and significant in spite of analytical uncertainties. Volcanic input at the Lucky Strike seamount is certainly derived from local E-MORB type sources. At 38°N, it may also include material from the Azores islands. Differentiated volcanic products have not been observed in the main study area adjacent to the ridge axis.

6.4.2 Composition, temporal and spatial variability of detrital sources

Factor analysis reveals that at least two different sources of detritus are present in the study area: basic detritus enriched in Ti and Mg which may be derived locally from the ridge axis or from basaltic rocks of the Azores islands, and acidic detritus enriched in K which is presumably of continental origin. The ratios K/Al, Si/Al and Ti/Al have been used to distinguish between these two components (Paetsch 1991). Fig. 6.6 a-c demonstrates that there are significant variations in element ratios, which can be correlated spatially and/or temporally and which are interpreted in terms of several mixing trends.

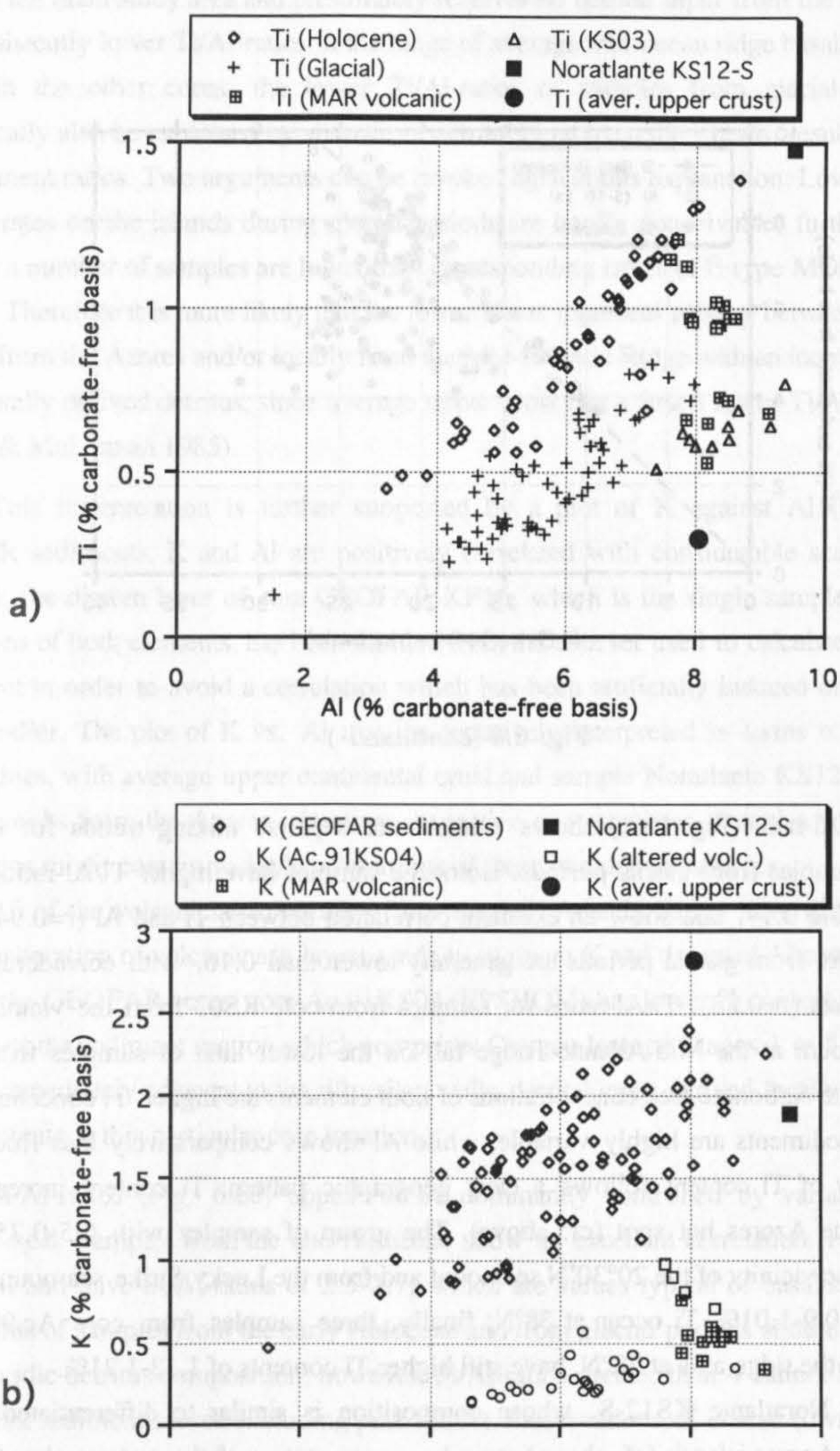

Fig. 6.6: Diagnostic element ratios interpreted in terms of detrital sediment sources (see text) [average upper crustal values from Taylor & McLennan 1985] *(continued on following page)*

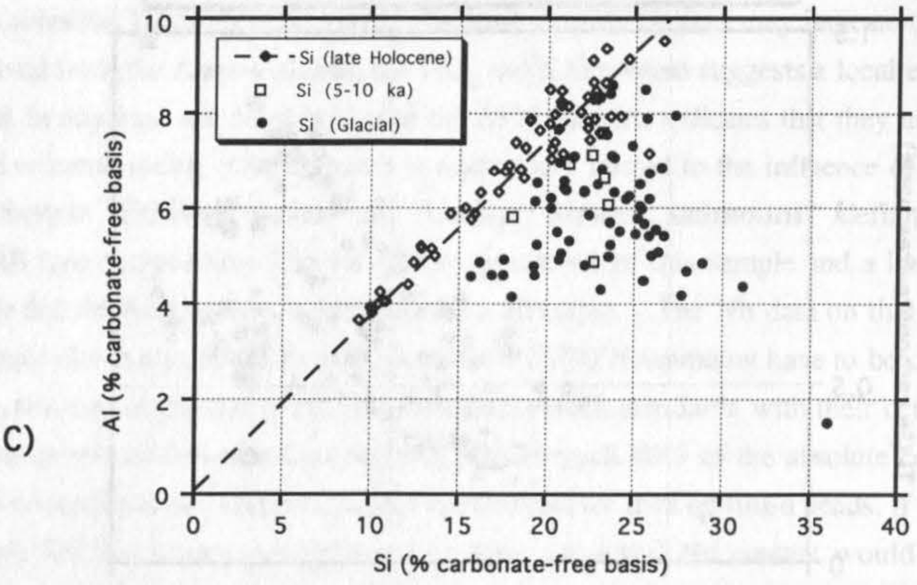

Fig. 6.6 (*continued*)

The Ti/Al-ratio (Fig. 6.6a) shows evidence of separate mixing trends for Holocene samples and samples from glacial periods. Holocene samples have higher Ti/Al-ratios, mostly between 0.13 and 0.17, and show an excellent correlation between Ti and Al (r=0.94). Ti/Al-ratios of samples from glacial periods are generally lower than 0.10, with considerably more scatter in the data (r=0.83). Ti/Al-ratios for samples from core KS03 from the vicinity of the 20°30'N seamount at the Mid-Atlantic Ridge fall on the lower limit of samples from glacial periods, absolute carbonate-free concentrations of both elements are higher. Ti concentrations of volcaniclastic sediments are highly variable, while Al shows comparatively less fluctuations. This variability of Ti content follows a clear geographic pattern: Ti content increases with proximity to the Azores hot spot (cf. above). The group of samples with 0.5-0.75% Ti is derived from the vicinity of the 20°30'N seamount and from the Lucky Strike seamount (37°N). Samples with 0.9-1.01% Ti occur at 38°N; finally, three samples from core Ac.92 KS04, located NW of the ridge axis at 38°N, have still higher Ti contents of 1.13-1.21%.

Sample Noratlante KS12-S, whose composition is similar to differentiated volcanic rocks from the Azores islands (cf. above), may be representative of the end member for Holocene samples. Alternatively, Ti/Al-ratios of 0.13-0.17 could be obtained by mixing between basaltic or mugearitic rocks from the Azores islands with Ti/Al = 0.27 or 0.20, respectively (Davies et al. 1989, Storey et al. 1989, Widom et al. 1992, Mungall & Martin 1995), and MAR basalts whose Ti/Al-ratio is approximately 0.10 (e.g. Wilson 1989). In any case, the Holocene "basic end member" necessarily includes a contribution derived from basic volcanic rocks of the

Azores islands. This might explain why core GEOFAR KS03, which is located at 20°30'N south of the main study area and presumably receives no detrital input from the Azores islands, has consistently lower Ti/Al-ratios in the range of average mid-ocean ridge basalts.

In the other cores, the lower Ti/Al-ratios of samples from glacial periods could theoretically also be explained by absence of detrital input from the islands, resulting in MORB-type element ratios. Two arguments can be invoked against this explanation: Lower or even zero erosion rates on the islands during glacial periods are hardly conceivable; furthermore, Ti/Al-ratios in a number of samples are lower than corresponding ratios of E-type MORB of the same latitude. Therefore it is more likely that the lower ratios represent mixing between basic detritus derived from the Azores and/or locally from the Mid-Atlantic Ridge with an increased portion of continentally derived detritus, since average upper crust has a much lower Ti/Al-ratio of 0.037 (Taylor & McLennan 1985).

This interpretation is further supported by a plot of K against Al (Fig. 6.6b). In GEOFAR sediments, K and Al are positively correlated with considerable scatter in the data (r=0.62); the diatom layer of core GEOFAR KF16, which is the single sample with low concentrations of both elements, has been omitted from the data set used to calculate the correlation coefficient in order to avoid a correlation which has been artificially induced or enhanced by a single outlier. The plot of K vs. Al may be tentatively interpreted in terms of two bounding mixing lines, with average upper continental crust and sample Noratlante KS12-S representing evolved rocks from the Azores islands as respective end members. Samples with intermediate K/Al-ratios might contain variable proportions of these two detrital sources.

All of the volcaniclastic samples from the Mid-Atlantic Ridge have distinctly lower K content; alteration of volcanic ash layers tends to augment K and decrease Al content. Compared to all of the GEOFAR cores, core Ac.91KS04 (EPSHOM) has lower K content and K/Al-ratios throughout the sediment section which comprises Oxygen Isotope Stages 1 to 5.1. This core is located immediately adjacent to the rift valley walls, detrital input derived locally from the MAR may dominate at this particular core location.

Si/Al-ratios (Fig. 6.6c) appear to be dominantly controlled by variable amounts of biogenic opal. Samples from the late Holocene show an excellent correlation (r=0.95) between Si and Al and have Si/Al-ratios of 2.5-2.7, which are values typical of basaltic rocks. Higher Si/Al-ratios of samples from the early Holocene and from glacial periods should partially reflect a more acidic detritus composition; however, Si/Al-ratios greater than 4 cannot be explained by any detrital sediment source excluding pure quartz. Observations of coarse (own data) and fine fractions (Müller 1995) indicate increased abundance of biogenic opal during glacial periods. In the Norwegian-Greenland Sea, the Si/Al-ratio can be used to trace detrital sources (Paetsch 1991), since biogenic silica production has generally been low in this area throughout the last 300.000 years (Bohrmann 1988). At the MAR south of the Azores, this has apparently not been the case; consequently, the Si/Al-ratio cannot be used to trace detrital sediment sources.

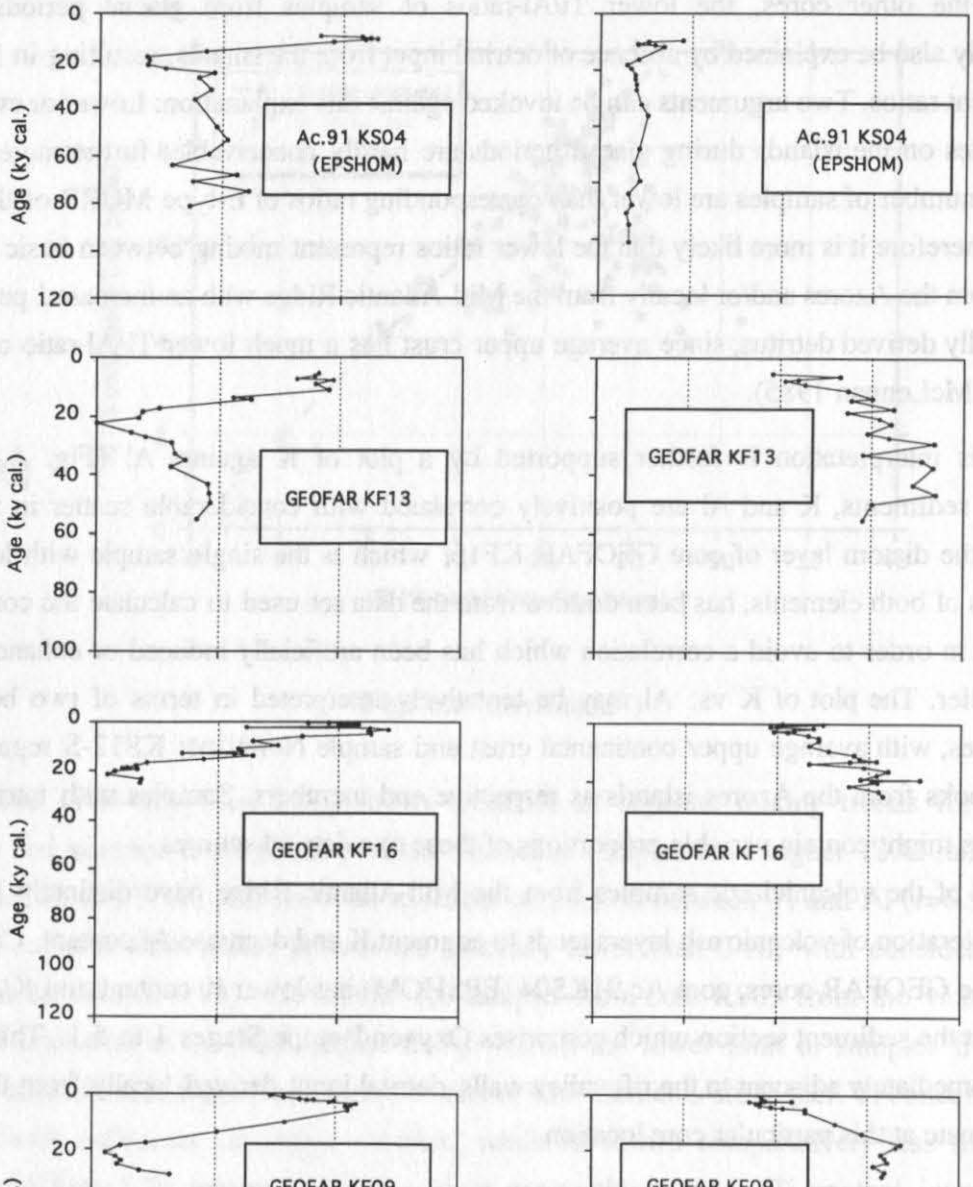

Fig. 6.7: Ti/Al (*left*) and K/Al (*right*) - ratios vs. time, representing basic and acidic detritus

Temporal fluctuations of Ti/Al and K/Al - ratios (Fig. 6.7 a and b) can be correlated between the four cores studied geochemically and stratigraphically. As discussed above, higher K/Al- and lower Ti/Al-ratios suggest an increased amount of continentally-derived detritus during glacial periods. In core Ac.91KS04, consistently low K/Al-ratios and higher Ti/Al-ratios throughout most of the time period studied are compatible with the interpretation that detritus has a dominantly basaltic composition and is derived locally from the MAR at this particular core location. Surficial peaks of the Ti/Al-ratio occur in oxidized surface layers, which may indicate that Ti is also present as an adsorbed ion on Fe-Mn oxyhydroxides of hydrothermal origin, which has been previously described from the East Pacific Rise (Marchig & Gundlach 1982). These oxyhydroxides have subsequently been diagenetically remobilized and reprecipitated in oxidized surface layers. However, this diagenetic process is superposed on a continuous increase of Ti/Al-ratios during Termination I and generally elevated ratios during the Holocene; the existence of this additional source of Ti should not invalidate the interpretations concerning composition and temporal variability of detrital sediment sources presented in this section.

6.5 Conclusions

While biogenic carbonate dominates the chemical composition of most samples, factor analysis has shown that volcanic, ultramafic, detrital and hydrothermal sediment sources are all present. Volcanic and ultramafic input is most important in some samples from allochthonous layers. A N-S gradient in the chemical composition of volcaniclastic sediments reflects the decreasing influence of the Azores hot spot. Detrital sources are more widespread, at least one basic and one acidic component can be distinguished. The basic component is more important during the Holocene, continentally-derived acidic detritus is more important during glacial periods. Ti/Al- and K/Al-ratios, respectively, are effective indicators of these two sources. The hydrothermal component includes metals derived from hydrothermal solutions (Fe, Mn, Cu) and elements scavenged from the water column (P, V, As). Hydrothermal factor scores are highest in oxidized surface layers due to diagenetic remobilization of metals and coprecipitated elements; furthermore, the distribution of factor scores suggests maximum hydrothermal influence in core KF09, south of the *Lucky Strike* vent field.

7. Metal accumulation rates in Mid-Atlantic Ridge sediments: primary fluxes of potential hydrothermal tracers and secondary diagenetic modification

7.1 Introduction

In this chapter, **metal accumulation rates** are discussed in order to quantify fluxes of potential hydrothermal tracers, investigate their spatial and temporal variability in the study area and compare these fluxes with published data from other hydrothermally influenced marine environments. The existence of hydrothermal activity in the study area has been confirmed by the recent discovery of the *Lucky Strike* and *Menez Gwen* hydrothermal sites; additionally, particle-rich plumes and chemical anomalies (Mn, ^{3}He, CH_4) in the water column suggest the presence of other currently undiscovered vent fields on the seafloor. While some input from hydrothermal **sulfides** is present, especially at the Lucky Strike seamount (cf. Chapter 8), the hydrothermal contribution to pelagic sediments in the study area should dominantly consist of fine-grained **Fe-Mn-oxyhydroxides**, which may be laterally dispersed in hydrothermal particle plumes over considerable distances. At the Mid-Atlantic Ridge, plumes generally remain confined within the axial valley. Fallout from hydrothermal particle plumes in sediments includes elements scavenged from the water column by oxyhydroxide particles, in particular V, P and As. Sequential leaching (Robbins et al. 1984) and Mössbauer spectroscopy on selected samples have been performed to give clues on speciation and bonding state of iron and manganese. Discussion of results particularly focuses on post-depositional diagenetic modification of primary fluxes.

7.2 Results

7.2.1 Metal accumulation rates

Metal accumulation rates were calculated using the relationship:

$$\mathbf{A_e = C_e \; \rho \; S}$$

where $\mathbf{A_e}$ is the accumulation rate of element e in mg or μg/cm^2 ky, $\mathbf{C_e}$ is the bulk concentration of the respective element, ρ is the dry bulk density in g/cm^3 and **S** is the sedimentation rate in cm/ky. Sedimentation rates have been determined by linear interpolation between oxygen isotope events and AMS age data.

While the base of core GEOFAR KF16 is still within isotope stage 2, its age cannot be exactly constrained. Consequently, data from this core are presented on a depth rather than age scale and minimum accumulation rates are shown for stage 2. Since volcanic ash layers in core Ac.91KS04 (EPSHOM) have been deposited in „near zero time“ disrupting the continuous accumulation of pelagic sediments, their thickness has been subtracted from the thickness of corresponding sediment sections used to calculate pelagic sedimentation rates, and geochemical data from volcanic layers have not been considered for calculation of metal accumulation rates.

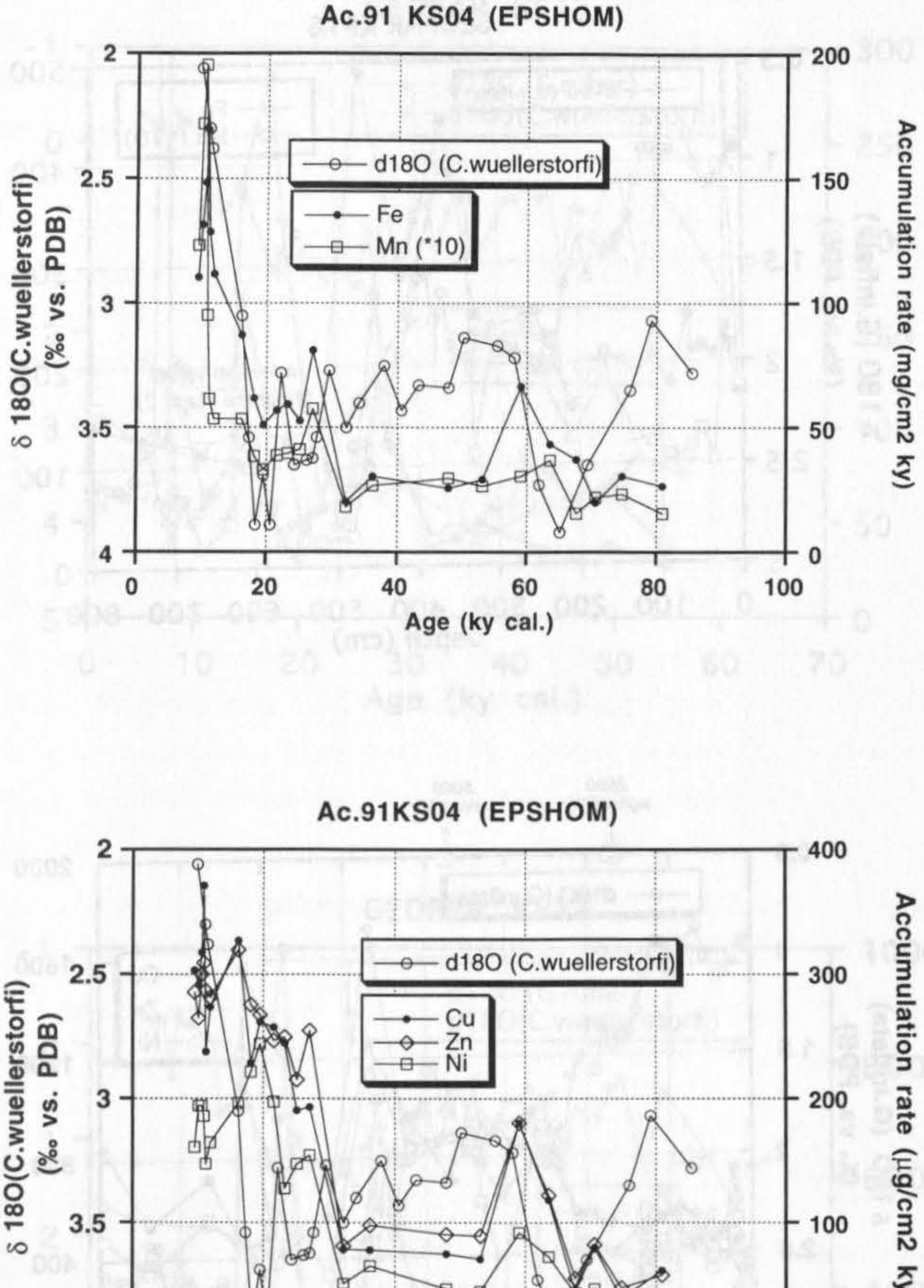

Fig. 7.1: Temporal variability of metal accumulation rates in core Ac.91 KS04 (EPSHOM)

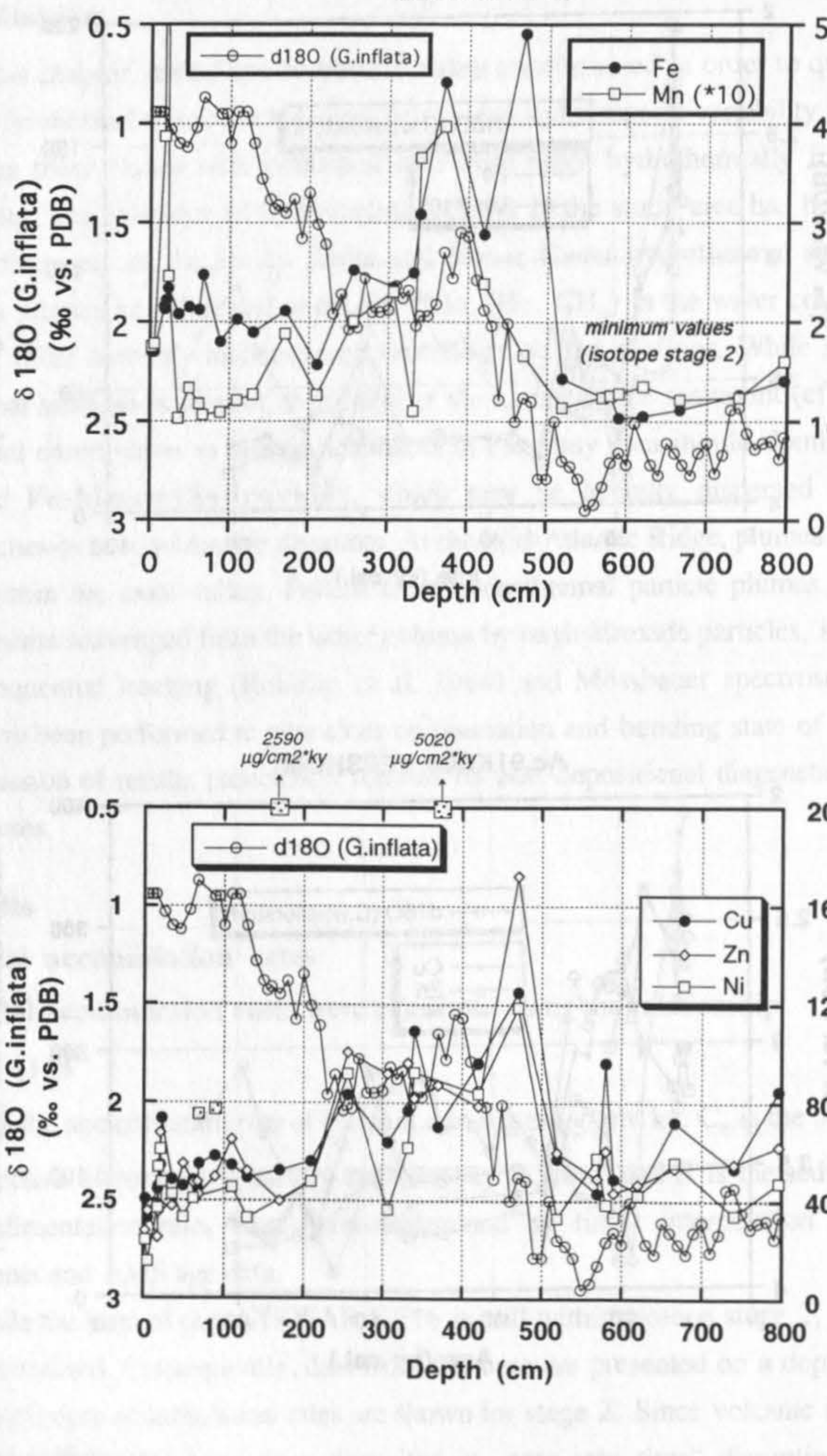

Fig. 7.2: Temporal variability of metal accumulation rates in core KF16. Minimum values plotted for isotope stage 2 (core depth >500 cm). Filled squares represent Ni data for samples affected by admixture of serpentine material.

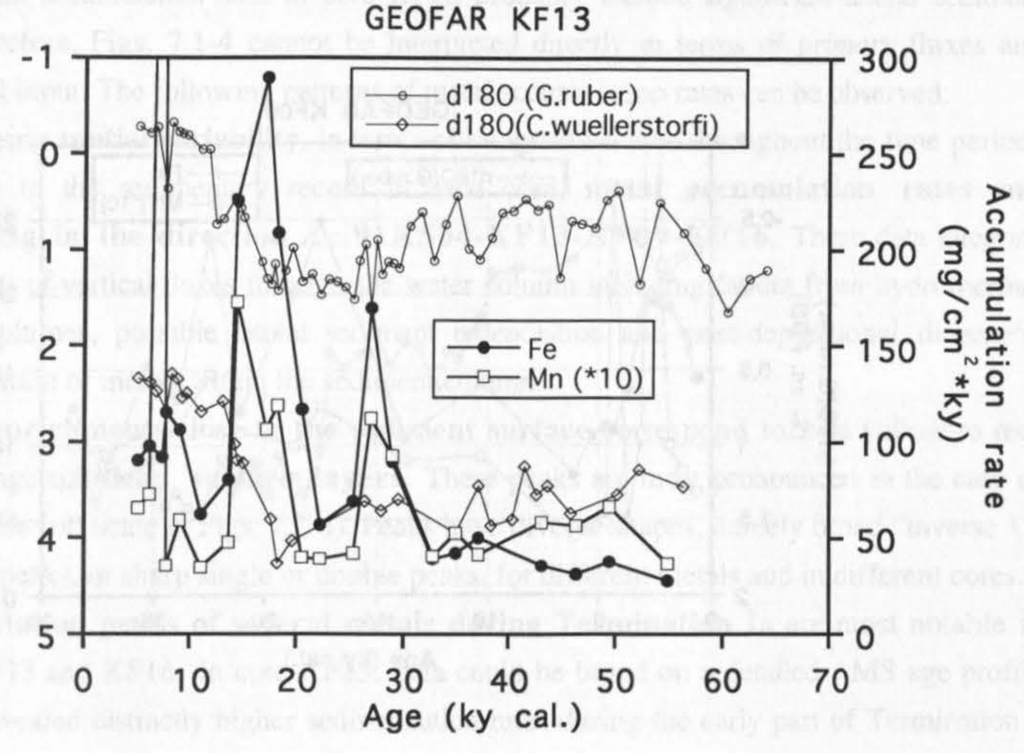

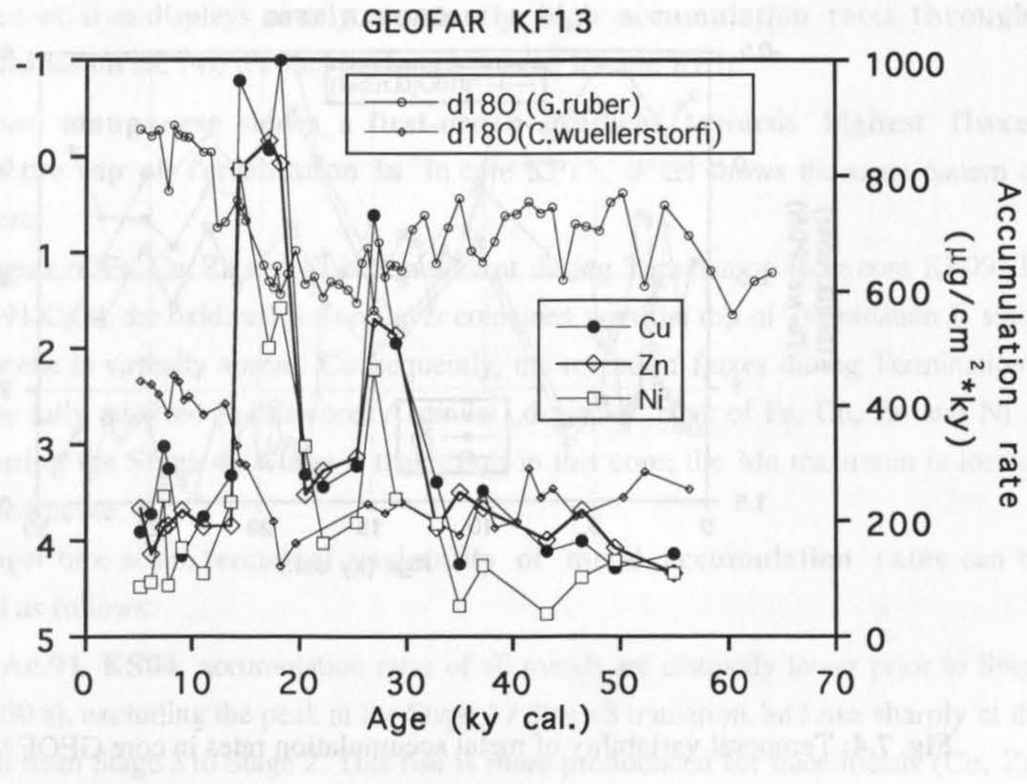

Fig. 7.3: Temporal variability of metal accumulation rates in core GEOFAR KF13

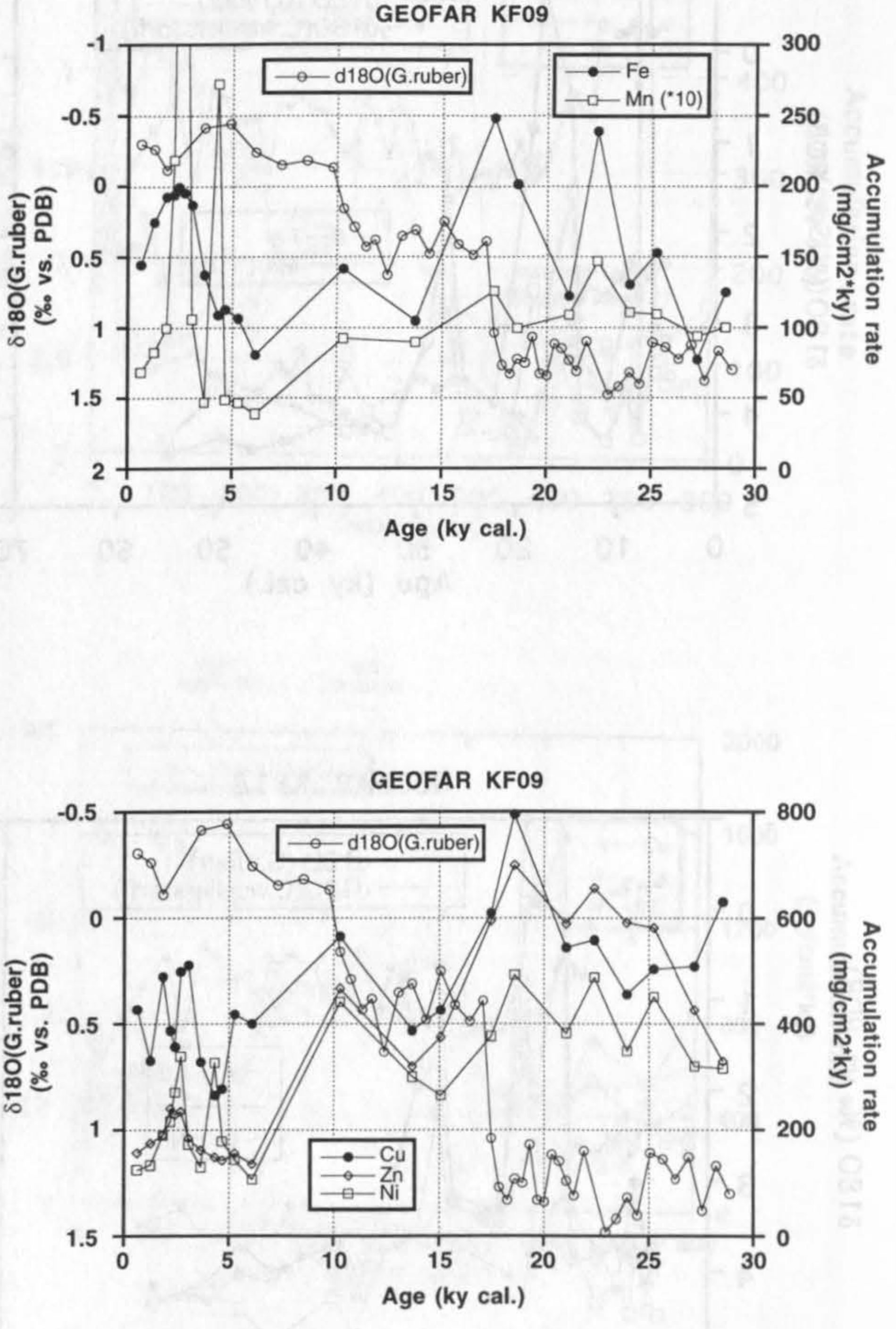

Fig. 7.4: Temporal variability of metal accumulation rates in core GEOFAR KF09

Accumulation rates of Fe, Mn, Cu, Zn and Ni are shown in Figs. 7.1-4. As discussed below, there is strong evidence for a diagenetic origin of some peaks in accumulation rates, and metal and bulk accumulation rates in core KF16 probably include significant lateral sediment supply. Therefore, Figs. 7.1-4 cannot be interpreted directly in terms of *primary* fluxes and hydrothermal input. The following patterns of metal accumulation rates can be observed:

(1) Considering **spatial variability**, in terms of integrated fluxes throughout the time periods available in the sedimentary record in each core, **metal accumulation rates are increasing in the direction Ac.91KS04-KF13-KF09-KF16**. These data integrate the effects of vertical fluxes through the water column including fallout from hydrothermal particle plumes, possible lateral sediment redeposition and post-depositional diagenetic redistribution of metals within the sediment column.

(2) Metal enrichments close to the sediment surface correspond to pale yellow to reddish orange **oxidized surface layers**. These peaks are most pronounced in the case of manganese (off scale in Figs. 7.2-4). Peaks have diverse shapes, namely broad "inverse U-shaped" peaks, or sharp single or double peaks, for different metals and in different cores.

(3) Accumulation peaks of several metals during Termination Ia are most notable in cores KF13 and KF16. In core KF13, data could be based on a detailed AMS age profile which revealed distinctly higher sedimentation rates during the early part of Termination I subsequent to the Last Glacial Maximum (cf. stratigraphy section). If, by analogy, similar sedimentation pulses had occurred in the other cores, the amplitude of accumulation peaks would be enhanced accordingly.

- In both cores, **iron** displays **nearly constantly high accumulation rates throughout Termination Ia**, two distinct peaks are present in core KF16.
- In contrast, **manganese** shows a **first-order gradient towards highest fluxes close to the top of Termination Ia**. In core KF13, nickel shows the same pattern as manganese.

A peak of Fe, Cu, Zn and Ni is also present during Termination Ib in core KF09. In core Ac.91KS04, the oxidized surface layer coincides with the top of Termination I, since the Holocene is virtually absent. Consequently, the record of fluxes during Termination I cannot be fully resolved in this core. A similar „deglacial" peak of Fe, Cu, Zn and Ni is found during the **Stage 4 / Stage 3 transition** in this core; the Mn maximum is located further downcore.

(4) On a longer time scale, **temporal variability of metal accumulation rates** can be observed as follows:

- In core **Ac.91 KS04**, accumulation rates of all metals are distinctly lower prior to Stage 2 (>30,000 a), excluding the peak at the Stage 4 / Stage 3 transition, and rise sharply at the transition from Stage 3 to Stage 2. This rise is more pronounced for trace metals (Cu, Zn, Ni) compared to iron and manganese, which, by contrast, show a comparatively higher degree of enrichment in oxidized surface layers.

- In core **KF09**, accumulation rates of all metals are consistently elevated during Stage 2 compared to Holocene "baseline values" beneath oxidized surface layers. The same may be the case in core **KF16**, since minimum values plotted for Stage 2 sediments are already comparable to Holocene values in the case of Mn, Cu, Zn and Ni.
- In core **KF13**, metal accumulation rates prior to the Last Glacial Maximum (18,300 a) show considerable fluctuations. A second peak during early Stage 2 is also located within an interval of higher sedimentation rates During Stage 3, accumulation rates are slightly lower in the case of iron, especially prior to 40,000 years, and in the same range for Cu, Zn and Ni, if compared to Holocene baseline values.

7.2.2 Metal distribution in oxidized surface layers

Enrichments of metals and associated elements at the sediment surface follow two different patterns (Fig. 7.5): Manganese is enriched up to seven-fold in brown-colored cm-thick layers; cobalt and nickel are similarly enriched in these layers. In contrast, iron shows broader enrichments throughout the oxidized surface layers, with a tendency towards highest concentrations close to the sediment-water interface. P, V and As, elements known to be scavenged from the water column by hydrothermal Fe-oxyhydroxides, show similar patterns.

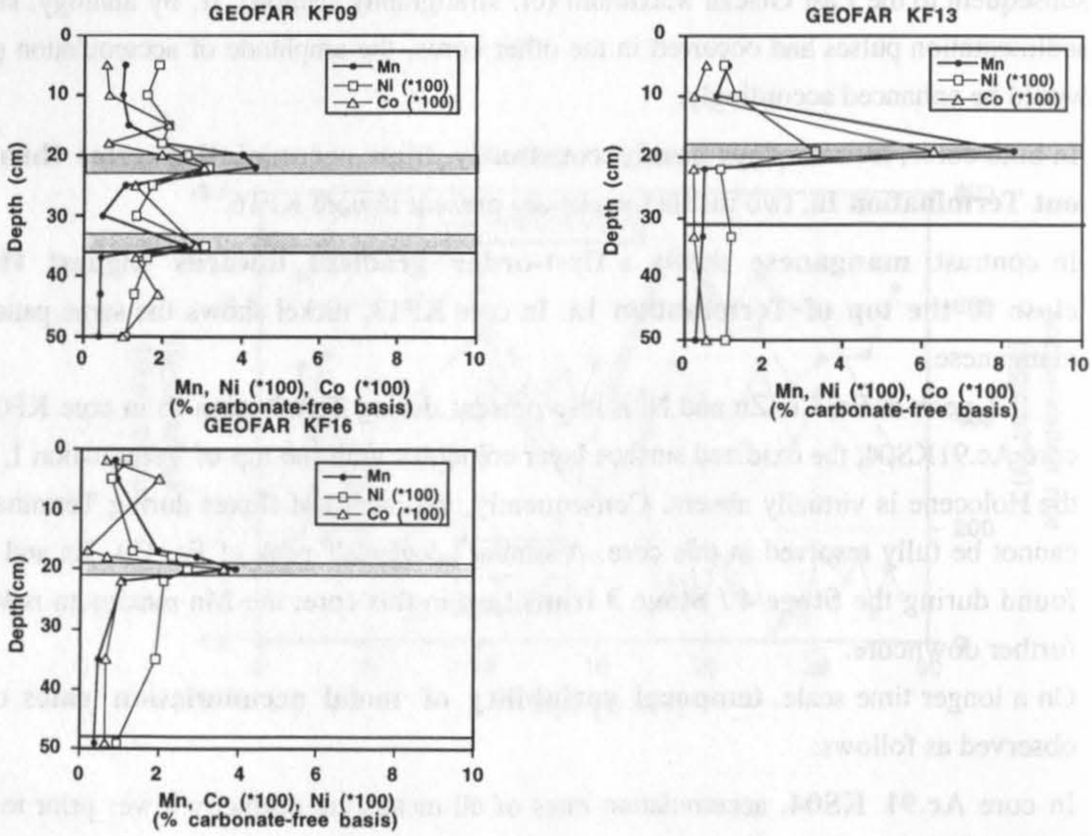

Fig. 7.5 *(continued on following page)* **:** Distribution of metals and associated elements in oxidized surface layers. Shaded pattern indicates brown-colored layers, bold vertical lines show base of oxidized surface zone in each core.

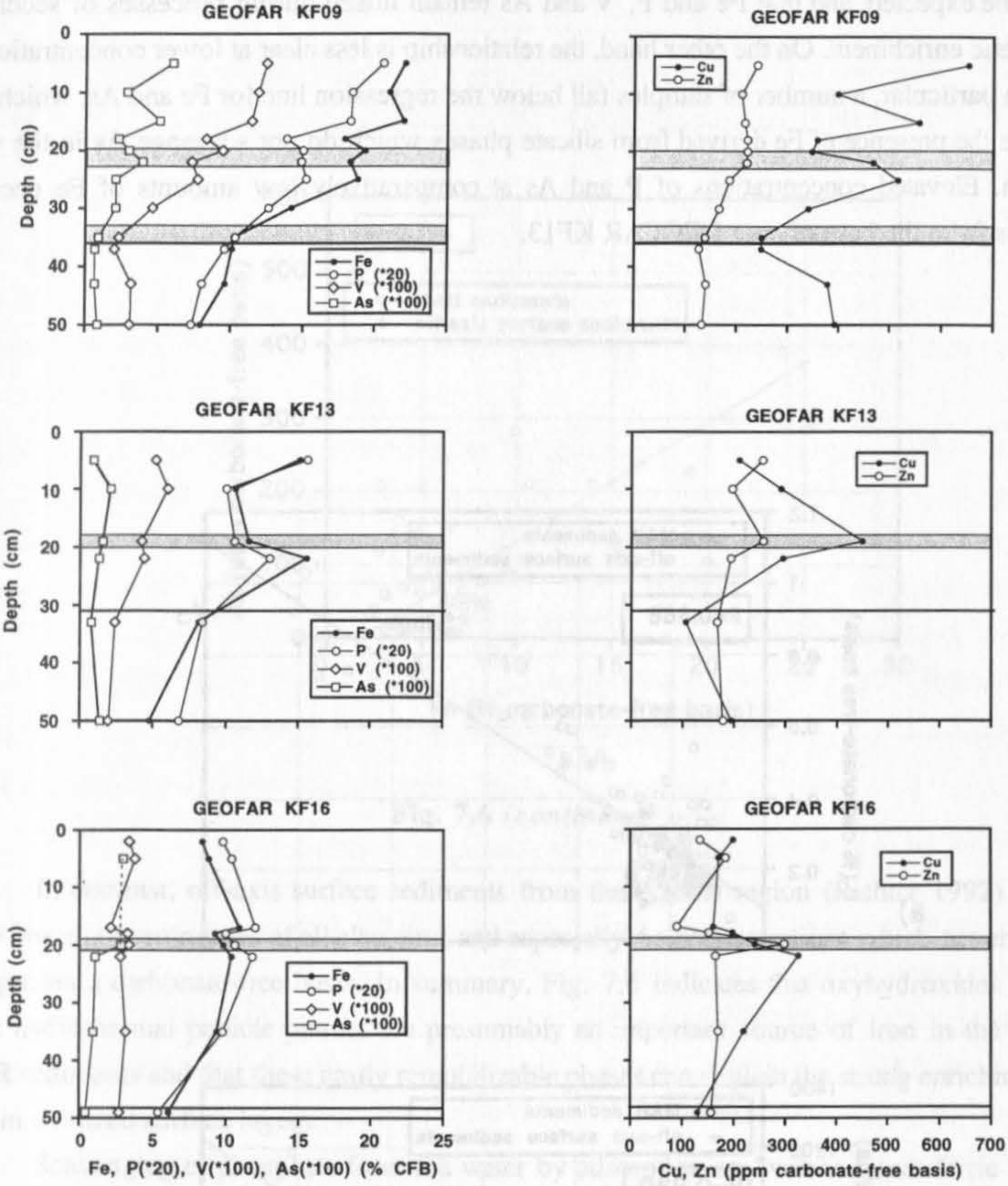

Fig. 7.5 (*continued*)

7.2.3 P, V and As: scavenging from the water column by hydrothermal oxyhydroxides

Figure 7.6 shows scatter plots of Fe vs. P, V and As, respectively. Samples with bulk As-concentrations below the detection limit (12 ppm) have not been plotted. In spite of some scatter in the data, in particular for P and As, there is a relationship evident between iron and these three elements. The association between Fe and P, V and As may primarily result from scavenging of the latter elements by Fe-oxyhydroxides in hydrothermal particle plumes in the water column. Highest concentrations of all elements occur in oxidized surface layers. This suggests that Fe-oxyhydroxide phases are susceptible to early diagenetic remobilization, as would be expected, and that Fe and P, V and As remain linked during processes of secondary diagenetic enrichment. On the other hand, the relationship is less clear at lower concentrations of iron. In particular, a number of samples fall below the regression line for Fe and As, which may indicate the presence of Fe derived from silicate phases which do not scavenge As in the water column. Elevated concentrations of P and As at comparatively low amounts of Fe occur in samples from the base of core GEOFAR KF13.

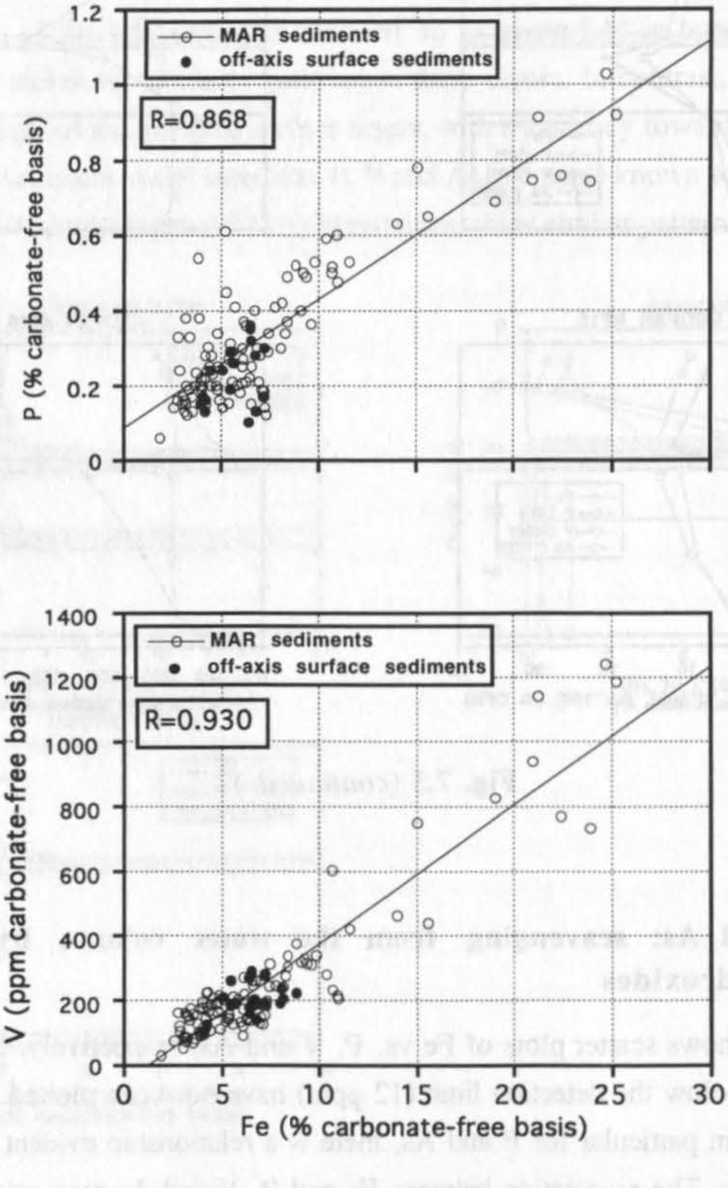

Fig. 7.6 : Scatter plots of Fe vs. P, V and As (elements scavenged from the water column by hydrothermal Fe-oxyhydroxides). Off-axis surface sediment data from Richter (1992), regression lines drawn for Mid-Atlantic Ridge sediments only.

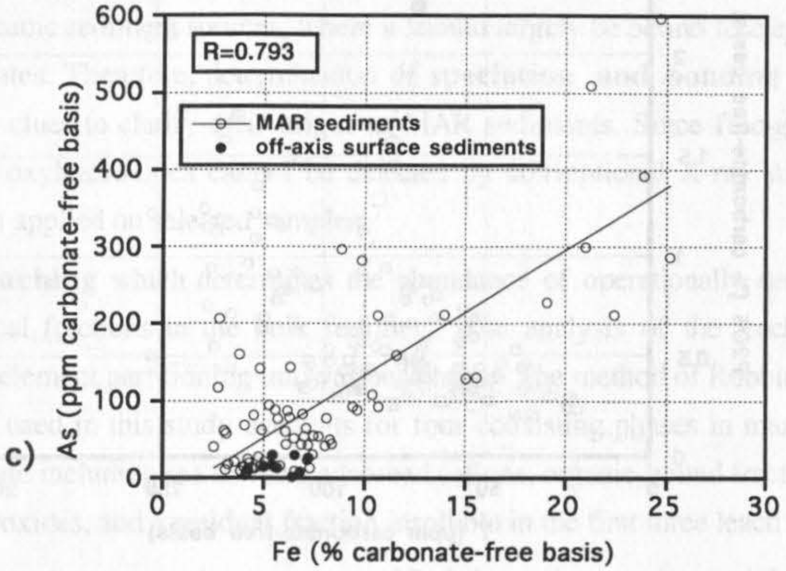

Fig. 7.6 *(continued)*

In contrast, off-axis surface sediments from the Azores region (Richter 1992) always have lower concentrations of all elements, and especially As concentrations which never exceed 30 ppm on a carbonate-free basis. In summary, Fig. 7.6 indicates that oxyhydroxides derived from hydrothermal particle plumes are presumably an important source of iron in the studied MAR sediments and that these easily remobilizable phases can explain the strong enrichments of iron in oxidized surface layers.

Scavenging of phosphate from sea water by adsorption on "volcanogenic ferric oxides" has been described as early as the 1970's (Berner 1973, Froelich et al. 1977). On the other hand, phosphorus may also occur in apatite contained in skeletal remains. The P_2O_5/Y-ratio has been proposed as a means to distinguish between biogenic apatite and hydrothermally-derived phosphorus, since biogenic apatite tends to be enriched in yttrium, while phosphorus coprecipitated with hydrothermal Fe-oxides contains no Y (Marchig et al. 1982, 1990, Marchig & Erzinger 1984). Therefore, P and Y show a significant correlation in average deep-sea sediments and diagenetic metalliferous sediments, whereas hydrothermal metalliferous sediments have significantly lower contents of Y at comparable contents of P and no correlation between these two elements. It is not surprising that average pelagic clay (Turekian & Wedepohl 1961) falls on the regression line for pelagic sediments without hydrothermal influence established by Marchig and co-workers.

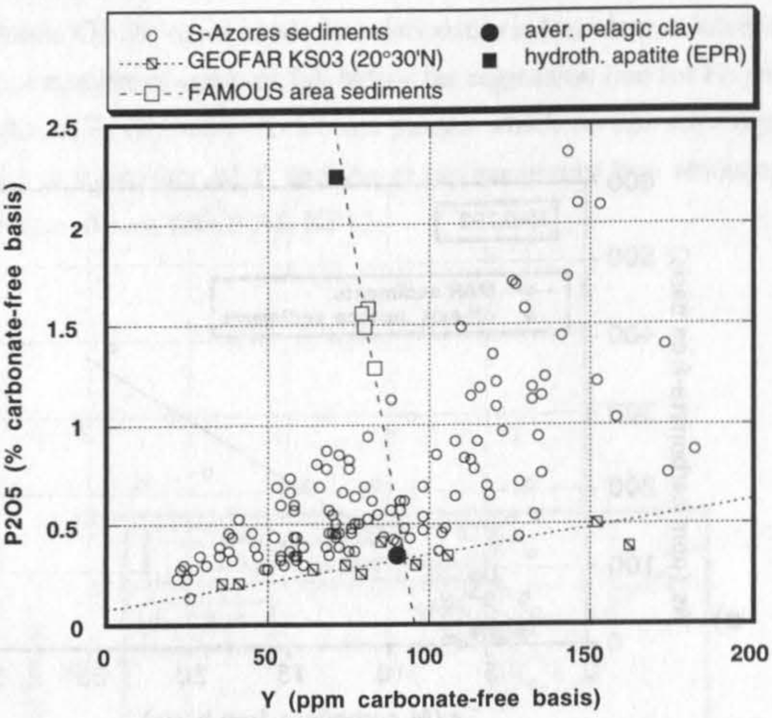

Fig. 7.7: P_2O_5 and Y, both on a carbonate-free basis. FAMOUS area sediments from Richter (1992), average pelagic clay from Turekian & Wedepohl (1961), "hydrothermal apatite" from Marchig et al. (1990).

Figure 7.7 shows the P_2O_5 and Y content of MAR sediments analyzed in this study compared to average pelagic clay (Turekian & Wedepohl 1961) and the "hydrothermal apatite" value of hydrothermal metalliferous sediments from the East Pacific Rise (Marchig et al. 1990). In MAR sediments south of the Azores, P_2O_5 and Y are correlated with each other (r=0.73), albeit with a considerable degree of scatter. However, for similar P_2O_5-content, their Y-content is lower than expected for pelagic clay, implying that some phosphorus is likely to be of hydrothermal origin. Yet this contribution is presumably smaller than that of biogenic apatite, and therefore can only diminish, but does not obliterate the correlation between P_2O_5 and Y. Sediments from core GEOFAR KS03 at 20°30'N plot close to the "pelagic clay" line, which means that they apparently received no hydrothermally derived phosphorus. On the other hand, FAMOUS area sediments (Richter 1992) are significantly enriched in phosphate relative to yttrium, and plot very close to a mixing line between pelagic clay and the hydrothermal end member. While the apparent negative correlation between P_2O_5 and Y in the FAMOUS samples is statistically not significant since it is based on only four samples, it would indicate that hydrothermal phosphorus is dominating in the FAMOUS area.

7.2.4 Speciation of iron and manganese: information from selective leaching and Mössbauer spectroscopy

Iron, manganese and other metals and coprecipitated elements are affected by secondary diagenetic remobilization and precipitation in oxidized surface layers. Furthermore, in addition to oxyhydroxides derived from hydrothermal particle plumes, iron can also originate from detrital and/or volcanic sediment sources, where it should largely be bound to clay minerals and other aluminosilicates. Therefore, determination of **speciation and bonding state of Fe and Mn** can give clues to clarify their origin in MAR sediments. Since fine-grained, poorly crystalline Fe-Mn oxyhydroxides cannot be detected by conventional X-ray diffraction, two methods have been applied on selected samples:

- **Sequential leaching** which determines the abundance of operationally defined chemical and mineralogical fractions in the bulk sediment. The analysis of the leachates provides information on element partitioning into various phases. The method of Robbins et al. (1984) which has been used in this study accounts for four coexisting phases in marine sediments: calcium carbonate including sea salt and adsorbed cations, organic-bound fraction, ferromanganese oxyhydroxides, and a residual fraction insoluble in the first three leach solutions.
- **Mössbauer spectroscopy** gives more specific information on chemical forms of iron in marine sediments (Haxel 1987, König 1990).

Twenty-two samples were selected for sequential leaching. The sample set included the various lithologies encountered, namely oxidized surface layers, underlying suboxic sediments, organic-rich (>1% $C_{org.}$) samples from the reduced part of core GEOFAR KF16 (KF16-580 and -620), and samples with major volcaniclastic input (KG18-S, KS03-85, KG18-13). Figure 7.8 a shows the fractions of bulk sediment soluble in the first three leaches and present in the residual fraction. Since biogenic carbonate is the dominant sediment component in most samples, it is not surprising that generally >80% of the bulk samples is soluble in the first leach. Notable exceptions are only samples with major volcanic input. Therefore plotting relative proportions of organic-bound, oxyhydroxide and residual phases in the residue after the first leach (Fig. 7.8 b), a procedure similar to recalculating geochemical data on a carbonate-free basis, gives more meaningful information, especially on the abundance of ferromanganese oxyhydroxides including hydrothermal and diagenetic components.

Figure 7.9 a demonstrates that, while there is an excellent correlation, slightly higher percentages of bulk sediment are soluble in the **carbonate** leach than the corresponding amounts of $CaCO_3$ determined independently (Carlo Erba CHN analyzer). This “excess“ is apparently mostly due to a contribution from sea salt, as indicated by the chloride determinations, and may include an adsorbed component in some samples. Sample KS03-85 is the only one with a strikingly different distribution pattern. 37.5% of the bulk sediment are soluble in the first leach, compared to a $CaCO_3$ content of only 10.5 %. This sample contains abundant smectite which is presumably derived from alteration of volcanic material. Possibly smectites, in

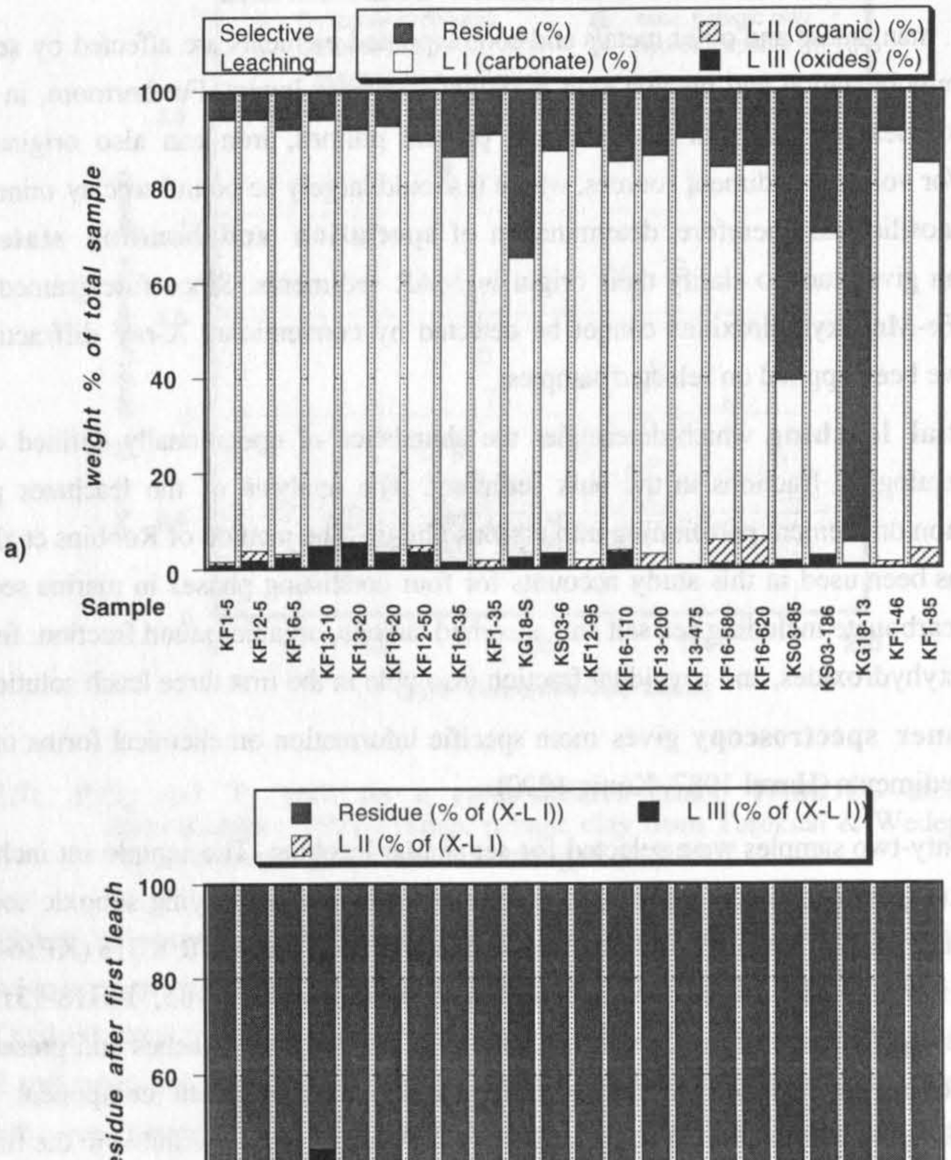

Fig. 7.8: a) Partitioning of bulk sediment into carbonate-bound, organic-bound, oxide and residual phases

b) Recalculated percentages of organic-bound, oxide and residual phases on a carbonate- and salt-free basis (residue after first leach).

particular interlayer sites, have been partially attacked by the buffered acetic acid leach. Since silicates, especially iron-rich phyllosilicates, are vulnerable to dissolution at low pH, it could be speculated that this is related to a drop in pH. However, the buffering capacity of the acetic acid - sodium acetate leach is sufficiently high to keep the pH at nearly constant values (Robbins et al. 1984).

The second leach which dissolves the **organic-bound** fraction apparently gave less reliable results. While a general relation with the amount of organic carbon is evident (Fig. 7.9 b), a number of samples show no weight loss or even a slight (< 1%) gain of weight after the second leach, which most likely indicates that precipitation from the leach solution occurred. Maximum weight losses in organic-rich samples KF16-580 and -620 were 4.9 and 5.7%, respectively, or 22 and 25% on a carbonate- and salt-free basis. No chemical analysis have been done on these leach solutions; the primary purpose of this step was to avoid scavenging of metals derived from the oxyhydroxide fraction by sedimentary organic matter, rather than chemically characterize the leach.

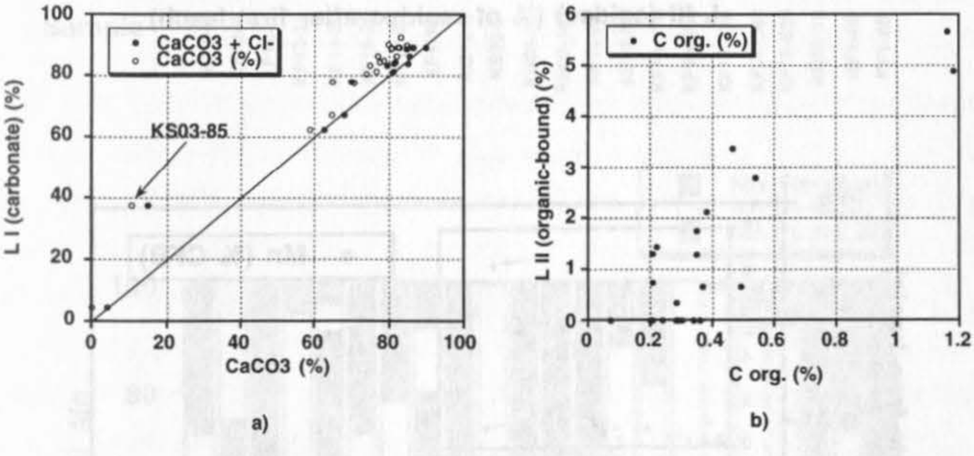

Fig. 7.9: Results from selective leaching vs. **a)** CaCO3- and **b)** C org.-determinations (Carlo Erba CHN Analyzer).
Sample KS03-85 (smectite-rich altered volcaniclastic material) discussed in text.

In the **oxyhydroxide** leach, maximum weight losses of 1-5.5% occur in samples from oxidized surface layers, corresponding to 10-45% on a carbonate- and salt-free basis. In most other samples, less than 1% weight loss of the bulk sediment (< 5% on a carbonate-and salt-free basis) is associated with the third leach. Figure 7.10 shows that there is a general relationship between Fe- and Mn-concentrations on a carbonate-free basis and percentages of the residue after Leach I soluble in the oxyhydroxide leach.

Partitioning of iron and manganese between carbonate/adsorbed, oxyhydroxide and residual fractions has been determined by spectrophotometric analysis of the leachates; the relative amount of Fe and Mn in the residual fraction has been computed by difference to bulk values from X-ray fluorescence, assuming that amounts of these metals in the organic-bound fraction are negligible (Fig. 7.11).

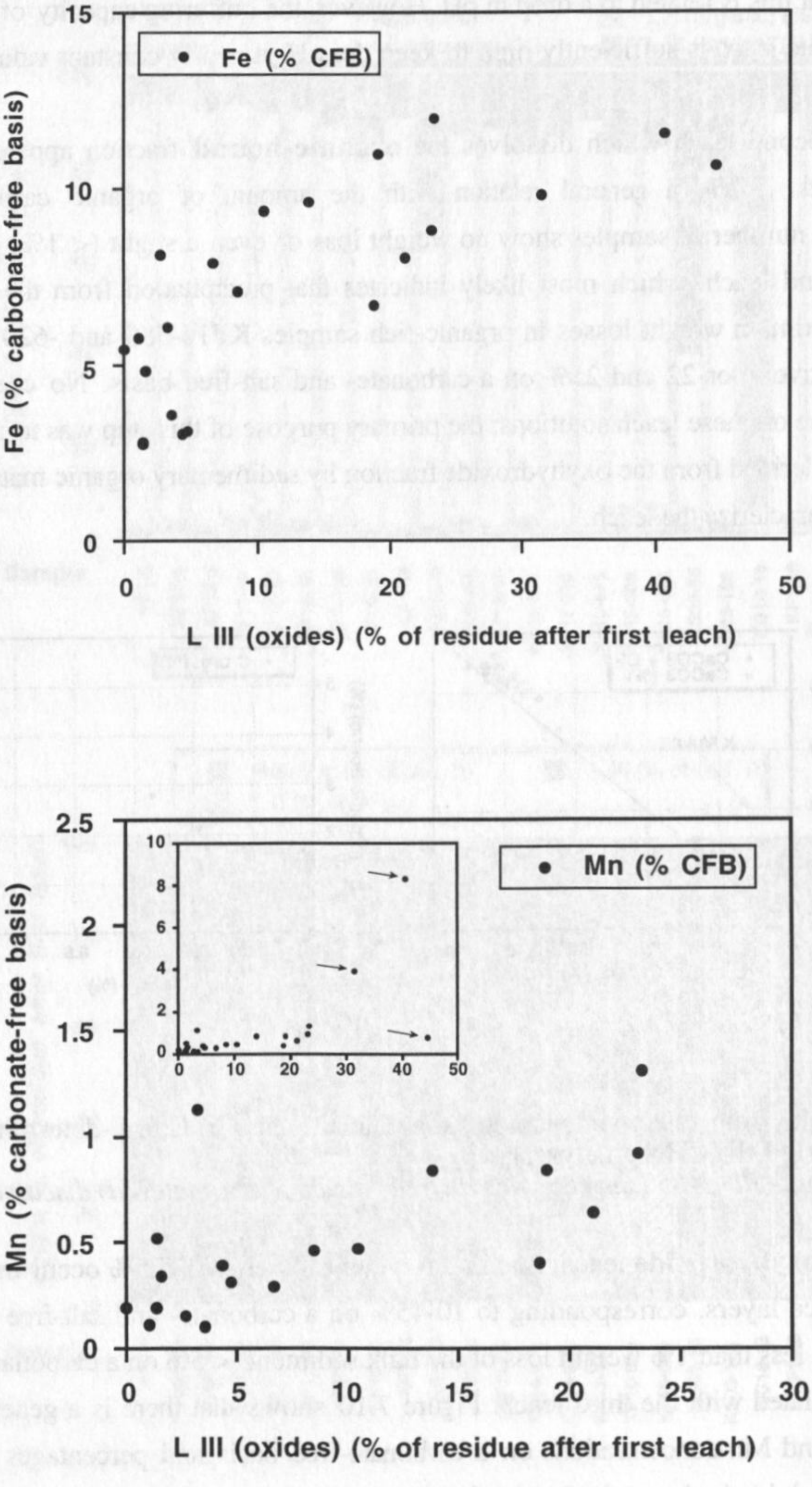

Fig. 7.10: Fe- and Mn-concentrations (carbonate-free basis) vs. percentages of residue after first leach soluble in oxyhydroxide leach. Lower graph shows relationship between Mn and oxyhydroxide fraction at low Mn concentrations, insert (same x- and y-variables) gives entire data set. Samples marked by arrows include two Mn-enriched samples from brown layers, and Fe-enriched sample KF13-10 (44.5% soluble, 0.78% Mn, 11% Fe).

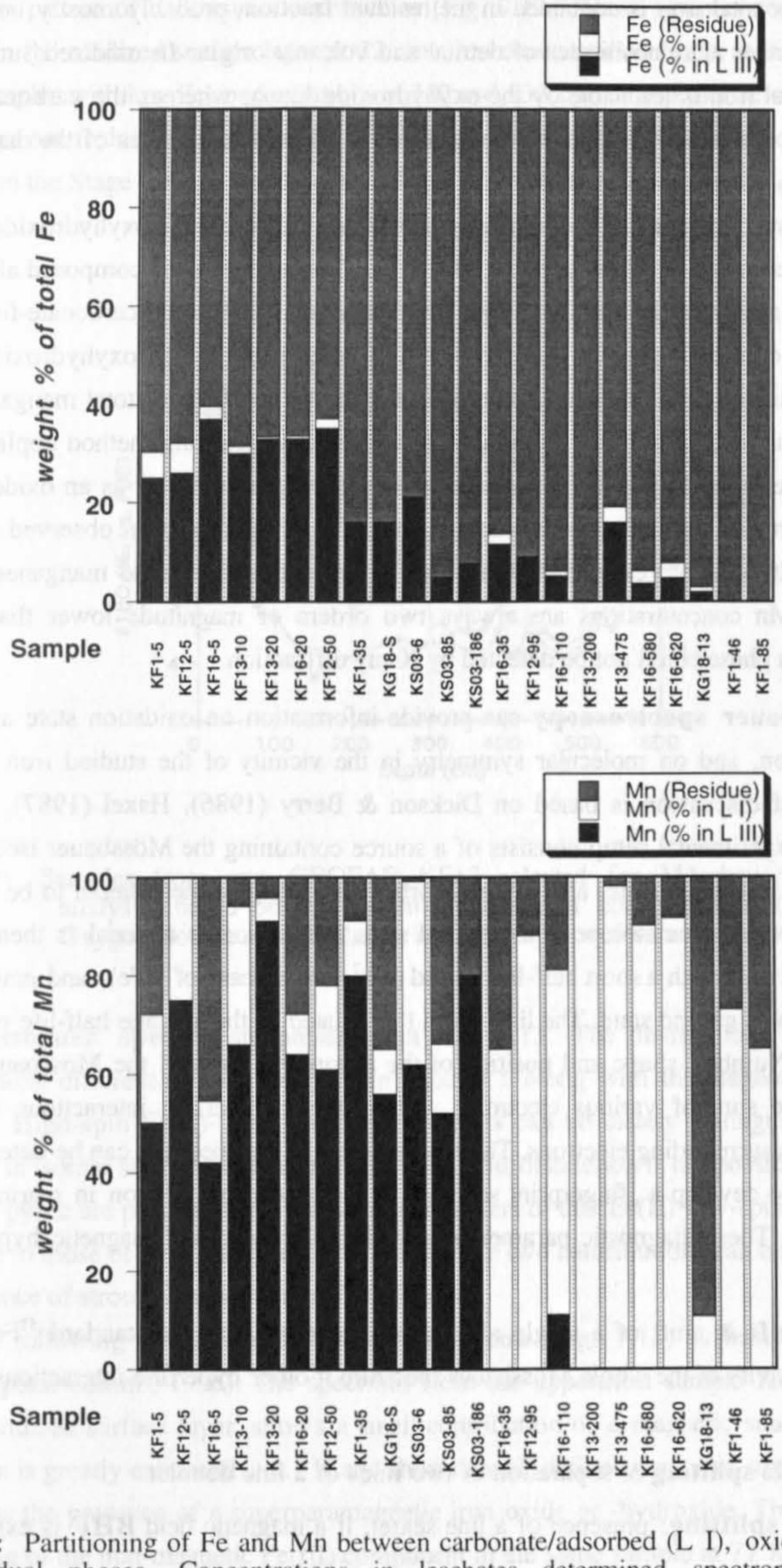

Fig. 7.11: Partitioning of Fe and Mn between carbonate/adsorbed (L I), oxide (L III), and residual phases. Concentrations in leachates determined spectrophotometrically, concentrations in residue calculated by difference to bulk values determined by X-ray fluorescence assuming negligible amounts in the organic-bound fraction.

Iron and manganese show noticeably different partitioning patterns: In all samples, more than half of the total iron is contained in the residual fraction, probably mostly bound to clay minerals and other aluminosilicates of detrital and volcanic origin. In oxidized surface layers, 30-37% of total iron is leachable by the oxyhydroxide leach, whereas the carbonate/adsorbed component accounts for 3% or less of the total iron in all but two samples of the data set, and a maximum of 6.1% in sample KF12-5.

In contrast, manganese is dominantly partitioned either into the oxyhydroxide or the carbonate/adsorbed phase in all samples but KG18-13. This last sample is composed almost entirely of volcaniclastic material and has a low Mn content of 0.11% on a carbonate-free basis. In samples from oxidized sediment sections, 40-90% is leachable by the oxyhydroxide leach. In samples from underlying sediments, more than 60 and up to 100% of total manganese is contained in the carbonate/adsorbed fraction. With the selective leaching method applied, it is not possible to determine whether Mn is present as manganese carbonate or as an oxide coating on surfaces of particles. No manganese coatings on foraminifera have been observed in the sand-size fraction. It is therefore more likely that Mn is present as a separate manganese carbonate phase; since Mn concentrations are always two orders of magnitude lower than carbonate content, such a phase could not be detected by X-ray diffraction.

Mössbauer spectroscopy can provide information on oxidation state and chemical bonding of iron, and on molecular symmetry in the vicinity of the studied iron atoms. The following brief discussion is based on Dickson & Berry (1986), Haxel (1987), and König (1990): The experimental setup consists of a source containing the Mössbauer isotope (in this case, ^{57}Fe) in an excited state, and of an absorber consisting of the material to be investigated which contains the same isotope in its ground state. The absorber material is then transferred into an excited state with a short half-life period (10^{-7} s in the case of ^{57}Fe), and emits a γ-quant on returning to its ground state. The line width Γ is related to the average half-life period of the excited state. Number, shape and position of the absorption lines in the Mössbauer spectrum result from the sum of various electronic and magnetic hyperfine interactions between the nucleus and its surrounding electrons. Three parameters of the spectrum can be determined, and were applied to develop a „fingerprint scheme“ to identify forms of iron in marine sediments (König 1990): These diagnostic parameters related to electronic and magnetic hyperfine interactions are

- **Isomer shift** δ: shift of a single absorption line relative to the standard ^{57}Fe-source, or center of gravity of the whole Mössbauer spectrum if other hyperfine interactions are present (cf. below).
- **Quadrupole splitting** Δ: separation of two lines of a line doublet.
- **Magnetic splitting**: presence of a line sextet, if a magnetic field **BHF** is experienced by the nucleus.

Six samples from core KF13 have been selected for Mössbauer spectroscopic studies based on the pattern of bulk iron concentrations (Fig. 7.12). These samples comprise the iron maximum in the oxidized surface layer at 22 cm, iron concentration peaks at 69, 120 and 180 cm, and samples with low Fe concentrations at 310 and 533 cm. The peaks below the oxidized surface layer occur during Termination I and Isotope Stage 2, the two lowermost samples are derived from the Stage 4/Stage 3 and Stage 3/Stage 2 transition, respectively.

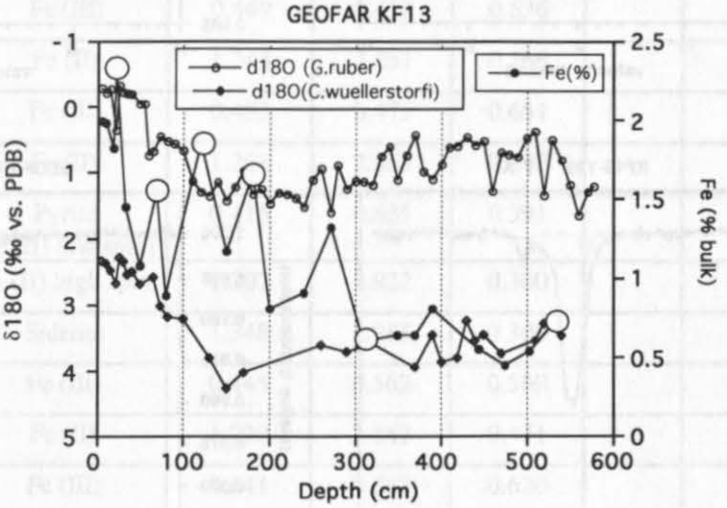

Fig. 7.12: Samples from core GEOFAR KF13 selected for Mössbauer spectroscopic analysis, based on the pattern of bulk iron concentrations (white circles). Oxygen isotope records shown as stratigraphic reference

Mössbauer spectra are presented in Fig. 7.13. The distributions of iron in the samples among different species are given in Table 7.1 along with the diagnostic Mössbauer parameters. High-spin Fe(II)- and Fe(III)-components can be clearly distinguished based on differences in isomer shift and quadrupole splitting. This distinction is not possible if significant amounts of pyrite are present. The Mössbauer parameters of this Fe(II) low-spin compound are comparable to those of Fe(III) species. Therefore, these two contributions can only be separated in the presence of strong external magnetic fields.

The following discussion of Mössbauer spectra (Fig. 7.13) is based on M. Drodt (written & pers. comm., 1996): The spectrum from the uppermost sample **KF13-22**, taken from the oxidized surface layer, shows a small contribution of a magnetic subspectrum. This contribution is greatly enhanced at 4.2 K and shows a well-defined magnetic sextet (Fig. 7.14). This implies the presence of a superparamagnetic iron oxide or -hydroxide. The large quadrupole splitting of the non-magnetic Fe(III) component in the same sample at 77 K similarly indicates iron-rich oxides or hydroxides; however, these Fe(III) phases have not yet developed magnetic ordering.

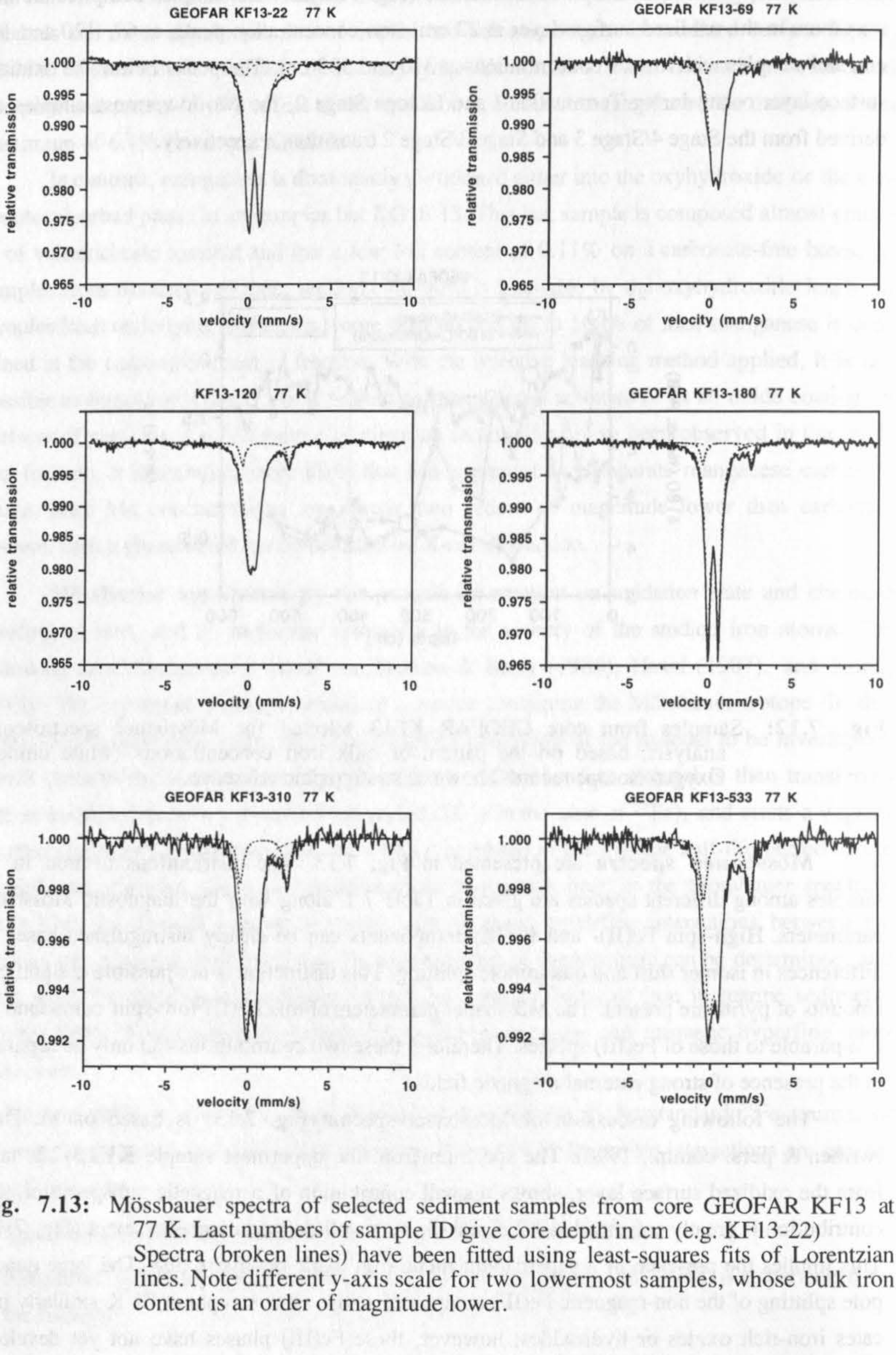

Fig. 7.13: Mössbauer spectra of selected sediment samples from core GEOFAR KF13 at 77 K. Last numbers of sample ID give core depth in cm (e.g. KF13-22) Spectra (broken lines) have been fitted using least-squares fits of Lorentzian lines. Note different y-axis scale for two lowermost samples, whose bulk iron content is an order of magnitude lower.

Sample	Component	δ (mm/s)	Δ (mm/s)	Γ(mm/s)	BHF	rel. area (%)
KF13-22 (77 K)	Fe (III)	0.473	0.722	0.537		85.59 ± 0.39
	Fe (II)	1.228	2.796	0.572		8.08 ± 0.56
	Fe (III) magnetic	0.484	- 0.180	0.353	52.645	6.33 ± 0.73
KF13-22 (4.2 K)	Fe (III)	0.463	0.602	0.500		12.03 ± 0.28
	Fe (II)	1.224	2.800	0.500		1.75
	Fe (III) magnetic	0.484	- 0.097	0.536	48.700	86.22
KF13-69 (77 K)	Fe (III)	0.449	0.458	0.636		94.63 ± 1.73
	Fe (II)	1.245	2.861	0.266		5.37 ± 1.48
KF13-120 (77 K)	Fe (III)	0.453	0.475	0.651		88.34 ± 0.87
	Fe (II)	1.268	2.866	0.342		11.66 ± 0.84
KF13-180 (77 K)	Pyrite [Fe (II) low spin]	0.415	0.631	0.391		89.86 ± 0.74
	Fe (II) high spin	1.207	2.922	0.300		7.73 ± 0.55
	Siderite	1.348	1.988	0.300		2.42 ± 0.58
KF13-310 (77 K)	Fe (III)	0.445	0.562	0.580		81.16 ± 1.69
	Fe (II)	1.229	2.862	0.471		18.84 ± 1.94
KF13-533 (77 K)	Fe (III)	0.441	0.567	0.620		75.51 ± 1.65
	Fe (II)	1.250	2.764	0.474		24.49 ± 1.75

Table 7.1: Mössbauer parameters of MAR sediment samples.
δ - isomer shift relative to α-Fe; Δ - quadrupole splitting; Γ - line width;
BHF - magnetic hyperfine field

The apparent Fe(III) contribution in sample **KF13-180** shows a smaller isomer shift (0.415 mm/s) and a fairly large quadrupole splitting (0.63 mm/s) compared to the other samples. These parameters are close to Mössbauer parameters of pyrite at this temperature (δ=0.407±0.001 mm/s; Δ=0.624±0.002 mm/s; Evans et al. 1992). With the present measurements, it is not possible to determine whether Fe(III) species are present in addition to pyrite with very similar Mössbauer parameters; however, it is possible that the apparent Fe(III) contribution is entirely due to low-spin Fe(II) from pyrite. A very small part of the high-spin Fe(II) component in the same sample shows a small quadrupole splitting of 1.99 mm/s, which is close to the value for siderite at this temperature (2.03±0.01 mm/s; Drodt 1996). This accounts for a maximum of 2-3% of total iron. In the other samples, iron is apparently mostly contained in clay minerals and is present both as Fe(II) and Fe(III). No significant depth-dependent variations of Mössbauer parameters were observed.

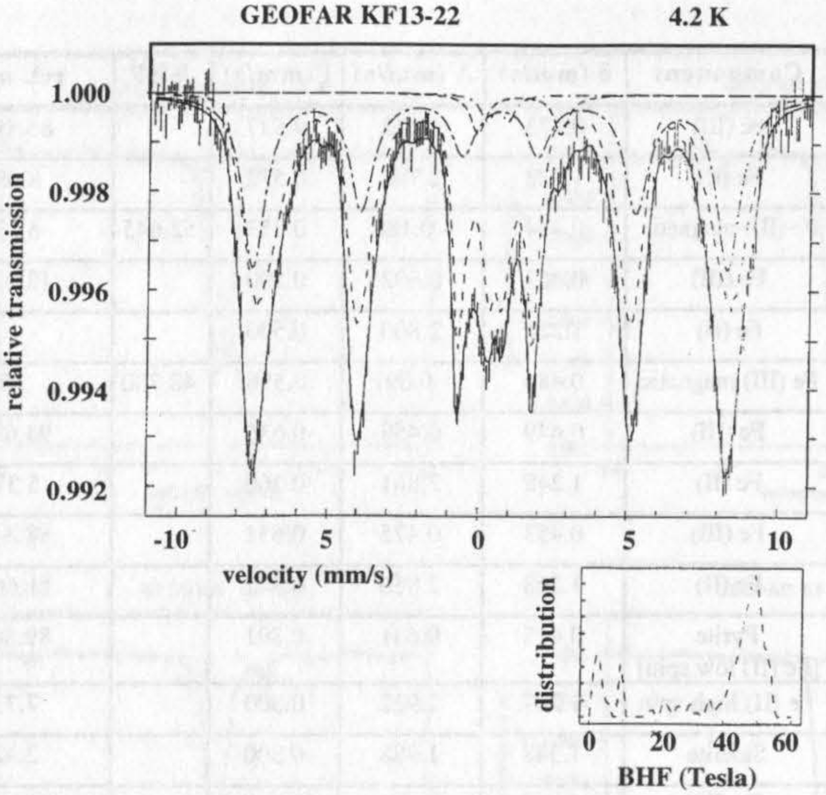

Fig. 7.14: Mössbauer spectrum of sample KF13-22 at 4.2 K, showing a well-defined magnetic sextet.

The Fe(II) share of total iron appears to increase slightly with depth (Fig. 7.15). The sample at 180 cm falls off this trend. However, this is due to the fact that only high-spin Fe(II) has been considered. Low-spin Fe(II) in pyrite cannot be distinguished from Fe(III), this contribution appears together with the Fe(III) share of total iron.

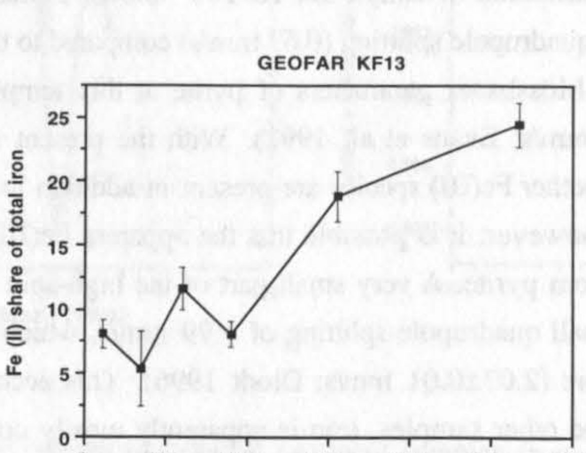

Fig. 7.15: Variation of Fe (II) (only high-spin component) with depth. Sample KF13-180 contains abundant low-spin Fe(II) contained in pyrite, which is calculated as Fe(III).

7.3 Discussion

7.3.1 Early diagenetic processes: modification of primary fluxes of metals

As early as 1965, surficial manganese enrichments in pelagic sediments have been described (Lynn & Bonatti 1965). These authors already proposed Mn dissolution upon burial in reduced sediments, ionic or molecular diffusion in pore solutions and accumulation under oxidizing conditions close to the surface as a mechanism for manganese redistribution in deep-sea sediments. Such **early diagenetic remobilization** can significantly modify primary fluxes of manganese and, to a lesser extent, iron and other metals.

Early diagenetic processes in marine sediments are primarily driven by the **decomposition of organic matter**. In this process, inorganic chemical species are successively used as terminal electron acceptors in the sequence O_2, nitrate, Mn-oxides, Fe-oxides, and finally sulfate. This **"biogeochemical zonation"** is related to decreasing energy yield per mole of organic carbon oxidized (e.g. Froehlich et al. 1979). Manganese is absent from pore waters in the oxic zone above the penetration depth of oxygen. It is mobilized downcore under reducing conditions, migrates upwards in the pore water and reprecipitates under oxidizing conditions close to the sediment-water interface. Under steady-state conditions, sharp **solid-phase manganese spikes** are expected to occur where the downward diffusive flux of oxygen is balanced by the flux of Mn-II diffusing upwards (Froehlich et al. 1979, Burdige & Gieskes 1983, Burdige 1993). It appears reasonable that manganese fluxes *above* the diagenetic Mn spikes may represent *primary* fluxes at the sediment-water interface which, in the area of the present study, might be dominantly derived from hydrothermal particle plumes. Solid-phase manganese is stable under oxidizing conditions; if newly deposited organic matter is decomposed by oxygen, no diagenetic remobilization of Mn would occur over this depth interval. Mn(II) diffusing upwards in porewaters from deeper reducing sediment sections will be oxidized and precipitate within the underlying brown layer and thus be prevented from moving higher up in the sediment. Some material derived from the manganese spike may be displaced upwards by bioturbation. However, recent modeling has shown that sharp manganese peaks near the sediment redox boundary can only occur if the redox boundary is deeper than the zone of maximum active bioturbation, assumed to be 8-10 cm (Dhakar & Burdige 1996).

Double manganese peaks reflect non-steady state conditions, such as a recent change in bottom water oxygenation or organic matter burial rate. Metal enrichments related to non-steady state diagenetic processes have been attributed to various scenarios, including decreasing rates of sedimentation and organic carbon supply at the glacial/Holocene transition (Berger et al. 1983, Thomson et al. 1984a, 1996, Wallace et al. 1988), episodic and rapid deposition of organic-rich turbidites (Colley et al. 1984, Wilson et al. 1985, 1986, Jarvis & Higgs 1987, Buckley & Cranston 1988), and formation of sapropels (Pruysers et al. 1993, Thomson et al. 1995). Iron also undergoes early diagenetic remobilization; however, the fraction of total iron affected by these processes is likely to be lower, since a comparatively larger fraction of total iron is structurally bound in mineral lattices of clay minerals and other phases, and cannot be mobilized by reducing processes.

Since no detailed porewater data are available for the cores from the area of study, solid phase distributions of iron and manganese are compared with organic carbon profiles to yield clues on early diagenetic processes (Fig. 7.16). The coincidence of sharp manganese peaks with organic carbon minima in cores Ac.91KS04, KF16 and KF09 strongly suggests a diagenetic origin. The double manganese peak in core KF09 may indicate non-steady state diagenetic conditions related to a recent increase in productivity. This interpretation is supported by an increase in δ^{13}C-values of the surface-dwelling planktonic foraminifera *Globigerinoides ruber* during the last 5,000 years (cf. Chapter 4) which could indicate an enhanced supply of nutrients in the water column. The lower peak is interpreted as a metastable relict manganese peak, whereas the upper peak, which is also enriched in iron, is the presently active peak, i.e. the location where manganese presently diffusing upwards in pore water solution will precipitate as Mn (III) in the solid phase. Similar non-steady state conditions related to a recent increase in organic carbon supply during the late Holocene - in this case, after 1900-1350 years ago - have been invoked to explain double manganese peaks above Mediterranean sapropels (Pruysers et al. 1993). In the cores sampled at the Mid-Atlantic Ridge during the GEOFAR cruise, double brown layers only occur at 37°N, at the southern limit of the study area. This local effect may result from processes occurring in surface waters; there is no evidence for a causal relationship to hydrothermal input from the nearby *Lucky Strike* vent field.

In three of the cores shown in Fig. 7.16, the maximum iron enrichment occurs *just below* the sharp manganese peaks. This is consistent with the fact that manganese is mobilized preferentially to iron under steady-state conditions due to thermodynamics and kinetics (Stumm & Morgan 1981). In core KF09, iron shows a broad “inverse U-shaped“ pattern. This iron profile is certainly “smeared“ by the effects of bioturbation, which appears to be more intense at this location compared to the other cores studied: While brown layers usually show a well-defined base, all color limits in the oxidized zone are gradual in this particular core. Additionally, determining the location of maximum iron enrichment would require fine-scale sampling on the cm-scale or less, and be limited by analytical uncertainties. Based on the available data, it is possible that the iron maximum *exactly* coincides with the upper manganese peak. This could indicate that the oxidation front is still retreating upwards following the proposed increase in organic carbon supply, and that steady-state conditions have not yet been reestablished.

In core KF13, enrichments of iron, manganese and other metals (Fig. 7.5, Fig. 7.16) in surface sediments are similar as in the other cores, but are associated with a local maximum of organic carbon. The organic carbon profile in this core is fairly irregular during the Holocene, which is tentatively interpreted in terms of fluctuations in productivity. In core Ac.91KS04 (EPSHOM), the diagenetic sequence seems to be “condensed“: iron, just as manganese, shows a sharp “inverse V-shaped“ peak within the oxidized surface layer. This is presumably related to the fact that little or no material has been deposited at this particular location during the Holocene. The presence of an oxidized surface layer with well-defined metal

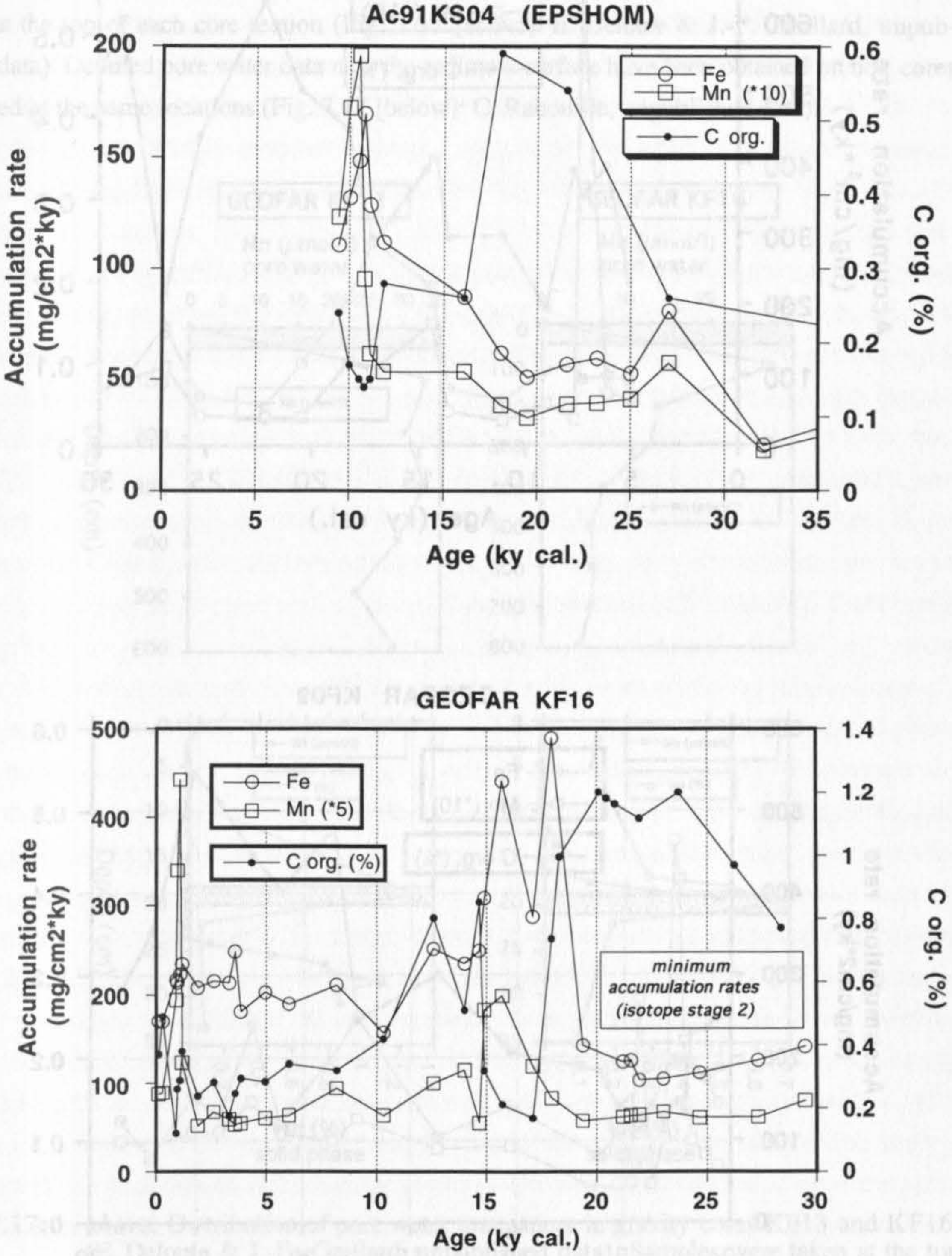

Fig. 7.16: Apparent fluxes (including diagenetic enrichment) of Fe and Mn during Holocene and Stage 2. For core KF16, minimum accumulation rates have been plotted for Isotope Stage 2, since the age of the base of the core cannot be exactly constrained, and samples from an allochthonous serpentine layer with high Fe content are not shown.

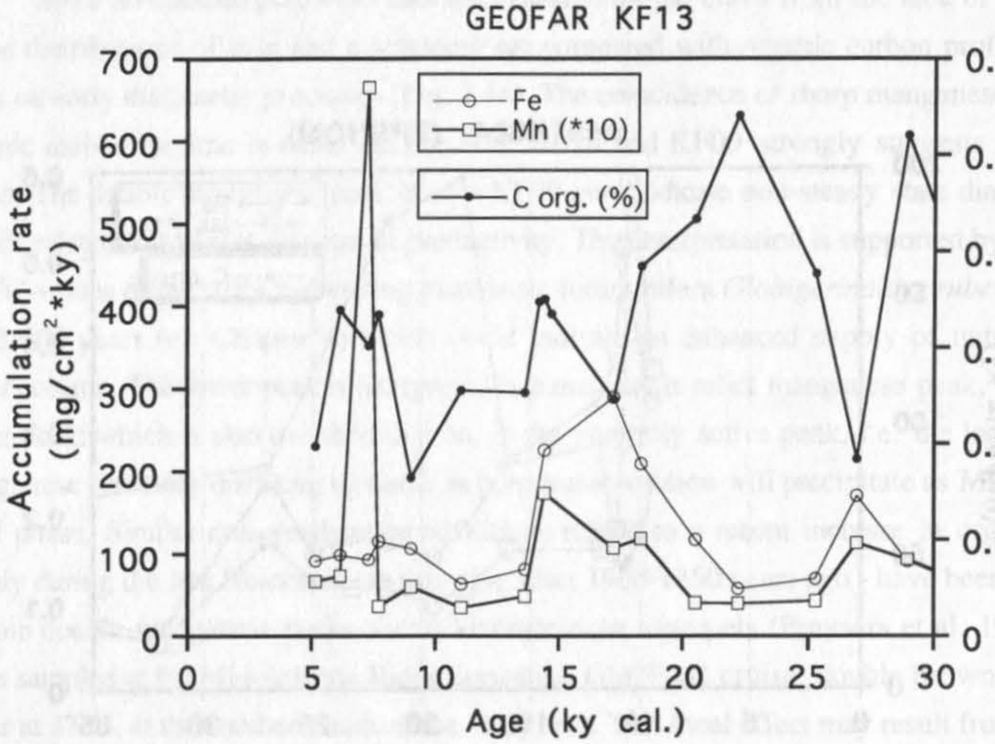

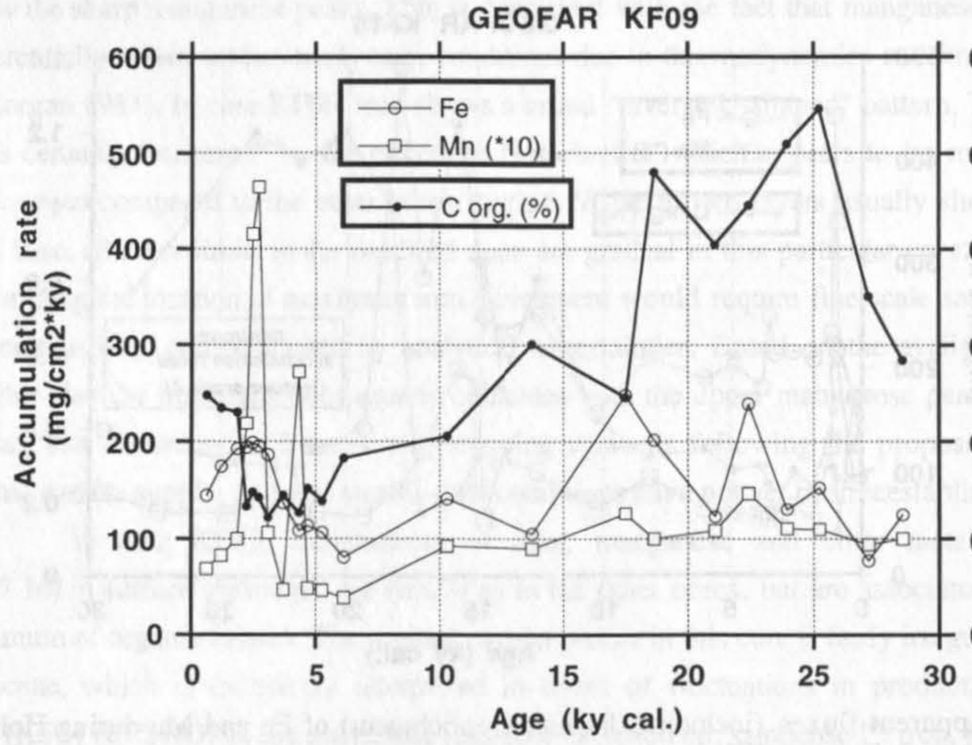

Fig. 7.16 (*continued*)

enrichments should indicate that possible core loss has been limited; the apparent absence of a Holocene sediment section, i.e. the lack of an isotopic "Holocene plateau" (cf. Chapter 4) does not mean that a sizable Holocene sediment section was originally present, and was entirely lost during the coring process.

For cores KF13 and KF16, manganese pore water profiles are available with samples taken at the top of each core section (Fig. 7.17 [above]: E. Deloule & J.-F. Gaillard, unpublished data). Detailed pore water data near the sediment surface have been obtained on box cores retrieved at the same locations (Fig. 7.17 [below]: C. Rabouille, unpublished data).

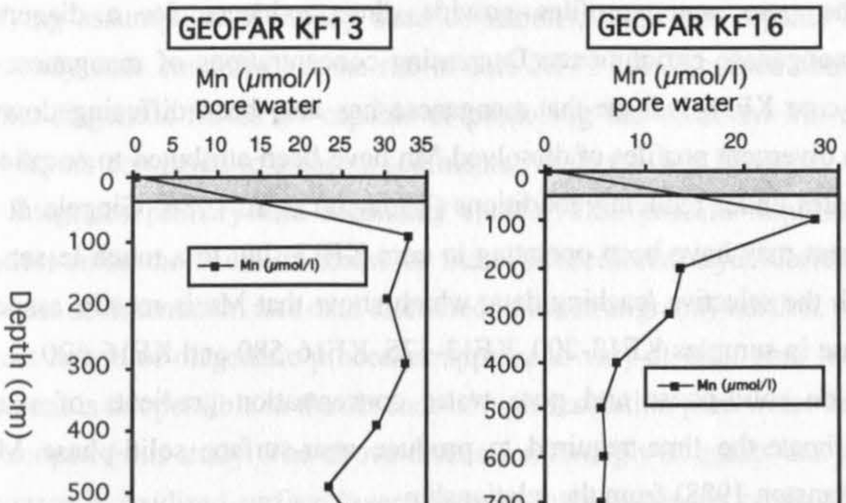

Fig. 7.17: ***above:*** Distribution of pore water manganese in gravity cores KF13 and KF16. (E. Deloule & J.-F. Gaillard, unpublished data). Samples were taken at the top of each core section; shaded rectangles indicate areas shown enlarged below. ***below:*** Solid-phase manganese distribution in oxidized surface layers of cores KF13 and KF16 and pore water profiles (C. Rabouille, unpublished data) from box cores taken at the same location. Stippled rectangles indicate brown-colored layers enriched in solid-phase Mn.

Pore water profiles show that manganese is absent or nearly absent from pore waters at the core surface. As discussed above, the first appearance of Mn in pore waters should correspond to the penetration depth of oxygen. According to the diagenetic zonation of Froehlich et al. (1979), solid-phase manganese enrichments visible as brown-colored layers should occur at the same core depth. The slight disagreement between pore water and solid-phase records could be due to small-scale variations in the penetration depth of oxygen: while gravity and box cores have been sampled at the same location, the exact coring locations are 110 and 185 m apart for core KF13 and KF16, respectively. In the case of core KF13, some loss of sediment at the top of the gravity core may have occurred, whereas the surface of the corresponding box core was well preserved. The pore water profiles provide direct evidence for a diagenetic origin of near-surface manganese enrichments. Decreasing concentrations of manganese in pore water below 1 m in core KF16 indicate that manganese has also been diffusing downwards at this location. Such divergent profiles of dissolved Mn have been attributed to sorption of dissolved Mn on carbonates under reducing conditions (Thomson et al. 1986, Gingele & Kasten 1994). A similar process may have been operating in core KF13, but to a much lesser extent. This is consistent with the selective leaching data, which show that Mn is mostly associated with the carbonate phase in samples KF13-200, KF13-475, KF16-580 and KF16-620.

Based on solid-phase and pore water concentration gradients of manganese, it is possible to estimate the time required to produce near-surface solid-phase Mn enrichments (Buckley & Cranston 1988) from the relationship

$$\frac{\frac{dC_{Mn}}{dZ} \cdot K_Z \cdot t \cdot AWT}{X \cdot \rho} = En$$

dC_{Mn}/dZ is the concentration gradient of dissolved Mn between its maximum concentration and low or zero concentrations above the solid-phase enrichment, K_z is the diffusion coefficient ($2 \cdot 10^{-6}$ cm^2/s) for Mn^{2+} (Aller 1980), t is time in years, AWT is a constant including conversion factors for moles to mass and time in seconds to years, X is the thickness of the enrichment zone, ρ is the dry bulk density of the sediment and En is the observed Mn enrichment, i.e. the difference between solid-phase Mn concentrations within and below the enriched layer. Solving for t indicated the time necessary to produce the observed solid-phase Mn enrichment.

Based on the available pore water data, the location of the maximum of dissolved Mn cannot be adequately constrained. Therefore, only a very rough estimation is possible based on the pore water data from the gravity cores, owing to the widely spaced samples. On the other hand, the gradient of dissolved manganese in box cores can yield a minimum value for t. As pore water profiles from the gravity cores clearly show that the maximum of dissolved manganese is located below the base of the box cores, the diffusion path of dissolved Mn is actually longer, increasing the time required to produce the observed solid-phase Mn enrichment.

In core KF13, the solid-phase Mn maximum occurs at 19 cm core depth, and the dissolved maximum at 90 cm at the base of the first core section. With $dC_{Mn}/dZ = 33.16$ µmol/l • 71 cm^{-1}, X = 2 cm (thickness of the brown layer), r = 0.77 g/cm^3 and En = 13,090 - 720 ppm = 12,370 ppm, solving for t results in an estimate of 12,000 years to produce the observed Mn enrichment. As an underlying sample at 22 cm core depth has been AMS dated at 7,700 years (^{14}C age converted into calendar years), this would imply that diagenetic fluxes of manganese by upward diffusion in porewaters have been continuous at least since the Last Glacial Maximum (18,300 years B.P.). The minimum value for t, based on the box core data ($dC_{Mn}/dZ = 22$ µmol/l • 6 cm^{-1}), is 1500 years. These estimations are approximate and based on the simplifying assumption of steady state conditions, while the organic carbon profile suggests non-steady state conditions at the site of core KF13 (as discussed above). However, they indicate that diagenetic fluxes are capable of producing the observed Mn enrichments in brown-colored layers compared to adjacent sediments, while the Mn inventory in the brown-colored layer integrates primary and secondary fluxes. This process requires considerably longer timescales, since the 2 cm-thickness of the brown-colored layer corresponds to 260 years, based on the sedimentation rate data discussed in the stratigraphy section.

The exact nature of diagenetic processes appears to vary at each core location; a more detailed assessment is not possible in the absence of high-resolution pore water data, and would be beyond the scope of this study. The above discussion strongly suggests that enrichments of iron and manganese in oxidized surface layers have an early diagenetic origin. This interpretation is compatible with the results of selective leaching and Mössbauer spectroscopy, which indicate that these enrichments are related to the presence of oxide phases mobile in diagenetic processes. The fact that manganese is dominantly associated with the carbonate/adsorbed phase in samples taken beneath the oxidized surface layer is in accord with sorption of remobilized Mn to carbonates under reducing conditions (Thomson et al. 1986, Gingele & Kasten 1994), and implies that, contrary to iron, only minor amounts of Mn are contained in detrital mineral phases.

In addition to Mn and Fe, a number of other elements are enriched in oxidized surface layers (Fig. 7.5). The close association of Co and Ni with Mn in brown layers reflects the well-known solid-phase association of these elements with manganese oxides (Bonatti et al. 1971, Hartmann 1979, Klinkhammer 1980, Sawlan & Murray 1983). The distribution patterns of copper and zinc are more irregular. These elements show some evidence of association with Mn-phases, in accord with the results of Hartmann (1979) and Fernex et al. (1992). Copper also appears to be enriched close to the sediment-water interface. This fraction of copper may be associated with labile organic matter, which is rapidly oxidized, and copper is subsequently released to the bottom water (Klinkhammer 1980).

On the other hand, similar distribution patterns of Fe and P, V and As suggest that the last three elements, which are known to be scavenged from the water column by Fe-oxyhydroxides in hydrothermal particle plumes, are primarily associated with Fe-phases. Figure 7.6 shows that P, V and As are correlated with iron in Mid-Atlantic Ridge sediments, albeit with a considerable degree of scatter, but that this correlation breaks down in the case of off-axis sediments. In various studies dealing with off-axis sediments, V was found to be enriched under reducing conditions (Bonatti et al. 1971, Colley et al. 1984, Thomson et al. 1993, 1995); it has also been reported that black shales formed in a sulphidic environment are enriched in vanadium (Brumsack 1986). Enrichment of V in oxidizing conditions, with a distribution pattern similar to iron, should then indicate that V had been *primarily* associated with iron prior to diagenetic remobilization, and has been remobilized along with its carrier phase. This, in turn, suggests that mobile iron oxide phases in sediments have been derived from iron oxides in hydrothermal particle plumes.

Mn-peaks during Termination I, frequently associated with enhanced fluxes of various other metals, may also be influenced by diagenetic remobilization. In core **KF13**, the maximum manganese enrichment during Termination I occurs at a core depth of 80 cm; it is accompanied by a distinct Ni peak and enrichments of Fe and Cu. The age of this sample is constrained by two AMS ages at 73 cm (12,230±130 ^{14}C years) and 100 cm (13,030±140 ^{14}C years), linear interpolation yields an age of about 14,400 years on the calendar scale. The organic carbon profile shows a general trend towards lower values in the early Holocene (Fig. 7.16), one sample with an age of approximately 17,000 years falls off this trend, which is presumably due to dilution by enhanced terrigenous input (cf. below and Chapter 8). The Mn peak coincides with a distinct downward step in the organic carbon profile (Fig. 7.16). A Mn peak is also present in core **KF16** near the top of Termination Ia at approximately 15,700 years. A contemporaneous iron peak and very elevated Ni accumulation rates include the effects of admixture of Ni-rich serpentine material, which is clearly the dominant controlling factor in the case of Ni. In core **KF09**, two accumulation peaks of various metals are present during Termination I with interpolated ages of 17,500 and 10,300 years, respectively; these peaks similarly coincide with steps in the organic carbon profile. Mn enrichments are comparatively minor in this core. In core **Ac.91KS04**, the top of Termination I concurs with the oxidized surface layer; therefore, fluctuations of metal accumulation rates during this time period cannot be fully resolved. A peak of Cu and Zn early during Termination I has an interpolated age of 16,100 years; the shape of the Mn profile could indicate that a Mn peak was formerly present and has been nearly completely "eroded". Another peak of Fe, Cu, Zn and Ni is present at the Stage 4/Stage 3 transition, with the local Mn maximum occurring slightly further downcore.

Manganese spikes during the last glacial-interglacial transition have been observed in other studies (e.g. Berger et al. 1983), similar spikes were also found to be associated with earlier glacial-interglacial boundaries down to the stage boundary 12/11 (Finney et al. 1988, Gingele & Kasten 1994). A decrease in the sedimentation rate and/or in the rate of organic carbon supply results in a downward shift of the penetration depth of oxygen and hence of the manganese redox boundary. An "old" surficial manganese peak is therefore initially conserved in the oxic zone. Even when it is buried down to the new redox boundary by continuing sediment accumulation and again involved in diagenetic recycling, some or all of the "old" peak may "survive", becomes buried in the manganese reduction zone and will subsequently slowly dissolve (Burdige 1993). Since these "fossil" peaks are finally again subject to diagenetic remobilization, which will variably affect the different metals, it is not surprising that the amplitude of the peaks and the particular metals involved do vary between the studied cores.

Mangini and co-workers have proposed an alternative explanation for deglacial manganese spikes (Mangini et al. 1990, 1994, Eckhardt 1992, Frank et al. 1994): These authors argue that manganese had a longer residence time in the glacial ocean due to generally lower bottom water oxygenation, and that Mn was precipitated from the water column during glacial/interglacial transitions, resulting in manganese spikes in sediment cores. This implies that deglacial manganese peaks have a primary origin, namely direct precipitation from the water column, rather than being the remnants of early diagenetic peaks. In the Atlantic Ocean, lower bottom water oxygenation during glacial periods could be related to decreased production of well-oxygenated North Atlantic Deep Water (NADW), as proposed by various authors (e.g. Boyle & Keigwin 1985/86, Oppo & Fairbanks 1987, Duplessy et al. 1988). Furthermore, NADW production repeatedly came to a complete stop during the last glacial cycle following major meltwater incursions, including two prominent events during Termination I at 16.9-17.1 ky cal. and near the end of and immediately subsequent to the Younger Dryas event (Sarnthein et al. 1994).

Two lines of evidence suggest that deglacial manganese peaks in the study area have a secondary rather than primary origin:

- Manganese peaks are always accompanied by iron peaks of comparable or even higher magnitude. As manganese, iron is subject to early diagenetic remobilization, even though a smaller proportion of total iron is mobile in diagenetic processes. On the other hand, a decrease in bottom water oxygenation would not affect fluxes of iron, unless bottom waters had become completely anoxic (Millero et al. 1987), which appears highly improbable.
- If Mn spikes were related to a regional or oceanic bottom water reoxygenation event, they should be time-synchronous in all cores in the study area. Age assignments for deglacial Mn peaks are based on linear interpolation between age control points; the detailed AMS age profile in core KF13 reveals that sedimentation rates may be highly variable during Termination I. Furthermore, the location of Mn peaks in each core has been determined based on a limited sampling resolution. Within the limits imposed by these facts, deglacial Mn peaks occur in sediments of different age in the studied cores. This would also suggest a diagenetic rather than primary origin, since the supply of organic carbon is more likely to be variable on a small spatial and temporal scale than the degree of bottom water oxygenation.

7.3.2 Spatial and temporal variability of metal accumulation rates

The downcore distribution of metals has obviously been modified by secondary diagenetic processes, which have caused metal enrichments in the oxidized surface layers and at the last glacial/interglacial transition, implying loss of metals from other sediment sections. With the exception of the behavior of vanadium, these processes which have been discussed above operate in a similar fashion in oxic/suboxic sediments throughout the world ocean. However, Mn concentrations in enriched horizons, recalculated on a carbonate-free basis (Table 7.2), are significantly elevated in the studied MAR sediments: In various studies cited above (Colley et al. 1984, Wallace et al. 1988, Pruysers et al. 1993, Thomson et al. 1993, 1995, Gingele & Kasten 1994), Mn concentrations never exceed 1% on a carbonate-free basis. The only exceptions are Finney et al. (1988), with maximum values of 3.94%, 8.43% and 6.72% Mn (CFB) in three cores, and Frank et al. (1994), with a maximum value of 2.24% CFB.

	GEOFAR KF09 (37°07N 32°17W)	**GEOFAR KF13** (37°35N 31°51W)	**GEOFAR KF16** (37°60N 31°08W)	**Ac.91KS04 (EPSHOM)** (38°05N 30°36W)	*FAMOUS area sediments*
Fe (%)	22.0	15.6	10.9	8.4	13.8
Mn (%)	4.3	8.3	3.9	1.1	0.87
P (%)	1.03	0.78	0.60	0.37	0.69
Cu (ppm)	650	450	325	180	370
Zn (ppm)	240	260	300	170	160
Ni (ppm)	320	330	270	110	90
V (ppm)	1240	600	380	310	900
As (ppm)	600	210	300	55	330

Table 7.2: Maximum concentrations of metals and coprecipitated elements in oxidized surface layers (all data on a carbonate-free basis). Surface sediment data from the FAMOUS area (Richter 1992) shown for comparison.

The cores studied by Finney et al. (1988) have sedimentation rates (0.65 cm/ky) an order of magnitude lower than the GEOFAR cores. The amount of Mn accumulated in the surficial Mn spike might be considered to represent the Mn that has been diagenetically remobilized over a considerable time period, maybe a full glacial-interglacial cycle. According to this interpretation, the time-integrated *fluxes* for the cores of Finney et al. (1988) are distinctly lower compared to those of the GEOFAR sediments, in spite of the fact that Mn *concentrations* are comparable. Frank et al. (1994) have studied sediments from the Galapagos microplate, where hydrothermal activity is likely to influence the sediment composition. The same authors have studied a second core from another area of the Galapagos microplate, where considerably less hydrothermal influence is suspected. In this core, maximum Mn concentrations only reach 0.93% on a carbonate-free basis.

The highest concentrations of Fe, Cu, P, V and As occur in core KF09, south of the Lucky Strike vent field. Mn concentrations are low, but this can be primarily ascribed to the presence of a double manganese spike, which causes a more homogenous distribution of the total amount of Mn that has been diagenetically remobilized. Zinc shows little variability and low concentrations in core KF09. In hydrothermal precipitates, Zn is contained in sulfide phases which are not likely to be transported laterally by hydrothermal particle plumes and accumulate in distal sediments, excluding very fine-grained sulfide particles. Likewise, nickel shows little variability in the three GEOFAR cores containing brown layers enriched in Mn, Ni and Co. The association of nickel with the potential hydrothermal tracer Mn might be due to postdepositional processes, i.e. similar diagenetic behavior. Nickel is not assumed to be derived from hydrothermal solutions. Generally, the data presented in Table 7.2 suggest decreasing hydrothermal influence in the sequence KF09 - KF13 - KF16 - Ac.91 KS04. Element concentrations are comparable to or higher than in FAMOUS area surface sediments sampled in an area where hydrothermal activity has also been described (Hoffert et al. 1978). Low concentrations of Mn and Ni in FAMOUS area samples are due to the fact that this data set only includes surface sediments, while the maximum enrichment of Mn and Ni generally occurs slightly downcore, depending on the oxygen penetration depth.

		Fe	Mn	Cu	Zn	Ni
		$(mg/cm^{2} \bullet ky)$		$(\mu g/cm^{2} \bullet ky)$		
Ac.KS04		20-87	1.6-5.8	40-330	50-320	40-245
	(average)	42	3.0	128	140	86
GEOFAR KF13		27-290	3.4-17	120-1000	110-860	40-810
	(average)	72	5.2	270	250	175
GEOFAR KF16		100-490	10-40	330-1250	275-1720	150-1190
	(average)	200	16.2	640	630	490
GEOFAR KF09		77-250	4.2-15	300-795	150-700	120-490
	(average)	140	8.7	490	390	300
Nares Abyssal Plain	(total)	18-35	1.4-1.7	40-60	40-80	30-60
(NW Atlantic) *(1)*	(authigenic)	0.6-2	1.2-1.4	20-30	3-7	1.5-2.3
Bermuda Rise *(2)*	(total)	---	39	700	---	422
	(scavenging)	---	4.3±1.1	76±26	(17±20)	46±16
East Pacific Rise *(3)*		4-124	1-36	50-590	---	30-160
	(average)	28	8.5	190	---	75
East Pacific Rise *(4)*		40-96	10-35	100-440	30-250	---
North Fiji Basin *(5)*		4-77	0.2-4.1	10-270	8-140	5-100
	(average)	24	1.9	95	52	40
Lau Basin *(6)*	(bulk)	26-250	5-18	100-740	50-500	---
	(non-detrital)	10-50	4.7-15	80-400	30-150	---

Table 7.3: Metal accumulation rates in MAR sediments south of the Azores (values beneath oxidized surface layers) compared to off-axis data from the Atlantic Ocean and to various hydrothermally influenced environments. Data from *(1)* Thomson et al. 1984b, *(2)* Bacon & Rosholt 1982, *(3)* McMurtry et al. 1981, *(4)* Barrett et al. 1987, *(5)* McMurtry et al. 1991, 1994, *(6)* Cronan et al. 1986.

In Table 7.3, the average and range of metal accumulation rates in MAR sediments south of the Azores are compared to data from off-axis sediments from the Atlantic Ocean (Bacon & Rosholt 1982, Thomson et al. 1984b) and to data from hydrothermally influenced environments such as the East Pacific Rise (McMurtry et al. 1981, Barrett et al. 1987) and the North Fiji (McMurtry et al. 1991, 1994) and Lau (Cronan et al. 1986) backarc basins. Thomson et al. (1984) investigated slowly accumulating sediments at the Nares Abyssal plain with an average sedimentation rate of 0.5-1 cm/ky; their data are considered representative of average off-axis conditions in the Atlantic Ocean without hydrothermal influence. Bacon & Rosholt (1982) discuss data from rapidly accumulating bottom current deposits from the Bermuda Rise, which are variably affected by sediment focusing and have high average sedimentation rates of 36 cm/ky. Total accumulation rates of Mn and Cu at the Bermuda Rise are comparable to hydrothermally influenced environments, even though hydrothermal input can be definitely excluded at this site, and metals are assumed to be dominantly of terrigenous origin. Elevated bulk and metal accumulation rates can be ascribed to lateral sediment transport. Lateral sediment supply cannot be excluded at any location in the ocean, consequently, calculated accumulation rates do not necessarily correspond to vertical fluxes through the water column (rain rates). However, very elevated and highly variable sedimentation rates indicate that this effect is particularly pronounced at the Bermuda Rise. The longer residence time and continuous resuspension of particles in the bottom nepheloid layer also causes significantly more efficient scavenging of transition metals from the water column at this location compared to average oceanic values. This is evident if the scavenging rates of Bacon & Rosholt (1982) are compared to authigenic metal accumulation rates of Thomson et al. (1984).

Data from hydrothermally influenced environments presented in Table 7.3 show that hydrothermal influence on the geochemical composition of sediments is comparatively minor at the North Fiji Basin. On the other hand, elevated iron accumulation rates in Lau Basin sediments compared to the East Pacific Rise include significant supply from volcaniclastic sources. In the Lau back-arc basin, considerable input of volcanic ash occurs from the adjacent Tofua island arc (e.g. Riech et al. 1990), providing another major source of iron in addition to hydrothermal precipitates. This is consistent with the fact that only 20-40% of total iron in Lau Basin sediments is present in carbonate and easily reducible phases in the selective leach procedure employed by Cronan et al. (1986), and interpreted to be of "non-detrital" origin by these authors. Volcaniclastic input could also be a significant source of zinc to Lau Basin sediments.

In the area of the present study at the Mid-Atlantic Ridge south of the Azores, highest metal accumulation rates are observed in core KF16, located in the central part of the 38°05'N fracture zone. Various lines of evidence suggest that these rates are influenced by lateral sediment supply:

- Sedimentation rates are an order of magnitude higher than in the other cores.
- The core is located in the deepest part of a basin, which most probably acts as a sediment trap. Sediment ponding in the central part of fracture zones is frequently observed at the MAR south of the Azores (B.Dennielou, written comm. 1996).

- A fine-grained serpentine layer is present from 74-87 cm (discussed in detail in Chapter 9). Since its mineralogy and geochemical composition bear no relationship to the surrounding pelagic sediments, it has evidently been redeposited. Serpentine is also present at 170 and 370 cm; in the geochemical data, this is apparent by high concentrations of Mg, Cr and Ni. These latter allochthonous deposits cannot be identified based on visual core investigation; it is therefore possible that other intervals of redeposited sediments are also present and have not been recognized.

Based on the nature of the oxygen isotope record, sedimentation has not been perturbed by major slumps involving redeposition of older material. Lateral sediment supply apparently has been continuous rather than episodic and may involve slow movement of particles down the walls of the fracture zone in this area of steep relief. While the depositional process is thus presumably a different one, fluxes at this site are anomalously elevated compared to the other cores studied in a similar way as they are in the Bermuda Rise bottom current deposits compared to Atlantic Ocean abyssal plain sediments. The relative importance of sediment redistribution compared to vertical fluxes through the water column could be quantified based on the pattern of excess ^{230}Th, i.e. ^{230}Th-fluxes exceeding production in the overlying water column (e.g. Suman & Bacon 1989, Francois et al. 1990, Frank et al. 1995); however, this is beyond the scope of this study. Based on the available data, it is evident that elevated metal accumulation rates cannot be interpreted in terms of maximum hydrothermal influence. In other words, data from core KF16 do *not* imply proximity to a presently undiscovered site of past or present hydrothermal activity.

Some lateral sediment supply cannot be excluded for the other cores in an area of rough topography such as the mid-oceanic ridge environment. However, it is assumed that these effects are of minor importance; accordingly, data from cores Ac.91KS04, GEOFAR KF13 and KF09 are considered to be comparable on a regional (MAR south of the Azores) and global scale. Among these cores, **average fluxes of all metals are highest in core KF09, located at 37°N south of the *Lucky Strike* vent field**, approximately 40% lower in core KF13 and 70% lower in core Ac.91KS04. In core KF13, maximum values occurring during Termination I have been based on a detailed AMS age profile revealing episodes of very rapid sedimentation during this time period. According to Table 7.3, maximum metal accumulation rates are slightly higher in core KF13 compared to KF09. However, if, by analogy, similar rapid sedimentation pulses are present in the latter core, maxima of metal accumulation rates should show the same pattern of spatial variability as average values.

By contrast to the long-term trend, near-surface manganese fluxes, which may be the best estimation of recent primary fluxes, are about the same in core KF13 (6.6 mg/cm^2 ky) as in core KF09 (6.9 mg/cm^2 ky). These different patterns for recent fluxes and long-term trends can be compared to petrologic observations on the *Lucky Strike* and *Menez Gwen* hydrothermal fields: Core KF 13 is located in the vicinity of *Menez Gwen*, which appears to be a very young, but already very active site, with first chimneys just starting to grow and only a sparse vent community (Fouquet et al. 1994). At *Lucky Strike*, evidence exists for long-lasting, recently reactivated hydrothermal activity (Langmuir et al. 1993), with fluid compositional data suggesting extensive alteration zones below the sea floor (Klinkhammer et al. 1995). However, phase-separated hydrothermal fluids are emitted at the shallow *Menez Gwen* site (840 m water depth), these fluids are gas-enriched and have very low metal concentrations (Y. Fouquet, pers. comm. 1996). The apparently continuous hydrothermal influence during the last 30,000 years at the site of core KF09 might thus be derived from the *Lucky Strike* hydrothermal field, it may also include contributions from other fields which are suspected south of the study area, based on chemical anomalies in the water column (German et al. 1996). It could be proposed that near-surface fluxes for core KF13 comparable to KF09 are related to hydrothermal input from the younger *Menez Gwen* site. However, it is doubtful if hydrothermal plumes derived from metal-depleted fluids could leave a chemical signature in sediments. Furthermore, near-surface accumulation rates may not really correspond to *present-day* fluxes, since some sediment has probably been lost at the surface of the gravity core. A Holocene shift in bottom currents, transporting a comparatively higher share of total hydrothermal input to the water column derived from the *Lucky Strike* vent field in a northerly direction, could be an alternative explanation for the observed difference between recent and long-term spatial variability of metal accumulation rates.

Maximum values and average accumulation rates of all metals are significantly elevated compared to abyssal plain values, and comparable to values from hydrothermally influenced environments, whereas minimum values in core Ac.91KS04 are comparable to or even lower than values from the Nares Abyssal Plain. Iron accumulation rates are also frequently higher than at the East Pacific Rise and can be best compared with data from the Lau Basin, where volcaniclastic input provides another major source of iron in addition to hydrothermal precipitates. The study area at the Mid-Atlantic Ridge also receives significant volcaniclastic input presumably derived from the Azores Islands. Evidence for such a sediment source includes the frequent presence of minor amounts of volcanic glass in the coarse fraction, and a very similar leaching behavior of iron as in Lau Basin sediments (cf. above). The data in Table 7.3 also suggest that a volcaniclastic source may provide some zinc and nickel to the studied MAR sediments. Additionally, some iron may also have a continentally-derived, presumably eolian or possibly ice-rafted origin. In particular, the most pronounced iron accumulation peaks during Termination I in cores KF13, KF16 and KF09 are not accompanied by comparable enrichments of Mn, which argues against a diagenetic or hydrothermal origin. Instead, they are associated with marked $CaCO_3$ minima, and with maximum concentrations of a number of elements dominantly derived from detrital sources (e.g. Al, Mg, Ti, K). These peaks are therefore interpreted in terms of peaks of terrigenous detrital input. It can thus be concluded that iron may be derived from a variety of sources in addition to fallout from hydrothermal particle plumes.

On the other hand, selective leaching data suggest that manganese may be dominantly associated with a non-detrital source both in the MAR study area (cf. above) and in the Lau Basin (Cronan et al. 1986). McMurtry et al. (1991) proposed a simple rate calculation to estimate the contributions of detrital, authigenic and hydrothermal Mn in the North Fiji Basin:

$$[\text{Mn flux}]_{\text{total}} = [\text{Mn flux}]_{\text{detrital}} + [\text{Mn flux}]_{\text{authigenic}} + [\text{Mn flux}]_{\text{hydrothermal}}$$

$$= \mathbf{0.016\ Al_{flux} + 1.0\ g/cm^2\ ky \quad + MnH}$$

These authors related the detrital Mn flux to the Al flux using a ratio of Mn/Al = 0.016 for volcanic ashes in the North Fiji Basin, and assumed an authigenic Mn flux of 1.0 g/cm^2 ky. Their model has been applied to the MAR study area (Fig. 7.18). However, an authigenic Mn flux of 1.3 g/cm^2 ky was used in the calculations here, which represents a typical value for the Atlantic Ocean (Thomson et al. 1984b). The percentage of normative hydrothermal Mn should be a minimum estimate, since continentally-derived eolian dust might rather have a Mn/Al-ratio close to the one of average upper continental crust (Mn/Al = 0.0075; Taylor & McLennan 1985), which would decrease the relative amount of Mn assumed to be of detrital origin based on Al fluxes. Beneath oxidized surface layers with diagenetic Mn-enrichments and elevated Mn/Al-ratios, spatial variability of normative hydrothermal Mn percentages generally shows the same pattern as the accumulation rates, namely increasing values in the sequence Ac.KS04 - KF13 - KF09 - KF16. This implies that higher Mn accumulation rates are indeed related to enhanced hydrothermal input, confirming the results of selective leaching experiments that detrital sources of Mn are of minor importance. As discussed above, fluxes in core KF16 appear to be significantly amplified by lateral sediment redistribution and cannot be interpreted in terms of fallout from hydrothermal particle plumes in the water column. The minimum of hydrothermal manganese prior to 20,000 y in this core is related to a maximum of terrigenous input. For the other three cores, variability of hydrothermal Mn seems to be a function of distance to the *Lucky Strike* vent field: In core KF09, which is closest to the hydrothermal site and may also receive hydrothermal input from other sources located to the south of the study area, the percentage of normative hydrothermal Mn shows only minor fluctuations, excluding one data point at the base of the oxidized surface layer where Mn has presumably been diagenetically lost to overlying sediments. In core KF13, considerable temporal variations of normative hydrothermal Mn occur (27-68% MnH). In core Ac.KS04, the most distal site, similar fluctuations occur at lower percentages of hydrothermal manganese (0-51% MnH). In some samples from this core, metal accumulation rates are comparable to abyssal plain values lacking hydrothermal influence. However, the data in Table 7.3 show that minimum values in hydrothermally influenced environments may fall in the same range. For samples with zero hydrothermal Mn, actually a "negative" amount of MnH has been calculated, suggesting that the contributions from detrital and/or authigenic sources have been overestimated. These fluctuations seem to indicate that periodically less or no hydrothermal influence can be discerned at more distal sites.

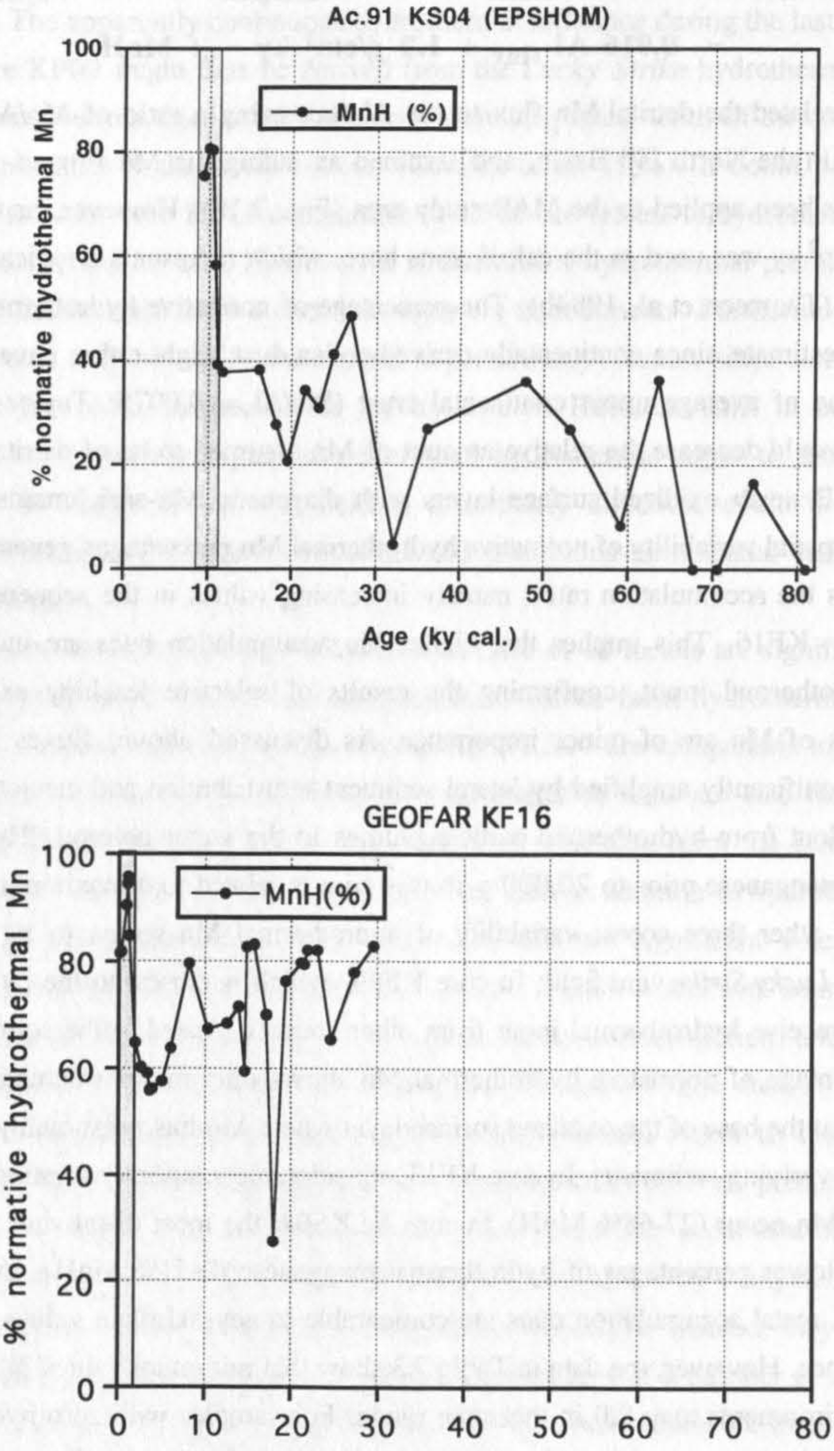

Fig. 7.18: Percentages of hydrothermal Mn in MAR sediments. Normative model (McMurtry et al. 1991) discussed in text. Stippled rectangles correspond to oxidized surface layers. Ages in core KF16 prior to 18,300 y are maximum ages.

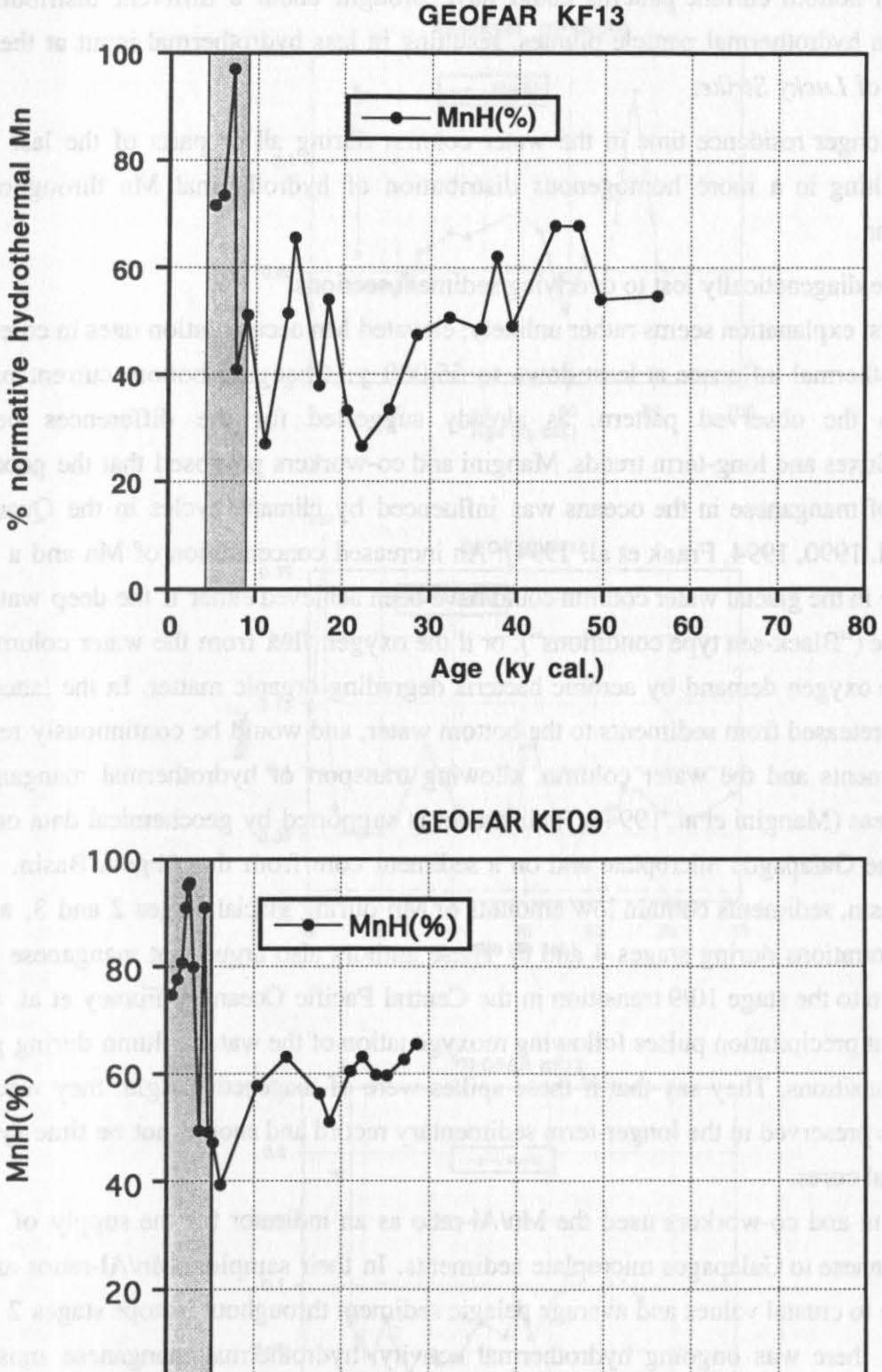

Fig. 7.18 *(continued)*

Several explanations could be proposed:

- There was no hydrothermal activity in the study area prior to 30,000 y.
- Changes in bottom current patterns could have brought about a different distribution of fallout from hydrothermal particle plumes, resulting in less hydrothermal input at the distal sites north of *Lucky Strike*.
- Mn had a longer residence time in the water column during all or parts of the last glacial cycle, resulting in a more homogenous distribution of hydrothermal Mn throughout the glacial ocean.
- Metals were diagenetically lost to overlying sediment sections.

The first explanation seems rather unlikely; elevated Mn accumulation rates in core KF13 suggest hydrothermal influence at least down to 55,000 y. Changing bottom current patterns could explain the observed pattern, as already suggested for the differences between near-surface fluxes and long-term trends. Mangini and co-workers proposed that the geochemical behavior of manganese in the oceans was influenced by climatic cycles in the Quaternary (Mangini et al. 1990, 1994, Frank et al. 1994): An increased concentration of Mn and a longer residence time in the glacial water column could have been achieved either if the deep water had become anoxic (“Black-sea type conditions“), or if the oxygen flux from the water column was lower than the oxygen demand by aerobic bacteria degrading organic matter. In the latter case, Mn would be released from sediments to the bottom water, and would be continuously recycled between sediments and the water column, allowing transport of hydrothermal manganese to more distal areas (Mangini et al. 1994). Their model is supported by geochemical data on sediments from the Galapagos microplate and on a sediment core from the Angola Basin. At the Galapagos Basin, sediments contain low amounts of Mn during glacial stages 2 and 3, and enhanced concentrations during stages 4 and 5. These authors also argue that manganese spikes observed down to the stage 10/9 transition in the Central Pacific Ocean by Finney et al. (1988) could represent precipitation pulses following reoxygenation of the water column during glacial/interglacial transitions. They say that if these spikes were of diagenetic origin, they would not be likely to be preserved in the longer-term sedimentary record and should not be time-synchronous in several cores.

Mangini and co-workers used the Mn/Al-ratio as an indicator for the supply of hydrothermal manganese to Galapagos microplate sediments. In their samples, Mn/Al-ratios are consistently close to crustal values and average pelagic sediment throughout isotope stages 2 and 3. Provided that there was ongoing hydrothermal activity, hydrothermal manganese must have been deposited elsewhere during this time period at the Galapagos microplate. By comparison, the Mn/Al-ratio is uniformly at least an order of magnitude higher than crustal values in the studied MAR sediments (Fig. 7.19). Near-surface diagenetic Mn-enrichments have very elevated Mn/Al-ratios. Minor Mn/Al-peaks during Termination I are related to Mn enrichments, which were also inferred to be of diagenetic origin. Lowest Mn/Al-ratios are observed in the vicinity of the Last Glacial Maximum (18,300 y B.P.). Below, these ratios show a first-order

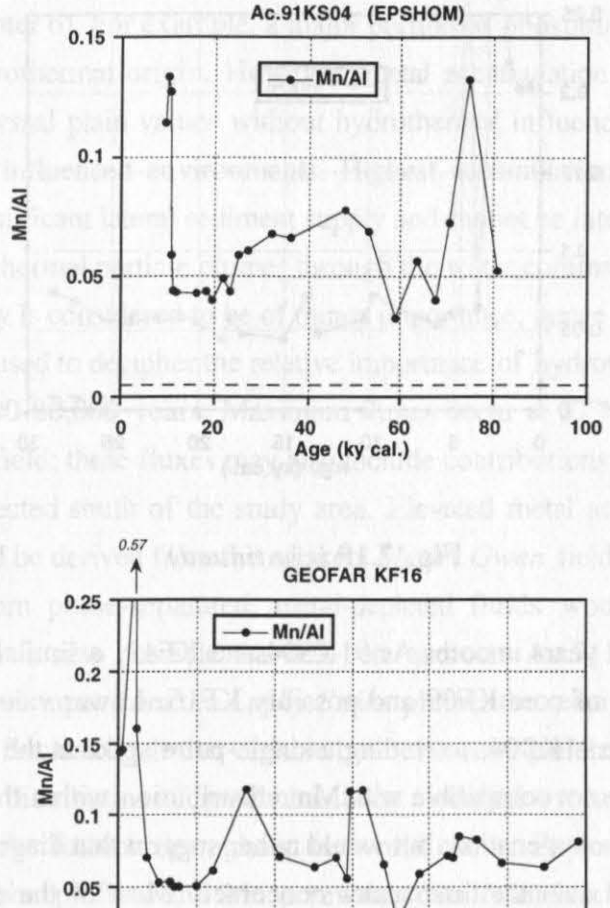

Fig. 7.19: Mn/Al-ratios vs. depth in MAR sediments. Broken line corresponds to crustal Mn/Al-ratio (Taylor & McLennan 1985) typical of average pelagic sediments.

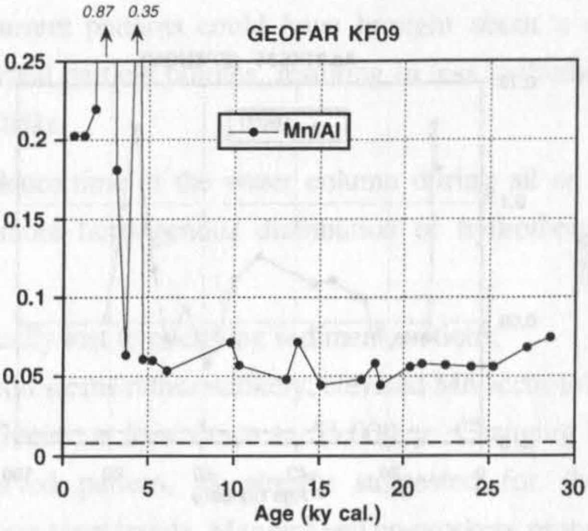

Fig. 7.19 *(continued)*

increase down to 50,000 years in cores Ac.91KS04 and KF13, a similar trend is suggested by higher values at the base of core KF09 and possibly KF16. Lower values occur again prior to 50,000 years in core Ac.91KS04, excluding a single-point spike at the stage 4 / stage 5 transition. These patterns are not compatible with Mn redistribution within the glacial water column due to low bottom water oxygenation, but would rather suggest that diagenetic remobilization of manganese has occurred over the time scales concerned. Most of the manganese remobilized should have diffused upwards towards the oxic/suboxic boundary, but some would diffuse downwards to deeper layers and may be taken up on carbonate surfaces or form a separate $MnCO_3$ phase (Thomson et al. 1986, Gingele & Kasten 1994), which could explain "divergent" solid phase manganese profiles. Early diagenetic remobilization of manganese and, to a lesser extent, iron, should have been more important during glacial stage 2 and late stage 3, because sediments from these periods generally have higher organic carbon content (cf. Chapter 5.2). This might also have affected the downcore distribution of trace metals and elements coprecipitated by hydrothermal Fe-Mn oxide phases.

On the other hand, the lowermost samples of core KF13 analyzed for organic carbon from early stage 3 have very low $C_{org.}$ contents of 0.085% and 0.075%, so it is feasible that no diagenetic remobilization has occurred, and that fluxes from this time period correspond to primary fluxes. Iron accumulation rates during this time period are rather low and within the range of abyssal plain values; on the other hand, manganese accumulation rates of 4.0-4.7 $mg/cm^2 \cdot ky$ are within the range of values observed in hydrothermally influenced environments.

7.4 Conclusions

Hydrothermal input in the studied MAR sediments is considerably diluted by biogenic carbonate as well as by biogenic opal, terrigenous and volcanic phases (cf. discussion in factor analysis section, Chapter 6). For example, a major portion of phosphorus appears to be of biogenic rather than hydrothermal origin. However, metal accumulation rates are frequently elevated compared to abyssal plain values without hydrothermal influence, and are comparable to other hydrothermally influenced environments. Highest accumulation rates in core KF16 are certainly related to significant lateral sediment supply and cannot be interpreted in terms of vertical fluxes from hydrothermal particle plumes through the water column. In the other three cores, lateral sediment supply is considered to be of minor importance; hence variations in metal accumulation rates can be used to decipher the relative importance of hydrothermal input at each site through the last 30,000-80,000 years. Maximum fluxes occur at 37°N (core KF09), south of the *Lucky Strike* vent field; these fluxes may also include contributions from other hydrothermal fields which are suspected south of the study area. Elevated metal accumulation rates in core KF13 (37°35'N) could be derived from the adjacent *Menez Gwen* field; however, it is doubtful if plumes derived from phase-separated, metal-depleted fluids would leave a geochemical imprint in sediments. It is also possible that this core and core Ac.91KS04, located at an even more distal site, received input from the *Lucky Strike* plume; the relative amount of this contribution may have been fluctuating due to variable bottom current patterns.

The downcore distribution of metals has been modified by early diagenetic processes, which operate in a similar fashion throughout the world ocean. Evidence for such processes is based on organic carbon profiles and Mn porewater data from box cores taken at the same location as the gravity cores analyzed in this study. Selective leaching data and Mössbauer spectroscopy indicate the presence of Fe- and Mn-oxide phases which are readily mobile in porewater solution and can reprecipitate under oxidizing conditions close to the sediment-water interface. Peaks of Mn and Fe during Termination I are interpreted as remnants of early diagenetic peaks, which have been preserved due to a decrease in sedimentation rates and organic carbon supply at the last glacial-interglacial transition. Earlier Fe peaks not accompanied by similar enrichments of Mn are considered to result from maxima of continentally-derived detrital input. Temporal variability of Mn during the last glacial cycle may be best explained by diagenetic remobilization followed by upward and downward diffusion in porewaters and immobilization as a manganese carbonate phase in suboxic sediments, consistent with the results of selective leaching experiments.

While diagenetic processes apparently have modified the pattern of temporal variability of metal accumulation rates, *average* accumulation rates are clearly indicative of continuous hydrothermal influence in the study area throughout the time periods available in each core, at least down to 55,000 years B.P. .

8. Barium in Mid-Atlantic Ridge sediments: Hydrothermal or biogenic origin and possible paleoceanographic implications

8.1 Introduction

Barium in deep-sea sediments may have many sources, including hydrothermal, biogenic and detrital (Church 1979, Dymond 1981). A **hydrothermal origin of barium in ridge-crest sediments** was proposed based on the correlation between Ba and a typical hydrothermal element association including Fe, Mn, Cu and Zn in East Pacific Rise sediments (Boström et al. 1973). In the MAR study area, hydrothermal deposits at the Lucky Strike and Menez Gwen sites contain abundant barite compared to other mid-ocean ridge sites, which was attributed to the enriched nature of the volcanic substrate, i.e. the higher barium content of Plume MORB in the vicinity of the Azores hot spot compared to average N-type MORB (Humphris et al. 1993, Fouquet et al. 1996).

However, it is not clear whether barite particles of hydrothermal origin may be transported laterally in hydrothermal particle plumes and accumulate in "far-field" pelagic sediments. Coarse-grained barite particles should behave in a similar manner as sulfide particles of similar size and density: According to the particle deposition model of Feely et al. (1987, 1990), pyrite particles larger than 50 µm with a density of 5.0 will settle out within 1300 m of the vent, while chalcopyrite and sphalerite particles with densities close to 4.0 will settle within 1500 m; barite has a density of 4.5 intermediate between these phases. At the Endeavour segment of the Juan de Fuca Ridge, barium fluxes in the upper portion of the plume are at most slightly elevated compared to background values from the overlying water column (Dymond & Roth 1988), suggesting no or limited lateral dispersal of hydrothermal barite particles. At 21°N at the East Pacific Rise, most of the hydrothermally injected Ba appears to remain in solution within the lower 22 m of the buoyant plume (Mottl & McConachy 1990); however, analytical data are highly variable, and the authors have indicated that redissolution of previously formed barite may have occurred either in the plume or subsequent to sampling. While particulate barium in the water column is correlated with particulate manganese at the East Pacific Rise (8°40'N to 11°50'N), both elements show concentration increases towards the bottom along the entire length of both segments studied, regardless of proximity to hydrothermal sites. This has been attributed to resuspension of bottom sediments enriched in Mn and Ba rather than to input from hydrothermal sources (Feely et al. 1994).

Two possibilities may still exist for accumulation of barium derived from hydrothermal sources in ridge-crest sediments: dispersal of very fine-grained barite particles in hydrothermal plumes and mass-wasting of hydrothermal sulfide/sulfate deposits. At the ASHES vent field at Axial Volcano, Juan de Fuca Ridge, barite particles with a size range of 10-30 µm have been observed in the upper part of the buoyant plume 26 m above the vent field, along with sphalerite, chalcopyrite and iron sulfide particles as small as 0.1 µm (Feely et al. 1990). Such fine-grained sulfide and sulfate mineral grains might be dispersed in hydrothermal particle plume in a similar way as fine-grained Fe and Mn oxyhydroxides and contribute to ridge flank metalliferous sediments (Feely et al. 1987). Redeposited sulfide material apparently constitutes a significant source of metalliferous sediments in the TAG area at 26°N on the Mid-Atlantic Ridge; this component has been distinguished from particulate fallout from neutrally buoyant plumes based on $^{230}Th/Fe$ ratios and rare earth element patterns (Mills et al. 1993, German et al. 1993).

A **biogenic origin of barium in deep-sea sediments** was initially proposed based on the elevated Ba content of sediments underlying highly productive surface waters (Goldberg & Arrhenius 1958). The nutrient-like behavior of Ba in the water column (Chan et al. 1977) also suggests an association of this element with the biogenic cycle. A correlation between particulate Ba and organic carbon has been observed in sediment traps (Dymond et al. 1992, François et al. 1995). The mechanism of barite formation in seawater is still poorly understood, since seawater is undersaturated with respect to $BaSO_4$. However, it seems to be generally accepted that barite forms primarily in microenvironments within decaying phytoplankton cells and fecal pellets, where the solubility product of $BaSO_4$ is locally exceeded due to sulfate production from decaying organic matter (Chow & Goldberg 1960, Dehairs et al. 1980, Bishop 1988). This interpretation is supported by the coincidence between particulate Ba maxima and the oxygen minimum and an inverse correlation between Ba and dissolved oxygen in the water column of the Southern Ocean. It is clear though that the barite flux increases with increasing water depth (von Breymann et al. 1992 b).

Since pore waters in oxic marine sediments are generally saturated with respect to barite (Church & Wolgemuth 1972), the distribution of Ba is not likely to be affected by post-depositional diagenetic processes. Consequently, Ba is more refractory than other productivity indicators such as organic carbon, biogenic opal or $CaCO_3$ and considered to exhibit more predictable preservation patterns. However, this assumption is not valid in anoxic sediments depleted in interstitial sulfate. In this case, porewaters become undersaturated with respect to barite, and barite is dissolved in sulfate-depleted intervals. Downward sulfate and upward barium diffusion then result in local precipitation of authigenic barite in diagenetic fronts near the termination of the sulfate reduction zone (Brumsack 1986, von Breymann et al. 1990, 1992 a, b, Torres et al. 1996). Furthermore, shallow-water shelf sediments underlying highly productive surface waters are not enriched in barium, consistent with the interpretation that barite formation occurs during settling of biogenic particles below the thermocline (von Breymann et al. 1990, 1992 b). These observations indicate that the use of Ba as a tracer of paleoproductivity should be restricted to oxic and suboxic deep water sediments. In anoxic sediments, the initial signal may still be partially retained in spite of diagenetic overprint, but care has to be taken in the interpretation of individual peaks (von Breymann et al. 1992 b).

Based on the evidence discussed above, various studies have used Ba in sediments as an indicator of paleoproductivity (e.g. Schmitz 1987, Shimmield & Mowbray 1991, Gingele & Dahmke 1994, Nürnberg 1995, Rutsch et al. 1995, Sirocko et al. 1996). The use of Ba as a tracer of paleoproductivity requires that detrital and hydrothermal sources of Ba are negligible, or that a correction can be applied to account for these sources. A correction for detrital sources of Ba has been proposed based on the Ba/Al-ratio, which assumes that this ratio in detrital aluminosilicates is constant to a first approximation and that Al is exclusively supplied from detrital sources. Dymond et al. (1992) assumed an average value of Ba/Al = 0.0075 in detrital aluminosilicates, based on a range of 0.005-0.01 commonly observed in crustal rocks. Rutsch et al. (1995) adapted a value of Ba/Al = 0.0045, based on their data points with lowest Ba/Al-ratios. In nearshore areas, detrital sources of Ba may be particularly important, and the choice of the correction for detrital Ba may even change the interpretation completely (Dymond et al. 1992). However, in most other areas, detrital sources of Ba are of minor importance. Likewise, hydrothermal sources can be neglected in most parts of the world ocean. While a small quantity of hydrothermal barite in off-axis sediments in the Pacific Ocean has been suggested based on Sr isotope analysis of barite separates, this contribution only accounts for 2-2.5% of total barite (Martin et al. 1995). However, the hydrothermal source is potentially significant in ridge-crest sediments, including the samples of the present study. Since both hydrothermal and biogenic barium is present as pure barite, it is not possible to differentiate between these sources based on the mineralogy.

In the area of the present study, Ba may be derived from hydrothermal, biogenic and/or detrital/volcaniclastic sources. A correction can be applied for detrital sources of Ba, which depends on the reliability of an assumed detrital Ba/Al-ratio. On the other hand, hydrothermal and biogenic sources may both be significant and cannot be easily distinguished from one another. In the following section, data will be presented on the distribution of Ba in distal MAR sediments. The relationship between Ba and Si and organic carbon in the studied sediments and the stratigraphic pattern of Ba abundances will be used to give clues on the origin of barium in the studied sediments, and possible paleoceanographic implications will be discussed. It will be demonstrated that barium is apparently primarily of hydrothermal origin in sediments on the flanks of the Lucky Strike seamount, where Ba is probably derived from redeposited hydrothermal precipitates. On the other hand, it is suggested that biogenic sources dominate in distal sediments. Particularly, time-synchronous Ba maxima in four cores during Termination I are compared with other geochemical and paleoceanographic data, and tentatively interpreted as indicators of productivity spikes.

8.2 Results

8.2.1 Relationship between Ba, Si and organic carbon

In Figure 8.1, barium concentrations are compared with silica and organic carbon. In this context, silica is used to indicate the abundance of biogenic opal; however, it has to be borne in mind that Si is also derived from detrital aluminosilicate and possibly hydrothermal sources. Significant correlations between Ba, Si and organic carbon seem to indicate that barium is dominantly of biogenic origin. For various reasons, several groups of samples fall off the general trend and have been omitted from the data set for calculation of regression lines:

- In a number of samples, silica is dominantly derived from non-biogenic sources such as volcanic glass or serpentine material from alteration of ultramafic rocks (cf. Chapter 9). Consequently, these samples are low in Ba and variously elevated in Si; several samples with Si content greater than 10% are not shown in Fig. 8.1 b) for scaling reasons. Two samples from the immediate vicinity of the Lucky Strike seamount plot above the regression line of Ba vs. organic carbon in Fig. 8.1 a). While these data points still fall within the range of scatter around the regression line observed in distal sediments, this may suggest significant input of hydrothermal Ba, which needs to be confirmed by other criteria.
- Near-surface sediments, particularly in oxidized surface layers, have elevated content of organic carbon and higher C_{org}/Ba-ratios. Newly deposited organic matter has not been as extensively degraded by early diagenetic processes as in underlying sediments; consequently, a higher proportion of the initial flux of organic carbon is still preserved. This is consistent with the fact that barite barium is more refractory than organic carbon in the longer-term sedimentary record.
- Samples from the lower part of core KF16 are lower in Ba at comparatively high content of silica and especially organic carbon. A strong smell of hydrogen sulfide and a yellowish-brownish color of extracted porewaters indicates that these sediments have encountered anoxic conditions. Two reasons can explain the lower Ba content compared to suboxic sediments:

- The burial efficiency of organic carbon could be enhanced in anoxic sediments; a higher proportion of the initial flux of C_{org} was preserved, resulting in a higher C_{org}/Ba-ratio, just as in surface sediments.
- Some barium has been diagenetically lost to overlying sediments. As discussed above, barium is diagenetically mobilized in anoxic sediments, and authigenic barite fronts may develop at the termination of the sulfate reduction zone.

These explanations are not mutually exclusive, and both processes probably contributed to the observed pattern. The significant correlation between Ba and organic carbon in samples from the lower part of core KF16 suggests that the barium distribution in anoxic sediments is also controlled by the input of organic carbon; however, the slope of the regression line is clearly different compared to the data set from suboxic sediments. Rapid settling of particles through the water column following a diatom bloom in surface waters may explain the low Ba content of the diatom-rich sample KF16-332. As mentioned above, barite presumably precipitates in microenvironments created during *decay* of organic matter settling through the water column. A smear slide investigation of the diatom layer showed that diatoms are well preserved and show no evidence of dissolution.

- Finally, a number of samples are low in organic carbon and high in barium. These represent "barium spikes" during Termination I, which will be discussed in later sections.

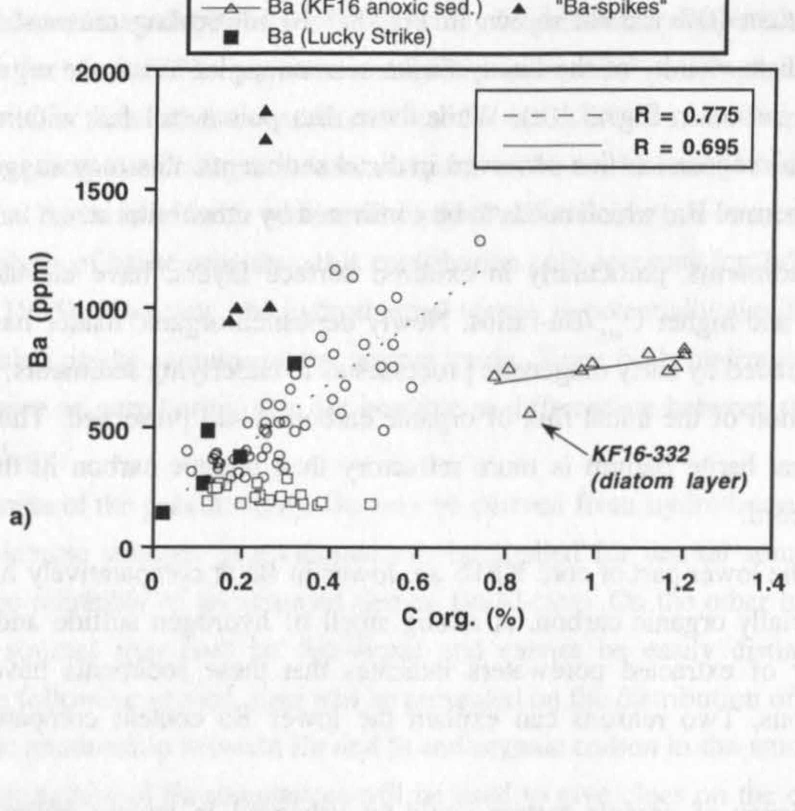

Fig. 8.1: Scatter plots of Ba vs. C org. and Si. Different groups of samples discussed in text. Regression lines (broken lines) calculated only for suboxic sediments (open circles). Volcanic ash layers from core Ac.91KS04, volcaniclastic sample KG18-13 (22.46% Si, 143 ppm Ba), and diatom-rich sample KF16-332 (22.47% Si, 569 ppm Ba) are not shown in Fig. 8.1b).

Since Si is supplied by both detrital aluminosilicates and biogenic opal, the Si/Al-ratio can be used as an indicator of the relative importance of these two sources of silica. This relies on the assumptions that Al in pelagic sediments is supplied exclusively from detrital sources, and that hydrothermal sources of silica in sediments are negligible. While amorphous silica of hydrothermal origin is present at the Lucky Strike seamount, it originates from low temperature diffuse flow (Fouquet et al. 1994) and should not be laterally transported in hydrothermal particle plumes and accumulate in distal sediments.

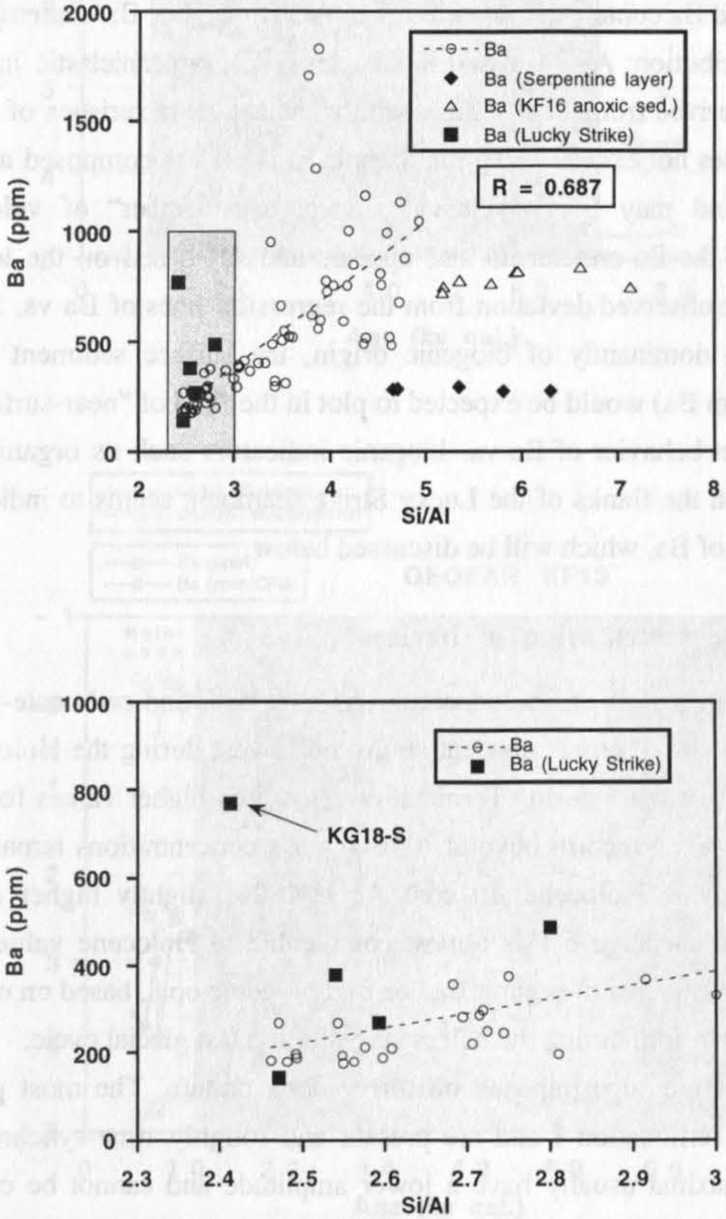

Fig. 8.2: Scatter plots of Ba vs. Si/Al as an indicator of the relative amount of biogenic opal vs. detrital aluminosilicates. Stippled rectangle defines data range shown enlarged in lower part of figure.

In a normative chemical model of Nazca Plate surface sediments, Dymond (1981) has assumed a detrital Si/Al-ratio of 3.0 for acidic continentally-derived detritus; in the study area, Si/Al-ratios are frequently lower, consistent with a significant contribution from basaltic detritus. Figure 8.2 again shows a significant correlation between Ba and Si/Al, albeit with a considerable degree of scatter especially at elevated ratios of Si/Al. Surface sediment samples from the flanks of the Lucky Strike seamount always have comparatively low Si/Al-ratios. This indicates that these samples contain little biogenic opal, as is generally the case for Holocene sediments in the study area, and abundant basaltic detritus which is evident from the presence of dark volcanic glass. Several samples, especially KG18-S, plot clearly above the regression line for Ba vs. Si/Al established for "far-field" pelagic sediments in the study area; these are the only samples with elevated Ba content at *low* ratios of Si/Al. The higher Ba content cannot be due to a volcaniclastic contribution: As discussed in Chapter 6.4.1, volcaniclastic input at the Lucky Strike seamount is derived from local sources with chemical characteristics of enriched MORB, whose Ba content does not exceed 150 ppm. Sample KG18-13 is composed almost exclusively of volcanic glass and may be considered a "local end-member" of volcaniclastic input. A biogenic origin of the Ba enrichment also appears unlikely based on the low abundance of biogenic opal and the observed deviation from the regression lines of Ba vs. Si/Al and organic carbon. If Ba were dominantly of biogenic origin, the surface sediment sample KG18-S (0.32% C_{org}., 769 ppm Ba) would be expected to plot in the field of "near-surface sediments" in Fig. 1a). The distinct behavior of Ba vs. biogenic indicators such as organic carbon, Si and Si/Al in sediments on the flanks of the Lucky Strike seamount seems to indicate a dominantly hydrothermal origin of Ba, which will be discussed below.

8.2.2 Stratigraphic distribution of barium

Figure 8.3 shows plots of Ba concentrations on a bulk and carbonate-free basis vs. age in four gravity cores. In all cores, concentrations are lowest during the Holocene and show a first-order continuous increase during Termination I towards higher values for isotope stage 2. In the two cores providing records beyond 30,000 y, Ba concentrations remain elevated during Stage 3 compared to the Holocene. In core Ac.91KS04, slightly higher contents occur in Stage 4, while Ba in substage 5.1 is almost comparable to Holocene values. These patterns correlate with higher amounts of organic carbon and biogenic opal, based on observations of the sand-size sediment fraction, during the colder stages of the last glacial cycle.

Several peaks are superimposed on this general pattern. The most pronounced peaks occur early during Termination I and are present and roughly time-synchronous in all four cores. Earlier Ba maxima usually have a lower amplitude and cannot be correlated between cores. Minor maxima also occur in Holocene sediments; in several cases, these variations are still well beyond the range of analytical error.

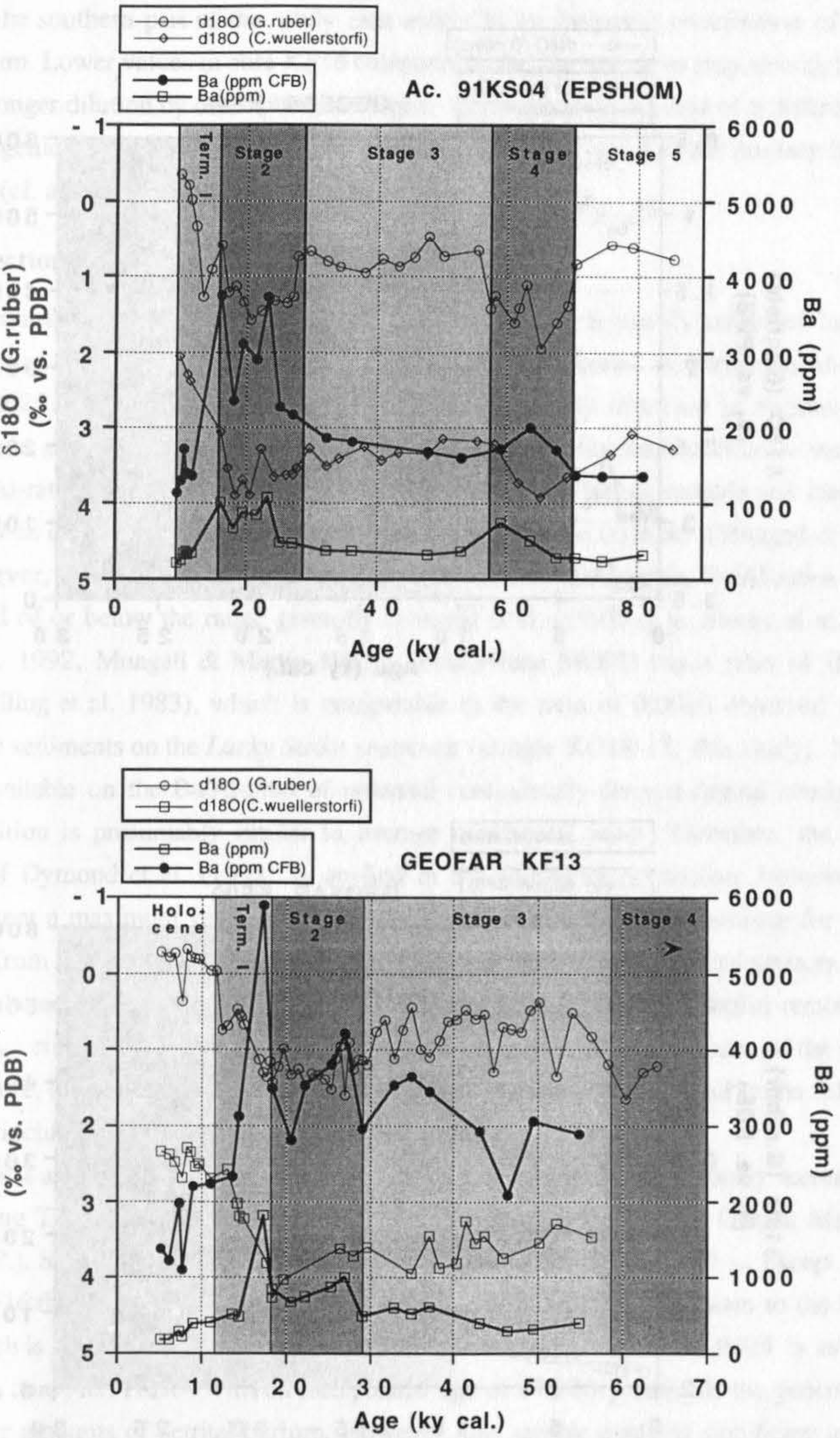

Fig. 8.3: Temporal variability of barium concentrations in Mid-Atlantic Ridge sediments. Shading indicates oxygen isotope stages, isotope records shown as stratigraphic reference.

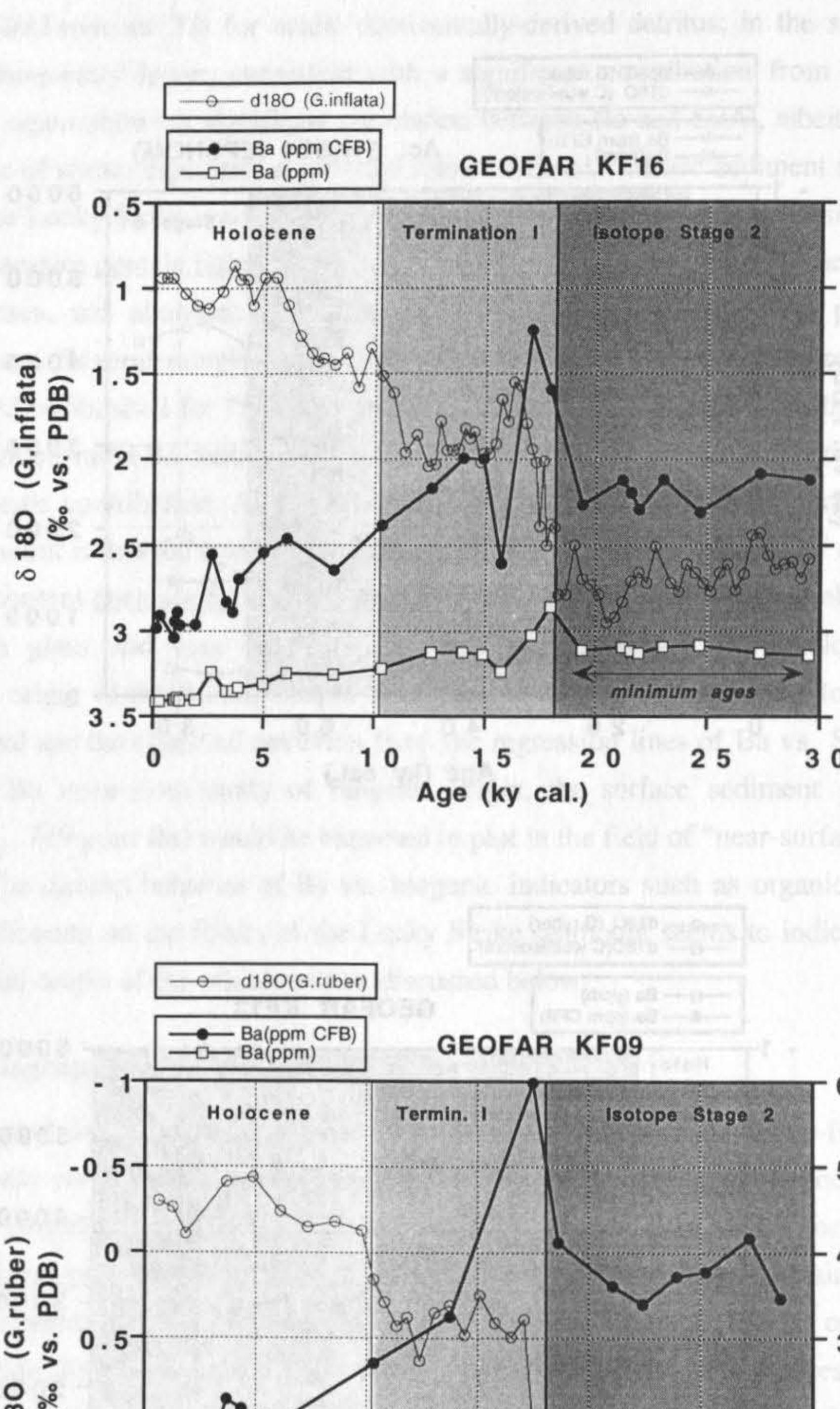

Fig. 8.3 *(continued)*

Both average bulk and carbonate-free barium concentrations and maximum values are increasing in the order Ac.91KS04 - KF16 - KF13 - KF09. This could be related to higher productivity in the southern part of the study area and/or to an increased contribution of hydrothermal barium. Lower values in core KF16 compared to the last two cores may also include the effects of stronger dilution by other phases at higher sedimentation rates and of a different ratio of Ba vs. biogenic opal and organic carbon due to higher preservation of the primary biogenic components (cf. above).

8.2.3 Correction for detrital sources of barium

The contribution of barium derived from detrital sources is usually estimated based on concentrations of Al and a constant Ba/Al-ratio of the detrital material. A detrital Ba/Al-ratio of 0.0075 ± 0.0025 has been proposed based on values commonly observed in various crustal rocks (Dymond et al. 1992). In the study area, detritus may be derived from a variety of sources: Ba/Al-ratios of volcanic rocks on the Azores islands are highly variable and may be as high as 0.019 in differentiated volcanic rocks such as comenditic trachytes (Mungall & Martin 1995). However, in most volcanic rock types encountered on the islands, Ba/Al-ratios fall on the lower end of or below the range given by Dymond et al. (1992) (e.g. Storey et al. 1989, Widom et al. 1992, Mungall & Martin 1995). Local Plume MORB has a ratio of Ba/Al = 0.0018 (Schilling et al. 1983), which is comparable to the ratio of 0.0016 observed in pure volcaniclastic sediments on the *Lucky Strike* seamount (sample KG18-13, this study). No data are readily available on the Ba/Al-ratio of potential continentally-derived detrital sources, but their composition is presumably similar to average continental crust. Therefore, the detrital Ba/Al-ratio of Dymond et al. (1992) is applied in the following discussion; however, this should represent a maximum value of detrital Ba/Al and thus a maximum estimate for the Ba contribution from detrital sources. While Ba which is not derived from detrital sources can be considered to be nearly entirely of biogenic origin in most parts of the world ocean remote from the global ridge crest system, hydrothermal barium may be significant in the area of the present study. Therefore, the general term "non-detrital barium" is used in Fig. 8.4 and in the following discussion to include biogenic and hydrothermal sources.

To a first approximation, the amount of non-detrital barium is continuously increasing in all cores during Termination I, with maximum values just prior to the Last Glacial Maximum (18,300 y B.P.). Subsequently, a slight decrease is observed down to 80,000 y, except in core GEOFAR KF16 that shows constantly elevated amounts of non-detrital Ba down to the base of the core, which is still in isotope stage 2. If a crustal Ba/Al-ratio of 0.0075±0.0025 is assumed, one sample in core Ac.91KS04 with an interpolated age of 67,700 y falls off the general trend and has higher amounts of detrital barium. However, this sample contains significant amounts of volcanic glass, and volcaniclastic detritus should be characterized by a distinctly lower Ba/Al-ratio. If a detrital Ba/Al-ratio of 0.0033±0.0005 is adapted based on Ba/Al-ratios of 0.0028, 0.0032 and 0.0038, respectively, in nearly pure volcanic ash layers in the same core, this sample contains 70.0±4.6% non-detrital Ba, which is comparable to data from over- and

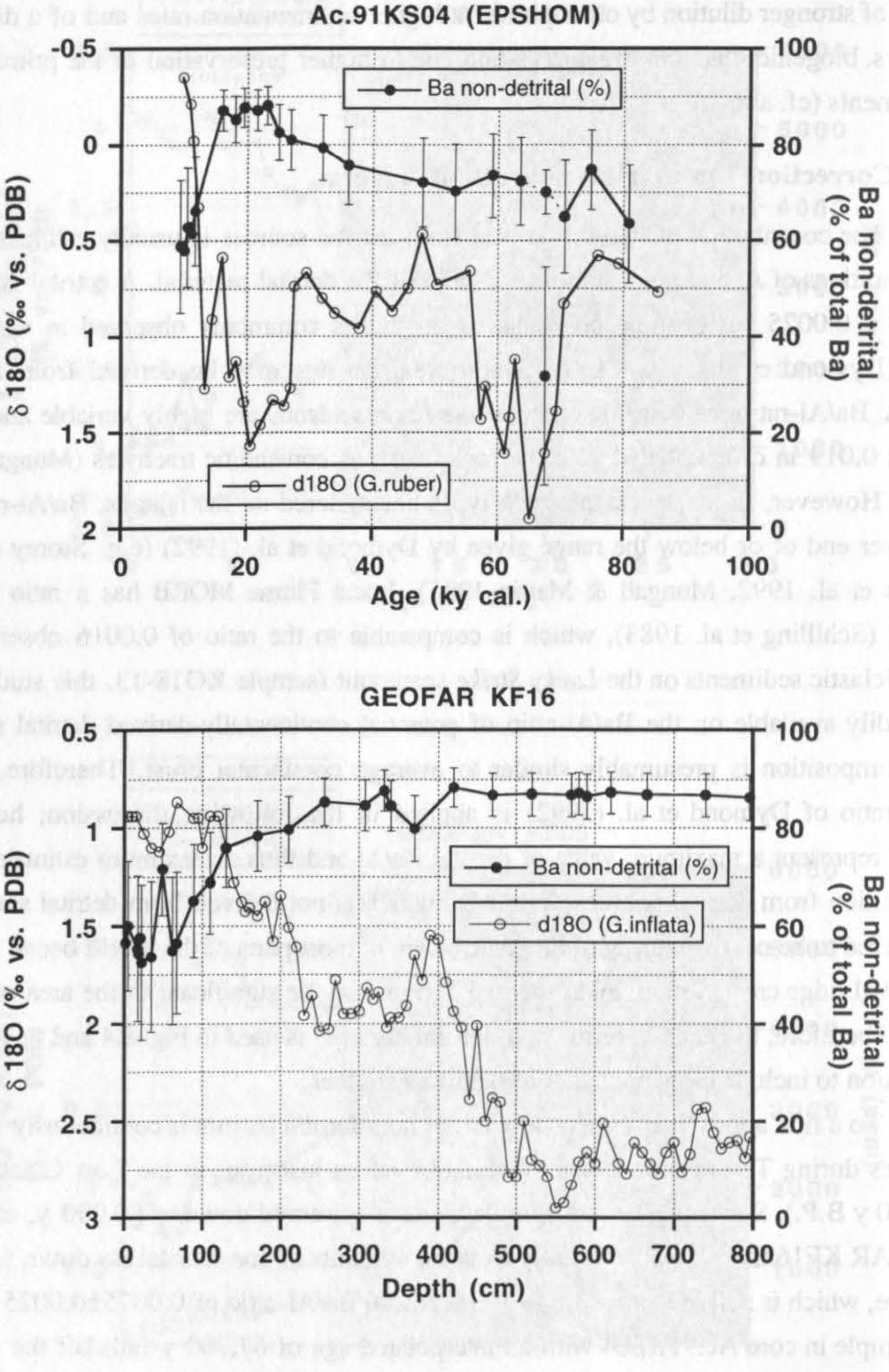

Fig. 8.4: Percentages of non-detrital Ba vs. time, based on a detrital Ba/Al-ratio of 0.0075±0.0025 (Dymond et al. 1992). Oxygen isotope records shown as stratigraphic reference. Data from core KF16 plotted vs. core depth, since the age of the base of the core cannot be constrained. Sample from early Stage 4 in core Ac.91KS04 (67,700 y B.P.) discussed in text.

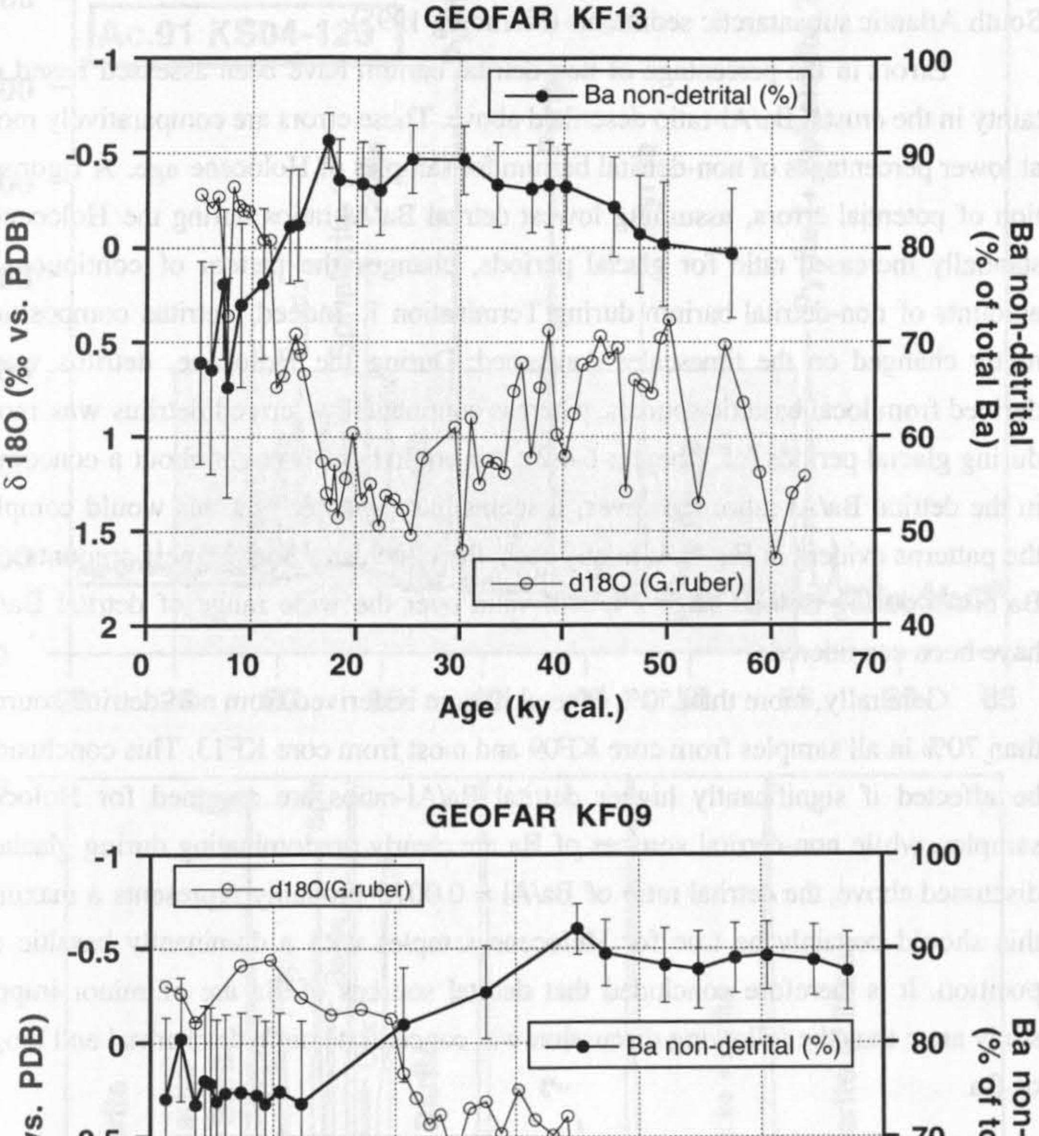

Fig. 8.4 *(continued)*

underlying pelagic samples. Similarly, a lower detrital ratio of Ba/Al = 0.0021, deduced from the composition of volcanic rocks in this area, has been applied for smectite-rich volcanogenic sediments of the Bransfield Strait, compared to a regional average detrital Ba/Al of 0.0067 in South Atlantic subantarctic sediments (Nürnberg 1995).

Errors in the percentage of non-detrital barium have been assessed based on the uncertainty in the crustal Ba/Al-ratio described above. These errors are comparatively more significant at lower percentages of non-detrital barium for samples of Holocene age. A rigorous consideration of potential errors, assuming lowest detrital Ba/Al-ratios during the Holocene and a substantially increased ratio for glacial periods, changes the pattern of continuously increasing amounts of non-detrital barium during Termination I. Indeed, detritus composition has apparently changed on the timescales concerned: During the Holocene, detritus was dominantly derived from local basaltic sources, whereas continentally-derived detritus was more significant during glacial periods (cf. Chapter 6.4.2); this could have brought about a concomitant increase in the detrital Ba/Al-ratio. However, it seems unreasonable that this would completely reverse the patterns evident in Fig. 8.4; in any case, the conclusion that highest amounts of non-detrital Ba occur during isotope stage 2 is still valid over the wide range of detrital Ba/Al-ratios that have been considered.

Generally, more than 50% of total barium is derived from non-detrital sources, and more than 70% in all samples from core KF09 and most from core KF13. This conclusion could only be affected if significantly higher detrital Ba/Al-ratios are assumed for Holocene sediment samples, while non-detrital sources of Ba are clearly predominating during glacial periods. As discussed above, the detrital ratio of Ba/Al = 0.0075 probably represents a maximum estimate; this should certainly be true for Holocene samples with a dominantly basaltic detritus composition. It is therefore concluded that detrital sources of Ba are of minor importance in the study area; thus the following discussion will concentrate on hydrothermal and biogenic sources of Ba.

8.2.4 Mineralogy of gravity concentrates

Whereas detrital Ba is contained as a minor component in mineral lattices, especially potassic feldspars and mica, biogenic and hydrothermal Ba is present as pure barite. Since Ba concentrations do not exceed 2000 ppm on a bulk or 6000 ppm on a carbonate-free basis (cf. Fig. 8.3), barite is below the detection limit of conventional X-ray diffraction. In order to confirm its presence, a **heavy mineral fraction** has been separated in selected samples with highest bulk Ba concentrations. A concentrated solution of sodium tungstate ($NaWO_4$) with a density of 3.0 g/cm^3 was used as heavy liquid. The heavy fraction was frozen with liquid nitrogen to improve the efficiency of the density separation; light and heavy fractions were then separated and repeatedly washed with distilled water to remove $NaWO_4$. Gravity concentrates, usually some mg for a bulk sample of approximately 30 g, were smeared onto a silicon disc for X-ray analysis. X-ray diffractograms are shown in Fig. 8.5 (following pages).

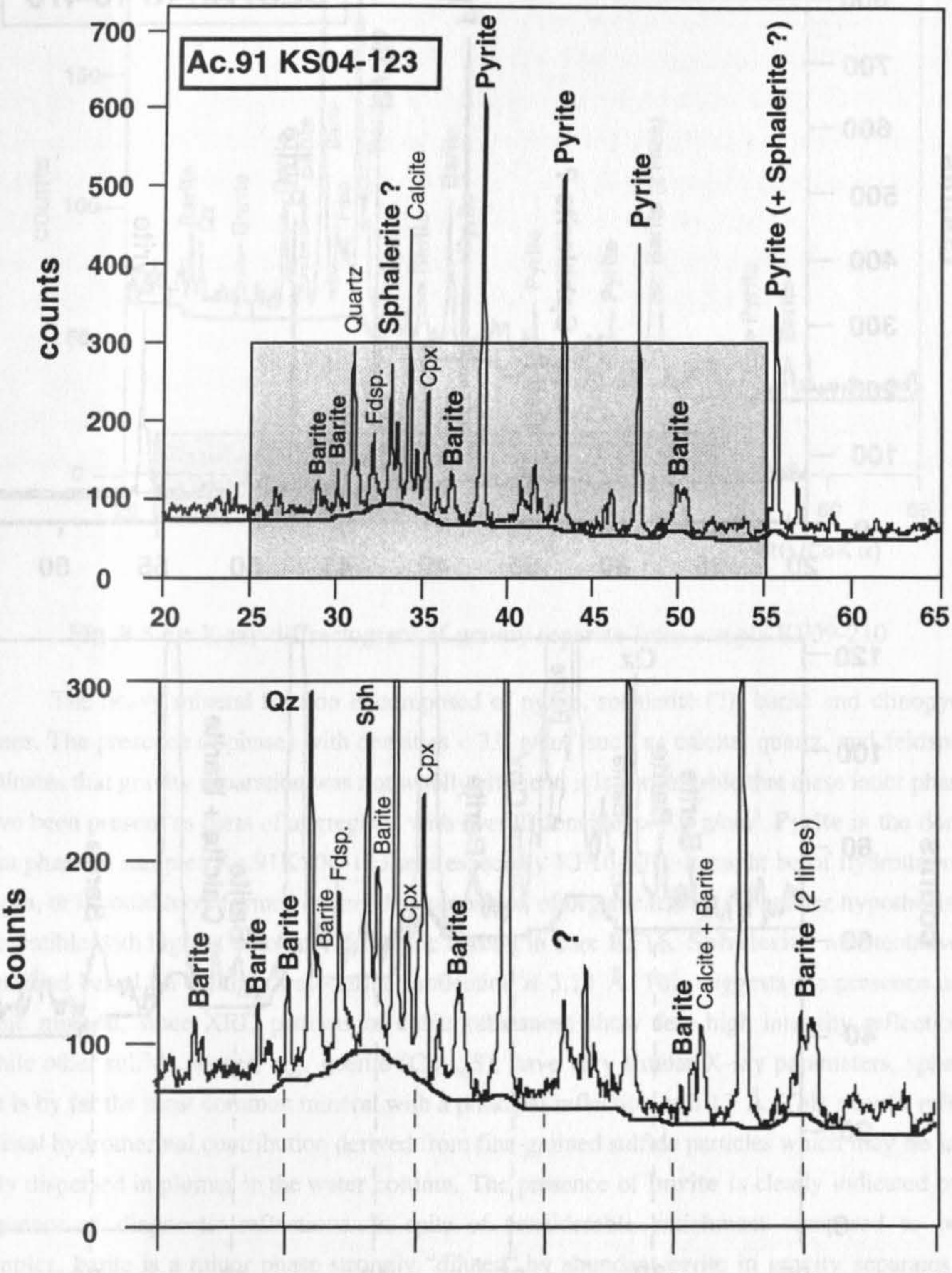

Fig. 8.5 a): X-ray diffractogram of gravity separate from sample Ac.91KS04-123 (Fdsp. = feldspar, Sph = sphalerite, Qz = quartz, Cpx = clinopyroxene)

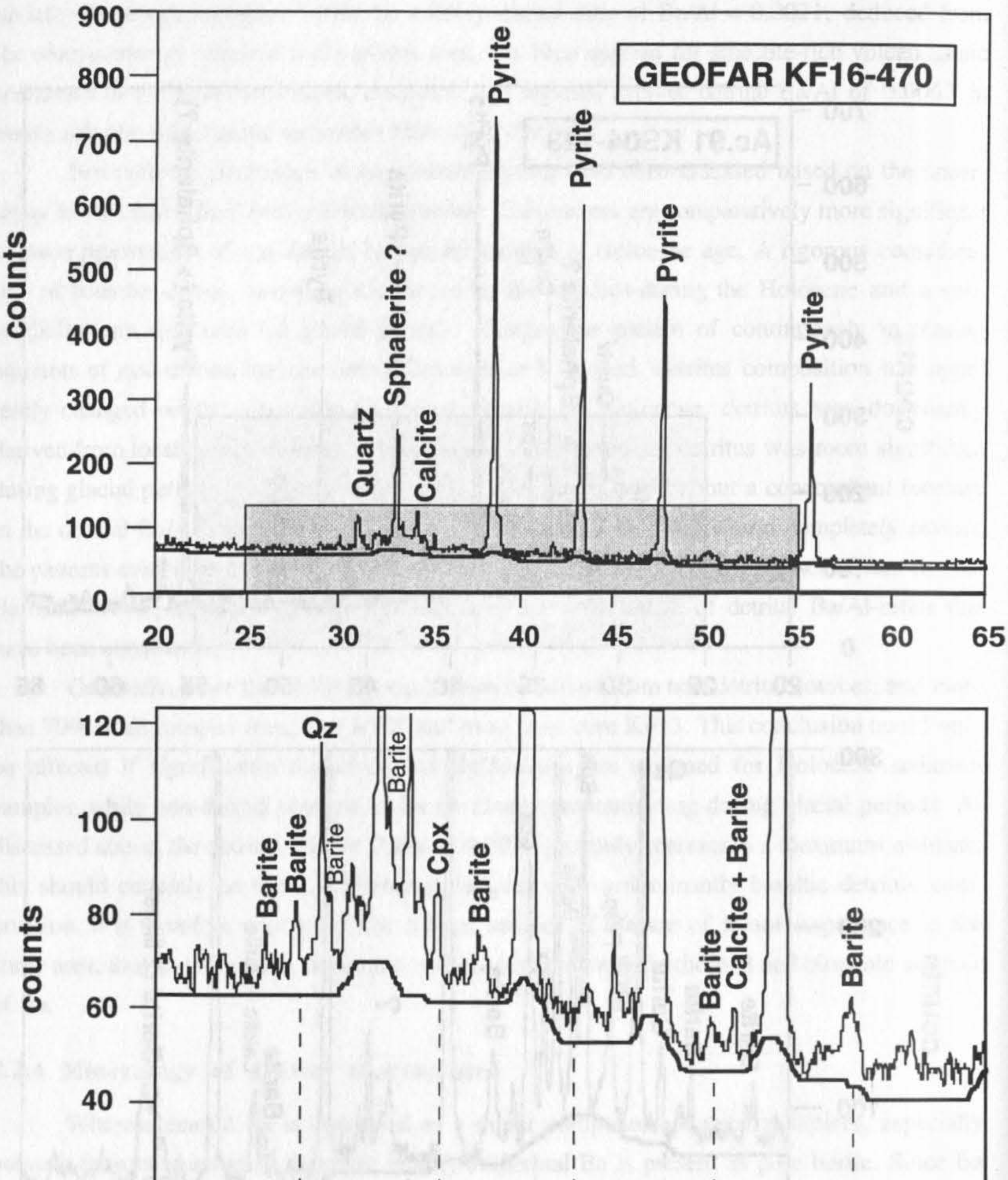

Fig. 8.5 b): X-ray diffractogram of gravity separate from sample KF16-470

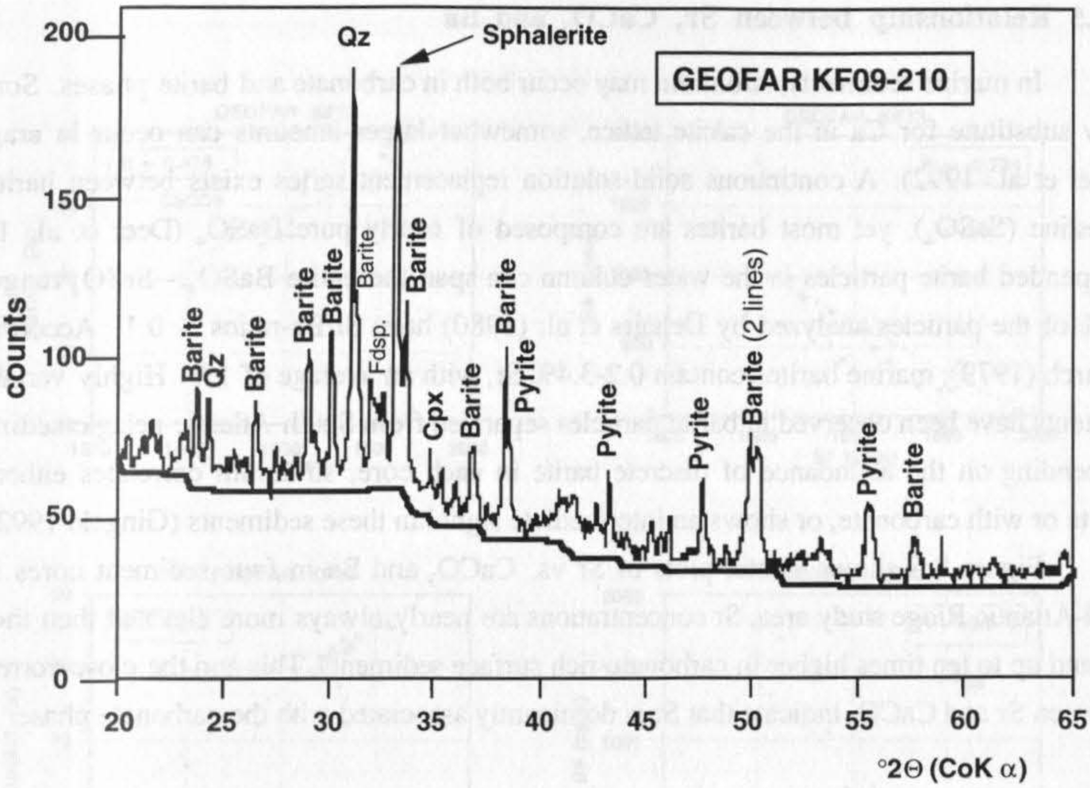

Fig. 8.5 c): X-ray diffractogram of gravity separate from sample KF09-210

The heavy mineral fraction is composed of pyrite, sphalerite (?), barite and clinopyroxenes. The presence of phases with densities < 3.0 g/cm^3 such as calcite, quartz, and feldspars indicates that gravity separation was not wholly efficient; it is conceivable that these latter phases have been present as parts of aggregates with overall densities > 3.0 g/cm^3. **Pyrite** is the dominant phase in samples Ac.91KS04-123 and especially KF16-470. It might be of hydrothermal origin, or it could have formed during decomposition of organic matter. The latter hypothesis is compatible with highest amounts of organic carbon in core KF16. **Sphalerite** was tentatively identified based on a single well-defined reflection at 3.13 Å. This suggests the presence of a cubic mineral, since XRD patterns of cubic substances show few high intensity reflections. While other sulfide phases, e.g. geerite ($Cu_{1.60}S$), have very similar X-ray parameters, sphalerite is by far the most common mineral with a principal reflection at 3.13 Å. This should reflect a distal hydrothermal contribution derived from fine-grained sulfide particles which may be laterally dispersed in plumes in the water column. The presence of **barite** is clearly indicated by a sequence of diagnostic reflections. In spite of considerable enrichment compared to bulk samples, barite is a minor phase strongly "diluted" by abundant pyrite in gravity separates of samples Ac.91KS04-123 and KF16-470. Clinopyroxenes, which also have densities greater than 3.0 g/cm^3, are present in variable but minor amounts; they are presumably of volcaniclastic origin.

8.2.5 Relationship between Sr, $CaCO_3$ and Ba

In marine sediments, strontium may occur both in carbonate and barite phases. Some Sr may substitute for Ca in the calcite lattice, somewhat larger amounts can occur in aragonite (Deer et al. 1992). A continuous solid-solution replacement series exists between barite and celestine ($SrSO_4$), yet most barites are composed of nearly pure $BaSO_4$ (Deer et al. 1992). Suspended barite particles in the water column can span the entire $BaSO_4$ - $SrSO_4$ range, but 67% of the particles analyzed by Dehairs et al. (1980) have Sr/Ba-ratios ≤ 0.1. According to Church (1979), marine barites contain 0.2-3.4% Sr, with an average of 1%. Highly variable Sr contents have been observed in barite particles separated from South Atlantic pelagic sediments. Depending on the abundance of discrete barite in each core, strontium correlates either with barite or with carbonate, or shows an intermediate signal in these sediments (Gingele 1992).

Figure 8.6 shows scatter plots of Sr vs. $CaCO_3$ and Ba in four sediment cores in the Mid-Atlantic Ridge study area. Sr concentrations are nearly always more elevated than those of Ba and up to ten times higher in carbonate-rich surface sediments. This and the close correlation between Sr and $CaCO_3$ indicate that Sr is dominantly associated with the carbonate phase.

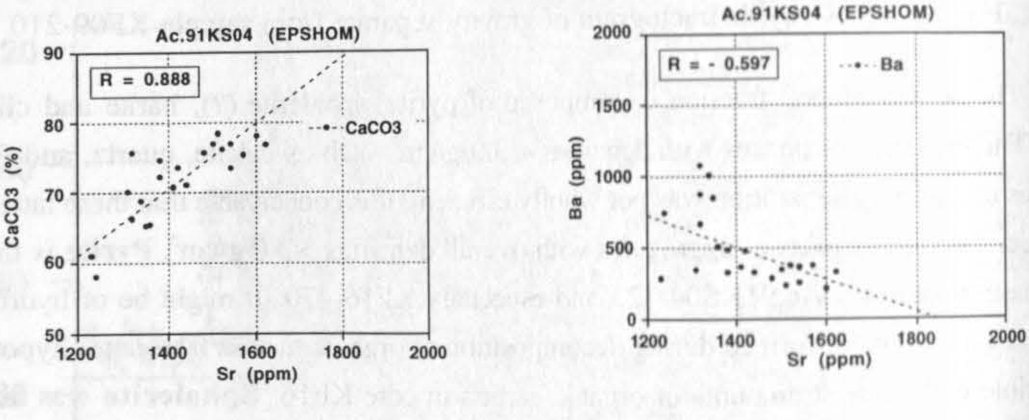

Fig. 8.6: Scatter plots of Sr vs. $CaCO_3$ and Ba

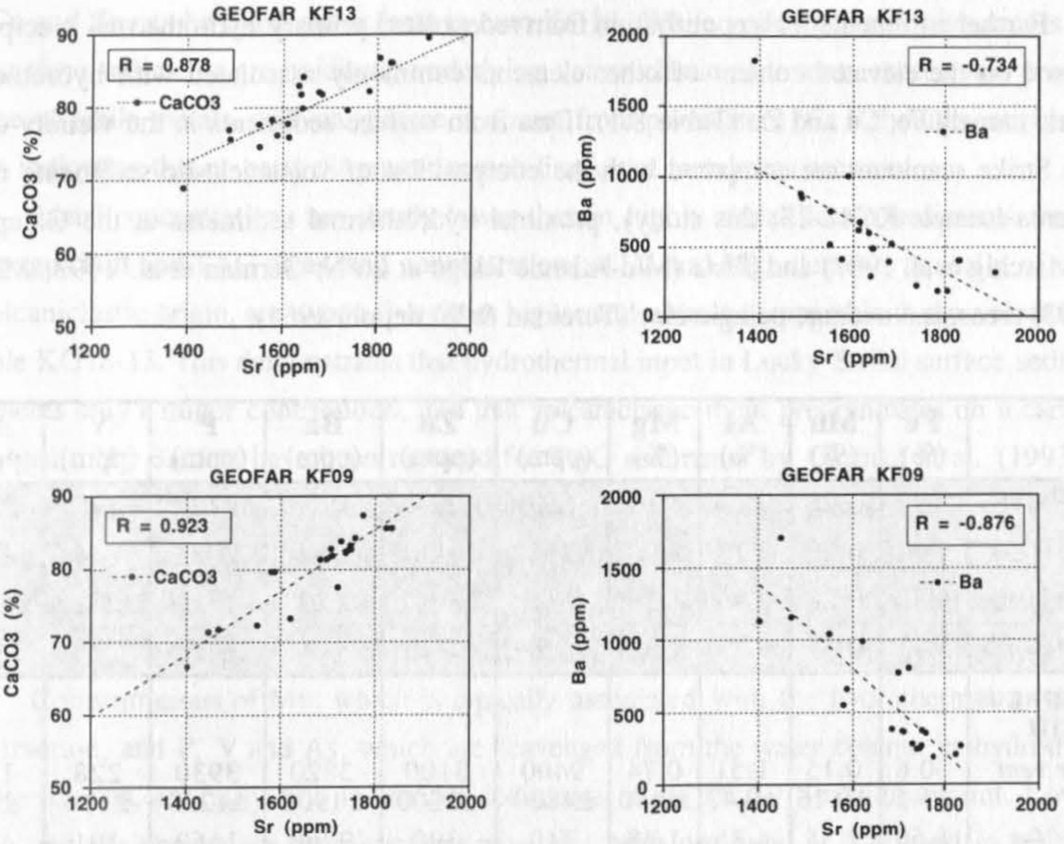

Fig. 8.6 *(continued)*

As higher Ba concentrations occur during glacial periods with lower amounts of $CaCO_3$, Sr is inversely correlated with Ba, which is simply a result of dilution by biogenic carbonate. This relationship is less clear in the case of core Ac.91KS04, because carbonate in this core is controlled by varying amounts of volcaniclastic detritus in addition to glacial-interglacial fluctuations.

8.3 Discussion

8.3.1 Barium in proximal sediments at the Lucky Strike seamount: evidence for hydrothermal origin

Sediments in the vicinity of the Lucky Strike seamount show a different relationship of barium vs. indicators of biogenic input, especially high concentrations of Ba at low ratios of Si/Al. This suggests that a significant amount of Ba is of hydrothermal origin in this region. In an area of steep topography, mass wasting of sulfide/sulfate material is a likely process to account for this contribution. Sediments from the immediate vicinity of the Lucky Strike seamount and hydrothermal site are characterized by numerous intervals of coarse, frequently normally grain-sorted redeposited material containing abundant volcanic glass. It is very feasible that such turbidites could also contain hydrothermal precipitates.

Further arguments for a contribution from redeposited primary hydrothermal precipitates are based on the elevated content of other elements commonly associated with hydrothermal sulfides, namely Fe, Cu and Zn (Table 8.1). Data from surface sediments in the vicinity of the Lucky Strike seamount are compared with the composition of volcaniclastic sediments in the same area (sample KG18-13; this study), proximal hydrothermal sediments at the Galapagos Rift (Marchig et al. 1987) and TAG (Mid-Atlantic Ridge at 26°N; German et al. 1993, Mills et al. 1993) areas, and average pelagic clay (Turekian & Wedepohl 1961).

	Fe (%)	**Mn** (%)	**Al** (%)	**Mg** (%)	**Cu** (ppm)	**Zn** (ppm)	**Ba** (ppm)	**P** (ppm)	**V** (ppm)	**As** (ppm)
KG18-S	7.90	0.29	7.85	4.19	650	224	1875	2290	275	66
KF 7-S	6.91	0.29	8.18	3.90	214	146	1030	2005	244	< 30 *
KS 10-S	6.55	0.28	8.17	4.56	187	106	620	1850	241	< 30 *
KG18-13	5.77	0.11	9.13	4.83	95	73	144	990	225	15
Galapagos Rift										
near vent	30.6 ±5.5	0.15 ±0.16	1.51 ±0.47	0.74 ±0.46	9400 ±4800	3100 ±2200	3820 ±1900	3930 ±1270	228 ±114	152 ±76
5-100m from vent	8.60 ±1.8	1.55 ±0.28	4.35 ±0.52	1.48 ±0.25	310 ±90	390 ±270	9260 ±188	1660 ±350	191 ±50	5.3 ±3.6
TAG										
German et al.	32.2 ±7.5	0.23 ±0.29	1.65 ±1.69	0.83 ±0.64	3360 ±1475	2130 ±855	---	---	---	---
Mills et al.	36.0 ±4.3	0.23 ±0.23	---	---	2055 ±1000	3460 ±4200	---	---	---	---
average pelagic clay	6.50	0.67	8.40	2.10	250	165	2300	1500	120	13

Table 8.1: Geochemical data from surface sediments on the flanks of the Lucky Strike seamount compared to sample KG18-13 ("local volcaniclastic end member"), data from proximal hydrothermal sediments at the Galapagos Rift (Marchig et al. 1987) and TAG hydrothermal field (MAR, 26°N; German et al. 1993, Mills et al. 1993) and average pelagic clay (Turekian & Wedepohl 1961). All data recalculated on a carbonate-free basis.
* Arsenic data based on detection limit of 12 ppm in bulk sediment samples

Concentrations of Cu, Ba and, to a lesser extent, Fe and Zn increase with proximity to the Lucky Strike hydrothermal site in the sequence KS10 - KF7 - KG18. Iron is also derived from volcaniclastic sediment sources; however, the Fe/Al-ratio is significantly higher than in underlying pure volcaniclastic sediments in box core KG18 (sample KG18-13), and is also steadily increasing in the same direction. Sample KG18-13 is composed almost exclusively of volcanic glass, with a $CaCO_3$ content of only 0.40%, and can be considered a "local volcaniclastic end member". As discussed in Chapter 6.4.1, its composition is representative of enriched

MORB, its Ba content, while higher than in average mid-ocean ridge basalt, cannot explain the elevated Ba content of surface sediments in the same area. A diagenetic origin of enrichments in Fe, Cu and Zn can be ruled out at least in core KG18. While yellowish-brownish colors show that surface sediments are oxidized, underlying volcaniclastic sediments should not provide a source of labile metals, and manganese is absent from porewaters (C. Rabouille, unpublished data), indicating that no early diagenetic remobilization of metals has occurred.

Metal concentrations are clearly lower than in highly metalliferous sediments from the Galapagos Rift and TAG areas, and concentrations of Al and Mg, elements typically of detrital or volcaniclastic origin, are two to five times higher and almost comparable to the volcaniclastic sample KG18-13. This demonstrates that hydrothermal input in Lucky Strike surface sediments represents only a minor contribution, and that volcaniclastic input predominates on a carbonate-free basis. No Ba data have been reported for TAG sediments by German et al. (1993) and Mills et al. (1993). Barite has not been observed in hydrothermal deposits of the TAG field (e.g. Rona et al. 1986, Thompson et al. 1988, Tivey et al. 1995), in contrast to hydrothermal sites at the East Pacific Rise and Juan de Fuca Ridge and to the Lucky Strike and Menez Gwen sites discovered more recently in the area of the present study.

Concentrations of Mn, which is typically associated with the hydrothermal oxyhydroxide fraction, and P, V and As, which are scavenged from the water column in hydrothermal particle plumes, are fairly low in surface sediments at the Lucky Strike seamount. Low and highly variable manganese concentrations have also been observed at TAG and in near vent-sediments at the Galapagos Rift (data in Table 8.1). This is consistent with observations in hydrothermal particle plumes that most of the total manganese remains in solution during buoyant plume rise and initial lateral dispersal (e.g. Trocine & Trefry 1988, Mottl & McConachy 1990). It has been suggested that bacterial Mn scavenging only occurs in more distal parts of the plume when concentrations of dissolved manganese have been strongly diluted by ambient seawater (Cowen et al. 1986, 1990). This process results in fractionation of Fe vs. Mn in ridge-crest sediments. P, V, and As show some enrichment with proximity to the Lucky Strike hydrothermal site, even though V is almost comparable to volcaniclastic sediments, i.e. about 80% of total V in sample KG18-S could be derived from volcaniclastic sources. Since concentrations of P and As are significantly higher than in average pelagic clay (Turekian & Wedepohl 1966), hydrothermal plume fallout appears to be present at the Lucky Strike seamount, but again as a minor component. The composition of „average pelagic clay" according to Turekian & Wedepohl (1961) includes data from Pacific Ocean sediments which tend to have higher concentrations of a number of elements compared to the Atlantic Ocean. For example, the barium value reported by these authors represents the mean of data for Pacific pelagic clays (4000 ppm) enriched in biogenic barium (Goldberg & Arrhenius 1958) and Atlantic deep-sea clays (700 ppm Ba). Similarly, data on various metals are based entirely (Fe) or partially (Mn, Cu) on slowly accumulating pelagic clays from the Pacific Ocean which are hydrogenetically enriched in metals. Therefore, data from the study area cannot be directly compared with Fe, Mn, Cu, and Ba concentrations of "average pelagic clay".

8.3.2 Geochemical and paleoceanographic context of Ba peaks in distal pelagic sediments

Figure 8.7 compares the downcore distribution of Ba in four cores with the depth profiles of a number of other elements and calcium carbonate. These data give clues as to the origin of Ba in distal pelagic sediments. Distal MAR sediments lack input from redeposited hydrothermal precipitates, but receive fallout from hydrothermal particle plumes which possibly includes some barite. On the other hand, barium could be derived from biogenic sources by water column processes operating throughout the world ocean.

Ba peaks are accompanied by maxima of a number of other elements and sometimes by minima of calcium carbonate (Fig. 8.7). Rubidium is most significantly and consistently enriched along with Ba. While most samples have Rb concentrations at or below the detection limit of 4 ppm, peak Rb concentrations reach up to 22 ppm. Potassium and, to a lesser extent, yttrium exhibit similar correlations with Ba-maxima. As discussed in Chapter 6, these elements are indicative of continentally-derived felsic detritus. A number of other elements with detrital associations, particularly Al, Fe, Si and Mg, show concomitant peaks. Concomitant Zn maxima could suggest a hydrothermal origin for some of the Ba. Sphalerite (ZnS) was tentatively identified in the heavy mineral fraction >3.0g/cm^3, which would indicate a distal hydrothermal contribution of fine-grained sulfides and possibly sulfides. On the other hand, it is feasible that an enhanced supply of Zn is also related to terrigenous input. As Zn peaks are less pronounced and do not consistently coincide with Ba maxima, it is improbable that hydrothermal input is the dominant controlling factor on Ba distributions in distal sediments, and that Ba peaks primarily represent episodes of enhanced deposition of hydrothermal barite.

The distribution of silica and iron is more complex, because these elements are also contained in biogenic silica and hydrothermal oxyhydroxides, respectively. Moreover, iron, as well as Zn, is diagenetically enriched in near-surface sediments (cf. Chapter 7). The described patterns of terrigenous influence are least pronounced in core Ac.91KS04, because input from local basaltic sources is invariably predominating at this location, as indicated by constantly low K concentrations compared to the other cores (cf. Chapter 6). Concurrent $CaCO_3$ minima occur in cores KF13 and KF16. The detailed AMS age data from core KF13 reveal that the early part of Termination I is characterized by distinctly higher sedimentation rates (cf. stratigraphy section). Therefore, the $CaCO_3$ minima are presumably related to enhanced terrigenous input rather than decreased supply of calcium carbonate.

Thus, **deglacial Ba peaks coincide with enhanced terrigenous input**. While the area of the present study is located just to the south of the main region of ice-rafted detritus (IRD) deposition in the glacial North Atlantic, extending from 40-55°N (Ruddiman 1977, Grousset et al. 1993), it is possible that a fine-grained ice-rafted component has reached the study area. Alternatively or additionally, eolian sources could be invoked. If Ba maxima in the study area are indicative of productivity peaks, these peaks could be related to enhanced supply of terrigenous nutrients.

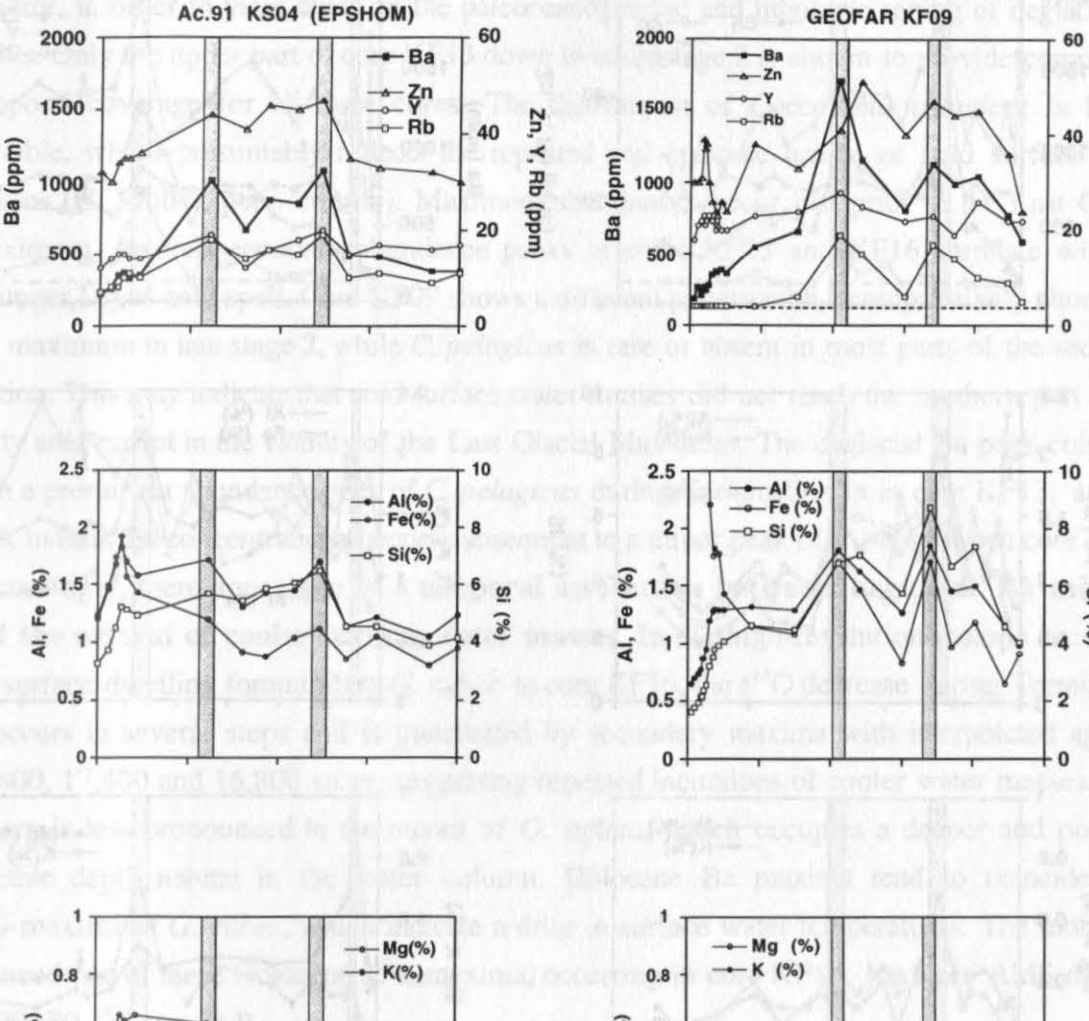

Fig. 8.7: Geochemical profiles showing association of various elements with Ba maxima (stippled rectangles). Broken lines represent detection limit for rubidium (4 ppm).

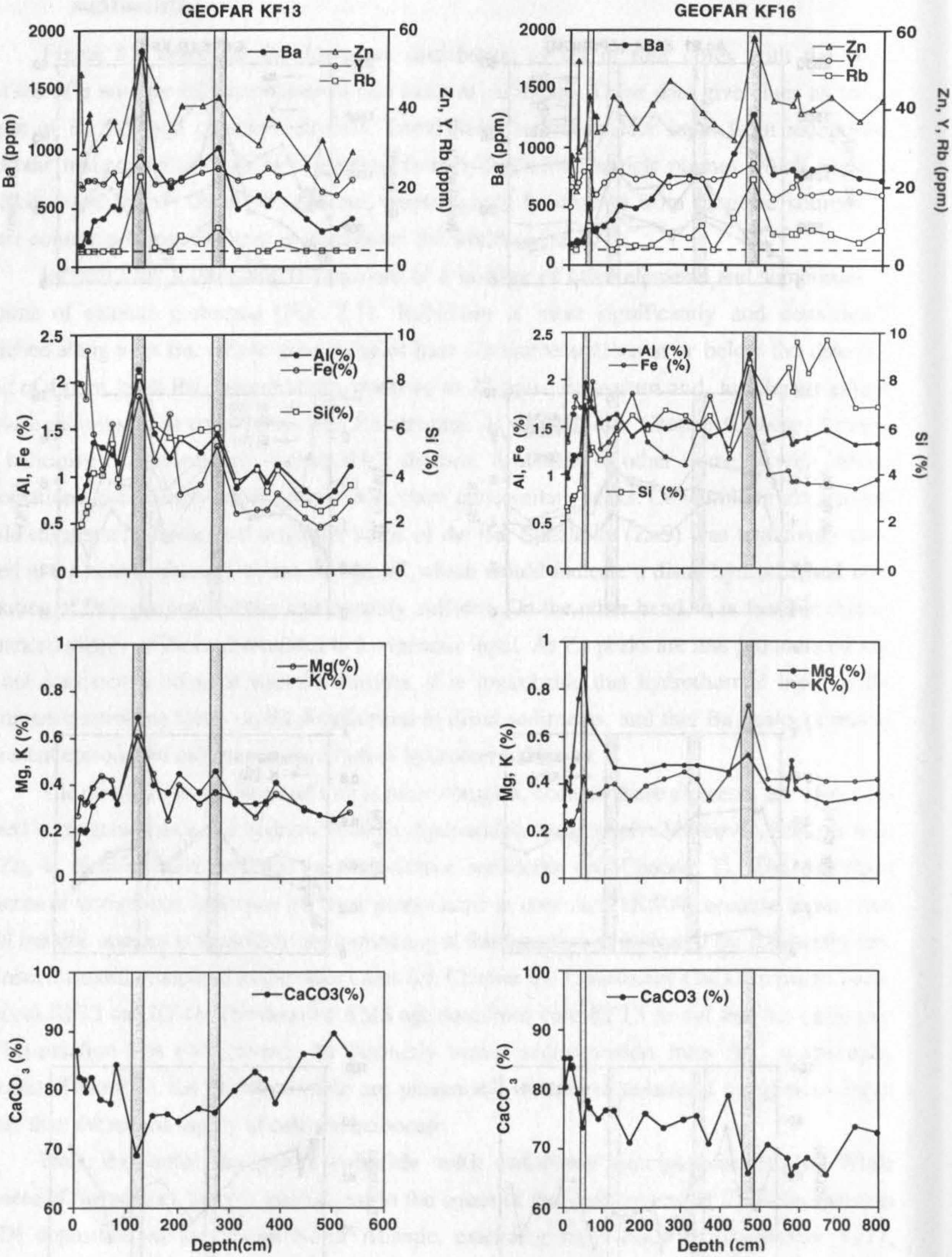

Fig. 8.7 *(continued)*

Figure 8.8 compares downcore Ba distributions with the abundance pattern of the cold-water nannoplankton species *Coccolithus pelagicus* (data from Müller 1995) and bulk sediment density, in order to yield clues on the paleoceanographic and lithologic setting of deglacial Ba peaks. Only the upper part of core KF13 down to early stage 2 is shown to provide comparable temporal coverage for all three cores. The distribution of *Coccolithus pelagicus* is highly variable, which presumably reflects the repeated and episodic arrival of cold surface water masses (C. Müller, pers. comm.). Maximum abundances occur just prior to the Last Glacial Maximum, several secondary abundance peaks in cores KF13 and KF16 correlate with the Younger Dryas cold spell. Core KF09 shows a different pattern with a comparatively short-lasting maximum in late stage 2, while *C. pelagicus* is rare or absent in most parts of the sediment section. This may indicate that cold surface water masses did not reach the southern part of the study area except in the vicinity of the Last Glacial Maximum. The deglacial Ba peak coincides with a prominent abundance peak of *C. pelagicus* during Termination Ia in core KF13, and the peak in bulk Ba concentrations occurs subsequent to a minor peak of *C. pelagicus* in core KF16. Accordingly, there appears to be a **temporal association between deglacial Ba maxima and the arrival of cooler surface water masses**. In the high-resolution isotope record of the surface-dwelling foraminifera *G. ruber* in core KF16, the $\delta^{18}O$ decrease during Termination Ia occurs in several steps and is punctuated by secondary maxima with interpolated ages of 17,800, 17,400 and 16,800 years, suggesting repeated incursions of cooler water masses. This pattern is less pronounced in the record of *G. inflata*, which occupies a deeper and possibly variable depth habitat in the water column. Holocene Ba maxima tend to coincide with $\delta^{18}O$-maxima of *G. ruber*, which indicate a drop in surface water temperatures. The most pronounced one of these Holocene $\delta^{18}O$-maxima, occurring in core KF13, has been AMS dated at 6,990±80 ^{14}C yrs. B.P. .

Two density records are shown in Fig. 8.8: non-destructive continuous measurements by gamma-densitometry performed at IFREMER Brest prior to core splitting, and data obtained on discrete samples. Both records are generally in good agreement with each other; discrepancies may be in part due to errors in volume determinations on discrete samples. To a first approximation, density records are a mirror image of stable isotope data, with lower densities corresponding to glacial periods with higher content of biogenic opal. Density minima consistently occur early during Termination Ia, at core depths coinciding with deglacial Ba peaks. Similar minima are present in early stage 2. It is tempting to assume that such density minima correspond to higher content of biogenic opal and thus to episodes of enhanced productivity. The earlier record in core KF13 (Fig. 8.9) is more irregular: The isotope record of *G. ruber* is rather "jagged" and suggests frequent incursions of cooler surface water masses throughout isotope stage 3 (cf. stratigraphy section). Likewise, the density record shows rapid short-term fluctuations, with numerous, mostly poorly defined minima.

The **age of deglacial Ba maxima** cannot be directly determined, because Ba peaks coincide with abundance minima of planktonic foraminifera, hence insufficient material might be available for AMS age dating and ages could be biased due to bioturbational mixing.

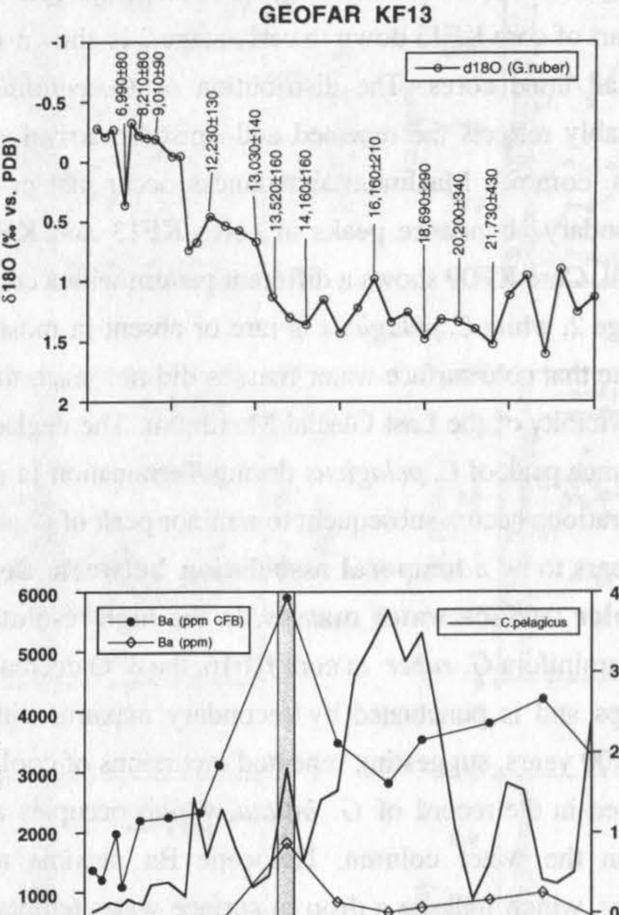

Fig. 8.8: Comparison of Ba distributions with oxygen isotope records and AMS ages (core KF13), abundance of *Coccolithus pelagicus* (data from Müller 1996), and bulk sediment density (line without markers represents continuous measurements by gamma-densitometry, broken line shows measurements on discrete samples).

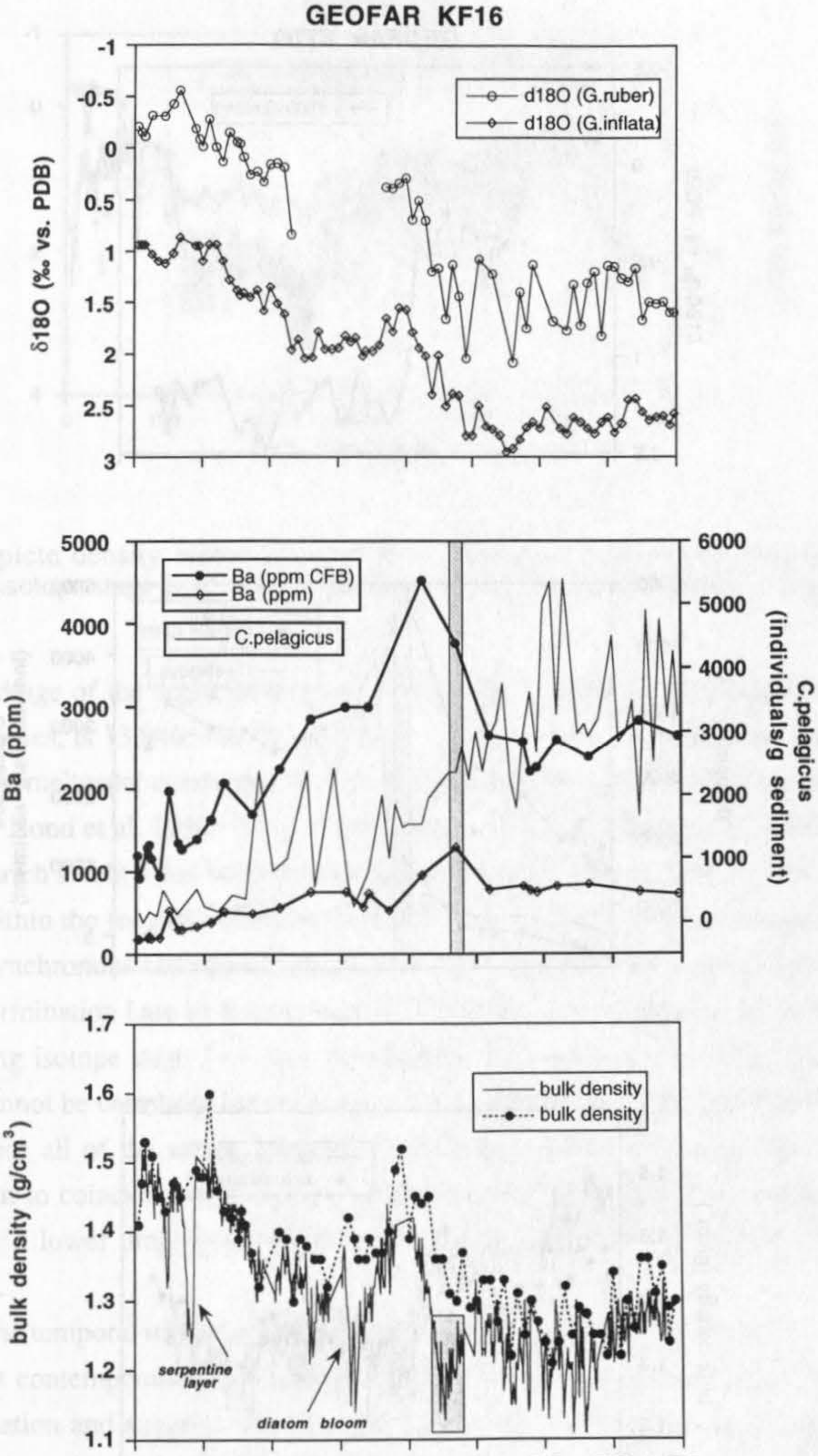

Fig. 8.8 *(continued)*

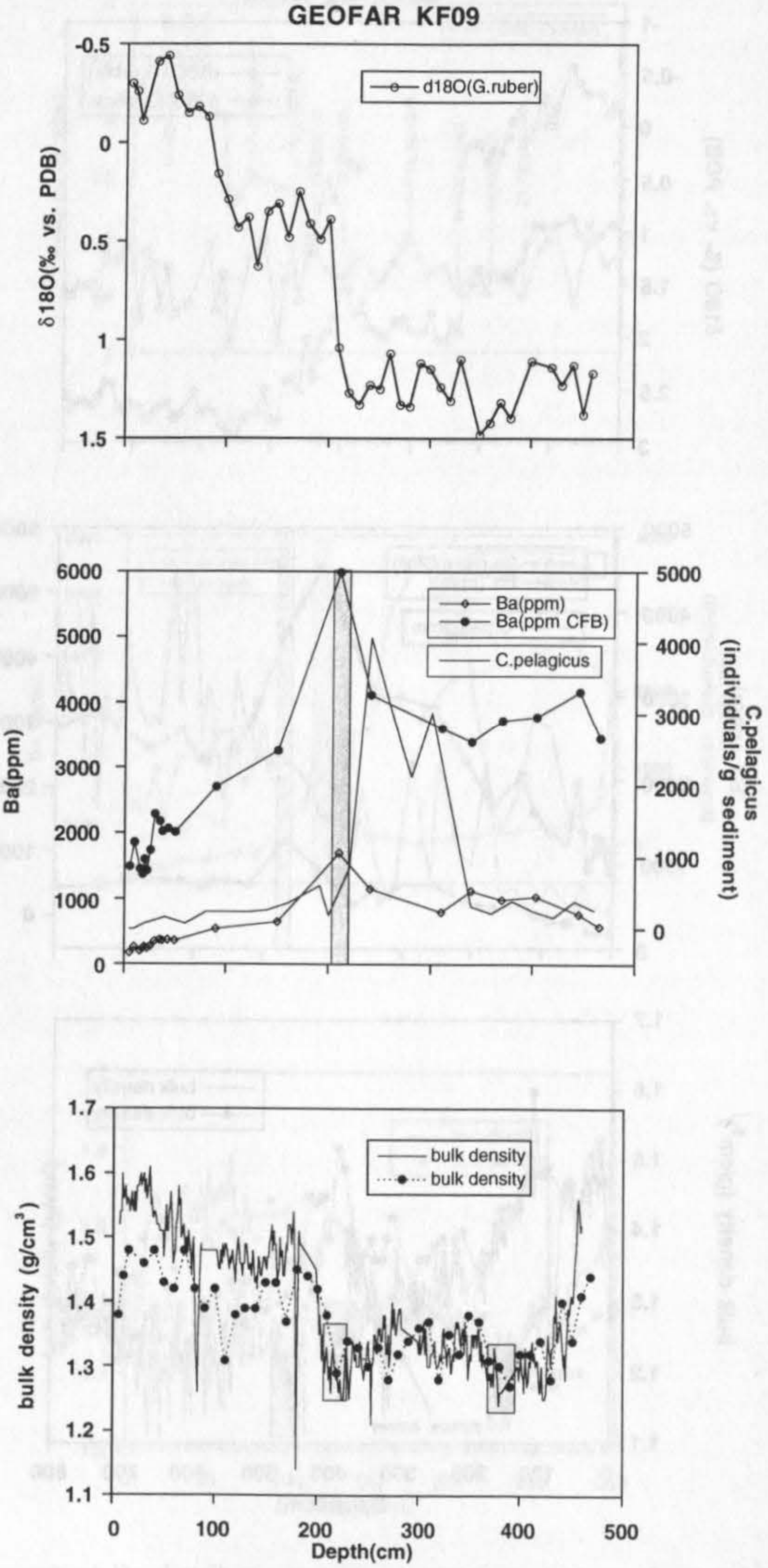

Fig. 8.8 *(continued)*

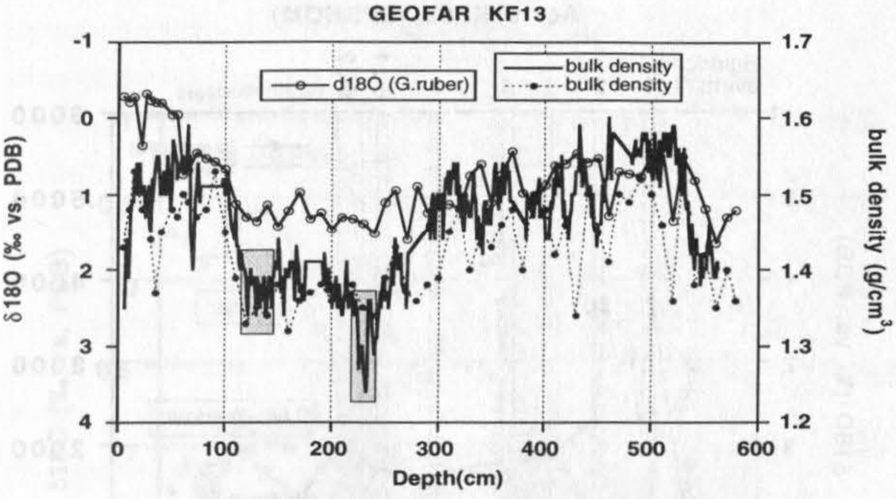

Fig. 8.9: Complete density record of core KF13, showing minima during Termination I and isotope stage 2 (stippled rectangles), and highly variable record in stage 3.

The interpolated age of the deglacial Ba peak in core KF13, based on AMS ages of over- and underlying samples, is 13,840±160 ^{14}C yrs. B.P. . This is coeval to **Heinrich Event 1**, the last of a series of meltwater events that have been described throughout the North Atlantic (e.g. Heinrich 1988, Bond et al. 1992, 1993, Broecker et al. 1992, Grousset et al. 1993, Auffret et al. 1996). Heinrich Event 1 has been radiocarbon dated to 13,490 - 14,590 ^{14}C yrs. B.P. (Bond et al. 1992). Within the temporal resolution available, deglacial Ba peaks in the other cores are roughly time-synchronous and should also be coeval to Heinrich Event 1 (Fig. 8.10). Ba peaks during early Termination I are by far the most pronounced ones, excluding one peak of similar amplitude during isotope stage 2 in core Ac.91KS04. Peaks occurring earlier during the last glacial cycle cannot be correlated between cores, which may be due to the limited sampling resolution. While not all of the earlier Heinrich events have associated Ba maxima, most of the peaks also seem to coincide with Heinrich meltwater events (Fig. 8.10). Ba peaks during the Holocene have a lower amplitude, which is in several cases still well beyond the range of analytical error.

While the temporal resolution of the Ba data is limited, the consistent pattern of deglacial Ba enrichments contemporaneous to Heinrich event 1 in four cores substantiates the observed temporal correlation and suggests that these peaks are a regional phenomenon with a common cause. Diagenetic redistribution of Ba may have been important in core KF16, which is characterized by higher content of organic carbon and sulfide-bearing porewaters, but should not have occurred in the other cores containing suboxic sediments. Based on the Ba/Al-ratio, it has been shown that detrital sources of Ba have been of minor importance throughout the time periods investigated in this study and especially during Termination I (Fig. 8.4).

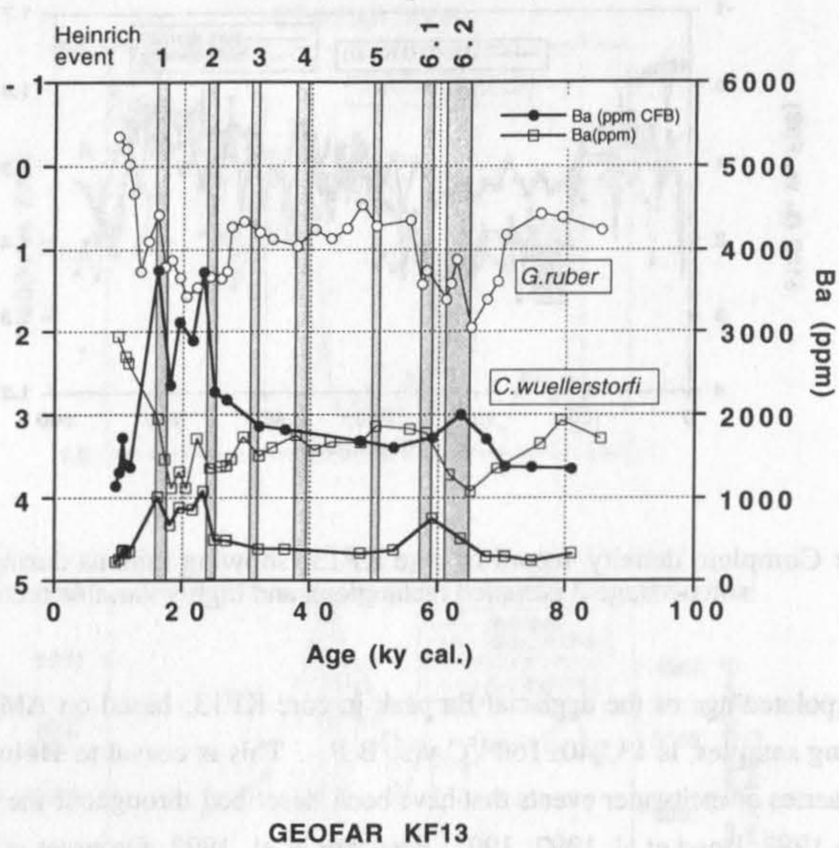

Fig. 8.10: Stratigraphic distribution of barium in Mid-Atlantic Ridge sediments. Barium maxima, particularly during Termination I, correlate with Heinrich meltwater events (stippled rectangles). Ages of Heinrich events after Jung (1996).

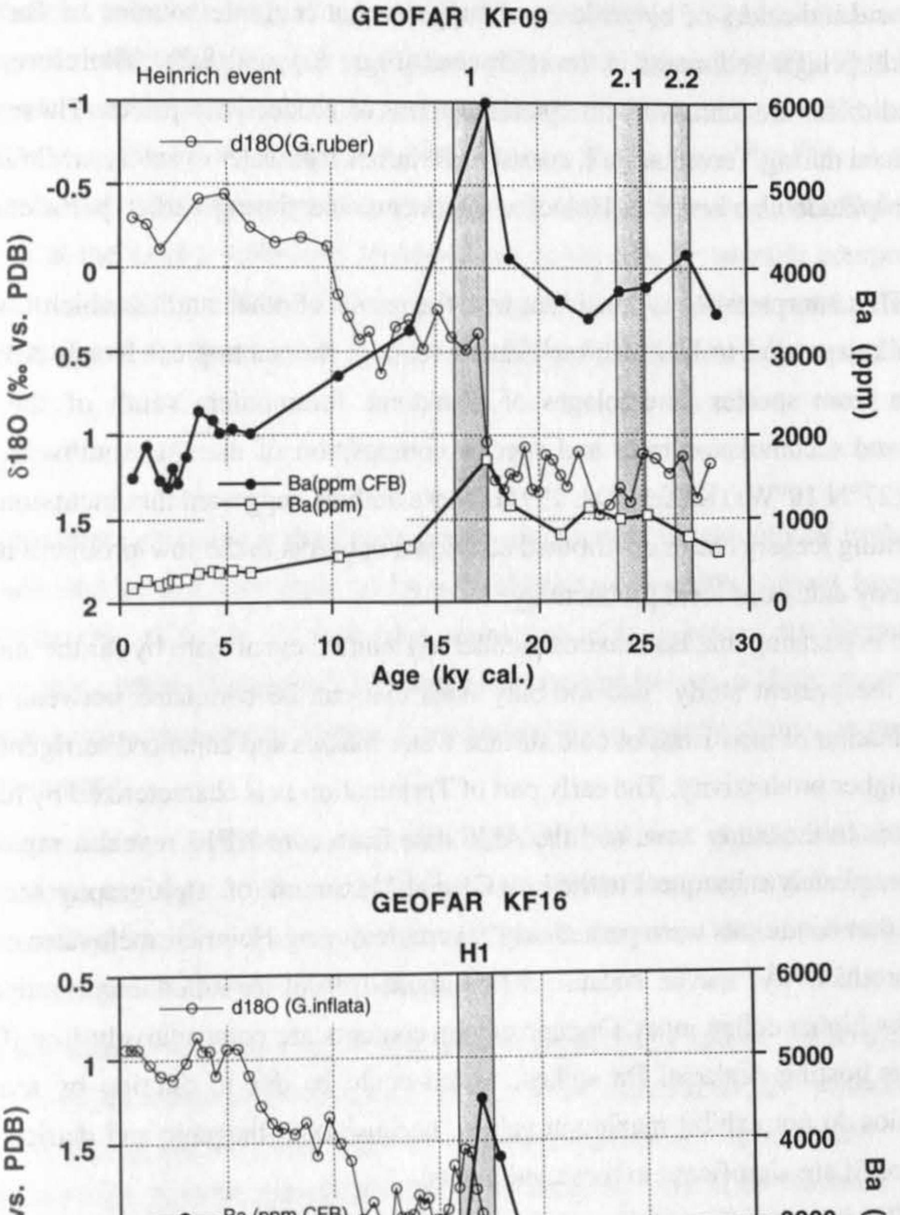

Fig. 8.10 (*continued*)

Hydrothermal input of Ba is possible; the probable presence of sphalerite (ZnS) in heavy mineral separates (cf. Fig. 8.5) suggests a distal hydrothermal contribution, some pyrite in these sediments could also be of hydrothermal origin. On the other hand, the correlation between barium and indicators of biogenic input suggests that biogenic sources of Ba predominate in "far-field" pelagic sediments in the study area (Figs. 8.1 and 8.2). Therefore, Ba maxima in distal sediments are tentatively interpreted in terms of productivity peaks. These peaks are most pronounced during Termination I, coeval to Heinrich meltwater event 1, while similar peaks of lower amplitude also occur in Holocene sediments and during earlier parts of the last glacial cycle.

This interpretation is consistent with the results of other studies which observed productivity spikes parallel to Heinrich meltwater events in the subtropical North Atlantic, based on evidence from species assemblages of planktonic foraminifera south of the Azores (38°N 27°W), and accumulation rates and species composition of diatoms southwest of the Canary Islands (27°N 19°W) (Kiefer et al. 1995). These authors suggested that incursions of freshwater from melting icebergs have contributed additional nutrients to the low-productivity "blue ocean" and thereby enhanced local productivity.

It is puzzling that Ba maxima parallel to Heinrich event 1 are by far the most pronounced ones in the present study, and the only ones that can be correlated between all four cores. A combination of incursions of cold surface water masses and enhanced terrigenous input might trigger higher productivity. The early part of Termination Ia is characterized by highest sedimentation rates in the study area, and the AMS data from core KF13 reveal a rapid sedimentation pulse immediately subsequent to the Last Glacial Maximum (cf. stratigraphy section). It is thus possible that conditions were particularly favorable during Heinrich meltwater event 1 to foster higher productivity, maybe because a fine-grained distal ice-rafted contribution was supplemented by higher eolian input. Organic carbon contents are comparatively low (0.17-0.26%) in sediments hosting deglacial Ba spikes, which could be due to dilution by terrigenous input. Si/Al-ratios do not exhibit maximum values, because both biogenic and detrital aluminosilicate sources of Si are significant in these sediments.

The interpretation of Ba maxima in terms of productivity peaks remains speculative, because there is no direct and unequivocal evidence that Ba in distal Mid-Atlantic Ridge sediments is indeed primarily of biogenic rather than hydrothermal origin. However, supporting evidence for the "productivity spike hypothesis" is derived from micropaleontological and oxygen isotope data, sediment physical properties and various geochemical parameters. It is difficult to imagine that peaks of hydrothermal Ba would, by mere coincidence, correlate with incursions of cooler surface waters, density minima and peaks of terrigenous input. On the other hand, all of these data could be integrated within the paleoceanographic context of Heinrich meltwater events and explain concomitant enhanced "blue ocean" productivity.

Strontium isotopic analysis of barite separates could provide direct evidence on the origin of barite. In areas without hydrothermal influence, marine barite records the strontium isotopic composition of seawater (Paytan et al. 1993, Martin et al. 1995), which has a contemporary $^{87}Sr/^{86}Sr$-ratio close to 0.70917 (e.g. Palmer & Edmond 1989, Hodell et al. 1990, Edmond 1992). On the other hand, barite from a hydrothermal vent chimney in the Mariana Trough has $^{87}Sr/^{86}Sr = 0.70475$ (Martin et al. 1995). As expected, this is close to the ratio of hydrothermal solutions, with a range of $^{87}Sr/^{86}Sr = 0.7029 - 0.7047$ and an average of 0.7035 at various sediment-barren ridges (compiled by Palmer & Edmond 1989). This is slightly more radiogenic than the composition of average MORB (0.7024 - 0.7030; Wilson 1989). Fluids at the TAG and Snake Pit fields at the Mid-Atlantic Ridge have $^{87}Sr/^{86}Sr = 0.7028 - 0.7039$ (Campbell et al. 1988, Edmond et al. 1995). No Sr isotope data are available for hydrothermal solutions at the Lucky Strike and Menez Gwen fields. The Sr isotopic composition of underlying basalts should be affected by the proximity of the Azores hot spot. Plume-type MORB in the vicinity of the Azores has $^{87}Sr/^{86}Sr = 0.7030 - 0.7035$ (Schilling et al. 1983).

8.4 Conclusions

- Barium in proximal sediments at the Lucky Strike seamount is dominantly of hydrothermal origin, as indicated by the association of Ba with elements potentially derived from hydrothermal sulfides (Fe, Cu) and the lack of a correlation with indicators for biogenic input (Si, Si/Al, organic carbon). Redeposited hydrothermal precipitates are a likely source for the Ba enrichment in these sediments. Fallout from hydrothermal particle plumes is presumably of minor importance.
- In distal sediments, the correlation between Ba and Si, Si/Al and organic carbon suggests primarily a biogenic origin of Ba. A hydrothermal contribution may also be present, but cannot be quantified based on the available data. Detrital sources of Ba are of minor importance in distal and proximal sediments in the study area.
- Ba maxima are tentatively interpreted as indicators of productivity spikes. These spikes could have been caused by a combination of cold surface water incursions and enhanced terrigenous input, supplying additional nutrients to the low-productivity "blue ocean". The most conspicuous maxima, present throughout the study area, are coeval to Heinrich meltwater event 1; terrigenous input in these samples could be derived from distal fine-grained ice-rafted and/or eolian sources. The association of Ba maxima with earlier Heinrich events is less clear. Similar but minor maxima are also present in Holocene sediments, and do also correlate with incursions of cold surface water masses.

9. A sedimentary serpentine layer: Alteration of marine ultramafic rocks at the 38°05'N fracture zone

9.1 Introduction

Exposures of **ultramafic rocks** are now recognized to be a common feature at the Mid-Atlantic Ridge, both in fracture zone and non-transform settings (summarized in Michael & Bonatti 1985a, Juteau et al. 1990). Interaction of seawater-derived fluids with ultramafic rocks frequently results in pervasive serpentinization of peridotites; associated alteration phases may include magnetite, talc, amphiboles and chlorite (e.g. Hébert et al. 1990). While studies to date have concentrated on mafic-hosted high-temperature hydrothermal systems, low- and high-temperature systems hosted in ultramafic rocks may account for a distinct, significant component of global hydrothermal fluxes (Rona et al. 1996), since fluid circulation in ultramafic rocks results in plumes in the water column with high methane concentrations, only minor manganese enrichments, and consequently low ratios of total dissolved manganese to methane (TDM/CH_4). Such plumes have been observed at the 15°20'N fracture zone at the Mid-Atlantic Ridge, at a water depth coinciding with major fault scarps in ultramafic rock exposures. Methane is inferred to be created abiotically during the serpentinization process (Charlou et al. 1991, Rona et al. 1992, Bougault et al. 1993). Hydrothermal alteration of ultramafic rocks may also affect the global Mg budget through precipitation of Mg-rich secondary phases such as serpentine, chlorite, talc and amphiboles.

In this section, a distinct serpentine occurrence at the Mid-Atlantic Ridge south of the Azores is described: An allochthonous serpentine layer is intercalated within pelagic sediments in core GEOFAR KF16, which has been retrieved from the deepest area of a basin located in the central part of the 38°05'N fracture zone. The presence of serpentine is particularly interesting at this location proximal to the Azores hot spot, because it is commonly assumed that a thickened crust is present in this area due to an enhanced magmatic budget, which should preclude the presence of upper-mantle rocks close to the seafloor. Along with a serpentinized peridotite dredged at the Kurchatov fracture zone at 43°N (Dick et al. 1984) and peridotites drilled at DSDP sites 556, 558 and 560 southwest of the Azores (Michael & Bonatti 1985 b), the sedimentary serpentine layer at 38°N represents the third indication for ultramafic rocks in the Azores area. Its geochemical composition, notably the Cr and Ni content, gives clues on the modal composition of the ultramafic protolith, which appears to be influenced by the proximity of the Azores hot spot, in agreement with previous petrological studies of peridotites at the Mid-Atlantic Ridge (Dick et al. 1984, Michael & Bonatti 1985 a). The mineral assemblage determined by X-ray diffraction of bulk and clay-size fractions and by transmission electron microscopy (TEM) is used to estimate alteration temperatures.

9.2 Core location and sedimentology

Core GEOFAR KF16 was retrieved from the deepest part of a basin oriented N80°E, in the central area of the 38°05'N fracture zone. The sedimentation rates are significantly above the regional average at the ridge axis implying that the basin acts as a sediment trap (cf. Chapter 3.1). An approximately 20 cm thick grayish green, fine-grained layer is intercalated within carbonate-rich pelagic sediments of Holocene age (Fig. 9.1).

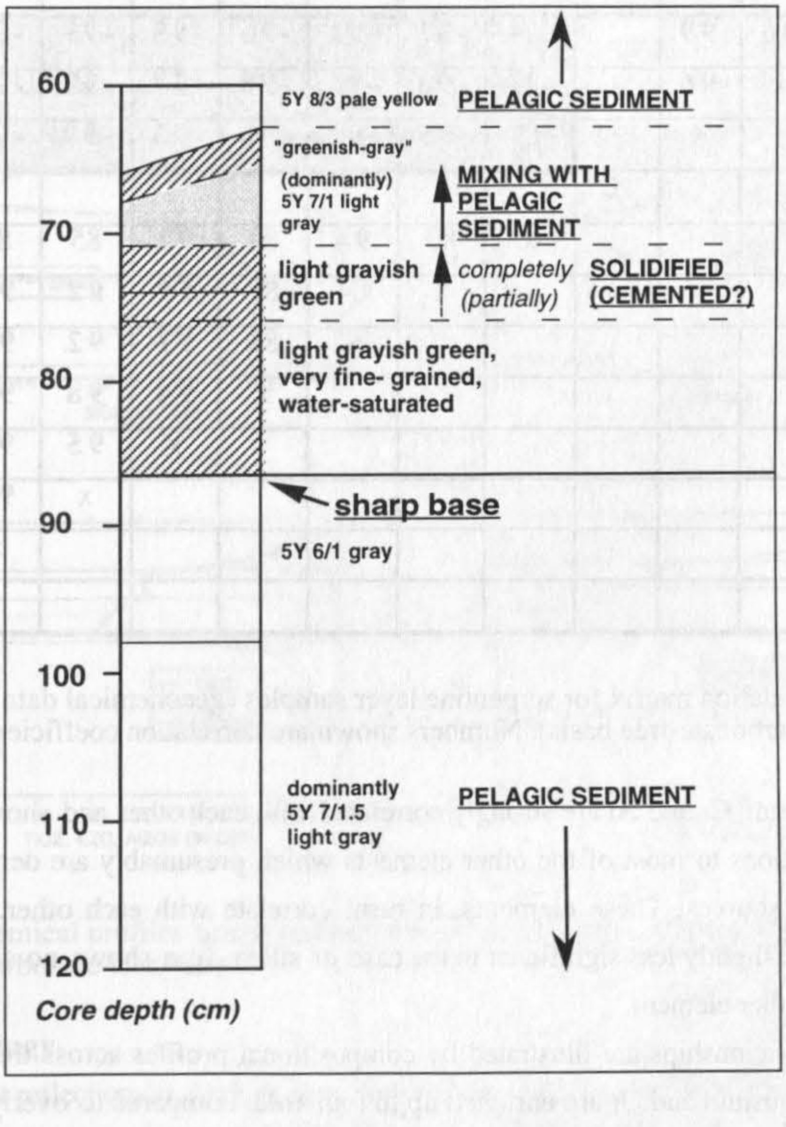
60
70
80
90
100
110
120
Core depth (cm)
5Y 8/3 pale yellow
PELAGIC SEDIMENT
"greenish-gray"
(dominantly)
5Y 7/1 light
gray
MIXING WITH
PELAGIC
SEDIMENT
light grayish
green
completely
(partially)
SOLIDIFIED
(CEMENTED?)
light grayish green,
very fine- grained,
water-saturated
sharp base
5Y 6/1 gray
dominantly
5Y 7/1.5
light gray
PELAGIC SEDIMENT

Fig. 9.1: Simplified lithological section across sedimentary serpentine layer intercalated within carbonate-rich pelagic sediments

The sharp base and gradational contact at the top indicate that the layer is **allochthonous**. The material could have been derived from the adjacent wall of the fracture zone. Most of the layer is fluid and water-saturated, while part of it is slightly more coherent (cemented ?), and mixing with pelagic sediment occurs near the top of the layer.

9.3 Results

9.3.1 Geochemistry

Calcium carbonate dominates the composition and decreases from 78% (normal pelagic sediment) to 58% at the base of the allochthonous layer. To eliminate variable dilution by biogenic carbonate, a correlation matrix for ten samples from the serpentine layer and the immediately over- and underlying sediments has been calculated on a carbonate-free basis (Table 9.1).

	Mg	Cr	Ni	Fe	Si	V	Y	Mn	Zn	P	Ti	K	Al
Mg	x	96	99		-84	-97	-91	-96	-95	-99	-99	-94	-99
Cr		x	96		-88	-90	-94	-98	-97	-97	-95	-96	-97
Ni			x		-84	-95	-92	-96	-95	-99	-99	-95	-99
Fe				x									
Si					x	80	94	89	92	85	84	92	86
V						x	84	89	90	92	95	91	93
Y							x	83	97	92	91	98	92
Mn								x	94	98	96	92	98
Zn									x	95	94	98	95
P										x	99	94	99
Ti											x	94	99
K												x	94

Table 9.1: Correlation matrix for serpentine layer samples (geochemical data recalculated on a carbonate-free basis). Numbers shown are correlation coefficients x 100.

Magnesium, Cr and Ni are strongly correlated with each other and show variably strong negative correlations to most of the other elements which presumably are derived from detrital and/or biogenic sources. These elements, in turn, correlate with each other. However, these relationships are slightly less significant in the case of silica. Iron shows no significant correlations with any other element.

These relationships are illustrated by compositional profiles across the serpentine layer (Fig. 9.2): Magnesium and Cr are enriched up to four-fold, compared to overlying pelagic sediment, and Ni up to seven-fold. The enrichments occur progressively from the top towards the base of the layer, with a distinct step in the geochemical profiles at the limit between the fluid and solidified parts. Iron is depleted at the top of the layer, and its concentration increases towards the base. Silica, while slightly depleted, shows little variability. A number of other elements (Al, K, Ti, Mn, P) and $CaCO_3$ are progressively depleted towards the base of the layer.

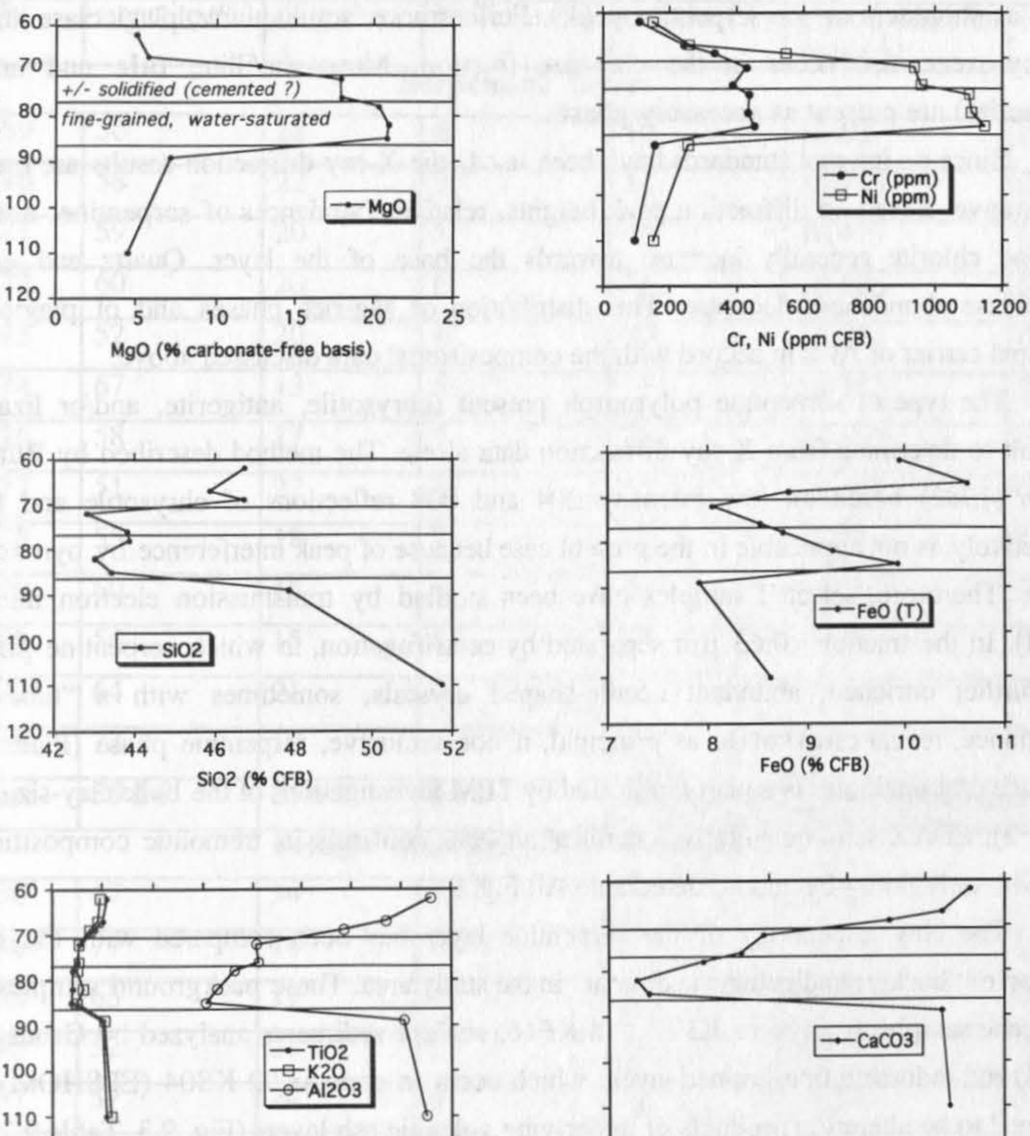

Fig. 9.2: Geochemical profiles across sedimentary serpentine layer (data recalculated on a carbonate-free basis)

9.3.2 Mineralogy

Dominant reflections at 3.65 Å and 7.30 Å with sharp peaks indicating **serpentine** as principal mineral phase were found in all carbonate-free bulk and clay-size fraction samples. In the bulk material, serpentine is accompanied by magnetite/spinel, quartz, plagioclase and clinopyroxene. In the clay fraction, broad reflections occur at approximately 14.25 Å, which, upon glycol saturation, expand and yield still broader reflections centered between 16.3Å and 16.7Å. This is indicative of an irregular mixed layer phase. Based on the entire mineral assemblage, a **smectite-chlorite mixed layer** is most likely. The number of expandable (17Å) smectite layers appears to increase towards the bottom of the profile, including possibly some discrete smectite. A distinct reflection which persists at 14.25Å upon glycolation and shows reduced intensity reveals the presence of discrete **chlorite**. Its higher order 002 and 004 reflections occur as shoulders on the serpentine peaks. Furthermore, some quartz, plagioclase and minor clinopyroxene also occur in the clay-size fraction. Muscovite/illite, **talc** and amphibole (**tremolite**) are present as accessory phases.

Since no internal standards have been used, the X-ray diffraction results are only semi-quantitative. Based on diffraction peak heights, relative abundances of serpentine, amphibole, talc and chlorite generally increase towards the base of the layer. Quartz and especially plagioclase abundances decrease. This distribution of Mg-rich phases and of plagioclase as principal carrier of Al is in accord with the compositional data discussed above.

The type of serpentine polymorph present (chrysotile, antigorite, and/or lizardite) is difficult to determine from X-ray diffraction data alone. The method described by Büttner and Saager (1982) based on low intensity 204 and 008 reflections of chrysotile and lizardite, respectively, is not applicable in the present case because of peak interference by pyroxenes and quartz. Therefore, selected samples have been studied by transmission electron microscopy (TEM). In the fraction <0.63 μm separated by centrifugation, in which serpentine phases are still further enriched, abundant needle-shaped crystals, sometimes with a "tube-in-tube" appearance, reveal **chrysotile** as principal, if not exclusive, serpentine phase (Plate 1). The presence of amphiboles is equally indicated by TEM investigations of the bulk clay-size fraction (Plate 2); EDAX semi-quantitative chemical analysis confirms its tremolitic composition (Mg-rich with only minor Fe and no detectable Al; Fig. 9.4).

The clay mineralogy of the serpentine layer has been compared with the clay-size fraction of "background pelagic sediment" in the study area. These background samples include Holocene samples from cores KF13 and KF16, surface sediments analyzed by Grousset et al. (1994) and indurated fine-grained layers which occur in core Ac.92 KS04 (EPSHOM) and are assumed to be alteration products of underlying volcanic ash layers (Fig. 9.3, Table 9.2).

Following Biscaye (1965), weighted peak areas of smectite (17Å glycolated peak), illite (10Å), kaolinite and chlorite (7Å - subdivided according to the relative proportion of each mineral in the 3.58Å/3.54Å kaolinite/chlorite doublet) have been used to calculate abundances of the four principal clay mineral groups. For the purpose of these calculations, peaks showing incomplete expansion (<17Å) have been treated as smectite. The ratio half height width/intensity of smectite peaks has been used as a qualitative indicator of smectite crystallinity. Lower ratios correspond to better crystallinity. Normalization to 100% assumes that these mineral groups represent 100% of the clay-size fraction. This is obviously not the case, since quartz and feldspar also occur in the clay-size fraction; moreover, the method of Biscaye (1965) does not accommodate the principal serpentine phase in samples KF16-(69-85). In these samples, the diagnostic peaks at 7Å, 3.54Å and 3.58Å occur as shoulders on serpentine peaks.

In all samples, "smectites" are the most important mineral group in the clay-size fraction. Compared to pelagic "background" sediments, samples from the serpentine layer of core KF16 are enriched in chlorite and depleted in kaolinite. The poorly defined shoulder peak at 3.58Å might even correspond to a Mg-rich chlorite phase, with no kaolinite at all being present.

Sample	smectite (%)	illite (%)	kaolinite (%)	chlorite (%)	glycol. smectite peak (Å)	HH/I
Serpentine layer						
KF16-69	56	28	6	10	16.687	0.011
KF16-70	58	22	9	11	16.935	0.013
KF16-71	59	20	5	16	16.473	0.014
KF16-72	60	20	6	14	16.526	0.008
KF16-73	52	20	8	20	16.394	0.012
KF16-74	67	13	5	15	16.342	0.008
KF16-76	58	17	3	22	16.660	0.008
KF16-77	51	22	9	18	16.526	0.013
KF16-78	55	18	7	20	16.742	0.013
KF16-79	60	15	4	21	16.660	0.011
KF16-80	56	15	5	24	16.687	0.008
KF16-82	64	21	4	12	16.796	0.008
KF16-85	73	10	4	14	16.687	0.006
Average	**59±6**	**19±5**	**6±2**	**17±4**	**16.624±0.17**	**0.010**
Pelagic „background“ sediments						
KF13-30	47	34	9	10	16.907	0.045
KF13-40	77	14	4	6	17.104	0.014
KF13-60	63	19	10	8	17.189	0.025
KF16-45	52	27	7	14	16.796	0.028
KF16-57	57	24	9	10	17.276	0.016
KF16-62	70	9	13	8	17.452	0.035
KF16-67	56	19	9	16	17.019	0.033
KF16-87	48	20	17	15	15.863	0.018
KF16-89	54	17	14	15	16.851	0.012
Average	**59±9**	**20±7**	**10±4**	**11±4**	**16.934±0.46**	**0.025**
surface sed. *	**46±12**	**27±10**	**13±6**	**15±8**	**---**	**---**
Alteration of volcanic ash layers (?)						
Ac.04 - 115	80	6	6	8	16.394	0.003
Ac.04 - 237	88	0	6	6	15.961	0.019
Ac.04 - 254	100 ?	0	0	0	16.213	0.010

Table 9.2: Comparative clay mineralogy of selected MAR sediment types (relative abundances of principal clay mineral groups calculated after Biscaye 1965). Serpentine sediments are characterized by higher amounts of chlorite, better smectite crystallinity (lower HH/I), and a shift in the position of principal smectite peaks to lower d-values caused by the presence of mixed-layer phases. * surface sediment data from Grousset et al. (1993) (14 samples)

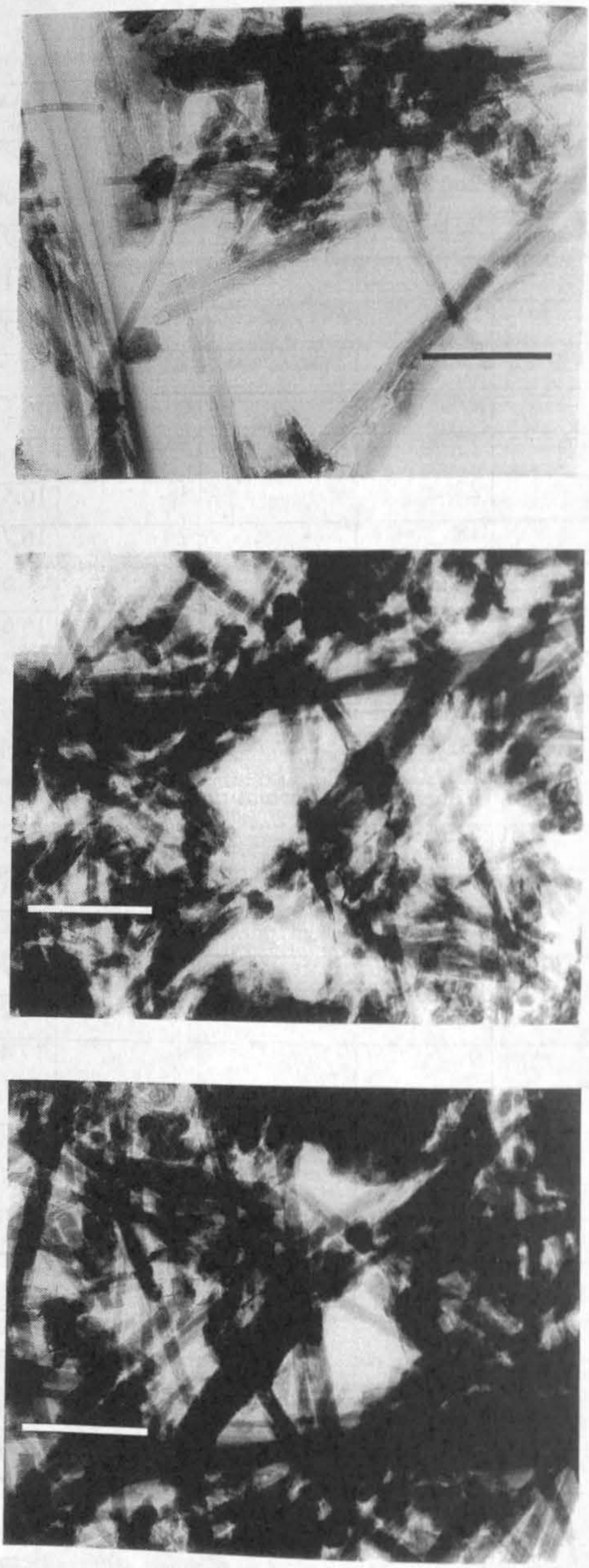

Plate 1: TEM micrographs showing hollow, needle-shaped tubes typical of **chrysotile** (samples KF16-82, fraction < 0.63 μm) (magnification 20,000 x, scale bar represents 1 μm).

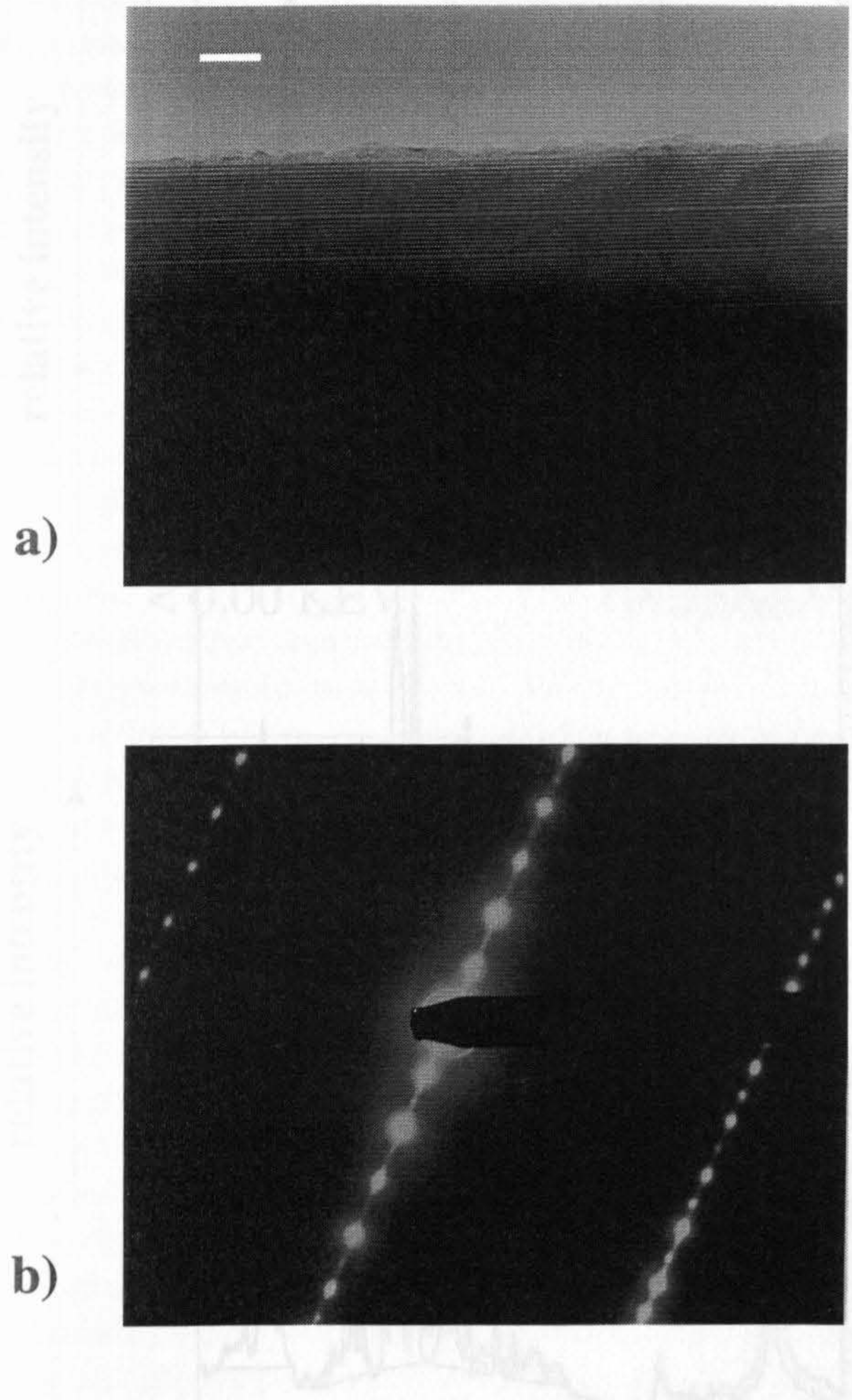

Plate 2: TEM micrographs of **amphibole** (sample KF16-85, fraction < 2µm)

a) lattice image (850,000 x, scale bar represents 0.1 µm)
b) electron diffraction pattern

Higher chlorite abundances compared to surrounding pelagic sediments should exclude a detrital origin of chlorite in serpentine layer samples. Glycolized smectite peaks occur consistently at <17Å. As discussed above, this suggests the presence of a smectite-chlorite mixed layer phase.

In pelagic background sediments, poorly crystallized smectites expanding to ≥ 17Å are most common. Since d(001) values of smectites represent the „summit“ of a broad hump including reflections derived from various clay phases, lower d(001) values for glycolized smectite peaks in samples KF16-87 and -89 may be related to admixture of phases from the overlying serpentine layer. Lower average percentages of smectite and higher percentages of illite in the surface sediment data from Grousset et al. (1993) indicate that basalt alteration, which is the principal source of smectites, may be less important in some surface sediments. Highest smectite abundances in surface sediments - 63 and 64% - have been observed in samples from the Lucky Strike seamount.

Indurated layers of core Ac.92 KS04 are composed almost exclusively of “smectite“. The location of glycolized peaks at 15.96-16.4 Å may indicate the presence of degraded smectites or smectites/vermiculites (Brindley & Brown 1984). Dominant 060 reflections at 1.511-1.513 Å suggest the presence of Fe-Mg rich dioctahedral smectites, which are derived from alteration of basalts or volcanic ash layers in sediments of the NW Pacific (Hein & Scholl 1978) and NE Atlantic (Parra et al. 1985, 1987). Further evidence for an origin of these layers by alteration of volcanic material comes from the presence of volcanic glass in bulk and clay-size fractions, and from very high feldspar abundances in bulk samples.

9.4 Discussion

9.4.1 Serpentine in the mid-oceanic ridge environment

Two principal types of serpentine occurrences at the global mid-oceanic ridge system were described: **precipitation from hydrothermal solutions** which reacted with basaltic rocks and **alteration of marine ultramafic rocks**. - In a hydrothermal sediment core from the Atlantis II Deep of the Red Sea, serpentine is associated with vermiculite/chlorite and minor amounts of talc. It overlies a layer composed almost exclusively of talc, which is in contact with the basaltic basement (Singer & Stoffers 1987). According to these authors, serpentine may have formed either as an alteration product of talc following a drop in reaction temperatures with increasing distance from the hydrothermal vent, or it may have been precipitated directly from hydrothermal brines. A hydrothermal origin was also postulated for a serpentine occurrence in a Hess Deep sediment core (Schmitz et al. 1982).

More commonly, serpentine frequently accompanied by magnetite, talc, amphiboles and chlorite occurs as an alteration product of marine ultramafic rocks. **Serpentinized peridotites** were described from a number of sites at the slow-spreading Mid-Atlantic Ridge, both in fracture zone and non-transform settings (summarized in Michael & Bonatti 1985a, Juteau et al. 1990). These include the Vema transform fault (Cannat & Seyler 1995), 15°N (Rona et al. 1987, Cannat et al. 1992) and MARK (23°N) areas (e.g. Karson et al. 1987, Hébert et al. 1990, Mével et al. 1991), and DSDP sites 556, 558 and 560 located in 35 Ma old (Sites 556 and 558) and 12 Ma old (Site 560) crust, respectively, (south)west of the Azores (Michael & Bonatti 1985b). In contrast, at the fast-spreading East Pacific Rise, outcrops of ultramafic rocks are restricted to specific geodynamic environments, such as the propagating rift of the Hess Deep (Francheteau et al. 1990, Hékinian et al. 1993, Agrinier et al. 1995) and the ultrafast Garrett transform fault (Cannat et al. 1990, Bideau et al. 1991, Hékinian et al. 1992). Serpentine phases in the Hess Deep were investigated more recently (Früh-Green et al. 1995, Stamoudi & Mével 1995, Stamoudi et al. 1995).

These differences between slow- and fast-spreading ridges have been explained by a large variability of magma supply at slow-spreading ridges, including phases of dominantly or purely tectonic extension („amagmatic spreading"). During these latter phases, deep crustal gabbroic and upper mantle rocks may become exposed due to uplift along low-angle normal faults or listric normal faults (Karson et al. 1987, Juteau et al. 1990, Mével et al. 1991); serpentine diapirism (Francis 1981) might also cause exposure of upper mantle rocks. - A similar process might explain the occurrence of serpentinized peridotites at the Galicia Margin (ODP Site 637, Agrinier et al. 1988, Kimball & Evans 1988), close to a passive continental margin. Evidence from the Red Sea suggests that, during the earliest stages of rifting, magma supply is limited and discontinuous (Bonatti 1985). This may have resulted in the production of a thin magmatic crust. Further thinning of this crust (or of the whole lithosphere) along normal faults may then have lead to the exposure of upper mantle rocks (Juteau et al. 1990).

The mineral assemblage of the sedimentary serpentine layer at the 38°05'N is compatible with an origin derived from alteration of ultramafic rocks. Cr and Ni are elements typically associated with this rock type. In particular, elevated Cr contents of the serpentine layer cannot be explained by hydrothermal leaching of basaltic rocks (Eckhardt 1992). Ultramafic rocks have not yet been described at the 38°05'N fracture zone. However, dredging operations have concentrated on the intersections with the rift axis, rather than the center of the fracture zone (Y. Fouquet, pers. comm.). Since ultramafic rocks have been frequently described from fracture zones at the slow-spreading Mid-Atlantic Ridge, the occurrence of this rock type close to the site of core KF16 would not be surprising.

The fact that chrysotile is apparently the dominant and possibly the only serpentine phase in the 38°05'N sediments is in striking contrast to most serpentine occurrences associated with marine ultramafic rocks. Pervasively serpentinized peridotites commonly contain antigorite and/or lizardite; if chrysotile is present, it usually occurs as a minor phase frequently in late-stage veins (H. Dick, pers. comm. 1996). A sedimentary deposit containing chrysotile and aragonite has been dredged at a fault scarp exposing harzburgites and dunites at the inner corner high of the south rift valley at the 15°20'N fracture zone of the Mid-Atlantic Ridge (H. Dick, pers. comm. 1996). A low-temperature hydrothermal origin was proposed for this deposit.

The geologic setting of the 15°20'N deposit is known, and the associated protolith has been sampled. In contrast, the serpentine sediments at 38°05'N are allochthonous and contain significant amounts of „externally supplied" pelagic material; no direct information on protolith and *in situ* geologic context is available. However, both deposits are very similar in lithology and serpentine mineralogy. It is therefore possible that all or part of the serpentine material investigated in this study also represents a **low-temperature hydrothermal deposit** associated with a fault that may occur in ultramafic rocks on the walls of the fracture zone. Such an origin could also explain the complete absence of the primary magmatic phases olivine and orthopyroxene. In an area of high relief, the fine-grained, water-saturated and poorly consolidated material could easily be redeposited subsequently.

9.4.2 Estimation of chlorite composition

Chemically, chlorites are hydrous aluminosilicates incorporating primarily Mg, Al and Fe, and occasionally Cr, Mn, Ni, V, Cu, Zn and Li (Bailey 1988). Their structure consists of the alternation of negatively charged tetrahedral-octahedral-tetrahedral 2:1 layers and positively charged brucite-like interlayers. Two series of ionic replacement occur (Foster 1962): Replacement of tetrahedral Al by Si causes a positive tetrahedral layer charge, which is compensated by replacement of octahedral Al by Mg. Replacement of Mg by Fe^{2+} involves only the octahedral layer and does not change the layer charges.

Since these ionic replacements change the cell parameters of chlorites, chlorite composition can be estimated by means of x-ray diffraction data, as summarized by Brindley & Brown (1980): The ionic attraction between 2:1 layers and brucite-like interlayers is related to the tetrahedral charge x, i.e. the amount of Al that substitutes for Si. Therefore, tetrahedral Al can be estimated based on d(001), using one of the following formulae (Brindley & Brown 1980)

$$\mathbf{d(001) = 14.648\text{Å} - 0.378\ x} \quad \underline{\text{or}}$$

$$\mathbf{d(001) = 14.55\text{Å} - 0.29\ x}$$

Over the range of $x = 0.8 - 1.6$ found in most chlorites, these yield fairly similar results. Since other structural variations may equally influence d(001) distances, calculation of Al^{IV} (Al in tetrahedral sites) by means of these formulae is accurate to within 7-10% (Bailey 1972).

Octahedral heavy atom content (essentially Fe, Cr and Mn, of which Fe is by far the most important) influences the relative intensities of basal 00l reflections; odd-order intensities weaken, with respect to the even-order reflections, with increasing heavy atom content. In order to estimate the Fe (or total heavy atom) content of chlorites, I(003) first has to be corrected for effects of asymmetric heavy atom distribution between octahedral layer and brucite-like interlayer. The heavy atom content can then be estimated based on

$$\mathbf{[I(002) + I(004)]\ /\ I(003)'.}$$

Details are discussed in Brindley & Brown (1980), where tables of relevant constants can be found.

In practice, this method is difficult to apply if kaolinite or serpentine interferences with chlorite 002 and 004 peaks are present (Moore & Reynolds 1989). In the case of the 38°N serpentine layer, the presence of significant amounts of kaolinite can be excluded based on the Al-poor bulk chemical composition. However, the exact position and intensity of the chlorite shoulder on serpentine peaks is fairly uncertain; the presence of two distinct shoulder peaks may indicate that two chlorite phases (Fe- and Mg-rich) might be present. Tetrahedral Al was calculated based on ethylene glycol-saturated oriented samples, using the position of the 14Å peak not affected by glycolation. Octahedral Fe was calculated using non-oriented powder samples, since preferred orientation may influence the relative intensities of basal reflections. Chlorite structural formulae have been calculated based on eight tetrahedral and twelve octahedral cations (Table 9.3). They are based on the assumption that equal amounts of tetrahedral and octahedral Al are present. Based on 154 published analysis of chlorites, Foster (1962) showed that this is frequently not the case: Some chlorites have „excess“ octahedral Al, with octahedral vacancies compensating the layer charge, while most have less octahedral Al, with Fe^{3+} and occasionally Cr^{3+} balancing the negative tetrahedral charge. Hence, octahedral and consequently total Al contents of chlorite were probably somewhat overestimated. The chemical composition of chlorites from the serpentine layer of this study was computed from structural formula as described by Foster (1962).

Depth (cm)	d (001) (Å)	Si IV	Al IV	Al VI	Fe VI	Mg VI	SiO2 (%)	FeO (%)	Al2O3 (%)	MgO (%)	Sum (%)
70	14.177	5.47	2.53	2.53	0.28	9.19	28.93	1.77	22.74	32.64	86.07
72	14.138	5.23	2.77	2.77	0.52	8.71	27.67	3.29	24.88	30.94	86.77
73	14.177	5.47	2.53	2.53	0.66	8.81	28.93	4.18	22.74	31.29	87.13
74	14.197	5.59	2.41	2.41	0.04	9.55	29.57	0.25	21.64	33.92	85.39
76	14.197	5.59	2.41	2.41	0.48	9.11	29.57	3.04	21.64	32.36	86.61
78	14.236	5.88	2.12	2.12	0.17	9.71	31.11	1.08	19.04	34.49	85.71
79	14.177	5.47	2.53	2.53	0.17	9.30	28.93	1.08	22.74	33.03	85.77
80	14.236	5.88	2.12	2.12	1.04	8.84	31.11	6.58	19.04	31.40	88.13
82	14.256	5.95	2.05	2.05	1.36	8.59	31.48	8.61	18.41	30.51	89.01
85	14.276	6.07	1.93	1.93	1.04	9.03	32.12	6.58	17.32	32.08	88.10

Table 9.3: Chlorite structural formulae and chemical composition (determined from X-ray diffraction data after Foster 1962, Bailey 1972, Brindley & Brown 1980 - see text).While much of the variability between samples is presumably due to uncertainties in peak statistics (H. Lange, pers. comm. 1996), chlorite in samples from the basal part of the layer is apparently richer in iron and contains slightly less Al.

For reasons discussed above, absolute values given for chlorite structural formulae and chemical compositions as determined from X-ray diffraction represent an approximation with considerable uncertainties. Much of the variability between samples can probably be ascribed to uncertainties in peak statistics (H. Lange, pers. comm. 1996). However, it seems clear that the chlorites are close to the Mg-rich end member; those with $Si^{IV} > 5.50$ can be classified as **clinochlore** according to the nomenclature of Foster (1962). Generally, there is a slight decrease in Al content with increasing depth, and samples at the base of the layer are richer in Fe. Both observations are considered reliable and are in accord with the bulk geochemical data.

Table 9.4 compares the estimated average chlorite composition with published data on chlorites derived from alteration of ultramafic rocks. Generally, compositions are fairly similar. The slightly higher Al content for the GEOFAR samples may be due to overestimation, as discussed above. Iron contents appear to be lower, which is not the case for samples from the base of the serpentine layer.

	MAR 38°N	Josephine Ophiolite, NW California	Islas Orcadas Fract. Zone, S Atlantic	Galicia Margin
	(this study)	(Kimball 1988)	(Kimball et al. 1985)	(Kimball & Evans 1988)
SiO2 (%)	29.94±1.43	28.68±2.62	33.97±1.47	36.03±1.72
Al2O3 (%)	21.02±2.42	19.10±1.33	14.11±1.48	12.15±0.84
FeO (%)	3.65±2.81	8.95±2.73	6.42±1.78	4.96±0.77
MgO (%)		28.22±2.43	32.05±2.39	32.76±0.92
Sum (%)	86.89±1.21	86.69±1.20	87.46±0.92	86.20±0.88

Table 9.4: Comparative mineral chemistry of chlorites derived from alteration of marine ultramafic rocks

9.4.3 A normative model of mineral abundances

Normative abundances of the principal phases serpentine, chlorite, plagioclase, quartz and magnetite (Table 9.5) have been estimated by means of a simple model as follows: Input data include carbonate-free bulk chemical composition of MAR sediment samples, published data on serpentine composition at the MAR (24°N) (Hébert et al. 1990), and chlorite compositions determined as described above for each sample separately. CaO and Ca-rich phases such as clinopyroxenes have not been included in the model - since Ca is principally associated with $CaCO_3$, small errors in the $CaCO_3$ determination yield potentially large errors in the amount of non-carbonate bound Ca. Furthermore, the accessory phases talc and tremolite have been omitted from the model. Consideration of these phases affected the robustness of the model, probably due to their Si-rich composition (62% and 58% SiO_2, respectively, for talc and tremolite; Deer et al. 1992), which frequently induced „negative" abundances of other phases. While significant in order to deduce the history of alteration temperatures discussed below, they can be neglected in normative calculations because of their low abundances. - A variety of feldspar compositions was tested (data from Deer et al. 1992). Finally, an andesine composition (An 38) was chosen. More basic compositions caused „negative" abundances of chlorite, since a disproportionate amount of Al was normatively assigned to the plagioclase phase. Since this composition is evidently not compatible with an ultramafic protolith, plagioclase was either „externally supplied" (i.e. of detrital origin, as quartz), or, alternatively, albitized plagioclase, possibly derived from gabbroic rocks, is present. - The solution consists of inverting the 5x5 - square matrix, and multiplying with a vector of carbonate-free sediment composition.

To a first approximation, the chemical composition can be modeled in terms of the relative abundances of two principal phases, serpentine and plagioclase, whose abundances are inversely correlated to each other. This pattern is further illustrated by Fig. 9.5. Serpentine abundances increase towards the base of the profile. It is the principal phase in all samples except sample KF16-69 from the zone of bioturbational mixing between serpentine sediments and overlying pelagic sediment. Feldspar abundances continuously decrease from the top to the bottom of the layer, which could reflect a decreasing detrital input. However, quartz is also assumed to be of detrital origin, and is present in essentially constant proportions based on normative calculations. Likewise, chlorite and magnetite appear to be present in nearly constant amounts, excluding a higher percentage of chlorite in the lowermost, iron-enriched sample.

	Serpentine	**Chlorite ***	**Plagioclase**	**Magnetite**	**Quartz**	***Sample composition (CFB)***
SiO2 *(%)*	37.5	27.6 - 32.1	58.1	0	100	43.76-47.06
FeO(T) *(%)*	4.98	0.25 - 6.58	0.18	100	0	7.91 - 9.10
MgO *(%)*	38.0	30.9 - 34.5	0.03	0	0	12.75-21.29
Al2O3 *(%)*	0	17.3 - 24.9	26.44	0	0	6.20-11.75
Na2O *(%)*		0	6.48	0	0	1.09-2.55
	Serp *(%)*	**Chl** *(%)*	**Plag** *(%)*	**Mt** *(%)*	**Qz** *(%)*	**Total** *(%)*
KF16-69	28.4	5.9	39.4	6.4	11.8	91.9
KF16-72	44.7	6.6	26.4	5.2	11.6	94.6
KF16-76	43.8	6.0	27.3	5.5	11.3	93.9
KF16-78	47.4	6.9	22.5	5.4	11.1	93.3
KF16-82	51.0	6.2	20.8	5.3	10.6	94.0
KF16-85	47.4	10.1	16.9	6.0	13.5	93.9

Table 9.5: Normative mineral abundances of principal phases serpentine, chlorite, plagioclase, magnetite and quartz (normative model described in text)

Based on these data, two processes could be invoked to account for the presence of "external" detrital phases in the serpentine layer:

- "Normal" pelagic sediment was taken up by the serpentine-bearing gravity deposit during the downslope movement on the walls of the fracture zone, and the relative amount of this material increased in the upper part of the layer.
- Allochthonous sedimentation, i.e. lateral supply of serpentine sediment, was sufficiently slow so that pelagic sedimentation continued at the same time at the prevailing high sedimentation rates, and the rate of lateral sediment input was decreasing towards the top of the layer.

Quartz may primarily be derived from eolian sources, which are ubiquitous throughout the Atlantic Ocean. In this case, the presence of nearly constant amounts of quartz could be explained by simultaneous deposition of air-borne dust as a minor sediment component, occurring at a constant rate.

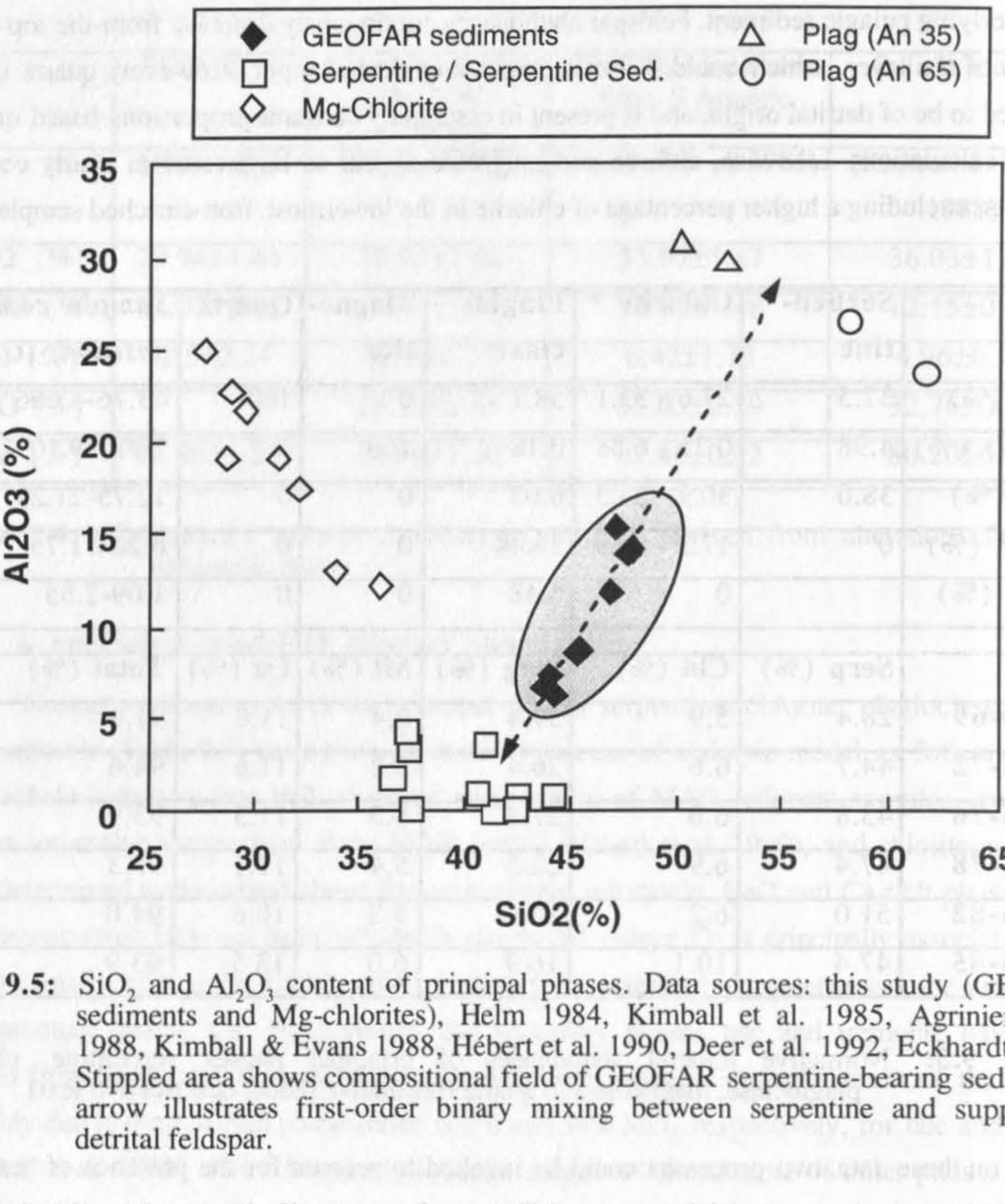

Fig. 9.5: SiO_2 and Al_2O_3 content of principal phases. Data sources: this study (GEOFAR sediments and Mg-chlorites), Helm 1984, Kimball et al. 1985, Agrinier et al. 1988, Kimball & Evans 1988, Hébert et al. 1990, Deer et al. 1992, Eckhardt 1992. Stippled area shows compositional field of GEOFAR serpentine-bearing sediments, arrow illustrates first-order binary mixing between serpentine and supposedly detrital feldspar.

9.4.4 Cr/Ni-ratios as indicators of protolith composition

In Figure 9.6, Cr/Ni-ratios of the investigated sediment samples are compared to published serpentine microprobe analytical data (Kimball et al. 1985, Agrinier et al. 1988, Kimball & Evans 1988, Hébert et al. 1990) and to bulk geochemical data from serpentine sediments (Helm 1984, Eckhardt 1992, Lagabrielle et al. 1992). Serpentine microprobe analytical data can be separated into two groups, one showing variably elevated Cr/Ni-ratios, and one with low values <0.25 (Fig. 9.6a). Bulk serpentine sediments reflect mixtures of variable proportions of these two groups, their Cr/Ni-ratios are therefore comprised within a narrower range of 0.1-1.3 (Fig. 9.6b).

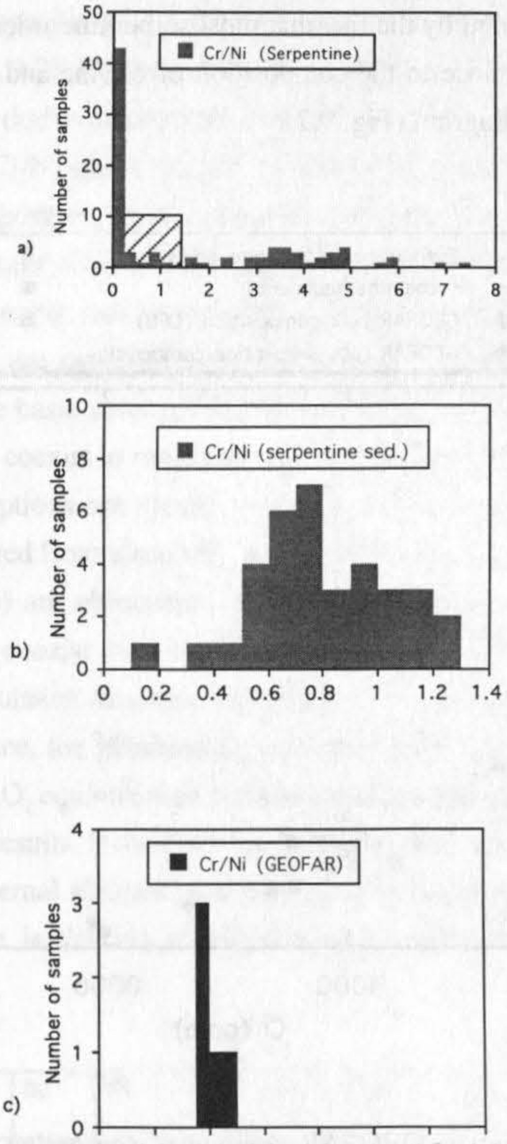

Fig. 9.6: Cr/Ni-ratios of GEOFAR samples compared to serpentine and serpentine sediments (Data source as in Fig. 9.5)

Cr/Ni-ratios of the MAR samples analyzed in this study vary between 0.35 and 0.5; these ratios fall at the lower end of the range of published analytical data (Fig. 9.6c).

Cr and Ni contents of serpentines can be related to the composition of primary magmatic phases. In thin sections of serpentinized peridotites in the MARK area (23°N) at the Mid-Atlantic Ridge, Hébert et al. (1990) have compared the mineral chemistry of olivine, clino- and orthopyroxene with the composition of immediately surrounding secondary serpentine phases. Olivine has high initial Ni content (3680±360 ppm) and low or no Cr (95±106 ppm), whereas pyroxenes always have less than 2000 ppm Ni, with an average of 450 and 1110 ppm for clino- and orthopyroxene, respectively, and variably elevated Cr contents which may exceed 8000 ppm. Serpentine pseudomorphs after olivine conserve low initial Cr contents and show some loss of Ni; pyroxene pseudomorphs show some gain of Ni and variable loss or gain of Cr. Generally, Cr/Ni-ratios of serpentine still reflect the trace metal content of magmatic precursor phases. This is demonstrated by the fact that most serpentine microprobe analysis published fall along two distinct trends close to the composition of olivine and clino- and orthopyroxene, respectively, in a Cr vs. Ni diagram (Fig. 9.7).

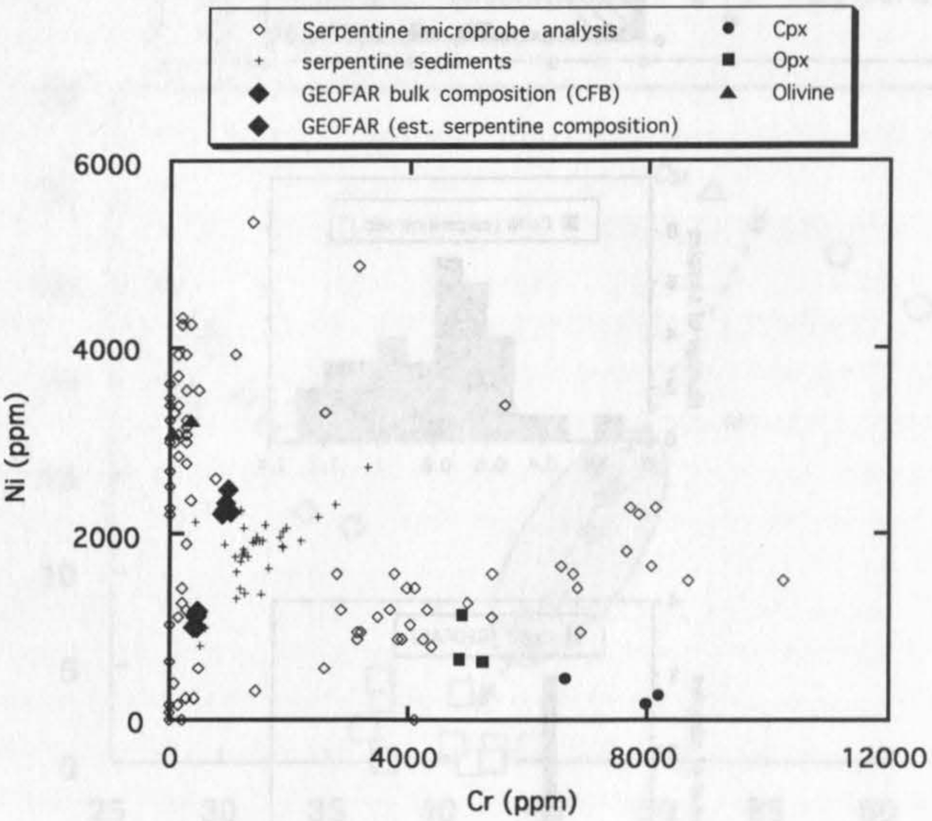

Fig. 9.7: Cr and Ni content of GEOFAR sediments, serpentine, serpentine sediments and magmatic precursor phases clinopyroxene (cpx), orthopyroxene (opx), and olivine (Serpentine data from Kimball et al. 1985 and Hébert et al. 1990; sediment data from Helm 1984, Eckhardt 1992 and Lagabrielle et al. 1992; pyroxenes and olivine from Cannat et al. 1990, 1992). GEOFAR estimated serpentine composition is based on normative serpentine abundance (Table 5) and on the assumption that all of the bulk Cr and Ni is associated with the serpentine phase.

Serpentine sediments show intermediate Cr/Ni-ratios, with absolute Cr and Ni concentrations frequently lower compared to serpentine microprobe analysis, reflecting dilution by other phases. The bulk composition on a carbonate-free basis of the 38°05'N MAR samples still falls at the lower end of the range of published data for serpentine sediments, indicating comparatively strong dilution by other phases. This is also evident from the presence of significant amounts of quartz and feldspars, and higher concentrations of Ti and Al. - An attempt was made to estimate serpentine composition, based on normative serpentine abundances discussed above and on the assumption that all of the Cr and Ni is contained in the serpentine phase. This latter assumption is not necessarily valid, especially in the case of Cr which may also be present in a Cr-spinel phase. Hence the Cr contents of serpentine may be overestimated. In any case, the "estimated serpentine composition" of GEOFAR samples falls close to the field of serpentines derived from olivine (Fig. 9.7). If Cr contents were indeed overestimated, the origin of serpentine phases as dominantly derived from olivine would be even more evident.

Accordingly, the Cr/Ni-ratios suggest an **ultramafic source material enriched in olivine**. The modal composition of the ultramafic precursor has been tentatively estimated by means of a modified "Pseudo"-CIPW-Norm calculation: In igneous petrology, the CIPW-Norm (Cross et al. 1903) is frequently used to calculate *normative* mineral abundances of a number of standard minerals. These are not necessarily the same as *modal* abundances based on thin section investigations. The basic assumptions of the CIPW-Norm are that certain minerals (e.g. quartz and olivine) cannot coexist in magmatic systems and that no OH-bearing mineral phases are present. These assumptions are clearly violated in the present case: Quartz coexists with minerals presumably derived from ultramafic source materials, and OH-bearing phases (serpentine, chlorite, amphiboles) are ubiquitous. In sedimentary rocks, minerals are derived from various sources, and may coexist even if they are not in thermodynamic equilibrium with each other. The following calculation assumes that (biogenic) calcite and (detrital) quartz have been "externally supplied"; hence, the geochemical data have been recalculated on a carbonate-free basis, and an amount of SiO_2 equivalent to the amount of normative quartz calculated above has been subtracted from the results. It has been ignored that other phases (feldspars, smectite) may also be derived from "external sources" and bear no relation to the ultramafic source material. Another basic assumption is that no chemical changes other than addition of fluids (OH^-) occurred during alteration.

Depth (cm)	or	ab	an	ne	di	C	hy	**ol**	mt	il	An (Plag)	Qz sed.	Sum
69	8.92	21.58	7.09			3.32	3.08	**24.11**	4.28	3.27	25	11.8	87.45
72	6.62	5.28	12.57	4.98	7.22			**35.39**	4.13	2.18	70	11.6	89.97
76	6.38	11.52	12.11	1.87	1.79			**36.67**	4.25	1.96	51	11.3	87.85
78	5.85	12.35	6.40			1.45	4.38	**37.52**	4.25	1.56	34	11.1	84.86
82	7.27	8.91	8.45	1.36	1.55			**42.05**	4.54	1.58	49	10.6	86.31
85	5.79	6.47	9.13	1.49	1.13			**42.69**	4.89	1.46	59	13.5	86.55

Table 9.6: "Pseudo-CIPW" - normative abundance of mineral phases, presumably related to the composition of the ultramafic source rock
(or - orthoclase, ab - albite, an - anorthite, ne - nepheline, di - diopside, C - corundum *, hy - hypersthene, ol - olivine, mt - magnetite, il - ilmenite, Qz sed. - "externally supplied" quartz (cf. Table 9.5))
* normative corundum reflects "excess Al2O3" (commonly associated with biotite or amphiboles in *modal* mineral abundances)

The results of this highly speculative approach are presented in Table 9.6. The scatter in normative feldspar composition and pyroxene abundances is due to uncertainties in the amount of Ca not bound to $CaCO_3$, since small errors in the $CaCO_3$ determination would yield large errors in non-carbonate Ca concentrations. This error would be further magnified by recalculation on a carbonate-free basis. However, the basic result is that olivine is by far the most important normative mineral phase, in accordance with independent evidence based on Cr and Ni trace element data. Sums of 85-90% normative mineral abundances in the Pseudo-CIPW calculations imply addition of approximately 14% H_2O during alteration, which is compatible with the H_2O+ content commonly encountered in serpentine and chlorite.

The modal composition of the ultramafic protolith as reflected by the serpentine chemistry can indicate the type of mantle material present along the mid-ocean ridge axis, namely refractory or fertile upper mantle (Hébert et al. 1990). An olivine-enriched ultramafic source material for the sedimentary serpentine layer at 38°05'N would be compatible with the results of petrologic studies of peridotites at mid-ocean ridges (Dick et al. 1984, Michael & Bonatti 1985). These two studies show that, at the Mid-Atlantic Ridge, the highest modal abundances of olivine accompanied by nearly complete depletion of clinopyroxene occur between 34° and 45°N. This refractory composition has been ascribed to an enhanced degree of partial melting, which presumably results from the presence of the Azores hot spot centered at 39°N. This conclusion is further substantiated by the mineral chemistry (Michael & Bonatti 1985). In particular, peridotites in the vicinity of the Azores are significantly more refractory than peridotites dredged or drilled near the Kane fracture zone, the best studied occurrence of ultramafic rocks at the MAR (Bryan & Juteau 1990, Cannat & Karson 1995).

9.4.5 Conditions of formation as indicated by the mineral assemblage

The following discussion is based on literature data on conditions of formation of serpentine, smectite/chlorite, amphiboles and talc applied to the mineral assemblage of the 38°N serpentine layer. Evidence comprises experimental and theoretical data, oxygen isotope measurements and temperature determinations in active geothermal fields. Since most reactions are primarily dependent on temperature rather than pressure (cf. Figs. 9.8 and 9.10), only formation temperatures will be discussed. Potential problems include the presence of metastable phases and of disequilibrium assemblages representing a wide range of temperature conditions. Furthermore, experimental setups are necessarily simplified compared to natural conditions: They may not reproduce fluid compositions encountered in natural systems, and cannot take into account reaction times on the order of several years or longer.

The presence of "externally supplied" detrital phases indicates that the sedimentary material which has been investigated in the present study represents a mixture of various sources. It is possible that the mineral assemblage related to alteration of ultramafic rocks was also derived from more than one source area on the walls of the 38°05'N fracture zone which may have experienced different alteration conditions. Serpentine, smectite and chlorite, and amphiboles and talc will be discussed separately. The deduced formation temperatures may be related to a sequence of alteration at one location or to differing conditions at several locations.

Of the three **serpentine** polymorphs, chrysotile is considered the low-P, low-T phase based on experimental data and field observations, whereas lizardite is the high-P and low-T mineral, and antigorite is the high-P, high-T mineral (Wicks & O'Hanley 1988). Evans et al. (1976) presented a stability diagram in the system $MgO-SiO_2-H_2O$ for the phases chrysotile, antigorite, brucite, talc, forsterite, and water (Fig. 9.8). According to these authors, antigorite is absent at temperatures <200°C, and coexists with chrysotile in the temperature range between 200 and 300°C. Chrysotile may be metastable at further increasing temperatures (Evans et al. 1976, O'Hanley et al. 1989). Based on oxygen isotope studies, serpentinization temperatures of 30-180°C were deduced for chrysotile-bearing mantle-derived ultramafic rocks in the equatorial Atlantic (Bonatti et al. 1984).

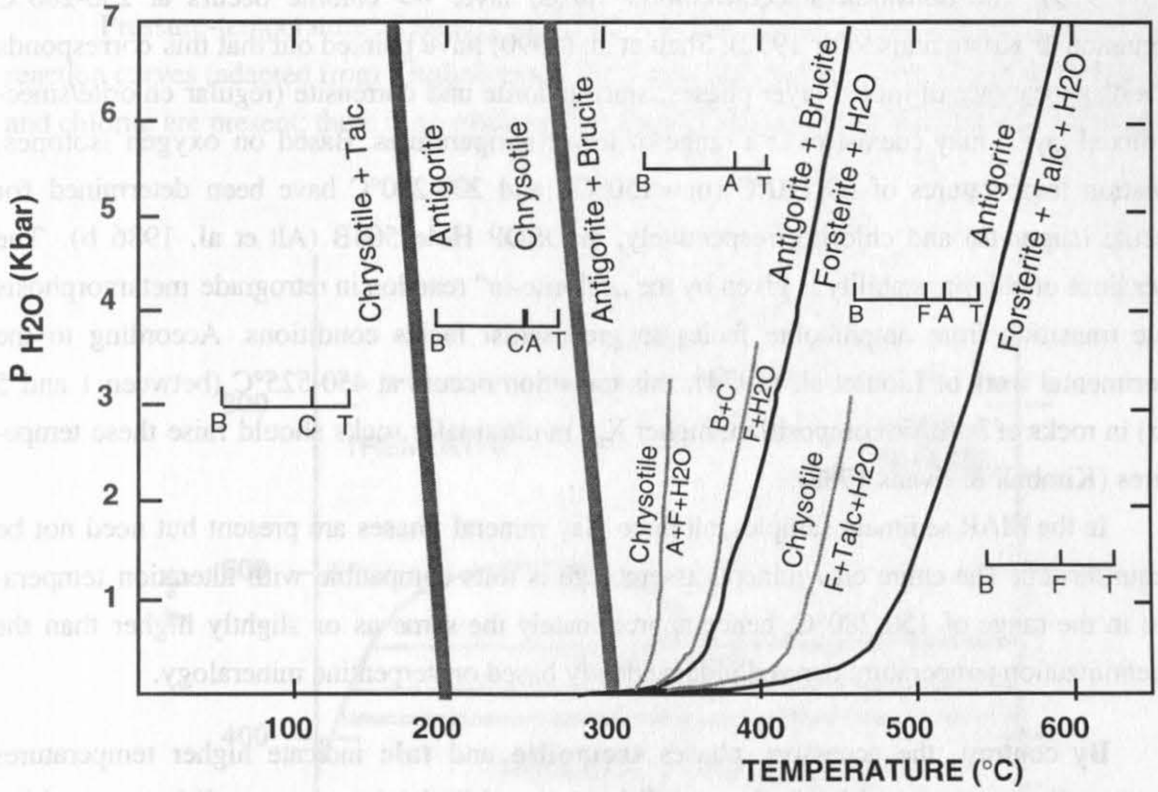

Fig. 9.8: Serpentine stability diagram (Evans et al. 1976). Black lines indicate stable, gray lines indicate metastable equilibria.

Based on TEM observations, chrysotile is the predominant serpentine phase in the 38°05'N samples, whereas antigorite and lizardite are probably absent. The phase equilibria cited above have been determined for prograde P-T-paths and are not necessarily valid under retrograde conditions (C. Mével, pers. comm. 1995). Therefore, exact reaction temperatures cannot be deduced; however, it can be assumed that serpentine was formed at comparatively low temperatures and pressures, possibly close to those at the sea floor.

The transition **smectite - smectite/chlorite mixed layer - chlorite** with increasing alteration temperatures has been observed in a variety of environments, including geothermal systems in Iceland (e.g. Tómasson & Kristmannsdóttir 1972, Kristmannsdóttir 1975, 1979, Sveinbjörnsdóttir 1992), Japan (Liou et al. 1985), and Mexico (Cathelineau & Izquierdo 1988), contact metamorphic rocks (Ferry et al. 1987, Inoue & Utada 1991), ophiolites (e.g. California Coast Range - Evarts & Schiffman 1983, Bettison & Schiffman 1988), and oceanic metabasalts (DSDP Hole 504 B - Alt et al. 1986 a, Shau & Peacor 1992, Gillis & Thompson 1993). Reaction temperatures are best constrained in active geothermal fields, but since fluid compositions might be different due to influence of meteoric water, and a variety of host rock compositions (including basalts, andesites and rhyolites) is involved, resulting mineral assemblages may not be directly comparable. The transition smectite --> smectite/chlorite mixed layer (+ chlorite) occurs at 150°C in the Newberry caldera, Oregon (Keith & Bargar 1988), and at 200°C in Icelandic geothermal fields (Tómasson & Kristmannsdóttir 1972, Kristmannsdóttir 1975, 1979). The transition smectite/chlorite mixed layer --> chlorite occurs at 230-280°C (Tómasson & Kristmannsdóttir 1972). Shau et al. (1990) have pointed out that this corresponds to the disappearance of mixed layer phases, since chlorite and corrensite (regular chlorite/smectite mixed layer) may coexist over a range of lower temperatures. Based on oxygen isotopes, formation temperatures of 60-110°C (or <150°C), and 200-250°C have been determined for smectite (saponite) and chlorite, respectively, in DSDP Hole 504B (Alt et al. 1986 b). The upper limit of chlorite stability is given by the „chlorite-in" reaction in retrograde metamorphosis at the transition from amphibolite facies to greenschist facies conditions. According to the experimental work of Liou et al. (1974), this transition occurs at 450-525°C (between 1 and 5 kbar) in rocks of *basaltic* composition; higher X_{Mg} in ultramafic rocks should raise these temperatures (Kimball & Evans 1988).

In the MAR sediment samples, all three clay mineral phases are present but need not be in equilibrium. The entire clay mineral assemblage is thus compatible with alteration temperatures in the range of 150-280°C, hence approximately the same as or slightly higher than the serpentinization temperature derived independently based on serpentine mineralogy.

By contrast, the accessory phases **tremolite** and **talc** indicate higher temperatures corresponding to **greenschist-facies conditions**. Amphiboles have a tremolitic composition in greenschist facies conditions. Unlike in metabasaltic and aluminous rocks, their composition remains close to the tremolite end member until conditions high in the amphibolite facies in ultramafic rocks (Evans 1982, Jenkins 1983). Between 450°C and 600°C (below the hornblende solvus in Fig. 9.8), two amphiboles with distinctly different Al contents coexist with each other; tremolite + olivine are stable until 810°C. The thermal stability of calcic amphiboles further increases with increasing Al content and increasing Na (+K) in A sites. Hence amphiboles are progressively enriched in pargasite (nomenclature after Leake 1978) with increasing metamorphic grade (Evans 1982, Jenkins 1983).

Talc has been synthesized experimentally only at temperatures >500°C (Mottl & Holland 1978). It remains stable over a wide metamorphic range of PT conditions (Evans & Guggenheim 1988). The equilibrium talc - chrysotile depends on the silica molality in solution, with talc occurring at higher silica activities (Hemley et al. 1977 a, b). In retrograde alteration, talc is involved in the following reactions (Kimball et al. 1985):

3 OPX + SiO_2 + H_2O --> Talc
T = 550 - 800°C (depending on pressure)
5 OPX + H_2O --> Olivine + Talc
T = 500 - 725°C
6 Olivine + Talc + 9 H_2O --> 5 SERP
T = 350 - 600°C (depending on pressure and serpentine type involved)
Talc + H_2O --> SERP + 2 SiO_2
T < 350°C (down to 150°C at 1 kbar)

Pressure-temperature diagrams of Figs. 9.9 and 9.10 show pertinent experimental reaction curves (adapted from Kimball et al. 1985 and Kimball & Evans 1988). Only tremolite and chlorite are present; there is no evidence for coexisting amphibole with higher Al content.

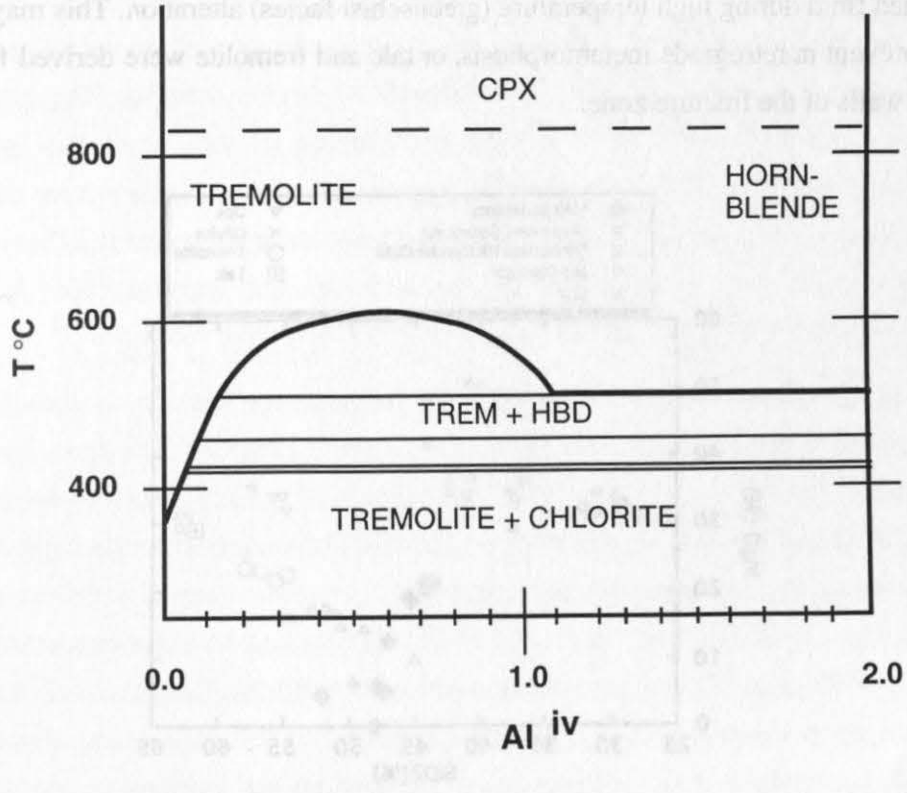

Fig. 9.9: Schematic actinolite-hornblende solvus, after Robinson et al. (1981) [Figure adapted from Kimball & Evans 1988]. In the 38°05'N samples, tremolite and chlorite are present, indicating temperatures < 450°C (greenschist facies conditions).

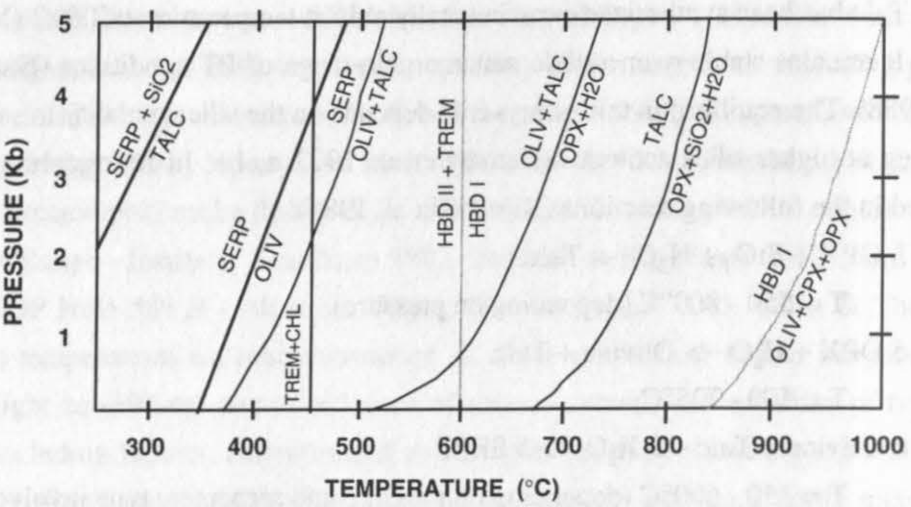

PRESSURE (Kb)
5
4
3
2
1
300
400
500
600
700
800
900
1000
TEMPERATURE (°C)
SERP SiO2
TALC
SERP
OLIV+TALC
SERP
OLIV
TREM+CHL
HBD II + TREM
HBD I
OLIV+TALC
OPX+H2O
TALC
OPX+SiO2+H2O
HBD I
OLIV+CPX+OPX

Fig. 9.10: Pressure-temperature diagram showing experimental reaction curves for alteration of ultramafic rocks (adapted from Kimball et al. 1985). Black lines indicate reactions discussed in text.

Accordingly, alteration temperatures < 450°C (greenschist facies conditions) can be deduced based on this mineral assemblage. While talc remains stable over a wide temperature range (Fig. 9.10), its presence is consistent with this interpretation. The elevated SiO_2-contents of talc and tremolite, compared to the bulk rock composition (Fig. 9.11), suggest the presence of a SiO_2-enriched fluid during high temperature (greenschist facies) alteration. This may correspond to an earlier event in retrograde metamorphosis, or talc and tremolite were derived from another area on the walls of the fracture zone.

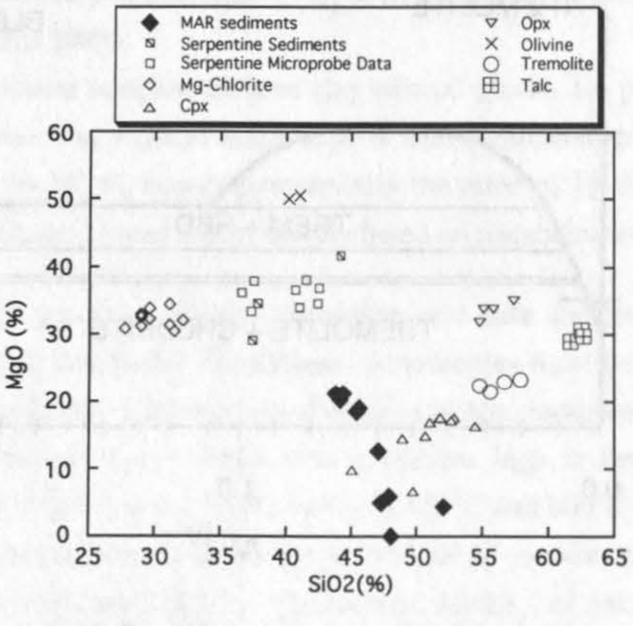

Fig. 11: SiO2 and MgO content of serpentine sediments and primary and alteration phases. Note the high SiO_2 content of greenschist facies minerals tremolite and talc, suggesting the presence of a SiO_2-enriched fluid during higher-temperature alteration.

9.5 Conclusions

The allochthonous sedimentary serpentine layer was derived from alteration of ultramafic rocks, it could represent a low-temperature hydrothermal deposit associated with a fault that may occur in upper-mantle rocks exposed on the walls of the fracture zone. While ultramafic rocks have not been observed in the study area, this rock type is fairly common in fracture zones at slow-spreading ridges such as the MAR. Cr/Ni-ratios of bulk sediment suggest an olivine-enriched protolith, in agreement with the results of petrologic studies of peridotites at the Mid-Atlantic Ridge. The high olivine content of peridotites has been ascribed to an enhanced degree of partial melting, due to the proximity of the Azores hot spot.

Since chrysotile is the dominant, if not only, serpentine prototype present, serpentinization took place at temperatures < 200°C. The same or slightly higher temperatures have been deduced for formation of smectite/chlorite mixed layer phases and chlorite, although with a larger uncertainty. By contrast, the presence of tremolite and talc indicates greenschist-facies conditions, which is compatible with alteration at higher temperatures and involving a SiO_2-enriched fluid. If retrograde metamorphosis was occurring, this event should have taken place prior to serpentine formation.

10. Summary and general conclusions

The objective of the GEOFAR cruise of RV Le Noroit was to investigate temporal and spatial variability of hydrothermal input in pelagic sediments at the Mid-Atlantic Ridge south of the Azores (37-39°N), in the vicinity of the recently discovered *Lucky Strike* and *Menez Gwen* hydrothermal fields. Four gravity cores from the area were selected for this study which, according to visual core descriptions, seemed to contain the most complete and undisturbed sediment record. A detailed chronostratigraphy was established based on oxygen isotopes of planktonic and benthic foraminifera and, in two cores, absolute ^{14}C ages obtained by accelerator mass spectrometry (AMS). Various geochemical and mineralogical analyses were performed on samples from these cores containing distal pelagic sediments, and on proximal sediments from the flanks of the *Lucky Strike* seamount.

Sediments are dominantly carbonate-rich pelagic oozes. The nature of the $\delta^{18}O$ records indicates that sedimentation was continuous and was not disturbed by major turbidites or hiatuses. Thus, the selected cores should provide a reliable record of sedimentary fluxes during the last 30,000 to 80,000 years. However, very high sedimentation rates in one core at the 38°05'N fracture zone can be ascribed to sediment ponding in a restricted basin, probably including significant lateral sediment supply.

Multivariate statistical analysis of geochemical data demonstrated that volcanic, ultramafic, detrital and hydrothermal sediment sources are present in addition to biogenic carbonate, which dominates the chemical composition of most samples. The composition of volcaniclastic sediments could be related to the influence of the Azores hot spot. Detritus comprises both a basic component which was presumably derived locally from the ridge axis and/or the Azores Islands, and a continentally-derived acidic component. The hydrothermal sediment source includes metals derived from hydrothermal solutions (Fe, Mn, Cu) and elements scavenged from the water column by hydrothermal oxyhydroxides (P, V, As).

Metal accumulation rates are significantly elevated compared to values from abyssal plains remote from the ridge axis, and fall in the range of literature data from hydrothermally influenced environments such as the East Pacific Rise and the Lau back-arc basin. While the downcore distribution of metals was obviously modified by early diagenetic processes, time-integrated average fluxes thus clearly indicate continuous hydrothermal influence in the study area at least down to 55,000 years B.P. . Selective leaching and Mössbauer spectroscopy show the presence of Fe- and Mn-oxide phases possibly derived from hydrothermal particle plumes and mobile in porewater solution during early diagenesis. Selective leaching also indicates that most (60-100%) of total iron is contained in a residual phase and could have been derived from volcaniclastic and/or detrital sources. On the other hand, manganese was dominantly derived from non-detrital sources and is associated either with oxide or with carbonate phases.

The distribution of hydrothermal factor scores and the spatial variability of metal accumulation rates suggest maximum hydrothermal influence at 37°N, south of the *Lucky Strike* vent field, which may also include contributions from other hydrothermal sites suspected south of the study area based on physical and chemical anomalies in the water column. Hydrothermal input at the other sites was possibly also derived from the *Lucky Strike* plume, the relative amount of this contribution could have been fluctuating due to variable bottom current patterns during the depositional history of sediments. Present-day metal input could also originate from the *Menez Gwen* field. However, phase-separated and metal-depleted fluids are emitted at this vent site due to its shallow water depth (840 m), which might not leave a chemical imprint in pelagic sediments.

While both the *Lucky Strike* and *Menez Gwen* fields contain abundant barite, barite dispersal in hydrothermal particle plumes should be limited by its high density. A minor contribution of plume-derived fine-grained sulfides and possibly sulfates in distal sediments is suggested by the presence of sphalerite, which was tentatively identified by X-ray diffraction in gravity concen-trates (>3.0 g/cm^3). However, the correlation between Ba and Si, Si/Al and organic carbon suggests primarily a biogenic origin of Ba in these sediments. On the other hand, Ba appears to be dominantly of hydrothermal origin in proximal sediments at the *Lucky Strike* seamount, where it is presumably derived from redeposited hydrothermal precipitates. This hydrothermal contribution apparently also includes sulfide phases, as indicated by concomitant enrichments in Fe, Cu and, to a lesser extent, Zn.

Ba-maxima in distal pelagic sediments are tentatively interpreted as indicators of productivity spikes. These spikes could result from a combination of cold surface water incursions, suggested by planktonic $\delta^{18}O$ maxima and/or abundance maxima of the cold-water nannoplankton species *C. pelagicus*, and enhanced terrigenous input supplying additional nutrients to the low-productivity "blue ocean". The most conspicuous maxima, present throughout the study area, are coeval to Heinrich meltwater event 1, terrigenous input in these samples could be derived from distal fine-grained ice-rafted and/or from eolian sources.

An allochthonous sedimentary serpentine layer in the deepest part of a basin in the central area of the 38°05'N fracture zone was derived from alteration of ultramafic rocks. Cr/Ni-ratios of serpentine material suggest an olivine-enriched ultramafic protolith, in accord with previous petrologic studies of peridotites at the Mid-Atlantic Ridge. As chrysotile is the dominant, if not only, serpentine polytype present, serpentinization took place at temperatures <200°C. The same or slightly higher temperatures were deduced for formation of smectite/chlorite mixed layer phases and chlorite, albeit with a greater uncertainty. The accessory phases tremolite and talc indicate greenschist facies conditions, which could have occurred earlier during a history of retrograde metamorphosis. Alternatively, tremolite and talc were derived from another source area on the walls of the fracture zone. The predominance of chrysotile rather than lizardite or antigorite may indicate a low-temperature hydrothermal origin of serpentine, which would be compatible with the complete absence of magmatic precursor phases. A similar deposit was dredged at the 15°20'N fracture zone at the Mid-Atlantic Ridge at a fault scarp exposing harzburgites and dunites (H. Dick, pers. comm.).

In conclusion, **three distinct hydrothermal contributions** are present in sediments in the study area:

- **Fe- and Mn-oxyhydroxides** are derived from **hydrothermal particle plume fallout** in distal pelagic sediments. This contribution includes **elements scavenged from the water column (P, V, As).** The spatial distribution of hydrothermal tracers and metal accumulation rates suggests that oxyhydroxide fallout is primarily derived from plumes originating at the *Lucky Strike* vent field, and could include contributions from other presently undiscovered vent sites south of the study area. While diagenetic processes apparently modified the pattern of temporal variability of metal accumulation rates, average accumulation rates clearly indicate continuous hydrothermal influence in the study area at least down to 55,000 years B.P.
- **Barite and hydrothermal sulfides** (sphalerite ? pyrite ?) are presumably derived from **redeposition of hydrothermal precipitates at the *Lucky Strike* seamount** and probably also occur as a minor **fine-grained contribution from hydrothermal particle plumes** in distal sediments. However, Ba is dominantly of biogenic origin in distal pelagic sediments. Ba maxima, particularly during early Termination I, were tentatively interpreted in terms of productivity spikes.
- **Serpentine (chrysotile)** and associated phases (**smectite/chlorite, chlorite, talc, tremolite**) were derived from alteration of ultramafic rocks and may correspond to an **ultramafic-hosted, low-temperature hydrothermal deposit**. In the area of the present study, these phases occur locally at the 38°05'N fracture zone. As samples of very similar lithology and mineralogical composition were dredged at the 15°20'N fracture zone at the MAR (H. Dick, pers. comm.), chrysotile-bearing muds may represent a common form of hydrothermal deposits at slow-spreading ridges. While low- and high-temperature hydrothermal systems associated with ultramafic rocks were little investigated to date, they may account for a distinct, significant component of global hydrothermal fluxes.

Further studies could focus on

- detremination of the hydrothermal and/or biogenic origin of Ba in sediments in the study area by means of Sr-isotope analyses of barite separates, and higher-resolution sampling across Termination I in order to confirm the presence of deglacial productivity spikes in the subtropical North Atlantic coeval to Heinrich meltwater event 1. This could give clues on the impact of Heinrich events beyond the IRD depositional belt in the Atlantic Ocean from 40-55°N.
- detailed investigations of the walls of the 38°05'N fracture zone to identify the source area and sample the protolith of serpentine sediments and comparative studies of serpentine-bearing muds from 15°20'N. This might constrain the nature and global significance of hydrothermal activity associated with ultramafic rocks.

References:

Agrinier, P., C. Mével, and J. Girardeau (1988): Hydrothermal alteration of the peridotites cored at the ocean/continent boundary of the Iberian Margin: Petrologic and stable isotopic evidence. *In* Boillot, G., Winterer, E.L., et al., *Proc. ODP, Sci. Results*, **103**: College Station, TX (Ocean Drilling Program), 225-233.

---, R. Hékinian, D. Bideau, and M. Javoy (1995): O and H stable isotope compositions of oceanic crust and upper mantle rocks exposed in the Hess Deep near the Galapagos Triple Junction. *Earth Planet. Sci. Lett.*, **136**, 183-196.

Aller, R.C. (1980): Diagenetic processes near the sediment-water interface, Long Island Sound. II Fe and Mn. *Advances Geophys.*, **22**, 351-415.

Alt, J.C., J. Honnorez, C. Laverne, and R. Emmermann (1986 a): Hydrothermal alteration of a 1 km section through the upper oceanic crust, Deep Sea Drilling Project Hole 504B: Mineralogy, chemistry, and evolution of seawater-basalt interactions. *J. Geophys. Res.*, **91**, B10, 10309-10335.

----, K. Muehlenbachs, and J. Honnorez (1986 b): An oxygen isotope profile through the upper kilometer of the oceanic crust, DSDP Hole 504 B. *Earth Planet. Sci. Lett.*, **80**, 217-229.

Auffret, G.A., H.D. Needham, Y. Fouquet, H. Bougault, P. Cambon, R. Kerbrat, and C. Langmuir (1991): Hydrothermal and volcanoclastic deposits on top of a Mid-Atlantic Ridge seamount. *EOS Trans. AGU*, **72** (44), 470.

---, A. Boelaert, C. Vergnaud-Grazzini, C. Müller, and R. Kerbrat (1996): Identification of Heinrich Layers in core KS 01 North-Eastern Atlantic (46°N, 17°W), implications for their origin. *Mar. Geol.*, **131**, 5-20.

Bacon, M.P., and J.N. Rosholt (1982): Accumulation rates of Th-230, Pa-231, and some transition metals on the Bermuda Rise. *Geochim. Cosmochim. Acta*, **46**, 651-666.

Bailey, S.W. (1972): Determination of chlorite composition by X-ray spacings and intensity. *Clays Clay Min.*, **19**, 129-132.

---- (1988): Chlorites: structures and crystal chemistry. *In* Bailey, S.W. (Ed.): Hydrous phyllosilicates (exclusive of micas). *Reviews in Mineralogy*, **19**, 347-398.

Baker, E.T., and G.J. Massoth (1987): Characteristics of hydrothermal plumes from two vent fields on the Juan de Fuca Ridge, northeast Pacific Ocean. *Earth Planet. Sci. Lett.*, **85**, 59-73.

Bard, E., B. Hamelin, R.G. Fairbanks, and A. Zindler (1990): Calibration of the ^{14}C timescale over the past 30,000 years using mass spectrometric U-Th ages from Barbados corals. *Nature*, **345**, 405-410.

---, M. Arnold, R.G. Fairbanks, and B. Hamelin (1993): ^{230}Th-^{234}U and ^{14}C ages obtained by mass spectrometry on corals. *Radiocarbon*, **35**, 191-199.

Barrett, T.J., P.N. Taylor, and J. Lugowski (1987): Metalliferous sediments from DSDP Leg 92: the East Pacific Rise transect. *Geochim. Cosmochim. Acta*, **51**, 2241-2253.

Becker, B., and B. Kromer (1993): The continental tree-ring record - absolute chronology, ^{14}C calibration and climatic change at 11 ka, *Palaeogeogr. Palaeoclimatol. Palaeoecol.*, **103**, 67-72.

Berger, W.H., R.C. Finkel, J.S. Killingley, and V. Marchig (1983): Glacial-Holocene transition in deep-sea sediments: manganese-spike in the east-equatorial Pacific. *Nature*, **303**, 231-233.

Berner, R.A. (1973): Phosphate removal from sea water by adsorption on volcanogenic ferric oxides. *Earth Planet. Sci. Lett.*, **18**, 77-86.

Bettison, L.A., and Schiffman, P. (1988): Compositional and structural variations of phyllosilicates from thePoint Sal ophiolite, California. *Amer. Mineral.*, **73**, 62-76.

Bideau, D., R. Hébert, R. Hékinian, and M. Cannat (1991): Metamorphism of deep-seated rocks from the Garrett ultrafast transform (East Pacific Rise near 13°25'N). *J. Geophys. Res.*, **96**, B6, 10079-10099.

Bishop, J.K.B. (1988): The barite-opal-organic carbon association in oceanic particulate matter. *Nature*, **332**, 341-343.

Bohrmann, G. (1988): Zur Sedimentationsgeschichte von biogenem Opal im nördlichen Nordatlantik und dem Europäischen Nordmeer (DSDP/ODP-Bohrungen 408, 642, 643, 644, 646 und 647). *Ber. Sonderforschungsber. 313, Universität Kiel,* **9**, 1-221.

Bonatti, E. (1985): Punctiform initiation of seafloor spreading in the Red Sea during transition from a continental to an oceanic rift. *Nature*, **316**, 33-37.

---, D.E. Fisher, O. Joensuu, and H.S. Rydell (1971): Postdepositional mobility of some transition elements, phosphorus, uranium and thorium in deep sea sediments. *Geochim. Cosmochim. Acta*, **35**, 189-201.

----, J.R. Lawrence, and N. Morandi (1984): Serpentinization of oceanic peridotites: temperature dependence of mineralogy and boron content. *Earth Planet. Sci. Lett*, **70**, 88-94.

Bond, G., H. Heinrich, W. Broecker, L. Labeyrie, J. McManus, J. Andrews, S. Huon, R. Jantschik, S. Clasen, C. Simet, K. Tedesco, M. Klas, G. Bonani, and S. Ivy (1992): Evidence for massive discharges of icebergs into the North Atlantic Ocean during the last glacial period. *Nature*, **360**, 245-249.

---, W. Broecker, S. Johnsen, J. McManus, L. Labeyrie, J. Jouzel, and G. Bonani (1993): Correlations between climate records from North Atlantic sediments and Greenland ice. *Nature*, **365**, 143-147.

Bostrøm, K. (1973): The origin and fate of ferromanganoan active ridge sediments. *Stockholm Contrib. Geol.*, **27**(2), 1-143.

---, and M.N.A. Peterson (1966): Precipitates from hydrothermal exhalations at the east Pacific Rise. *Econ. Geol.*, **61**, 1258-1265.

---, and --- (1969): The origin of aluminum-poor ferromanganoan sediments in areas of high heat flow at the east Pacific Rise. *Mar. Geol.*, **7**, 427-447.

---, ---, O. Joensuu, and D.E. Fisher (1969): Aluminum-poor ferro-manganoan sediments on active ocean ridges. *J. Geophys. Res.*, **74**, 3261-3270.

---, ---, C. Moore, B. Boström, M. Dalziel, and A. Horowitz (1973): Geochemistry of barium in pelagic sediments. *Lithos*, **6**, 159-174.

Bougault, H., and M. Treuil (1980): Mid-Atlantic Ridge: zero age geochemical variations between Azores and 22°N. *Nature,* **286**, 209-212.

---, J.-L. Charlou, Y. Fouquet, H.D. Needham, N. Vaslet, P. Appriou, P.J. Baptiste, P.A. Rona, L. Dmitriev, and S. Silantiev (1993): Fast and slow spreading ridges: Structure and hydrothermal activity, ultramafic topographic highs, and CH_4 output. *J. Geophys. Res.*, **98**, B6, 9643-9651.

---, J. Radford Knoery, J.L. Charlou, H.D. Needham, P. Appriou, M. Aballéa, P. Jean-Baptiste, C.R. German, M. Miranda, and C.H. Langmuir (1996): MARFLUX/ATJ. Hydrothermal activity along the Mid-Atlantic Ridge axis, in the area of the Azores Triple Junction. Mn, CH_4 plumes from dynamic hydrocasts. FARA-IR Mid-Atlantic Ridge Symposium, *J. Conf. Abstracts*, **1**, 761-762.

Boyle, E.A., and L.D. Keigwin (1985/86): Comparison of Atlantic and Pacific paleochemical records for the last 215,000 years: changes in deep ocean circulation and chemical inventories. *Earth Planet. Sci. Lett.*, **76**, 135-150.

Brindley, G.W., and G. Brown (1984): Crystal structures of clay minerals and their X-ray identification. Mineralogical Society Monograph No. 5, London.

Broecker, W., G. Bond, M. Klas, E. Clark, and J. McManus (1992): Origin of the northern Atlantic's Heinrich events. *Climate Dynamics*, **6**, 265-273.

Brumsack, H.J. (1986): The inorganic geochemistry of Cretaceous black shales (DSDP Leg 41) in comparison to modern upwelling sediments from the Gulf of California. *In* Summerhayes, C.P., and N.J. Shackleton (eds.): North Atlantic Paleoceanography. *Geol. Soc. London Spec. Publ.,* **21**, 447-462.

Bryan, W.B., T. Juteau, et al. (1990): *Proc. ODP, Sci. Results*, **106/109**: College Station, TX (Ocean Drilling Program).

Buckley, D.E., and R.E. Cranston (1988): Early diagenesis in deep-sea turbidites: The imprint of paleo-oxidation zones. *Geochim. Cosmochim. Acta*, **52**, 2925-2939.

Büttner, W., and R. Saager (1982): Rapid determination of the chrysotile/lizardite ratios in asbestos-bearing serpentinites. *Tschermaks Min. Petr. Mitt.*, **30**, 177-187.

Burdige, D.J (1993): The biogeochemistry of manganese and iron reduction in marine sediments. *Earth Sci. Rev.*, **35**, 249-284.

---, and J.M. Gieskes (1983): A pore water/solid phase diagenetic model for manganese in marine sediments. *Am J. Sci.*, **283**, 29-47.

Campbell, A.C., M.R. Palmer, G.P. Klinkhammer, T.S. Bowers, J.M. Edmond, J.R. Lawrence, J.F. Casey, G. Thompson, S.E. Humphris, P. Rona, and J.A. Karson (1988): Chemistry of hot springs on the Mid-Atlantic Ridge: TAG and MARK sites. *Nature*, **335**, 514-519.

Cannat, M., and M. Seyler (1995): Transform tectonics, metamorphic plagioclase and amphibolitization in ultramafic rocks of the Vema transform fault (Atlantic Ocean). *Earth Planet. Sci. Lett.*, **133**, 283-298.

---, D. Bideau, and R. Hébert (1990): Plastic deformation and magmatic impregnation in serpentinized ultramafic rocks from the Garrett transform fault (East Pacific Rise). *Earth Planet. Sci. Lett.*, **101**, 216-232.

----, ---, and H. Bougault (1992): Serpentinized peridotites and gabbros in the Mid-Atlantic Ridge axial valley at 15°37'N and 16°52'N. *Earth Planet. Sci. Lett.*, **109**, 87-106.

----, J.A. Karson, et al. (1995): *Proc. ODP, Init. Rep.*, **153**: College Station, TX (Ocean Drilling Program).

Cathelineau, M., and Izquierdo, G. (1988): Temperature-composition relationships of authigenic micaceous minerals in the Los Azufres geothermal system. *Contrib. Mineral. Petrol.*, **100**, 418-428.

Chan, L.H., D.H. Drummond, J.M. Edmond, and B. Grant (1977): On the barium data from the Atlantic GEOSECS expedition. *Deep Sea Res.*, **24**, 613-649.

Charlou, J.L., H. Bougault, P. Appriou, T. Nelsen, and P. Rona (1991): Different TDM/CH_4 hydrothermal plume signatures: TAG site at 26°N and serpentinized ultrabasic diapir at 15°05'N on the Mid-Atlantic Ridge. *Geochim. Cosmochim. Acta*, **55**, 3209-3222.

Chester, R., and M.J. Hughes (1967): A chemical technique for the separation of ferro-manganese minerals, carbonate minerals and adsorbed trace elements from pelagic sediments. *Chem. Geol.*, **2**, 249-262.

Chiswell, B., G. Rauchle, and M. Pascoe (1990): Spectrophotometric methods for the determination of manganese. *Talanta*, **37**, 237-259.

Chow, T.J., and E.D. Goldberg (1960): On the marine geochemistry of barium. *Geochim. Cosmochim. Acta*, **20**, 192-198.

Church, T.M. (1979): Marine barite. *In* Burns, R.G. (ed.): Marine minerals. *Reviews in Mineralogy*, **6**, 175-209.

---, and K. Wolgemuth (1972): Marine barite saturation. *Earth Planet. Sci. Lett.*, **15**, 35-44.

Coale, K.H., C.S. Chin, G.J. Massoth, K.S. Johnson, and E.T. Baker (1991): *In situ* chemical mapping of dissolved iron and manganese in hydrothermal plumes. *Nature*, **352**, 325-328.

Colley, S., J. Thomson, T.R.S. Wilson, and N.C. Higgs (1984): Post-depositional migration of elements during diagenesis in brown clay and turbidite sequences in the North East Atlantic. *Geochim. Cosmochim. Acta*, **48**, 1223-1235.

Converse, D.R., H.D. Holland, and J.M. Edmond (1984): Flow rates in the axial hot springs on the east Pacific Rise (21°N): implications for the heat budget and the formation of massive sulfide deposits. *Earth Planet. Sci. Lett.*, **69**, 159-175.

Coppedge, M.L., and W.L. Balsam (1992): Organic carbon distribution in the North Atlantic Ocean during the last glacial maximum. *Mar. Geol.*, **105**, 37-50.

Corliss, B.H. (1985): Microhabitats of benthic foraminifera with deep-sea sediments. *Nature*, **314**, 435-438.

Corliss, J.B., J. Dymond, L.I. Gordon, J.M. Edmond, R.P. Von Herzen, K. Green, D. Williams, A. Bainbridge, K. Crane, and T.H. Van Andel (1979): Submarine thermal springs on the Galapagos Rift. *Science*, **203**, 1073-1083.

Cowen, J.P., G.J. Massoth, and E.T. Baker (1986): Bacterial scavenging of Mn and Fe in a mid- to far-field hydrothermal particle plume. *Nature*, **322**, 169-171.

---, ---, and R.A. Feely (1990): Scavenging rates of dissolved manganese in a hydrothermal vent plume. *Deep Sea Res.*, **37**, 1619-1637.

Cronan, D.S., R. Hodkinson, D.D. Harkness, S.A. Moorby, and G.P. Glasby (1986): Accumulation rates of hydrothermal metalliferous sediments in the Lau Basin. *Geo-Mar. Lett.*, **6**, 51-56.

Cross, W., J.P. Iddings, L.V. Pirsson, and H.S. Washington (1903): Quantitative classification of igneous rocks. University of Chicago Press.

Curry, W.B., R.C. Thunell, and S. Honjo (1983). Seasonal changes in the isotopic composition of planktonic foraminifera collected in Panama Basin sediment traps. *Earth Planet. Sci. Lett.*, **64**, 33-43.

Davies, G.R., M.J. Norry, D.C. Gerlach, and R.A. Cliff (1989): A combined chemical and Pb-Sr-Nd isotopic study of the Azores and Cape Verde hot spots: the geodynamic implications. *In*: Saunders, A.D., and M.J. Norry (eds.): Magmatism in the Ocean Basins, *Geol. Soc. London Spec. Publ.*, **42**, 231-255.

De Carlo, E.H., G.M. McMurtry, and H.-W. Yeh (1983): Geochemistry of hydrothermal deposits from Loihi submarine volcano, Hawaii. *Earth Planet. Sci. Lett.*, **66**, 438-449.

Deer, W.A., R.A. Howie, and J. Zussman (1992): An introduction to the rock-forming minerals. Longman Scientific & Technical, Harlow, Essex, 2nd Ed. 1992.

Dehairs, F., R. Chesselet, and J. Jedwab (1980): Discrete suspended particles of barite and the barium cycle in the ocean. *Earth Planet. Sci. Lett.*, **49**, 528-550.

---, L. Goeyens, N. Stroobants, P. Bernard, C. Goyet, A. Poisson, and R. Chesselet (1990): On suspended barite and the oxygen minimum in the Southern Ocean. *Global Biogeochem. Cycles*, **4**, 85-102.

Detrick, R.S., H.D. Needham., and V. Renard (1995): Gravity anomalies and crustal thickness variations along the Mid-Atlantic Ridge between 33°N and 40°N. *J. Geophys. Res.*, **100**, B3, 3767-3787.

Deuser, W.G., E.H. Ross, C. Hemleben, and M. Spindler (1981): Seasonal changes in species composition, numbers, mass, size, and isotopic composition of planktonic foraminifera settling into the deep Sargasso Sea. *Palaeogeogr. Palaeoclimatol. Palaeoecol.*, **33**, 103-127.

Dhakar, S.P., and D.J. Burdige (1996): A coupled, non-linear, steady state model for early diagenetic processes in pelagic sediments. *Am. J. Sci.*, **296**, 296-330.

Dick, H.J.B., R.L. Fisher, and W.B. Bryan (1984): Mineralogic variability of the uppermost mantle along mid-ocean ridges. *Earth Planet. Sci. Lett.*, **69**, 88-106.

Dickson, D.P.E., and F.J. Berry (eds.) (1986): Moessbauer spectroscopy. Cambridge Univ. Press, 274 pp.

Drodt, M. (1996): Mössbauerspektroskopische Untersuchungen an Tiefseesedimenten aus dem Peru-Becken: Unterscheidung individueller Eisenmineralphasen. Diss. Med. Univ. Lübeck, *in prep.*

Duplessy, J.C., N.J. Shackleton, R.G. Fairbanks, L. Labeyrie, D. Oppo, and N. Kallel (1988): Deepwater source variations during the last climatic cycle and their impact on the global deepwater circulation, *Paleoceanogr.*, **3**, 343-360.

Dymond, J. (1981): Geochemistry of Nazca plate surface sediments: An evaluation of hydrothermal, biogenic, detrital, and hydrogenous sources. *In* Kulm, L.D., et al., eds., Nazca plate: Crustal formation and Andean convergence. *Geol. Soc. Am. Mem.*, **154**, 133-173.

---, and S. Roth (1988): Plume dispersed hydrothermal particles: A time-series record of settling flux from the Endeavour Ridge using moored sensors. *Geochim. Cosmochim. Acta*, **52**, 2525-2536.

---, E. Suess, and M. Lyle (1992): Barium in deep-sea sediment: A geochemical proxy for paleoproductivity. *Paleoceanogr.*, **7**, 163-181.

Eckhardt, J.-D. (1992): Geochemische Untersuchungen an jungen Sedimenten von der Galapagos-Mikroplatte: hydrothermale und stratigraphisch signifikante Signale. *Karlsruher Geochem. Hefte*, **3**, 1-157.

Edmond, J.M. (1992): Himalayan tectonics, weathering processes, and the strontium isotopic record in marine limestones. *Science*, **258**, 1594-1597.

---, C. Measures, R. McDuff, L.H. Chan, R. Collier, B. Grant, L.I. Gordon, and J.B. Corliss (1979): Ridge crest hydrothermal activity and the balances of major and minor elements in the ocean: The Galapagos data. *Earth Planet. Sci. Lett.*, **46**, 1-18.

---, K.L. Von Damm, R.E. McDuff, and C.I. Measures (1982): Chemistry of hot springs on the East Pacific Rise and their effluent dispersal. *Nature*, **297**, 187-191.

Edmond, J.M., A.C. Campbell, M.R. Palmer, G.P. Klinkhammer, C.R. German, H.N. Edmonds, H. Elderfield, G. Thompson, and P.A. Rona (1995): Time series studies of vent fluids from the TAG and MARK sites (1986, 1990) Mid-Atlantic Ridge: a new solution chemistry model and a mechanism for Cu/Zn zonation in massive sulphide orebodies. *In* Parson, L.M., C.L. Walker, and D.R. Dixon (eds.): Hydrothermal Vents and Processes. *Geol. Soc. London Spec. Publ.*, **87**, 77-86.

Evans, B.J., R.G. Johnson, F.E. Fenftle, G.B. Cecil, and F. Dulong (1992): The Fe^{57} Mössbauer parameters of pyrite and marcasite with different provenances. *Geochim. Cosmochim. Acta*, **46**, 761-775.

Evans, B.W. (1982): Amphiboles in metamorphosed ultramafic rocks. *In* Veblen, D.R., and P.H. Ribbe (eds.): Amphiboles: Petrology and experimental phase relations. *Reviews in Mineralogy*, **9B**, 98-113.

----, and S. Guggenheim (1988): Talc, pyrophyllite, and related minerals. *In* Bailey, S.W. (Ed.): Hydrous phyllosilicates (exclusive of micas). *Reviews in Mineralogy*, **19**, 225-280.

---, W. Johannes, H. Oterdoom, and V. Trommsdorff (1976): Stability of chrysotile and antigorite in the serpentinite multisystem. *Schweiz. Mineral. Petrogr. Mitt.*, **56**, 79-93.

Evarts, R.C., and Schiffman, P. (1983): Submarine hydrothermal metamorphism of the Del Puerto Ophiolite, California. *Amer. J. Sci.,* **283**, 289-341.

Fairbanks, R.G., P.H. Wiebe, and A.W.H. Bé (1980): Vertical distribution and isotopic composition of living planktonic foraminifera in the western North Atlantic. *Science*, **207**, 61-63.

---, M. Sverdlove, R. Free, P.H. Wiebe, and A.W.H. Bé (1982): Vertical distribution and isotopic fractionation of living planktonic foraminifera from the Panama Basin. *Nature*, **298**, 841-844.

Feely, R.A., M. Lewison, G.J. Massoth, G. Robert-Baldo, J.W. Lavelle, R.H. Byrne, K.L. Von Damm, and H.C. Curl Jr. (1987): Composition and dissolution of black smoker particulates from active vents on the Juan de Fuca Ridge. *J. Geophys. Res.*, **92**, B11, 11347-11363.

---, T.L. Geiselman, E.T. Baker, G.J. Massoth, and S.R. Hammond (1990): Distribution and composition of hydrothermal plume particles from the ASHES vent field at Axial Volcano, Juan de Fuca Ridge. *J. Geophys. Res.*, **95**, B8, 12855-12873.

---, G.J. Massoth, E.T. Baker, G.T. Lebon, and T.L. Geiselman (1992): Tracking the dispersal of hydrothermal plumes from the Juan de Fuca Ridge using suspended matter composition. *J. Geophys. Res.*, **91**, B3, 3457-3468.

---, J.F. Gendron, E.T. Baker, and G.T. Lebon (1994): Hydrothermal plumes along the East Pacific Rise, 8°40' to 11°50'N: Particle distribution and composition. *Earth Planet. Sci. Lett.,* **128**, 19-36.

Fernex, F., G. Février, J. Bénaim, and A. Arnoux (1992): Copper, lead and zinc trapping in Mediterranean deep-sea sediments: probable coprecipitation with Mn and Fe. *Chem. Geol.,* **98**, 293-306.

Ferry, J.M., Mutti, L.J., and Zuccala, G.J. (1987): Contact metamorphism/hydrothermal alteration of Tertiary basalts from the Isle of Skye, northwest Scotland. *Contrib. Mineral. Petrol.*, **95** , 166-181.

Finney, B.P., M.W. Lyle, and G.R. Heath (1988): Sedimentation at MANOP Site H (Eastern equatorial Pacific) over the past 400,000 years: Climatically induced redox variations and their effects on transition metal cycling. *Paleoceanogr.*, **3**, 169-189.

Fitzgerald, R.A., G.V. Winters, and D.E. Buckley (1987): Evaluation of a sequential leach procedure for the determination of metal partitioning in deep sea sediments. Geol. Survey of Canada, Open File Report 1701, 21 pp. .

Fornari, D.J., and R.W. Embley (1995): Tectonic and volcanic controls on hydrothermal processes at the mid-ocean ridge: An overview based on near-bottom and submersible studies. *In* Humphris, S.E., R.A. Zierenberg, L.S. Mullineaux, and R.E. Thomson (eds.): Seafloor hydrothermal systems: Physical, chemical, biological, and geological interactions. *Geophysical Monogr. Ser.,* **91**, 1-46.

Foster, M.D. (1962): Interpretation of the composition and a classification of the chlorites. U.S. Geol. Survey Prof. Paper 414-A, 33 pp. .

Fouquet, Y., U. Von Stackelberg, J.P. Charlou, J.P. Donval, J. Erzinger, J.P. Foucher, P. Herzig, R. Mühe, S. Soakai, M. Wiedicke, and H. Whitechurch (1991 a): Hydrothermal activity and metallogenesis in the Lau Basin. *Nature*, **349**, 778-781.

---, ---, ---, ---, J.P. Foucher, J. Erzinger, P. Herzig, R. Mühe, M. Wiedicke, S. Soakai, and H. Whitechurch (1991 b): Hydrothermal activity in the Lau back-arc basin: Sulfides and water chemistry. *Geology*, **19**, 303-306.

---, J.-L. Charlou, I. Costa, J.-P. Donval, J. Radford-Knoery, H. Pellé, H. Ondréas, N. Lourenço, M. Ségonzac, and M. K. Tivey (1994): A detailed study of the Lucky Strike hydrothermal site and discovery of a new hydrothermal site: Menez Gwen: Preliminary results of the DIVA 1 Cruise (5-29 May, 1994). *InterRidge News*, **3**(2), 14-17.

---, H. Ondréas, J.-L. Charlou, J.-P. Donval, J. Radford-Knoery, I. Costa, N. Lourenço, and M.K. Tivey (1995): Atlantic lava lakes and hot vents. *Nature*, **377**, 201.

---, P. Murphy, M.K. Tivey, K. Henry, F. Barriga, I. Costa, P. Cambon, H. Bougault, C. Langmuir, D. Prieur, P. Rona, S. Krasnov, and I. Poroshina (1996): Comparison of sulfide mineralisation related to slow spreading ridges with high magmatic budget (Lucky Strike and Menez Gwen sites) and low magmatic budget (15°N area). FARA-IR Mid-Atlantic Ridge Symposium, *J. Conf. Abstracts*, **1**, 789-790.

Francheteau, J., R. Armijo, J.L. Cheminée, R. Hékinian, P. Lonsdale, and N. Blum (1990): 1 Ma East Pacific Rise oceanic crust and uppermost mantle exposed by rifting in Hess Deep (equatorial Pacific Ocean). *Earth Planet. Sci. Lett.*, **101**, 281-295.

Francis, T.G. (1981): Serpentinization faults and their role in the tectonics of slow spreading ridges. *J. Geophys. Res.*, **86**, B12, 11616-11622.

François, R., M.P. Bacon, and D.O. Suman (1990): Thorium 230 profiling in deep-sea sediments: High-resolution records of flux and dissolution of carbonate in the equatorial Atlantic during the last 24,000 years. *Paleoceanogr.*, **5**, 761-787.

---, S. Honjo, S.J. Manganini, and G.E. Ravizza (1995): Biogenic barium fluxes to the deep sea: Implications for paleoproductivity reconstructions. *Global Biogeochem. Cycles*, **9**, 289-303.

Frank, M., J.-D. Eckhardt, A. Eisenhauer, P.W. Kubik, B. Dittrich-Hannen, M. Segl, and A. Mangini (1994): Beryllium 10, thorium 230, and protactinium 231 in Galapagos microplate sediments: Implications of hydrothermal activity and paleoproductivity during the last 100,000 years. *Paleoceanogr.*, **9**, 559-578.

---, A. Eisenhauer, W.J. Bonn, P. Walter, H. Grobe, P.W. Kubik, B. Dittrich-Hannen, and A. Mangini (1995): Sediment redistribution versus paleoproductivity change: Weddell Sea margin sediment stratigraphy and biogenic particle flux of the last 250,000 years deduced from $^{230}Th_{ex}$, ^{10}Be and biogenic barium profiles. *Earth Planet. Sci. Lett.*, **136**, 559-573.

Froelich, P.N., M.L. Bender, and G.R. Heath (1977): Phosphorus accumulation rates in metalliferous sediments on the east Pacific Rise. *Earth Planet. Sci. Lett.*, **34**, 351-359.

---, G.P. Klinkhammer, M.L. Bender, N.A. Luedtke, G.R. Heath, D. Cullen, P. Dauphin, D. Hammond, B. Hartman, and V. Maynard (1979): Early oxidation of organic matter in pelagic sediments of the eastern equatorial Atlantic: suboxic diagenesis. *Geochim. Cosmochim. Acta*, **43**, 1075-1090.

Früh-Green, G.L., A. Plas, B. Grobéty, and C. Lécuyer (1995): Multi-stage hydrothermal alteration and antigorite serpentinisation of EPR shallow mantle at Hess Deep. *Terra Abstracts*, **7**, Abstr. Suppl. No. 1, 208.

Ganssen, G., and M. Sarnthein (1983): Stable-isotope composition of foraminifers: The surface and bottom water record of coastal upwelling. *In* Suess, E. and J. Thiede (eds.): Coastal upwelling. Its sediment record. NATO ASI Series, Plenum Press, New York, 99-121.

German, C.R., A.C. Campbell, and J.M. Edmond (1991): Hydrothermal scavenging at the Mid-Atlantic Ridge: Modification of trace element dissolved fluxes. *Earth Planet. Sci. Lett.*, **107**, 101-114.

---, N.C. Higgs, J. Thomson, R. Mills, H. Elderfield, J. Blusztajn, A.P. Fleer, and M.P. Bacon (1993): A geochemical study of metalliferous sediment from the TAG Hydrothermal Mound, 26°08'N, Mid-Atlantic Ridge. *J. Geophys. Res.*, **98**, B6, 9683-9692.

German, C.R., J. Briem, C. Chin, M. Danielsen, S. Holland, R. James, A. Jónsdóttir, E. Ludford, C. Moser, J. Ólafsson, M.R. Palmer, and M.D. Rudnicki (1994): Hydrothermal activity on the Reykjanes Ridge: the Steinahóll vent field at 63°06'N. *Earth Planet. Sci. Lett.*, **121**, 647-654.

---, E.T. Baker, and G. Klinkhammer (1995): Regional setting of hydrothermal activity. *In* Parson, L.M., Walker, C.L., and Dixon, D.R. (eds.): Hydrothermal vents and processes, *Geol. Soc. London Spec. Publ.*, **87**, 3-15.

---, L. M. Parson, and HEAT Scientific Team (1996): Hydrothermal exploration near the Azores Triple Junction: tectonic control of venting at slow-spreading ridges ? *Earth Planet. Sci. Lett.*, **138**, 93-104.

Gillis, K.M., and Thompson, G. (1993): Metabasalts from the Mid-Atlantic Ridge: new insights into hydrothermal systems in slow-spreading crust. *Contrib. Mineral. Petrol.*, **113**, 502-523.

Gingele, F. (1992): Zur klimaabhängigen Bildung biogener und terrigener Sediments und ihrer Veränderung durch die Frühdiagenese im zentralen und östlichen Südatlantik. *Ber. Fachber. Geowiss. Univ. Bremen*, **26**, 202 pp. .

---, and A. Dahmke (1994): Discrete barite particles and barium as tracers of paleoproductivity in South Atlantic sediments. *Paleoceanogr.*, **9**, 151-168.

---, and S. Kasten (1994): Solid-phase manganese in Southeast Atlantic sediments: Implications for the paleoenvironment. *Mar. Geol.*, **121**, 317-332.

Goldberg, E.D., and G. Arrhenius (1958): Chemistry of Pacific pelagic sediments. *Geochim. Cosmochim. Acta*, **13**, 153-212.

Gombos, A.M. Jr. (1984): Late Neogene diatoms and diatom oozes in the Central South Atlantic. *In* Hsü, K.J., LaBrecque, J.L., et al., *Init. Reps. DSDP*, **73**: Washington (U.S. Govt. Printing Office), 487-494.

Govindaraju, K. (1994): 1994 Compilation of working values and sample descriptions for 383 geostandards. *Geostandards Newsletter*, **18** (Spec. Issue), 1-158.

Graham, D.W., B.H. Corliss, M.L. Bender, and L.D. Keigwin (1981): Carbon and oxygen isotopic disequilibria of recent deep-sea benthic foraminifera. *Mar. Micropaleont.*, **6**, 483-497.

Grousset, F., C. Latouche, and M. Parra (1982): Late Quaternary sedimentation between Gibbs Fracture and the Greenland Basin: Mineralogical and geochemical data. *Mar. Geol.*, **47**, 303-330.

---, L. Labeyrie, J.A. Sinko, M. Cremer, G. Bond, J. Duprat, E. Cortijo, and S. Huon (1993): Patterns of ice-rafted detritus in the glacial North Atlantic (40-55°N). *Paleoceanogr.*, **8**, 175-192.

---, B. Thomas, and N. Maillet (1994): Etude minéralogique de quelques échantillons de surface de la mission GEOFAR 1993. Rapport interne IFREMER. Contrat no. 93-2-410506 DRO/GM.

Hartmann, M. (1979): Evidence for early diagenetic mobilization of trace metals from discolorations of pelagic sediments. *Chem. Geol.*, **26**, 277-293.

Haxel, C. (1987): Zur Anwendung der Mößbauer-Spektroskopie auf ausgewählte Mineralien und Fragestellungen zu deren Genese. *Heidelberger Geowiss. Abh.*, **9**, 268 pp. .

Heath, G.R., and J. Dymond (1977): Genesis and transformation of metalliferous sediments from the East Pacific Rise, Bauer Deep, and Central Basin, Northwest Nazca Plate. *Geol. Soc. Am. Bull.*, **88**, 723-733.

Hébert, R., A.C. Adamson, and S.C. Komor (1990): Metamorphic petrology of ODP Leg 109, Hole 670A serpentinized peridotites: Serpentinization processes at a slow spreading ridge environment. *In* Detrick, R., Honnorez, J., Bryan, W.B., Juteau, T., et al., *Proc. ODP, Sci. Results*, **106/109**: College Station, TX (Ocean Drilling Program), 103-115.

Hein, J.R., and D.W. Scholl (1978): Diagenesis and distribution of late Cenozoic volcanic sediment in the southern Bering Sea. *Geol. Soc. Am. Bull.*, **89**, 197-210.

Heinrich, H. (1988): Origin and consequences of cyclic ice-rafting in the Northeast Atlantic Ocean during the last 130,000 years. *Quat. Res.*, **29**, 142-152.

Hékinian, R., M. Février, F. Avedik, P. Cambon, J.L. Charlou, H.D. Needham, J. Raillard, J. Boulegue, L. Merlivat, A. Moinet, S. Manganini, and J. Lange (1983): East Pacific Rise near 13°N: Geology of new hydrothermal fields. *Science*, **219**, 1321-1324.

Hékinian, R., D. Bideau, M. Cannat, J. Francheteau, and R. Hébert (1992): Volcanic activity and crust-mantle exposure in the ultrafast Garrett transform fault near 13°28'S in the Pacific. *Earth Planet. Sci. Lett.*, **108**, 259-275.

---, ---, J. Francheteau, J.L. Cheminée, R. Armijo, P. Lonsdale, and N. Blum (1993): Petrology of the East Pacific Rise crust and upper mantle exposed in Hess Deep (Eastern Equatorial Pacific). *J. Geophys. Res.*, **98**, B5, 8069-8094.

Helm, R. (1984): Mineralogy and geochemistry of weathered serpentinites, Deep Sea Drilling Project Leg 84. *In* von Huene, R., Aubouin, J., et al., *Init. Repts. DSDP*, **84**: Washington (U.S. Govt. Printing Office), 595-607.

Hemley, J.J., J.W. Montoya, G.L. Christ, and P.B. Hostetler (1977a): Mineral equilibria in the MgO-SiO_2-H_2O system: I Talc-chrysotile-forsterite-brucite stability relations. *Am. J. Sci.*, **277**, 322-351.

----, ----, D.R. Shaw, and R.W. Luce (1977a): Mineral equilibria in the MgO-SiO_2-H_2O system: II Talc - antigorite - forsterite - anthophyllite - enstatite stability relations and some geologic implications in the system. *Am. J. Sci.*, **277**, 353-383.

Hodell, D.A., G.A. Mead, and P.A. Mueller (1990): Variation in the strontium isotopic composition of seawater (8 Ma to present): Implications for chemical weathering rates and dissolved fluxes to the oceans. *Chem. Geol.*, **80**, 291-307.

Hodkinson, R.A., and D.S. Cronan (1991): Geochemistry of recent hydrothermal sediments in relation to tectonic environment in the Lau Basin, southwest Pacific. *Mar. Geol.*, **98**, 353-366.

---, and --- (1994): Variability in the hydrothermal component of the sedimentary sequence in the Lau back-arc basin (Sites 834-839). *In* Hawkins, J., Parson, L., Allan, J., et al., *Proc. ODP, Sci. Results*, **135**: College Station, TX (Ocean Drilling Program), 75-86.

Hoffert, M., A. Perseil, R. Hékinian, P. Choukroune, H.D. Needham, J. Francheteau, and X. Le Pichon (1978): Hydrothermal deposits sampled by diving saucer in Transform Fault „A“ near 37°N on the Mid-Atlantic Ridge, Famous area. *Oceanol. Acta*, **1**, 73-86.

---, J.-L. Cheminée, P. Larqué, and A. Person (1987): Dépôt hydrothermal associé au volcanisme sous-marin „intraplaque“ océanique. Prélèvement effectué avec Cyana sur le volcan sous-marin actif de Teahitia (Polynesie francaise). *C.R. Acad. Sci.*, Serie 2, **304**, 829-832.

Humphris, S.E., M.K. Tivey, Y. Fouquet, and Lucky Strike Team (1993): Comparison of hydrothermal deposits at the Lucky Strike vent field with other mid-ocean ridge vent sites. *EOS Trans. AGU*, **74**, 100.

---, R.A. Zierenberg, L.S. Mullineaux, and R.E. Thomson (eds.) (1995): Seafloor hydrothermal systems: Physical, chemical, biological, and geological interactions. *Geophysical Monogr. Ser.*, **91**. American Geophysical Union, Washington, D.C. .

Imbrie, J., J.D. Hays, D.G. Martinson, A. McIntyre, A.C. Mix, J.J. Morley, N.G. Pisias, W.L. Prell, and N.J. Shackleton (1984): The orbital theory of Pleistocene climate: Support from a revised chronology of the marine $\delta^{18}O$ record. *In* Berger, A.L., et al. (eds.): Milankovitch and climate, Part I, 269-305. D. Reidel.

Inoue, A., and Utada, M. (1991): Smectite-to-chlorite transformation in thermally metamorphosed volcanoclastic rocks in the Kamikita area, northern Honshu, Japan. *Amer. Mineral.*, **76**, 628-640.

Jarvis, I., and N. Higgs (1987): Trace-element mobility during early diagenesis in distal turbidites: late Quaternary of the Madeira Abyssal Plain, N Atlantic. *In* Weaver, P.P.E., and J. Thomson (eds.): Geology and geochemistry of abyssal plains, *Geol. Soc. London Spec. Publ.*, **31**, 179-213.

Jenkins, D.M. (1983): Stability and composition relations of calcic amphiboles in ultramafic rocks. *Contrib. Mineral. Petrol.*, **83**, 375-384.

Jung, S.J.A. (1996): Wassermassenaustausch zwischen NE-Atlantik und Nordmeer während der letzten 300.000/80.000 Jahre im Abbild stabiler O- und C-Isotope. *Ber. Sonderforschungsber. 313, Universität Kiel*, **61**, 1-104.

Juteau, T., M. Cannat, and Y. Lagabrielle (1990): Serpentinized peridotites in the upper oceanic crust away from transform zones: A comparison of the results of previous DSDP and ODP Legs. *In* Detrick, R., Honnorez, J., Bryan, W.B., Juteau, T., et al., *Proc. ODP, Sci. Results*, **106/109**: College Station, TX (Ocean Drilling Program), 303-308.

Kadko, D. (1993): An assessment of the effect of chemical scavenging within submarine hydrothermal plumes upon ocean geochemistry. *Earth Planet. Sci. Lett.*, **120**, 361-374.

Kadko, D., N.D. Rosenberg, J.E. Lupton, R.W. Collier, and M.D. Lilley (1990): Chemical reaction rates and entrainment within the Endeavour Ridge hydrothermal plume. *Earth Planet. Sci. Lett.*, **99**, 315-335.

Karl, D.M., G.M. McMurtry, A. Malahoff, and M.O. Garcia (1988): Loihi Seamount, Hawaii: a mid-plate volcano with a distinctive hydrothermal system. *Nature*, **335**, 532-535.

Karson, J.A., and J.R. Brown (1988): Geologic setting of the Snake Pit hydrothermal site: An active vent field on the Mid-Atlantic Ridge. *Mar. Geophys. Res.*, **10**, 91-107.

---, G. Thompson, S.E. Humphris, J.M. Edmond, W.B. Bryan, J.R. Brown, A.T. Winters, R.A. Pockalny, J.F. Casey, A.C. Campbell, G. Klinkhammer, M.R. Palmer, R.J. Kinzler, and M.M. Sulanowska (1987): Along axis variations in seafloor spreading in the MARK area. *Nature*, **328**, 681-685.

Keith, T.E.C., and K. E. Bargar (1988): Petrology and hydrothermal mineralogy of U.S. Geological survey Newberry 2 drill core from Newberry caldera, Oregon. *J. Geophys. Res.*, **93**, B9, 10174-10190.

Kemp, A.E.S., and J.G. Baldauf (1993): Vast Neogene laminated diatom mat deposits from the eastern equatorial Pacific Ocean. *Nature*, **362**, 141-144.

---, ---, and R.B. Pearce (1995): Origins and paleoceanographic significance of laminated diatom ooze from the Eastern Equatorial Pacific Ocean. *In* Pisias, N.G., Mayer, L.A., Janecek, T.R., Palmer-Julson, A., and van Andel, T.H. (eds.): *Proc. ODP, Sci. Results*, **138**: College Station, TX (Ocean Drilling Program), 225-233.

Kennett, J.P. (1982): Marine Geology. Prentice-Hall, Inc., Eaglewood Cliffs, NJ, 813 pp..

Kiefer, T., F. Abrantes, M. Sarnthein, M. Weinelt, and L. Labeyrie (1995): Prominent productivity spikes in the subtropical North Atlantic parallel Heinrich meltwater events. 5th International Conference on Paleoceanography, Halifax, Abstract Volume, p.85.

Kimball, K.L. (1988): High-temperature hydrothermal alteration of ultramafic cumulates from the base of the sheeted dikes in the Josephine Ophiolite, NW California. *J. Geophys. Res.*, **93**, B5, 4675-4687.

---, and C.A. Evans (1988): Hydrothermal alteration of peridotite from the Galicia Margin, Iberian Peninsula. *In* Boillot, G., Winterer, E.L., et al., *Proc. ODP, Sci. Results*, **103**: College Station, TX (Ocean Drilling Program), 241-251.

----, F.S. Spear, and H.J.B. Dick (1985): High temperature alteration of abyssal ultramafics from the Islas Orcadas Fracture Zone, South Atlantic. *Contrib. Min. Petrol.*, **91**, 307-320.

Klinkhammer, G. P. (1980): Early diagenesis in sediments from the eastern equatorial Pacific, II. Pore water metal results. *Earth Planet. Sci. Lett.*, **49**, 81-101.

---, and A. Hudson (1986): Dispersal patterns for hydrothermal plumes in the South Pacific using manganese as a tracer. *Earth Planet. Sci. Lett.*, **79**, 241-249.

---, P.A. Rona, M. Greaves, and H. Elderfield (1985): Hydrothermal manganese plumes in the Mid-Atlantic Ridge rift valley. *Nature*, **314**, 727-731.

---, H. Elderfield, M. Greaves, P. Rona, and T. Nelsen (1986): Manganese geochemistry near high-temperature vents in the Mid-Atlantic Ridge rift valley. *Earth Planet. Sci. Lett.*, **80**, 230-240.

---, C.S. Chin, C. Wilson, and C.R. German (1995): Venting from the Mid-Atlantic Ridge at 37°17'N: the Lucky Strike hydrothermal site. *In* Parson, L.M., C.L. Walker, and D.R. Dixon (eds.): Hydrothermal Vents and Processes, *Geol. Soc. London Spec. Publ.*, **87**, 87-96.

König, I. (1990): ^{57}Fe-Mößbauer-Spektroskopie an jungen Sedimenten - Entwicklung einer Anwendungstechnik zur Bestimmung individueller Eisenbindungsformen. Diss. Univ. Hamburg, 132 pp..

Kristmannsdóttir, H. (1975): Hydrothermal alteration of basaltic rocks in Icelandic geothermal areas. Proc. 2nd U.N. Symposium on the development and use of geothermal resources, 1: 441-445. San Francisco 1975.

---- (1979): Alteration of basaltic rocks by hydrothermal activity at 100-300°C. Proc. Intern. Clay Conference, Amsterdam 1978, 359-367.

Lackschewitz, K.S. (1991): Sedimentationsprozesse am aktiven mittelatlantischen Kolbeinsey Rücken (nördlich von Island). *GEOMAR Rep.*, **9**, 1-133.

---, H.-J. Wallrabe-Adams, and D. Garbe-Schönberg (1994): Geochemistry of surface sediments from the mid-oceanic Kolbeinsey Ridge, north of Iceland. *Mar. Geol.*, **121**, 105-119.

Lagabrielle, Y., A.-M. Karpoff, and J. Cotten (1992): Mineralogical and geochemical analyses of sedimentary serpentinites from Conical Seamount (Hole 778 A): Implication for the evolution of serpentine seamounts. *In* Fryer, P., Pearce, J.A., Stokking, L.B., et al., *Proc. ODP, Sci. Results*, **125**: College Station, TX (Ocean Drilling Program), 325-342.

Lalou, C., G. Thompson, M. Arnold, E. Brichet, E. Druffel, and P.A. Rona (1990): Geochronology of TAG and Snakepit hydrothermal fields, Mid-Atlantic Ridge: witness to a long and complex hydrothermal history. *Earth Planet. Sci. Lett.*, **97**, 113-128.

---, J.-L. Reyss, E. Brichet, M. Arnold, G. Thompson, Y. Fouquet, and P.A. Rona (1993): New age data for Mid-Atlantic Ridge hydrothermal sites: TAG and Snakepit chronology revisited. *J. Geophys. Res.*, **98**, B6, 9705-9713.

---, ---, ---, P.A. Rona, and G. Thompson (1995): Hydrothermal activity on a 10^5-year scale at a slow-spreading ridge, TAG hydrothermal field, Mid-Atlantic Ridge 26°N. *J. Geophys. Res.*, **100**, B9, 17855-17862.

Langmuir, C., and Lucky Strike Team (1993): Geological setting and characteristics of the Lucky Strike vent field at 37°17'N on the Mid-Atlantic Ridge. *EOS Trans. AGU*, **74**, 99.

Lavelle, J.W., J.P. Cowen, and G.J. Massoth (1992): A model for the deposition of hydrothermal manganese near ridge crests. *J. Geophys. Res.*, **97**, C5, 7413-7427.

Leake, B.E. (1978): Nomenclature of amphiboles. *Can. Mineral.*, **16**, 501-520.

Leg 73 Scientific Party (1984): Site 520. *In* Hsü, K.J., LaBrecque, J.L., et al., Init. Reps. DSDP, **73**: Washington (U.S. Govt. Printing Office), 487-494.

Leinen, M. (1987): The origin of paleochemical signatures in North Pacific pelagic clays: Partitioning experiments. *Geochim. Cosmochim. Acta*, **51**, 305-319.

---, and N. Pisias (1984): An objective technique for determining end-member compositions and for partitioning sediments according to their sources. *Geochim. Cosmochim. Acta*, **48**, 47-62.

Linke, P., and G.F. Lutze (1993): Microhabitats preference of benthic foraminifera - A static concept or a dynamic adaptation to optimize food acquisition ? *Mar. Micropaleontol.*, **20**, 215-234.

Liou, J.G., S. Kuniyoshi, and K. Ito (1974): Experimental studies of the phase relations between greenschist and amphibolite in a basaltic system. *Am. J. Sci.*, **274**, 613-632.

----, Y. Seki, R.N. Guillemette, and H. Saki (1985): Composition and paragenesis of secondary minerals in the Onikobe geothermal system, Japan. *Chem. Geol.*, **49**, 1-20.

Little, S.A., K.D. Stolzenbach, and R.P. Von Herzen (1987): Measurements of plume flow from a hydrothermal vent field. *J. Geophys. Res.*, **92**, B3, 2587-2596.

Lotter, A.F., B. Ammann, J. Beer, I. Hajdas, and M. Sturm (1992): A step towards an absolute time-scale for the Late-Glacial: Annually laminated sediments from Soppensee (Switzerland). *In* Bard, E., and W.S. Broecker (eds.): The last deglaciation: Absolute and radiocarbon chronologies. NATO ASI Ser., **I2**, Springer-Verlag, Berlin, 45-68.

Lupton, J.E., and H. Craig (1981): A major ^{3}He source on the East Pacific Rise. *Science*, **214**, 13-18.

---, J.R. Delaney, H.P. Johnson, and M.K. Tivey (1985): Entrainment and vertical transport of deep-ocean water by buoyant hydrothermal plumes. *Nature*, **316**, 621-623.

Lutze, G.F., and H. Thiel (1989): Epibenthic foraminifera from elevated microhabitats (*Cibicidoides wuellerstorfi, Planulina ariminensis*). *J. Foraminiferal Res.*, **19**, 153-158.

Lyle, M.W., R.M. Owen, and M. Leinen (1986): History of hydrothermal sedimentation at the East Pacific Rise, 19°S. *In* Leinen, M., Rea, D.K., et al. (eds.): *Init. Rep. DSDP*, **92**, 585-596. Washington, D.C., U.S. Govt. Printing Office.

---, M. Leinen, R.M. Owen, and D.K. Rea (1987): Late Tertiary history of hydrothermal deposition at the East Pacific Rise, 19°S: correlation to volcano-tectonic events. *Geophys. Res. Lett.*, **14**, 595-598.

Lynn, D.C., and E. Bonatti (1965): Mobility of manganese in diagenesis of deep-sea sediments. *Mar. Geol.*, **3**, 457-474.

Mandernack, K.W., and B.M. Tebo (1993): Manganese scavenging and oxidation at hydrothermal vents and in vent plumes. *Geochim. Cosmochim. Acta*, **57**, 3907-3923.

Mangini, A., A. Eisenhauer, and P. Walter (1990): Response of manganese in the ocean to the climatic cycles of the Quaternary. *Paleoceanogr.*, **5**, 811-821.

Mangini, A., H.-J. Rutsch, M. Frank, A. Eisenhauer, and J.-D. Eckhardt (1994): Is there a relationship between atmospheric CO2 and manganese in the ocean ? *In* Zahn, R., et al. (eds.): Carbon cycling in the glacial ocean: Constraints on the ocean's role in Global Change, *NATO ASI Ser.* I, **17**, Springer, Berlin, 87-104.

Marchig, V., and H. Gundlach (1982): Iron-rich metalliferous sediments on the east Pacific Rise: prototype of undifferentiated metalliferous sediments on divergent plate boundaries. *Earth Planet. Sci. Lett.*, **58**, 361-382.

Marchig, V., J. Erzinger, and H. Rösch (1987): Sediments from a hydrothermal field in the central valley of the Galapagos Rift spreading center. *Mar. Geol.*, **76**, 243-251.

Marchig, V., and J. Erzinger (1984): Chemical composition of Pacific sediments near 20°S: Changes with increasing distance from the East Pacific Rise. *In* Leinen, M., Rea, D.K., et al., *Init. Rep. DSDP*, **92**: Washington (US Govt. Printing Office), 371-381.

---, H. Gundlach, P. Möller, and F. Schley (1982): Some geochemical indicators for discrimination between diagenetic and hydrothermal metalliferous sediments. *Mar. Geol.*, **50**, 241-256.

---, J. Erzinger, and P.-M. Heinze (1986): Sediment in the black smoker area of the East Pacific Rise (18.5°S). *Earth Planet. Sci. Lett.*, **79**, 93-106.

---, H. Gundlach, and W. Schmitz (1990): Geochemical studies on sediment cores from the North Fiji Basin. *Geol. Jb.*, **D92**, 189-208.

Martin, E.E., D.J. Macdougall, T. Herbert, A. Paytan, and M. Kastner (1995): Strontium and neodymium isotopic analysis of marine barite separates. *Geochim. Cosmochim. Acta*, **59**, 1353-1361.

Martinson, D.G., N.G. Pisias, J.D. Hays, J. Imbrie, T.C. Moore Jr., and N.J. Shackleton (1987): Age dating and the orbital theory of the ice ages: Development of a high resolution 0 to 300,000 year chronostratigraphy. *Quat. Res.*, **27**, 1-29.

Mazaud, A., C. Laj, E. Bard, M. Arnold, and E. Tric (1992): A geomagnetic calibration of the radiocarbon time scale. *In* Bard, E., and W.S. Broecker (eds.): The last deglaciation: Absolute and radiocarbon chronologies. NATO ASI Ser., **12**, Springer, Berlin, 163-169.

McArthur, J.M., and A.T. Osborn (1989): Manganese analysis by the formaldoxime method: Problems with iron interference. *Mar. Chem.*, **26**, 81-85.

McCorkle, D.C., L.D. Keigwin, B.H. Corliss, and S.R. Emerson (1990): The influence of microhabitats on the carbon isotopic composition of deep-sea benthic foraminifera. *Paleoceanogr.*, **5**, 161-185.

McMurtry, G.M., H.H. Veeh, and C. Moser (1981): Sediment accumulation rate patterns on the northwest Nazca Plate. *In* Kulm, L.D., et al. (eds.): Nazca Plate: Crustal formation and Andean convergence. *Geol. Soc. Am. Mem.*, **154**, 211-249.

---, E.H. De Carlo, and K.H. Kim (1991): Accumulation rates, chemical partitioning, and Q-mode factor analysis of metalliferous sediments from the North Fiji Basin. *Mar. Geol.*, **98**, 271-295.

---, ----, and --- (1994): Geochemistry of North Central North Fiji Basin sediments. *In* Kroenke, L.W., and J.V. Eade (eds.): Basin formation, ridge crest processes and metallogenesis in the North Fiji Basin. Circum-Pacific Council for Energy and Mineral Resources, Earth Sci. Ser., Vol. 15 (Springer-Verlag), 137-169.

Mével, C., M. Cannat, P. Gente, E. Marion, J.M. Auzende, and J.A. Karson (1991): Emplacement of deep crustal and mantle rocks on the west median valley wall of the MARK area (MAR, 23°N). *Tectonophysics*, **190**, 31-53.

Metz, S., J.H. Trefry, and T.A. Nelsen (1988): History and geochemistry of a metalliferous sediment core from the Mid-Atlantic Ridge at 26°N. *Geochim. Cosmochim. Acta*, **52**, 2369-2378.

Michael, P.J., and E. Bonatti (1985a): Peridotite composition from the North Atlantic: regional and tectonic variations and implications for partial melting. *Earth Planet. Sci. Lett.*, **73**, 91-104.

----, and ---- (1985b): Petrology of ultramafic rocks from Sites 556, 558, and 560 in the North Atlantic. *In* Bougault, H., Cande, S.C., et al., *Init. Repts. DSDP*, **82**: Washington (U.S. Govt. Printing Office), 523-528.

Millero, F.J., S. Sotolongo, and M. Izaguirre (1987): The oxidation kinetics of Fe(II) in seawater. *Geochim. Cosmochim. Acta*, **51**, 793-801.

Mills, R.A., and H. Elderfield (1995): Hydrothermal activity and the geochemistry of metalliferous sediment. *In* Humphris, S.E., R.A. Zierenberg, L.S. Mullineaux, and R.E. Thomson (eds.): Seafloor hydrothermal systems: Physical, chemical, biological, and geological interactions. *Geophysical Monogr. Ser.*, **91**, 392-407.

---, ---, and J. Thomson (1993): A dual origin for the hydrothermal component in a metalliferous sediment core from the Mid-Atlantic Ridge. *J. Geophys. Res.*, **98**, B6, 9671-9681.

Mix, A.C., and R.G. Fairbanks (1985): North Atlantic control of Pleistocene deep-ocean circulation. *Earth Planet. Sci. Lett.*, **73**, 231-243.

Moore, D.M., and R.C. Reynolds Jr. (1989): X-ray diffraction and the identification and analysis of clay minerals. Oxford University Press.

Mottl, M., and H.D. Holland (1978): Chemical exchange during hydrothermal alteration of basalt by seawater: I Experimental results for major and minor components of seawater. *Geochim. Cosmochim. Acta*, **42**, 1103-1115.

---, and T.F. McConachy (1990): Chemical processes in buoyant hydrothermal plumes on the East Pacific Rise near 21°N. *Geochim. Cosmochim. Acta*, **54**, 1911-1927.

Müller, C. (1995): Résultats biostratigraphiques des carottes de la mission GEOFAR 1993 obtenus par l'étude des nannofossiles calcaires. Rapport IFREMER.

Mungall, J.E., and R.F. Martin (1995): Petrogenesis of basalt-comendite and basalt-pantelleriite suites, Terceira, Azores, and some implications for the origin of ocean-island rhyolites. *Contrib. Min. Petrol.*, **119**, 43-55.

Murton, B.J., G. Klinkhammer, K. Becker, A. Briais, D. Edge, N. Hayward, I. Mitchell, I. Rouse, M. Rudnicki, K. Sayanagi, H. Sloan, and L. Parson (1994): Direct evidence for the distribution and occurrence of hydrothermal activity between 27-30°N on the Mid-Atlantic Ridge. *Earth Planet. Sci. Lett.*, **125**, 119-128.

---, C. Van Dover, and E. Southward (1995): Geological setting and ecology of the Broken Spur hydrothermal vent field: 29°10'N on the Mid-Atlantic Ridge. *In* Parson, L.M., Walker, C.L., and Dixon, D.R. (eds.): Hydrothermal vents and processes, *Geol. Soc. London Spec. Publ.*, **87**, 33-41.

Nadeau, M.-J., M. Schleicher, P.M. Grootes, H. Erlenkeuser, A. Gottdang, D.J.W. Mous, M. Sarnthein, and H. Willkomm (1996): The Leibniz-Labor AMS facility at the Christian-Albrechts-University, Kiel, Germany. 7th International Conference on Accelerator Mass Spectrometry, Tucson 1996. *Nucl. Instr. Meth.* (*submitted*).

Needham, H.D., M. Voisset, V. Renard, H. Bougault, O. Dauteuil, R. Detrick, and C. Langmuir (1992): Structural and volcanic features of the Mid-Atlantic Rift Zone between 40°N and 33°N. *EOS Trans. AGU*, **73** (43), 552.

Nelsen, T.A., G.P. Klinkhammer, J.H. Trefry, and R.P. Trocine (1986/87): Real-time observation of dispersed hydrothermal plumes using nephelometry: examples from the Mid-Atlantic Ridge. *Earth Planet. Sci. Lett.*, **81**, 245-252.

Nürnberg, C.C. (1995): Bariumfluss und Sedimentation im südlichen Südatlantik - Hinweise auf Produktivitätsänderungen im Quartär. *GEOMAR Rep.*, **38**, 105 pp.

O'Hanley, D.S., J.V. Chernosky Jr., and F.J. Weiss (1989): The stability of lizardite and chrysotile. *Can. Mineral.*, **27**, 483-493.

Ondréas, H., Y. Fouquet, J.L. Charlou, I. Costa, J.P. Donval, J. Knoery, N. Lourenço, H. Pellé, M. Ségonzac, and M.K. Tivey (1995): DIVA 1 Cruise: In situ observation of the limit between effusive and explosive submarine volcanism on The Menez-Gwen and 38°20N segments of the Mid-Atlantic Ridge. *Terra Abstracts*, **7**, Abstr. Suppl. No. 1, 209.

Oppo, D.W., and R.G. Fairbanks (1987): Variability in the deep and intermediate water circulation of the Atlantic Ocean during the past 25,000 years: Northern Hemisphere modulation of the Southern Ocean. *Earth Planet. Sci. Lett.*, **86**, 1-15.

Paetsch, H. (1991): Sedimentation im Europäischen Nordmeer: Radioisotopische, geochemische und tonmineralogische Untersuchungen spätquartärer Ablagerungen. *Ber. Sonderforschungsber. 313, Universität Kiel*, **29**, 1-83.

Palmer, M.R., and J.M. Edmond (1989): The strontium isotope budget of the modern ocean. *Earth Planet. Sci. Lett.*, **92**, 11-26.

Parra, M., P. Delmont, A. Ferragne, C. Latouche, J.C. Pons, and C. Puechmaille (1985): Origin and evolution of smectites in recent marine sediments of the NE Atlantic. *Clay Minerals*, **20**, 335-346.

Parra, M., P. Delmont, J.C. Dumon, A. Ferragne, and J.C. Pons (1987): Mineralogy and origin of Tertiary interbasaltic clays from the Faeroe Islands, Northeastern Atlantic. *Clay Minerals*, **22**, 63-82.

Parson, L.M., C.L. Walker, and D.R. Dixon (eds.) (1995): Hydrothermal vents and processes, *Geol. Soc. London Spec. Publ.*, **87**.

Paytan, A., M. Kastner, E.E. Martin, J.D. MacDougall, and T.D. Herbert (1993): Barite: A new monitor of the oceanic Sr isotopic ratio. *Nature*, **366**, 445-449.

Pisias, N.G., D.G. Martinson, T.C. Moore Jr., N.J. Shackleton, W. Prell, J. Hays, and G. Boden (1984): High resolution stratigraphic correlation of benthic oxygen isotope records spanning the last 300,000 years. *Mar. Geol.*, **56**, 119-136.

Prell, W.L., J. Imbrie, D.G. Martinson, J.J. Morley, N.G. Pisias, N.J. Shackleton, and H.F. Streeter (1986): Graphic correlation of oxygen isotope stratigraphy: Application to the late Quaternary. *Paleoceanogr.*, **1**, 137-162.

Pruysers, P. A., G.J. de Lange, J.J. Middelburg, and D.J. Hydes (1993): The diagenetic formation of metal-rich layers in sapropel-containing sediments in the eastern Mediterranean. *Geochim. Cosmochim. Acta*, **57**, 527-536.

Puteanus, D., G.P. Glasby, P. Stoffers, and H. Kunzendorf (1991): Hydrothermal iron-rich deposits from the Teahitia-Mehitia and Macdonald hot spot areas, Southwest Pacific. *Mar. Geol.*, **98**, 389-409.

Radford-Knoery, J., J.-L. Charlou, J.-P. Donval, Y. Fouquet, H. Pellé, H. Ondréas, I. Costa, N. Lourenço, M.K. Tivey, and M. Ségonzac (1994): Sulfide as a hydrothermal plume tracer: Preliminary results from the Menez Gwen and Lucky Strike segments, Mid-Atlantic Ridge (MAR, DIVA1 diving cruise). *EOS Trans. AGU*, **75**, 313.

Richter, T. (1992): Geochemistry of pelagic sediments at the Mid-Atlantic Ridge south of the Azores: Sources of sediments and hydrothermal impact. *Rapp. DEA, Univ. Bretagne Occidentale*, Brest, 78 pp.

Riech, V., V. Marchig, G. Sunkel, and W. Weiss (1990): Hydrothermal and volcanic input in sediments of the Lau back-arc basin, SW Pacific. *Mar. Mining*, **9**, 183-203.

Robbins, J.M., M. Lyle, and G.R. Heath (1984): A sequential extraction procedure for partitioning elements among co-existing phases in marine sediments, *Ref. 84-3*, 64 pp., College of Oceanogr., Oregon State Univ., Corvallis.

Robinson, P., F.S. Spear, J.C. Schumaker, J. Laird, C. Klein, B.W. Evans, and B.W. Doolan (1981): Phase relations of metamorphic amphiboles: natural occurrences and theory. *In* Veblen, D.R., and P. H. Ribbe (eds.): Amphiboles: Petrology and experimental phase relations. *Reviews in Mineralogy*, **9B**, 1-228.

Rona, P.A. (1988): Hydrothermal mineralization at oceanic ridges. *Can. Mineral.*, **26**, 431-466.

---, and K.G. Speer (1989): An Atlantic hydrothermal plume: Trans-Atlantic Geotraverse (TAG) area, Mid-Atlantic Ridge crest near 26°N. *J. Geophys. Res.*, **94**, B10, 13879-13893.

---, G. Thompson, M.J. Mottl, J.A. Karson, W.J. Jenkins, D. Graham, M. Mallette, K. Von Damm, and J.M. Edmond (1984): Hydrothermal activity at the Trans-Atlantic Geotraverse hydrothermal field, Mid-Atlantic Ridge crest at 26°N. *J. Geophys. Res.*, **89**, B13, 11365-11377.

---, G. Klinkhammer, T.A. Nelsen, J.H. Trefry, and H. Elderfield (1986): Black smokers, massive sulfides and vent biota at the Mid-Atlantic Ridge. *Nature*, **321**, 33-37.

---, L. Widenfalk, and K. Boström (1987): Serpentinized ultramafics and hydrothermal activity at the Mid-Atlantic Ridge crest near 15°N. *J. Geophys. Res.*, **92**, B2, 1417-1427.

---, H. Bougault, J.L. Charlou, P. Appriou, T.A. Nelsen, J.H. Trefry, G.L. Eberhart, A. Barone, and H.D. Needham (1992): Hydrothermal circulation, serpentinization, and degassing at a rift-valley intersection: Mid-Atlantic Ridge near 15°N, 45°W. *Geology*, **20**, 783-786.

---, ---, ---, Y. Fouquet, and P. Jean-Baptiste (1996): Mafic- and ultramafic-hosted hydrothermal systems at the TAG (26°N) and Fifteen-Twenty Fracture Zone areas of the Mid-Atlantic Ridge rift valley. FARA-IR Mid-Atlantic Ridge Symposium, *J. Conf. Abstracts*, **1**, 850-851.

Ruddiman, W.F. (1977): Late Quaternary deposition of ice-rafted sand in the subpolar North Atlantic (lat 40° to 65°N). *Geol. Soc. Am. Bull.*, **88**, 1813-1827.

Rudnicki, M.D., and H. Elderfield (1992): Theory applied to the Mid-Atlantic Ridge hydrothermal plumes: the finite-difference approach. *J. Volcanol. Geoth. Res.*, **50**, 161-172.

Rudnicki, M.D., and H. Elderfield (1993): A chemical model of the buoyant and neutrally buoyant plume above the TAG vent field, 26 degrees N, Mid-Atlantic Ridge. *Geochim. Cosmochim. Acta*, **57**, 2939-2957.

Rutsch, H.-J., A. Mangini, G. Bonani, B. Dittrich-Hannen, P.W. Kubik, M. Suter, and M. Segl (1995): ^{10}Be and Ba concentrations in West African sediments trace productivity in the past. *Earth Planet. Sci. Lett.*, **133**, 129-143.

Sarnthein, M., K. Winn, S.J.A. Jung, J.-C. Duplessy, L. Labeyrie, H. Erlenkeuser, and G. Ganssen (1994): Changes in east Atlantic deepwater circulation over the last 30,000 years: Eight time slice reconstructions. *Paleoceanogr.*, **9**, 209-267.

Sawlan, J.J., and J.W. Murray (1983): Trace metal remobilization in the interstitial waters of red clay and hemipelagic marine sediments. *Earth Planet. Sci. Lett.*, **64**, 213-230.

Schilling, J.-G. (1975): Azores mantle blob: rare-earth evidence. *Nature*, **25**, 103-115.

---, M. Zajac, R. Evans, T. Johnston, W. White, J.D. Devine, and R. Kingsley (1983): Petrologic and geochemical variations along the Mid-Atlantic Ridge from 27°N to 73°N. *Am. J. Sci.*, **283**, 510-586.

Schmincke, H.-U. (1973): Magmatic evolution and tectonic regime in the Canary, Madeira, and Azores island groups. *Geol. Soc. Am. Bull.*, **84**, 633-648.

Schmitz, B. (1987): Barium, equatorial high productivity, and the northward wandering of the Indian continent. *Paleoceanogr.*, **2**, 63-77.

Schmitz, W., A. Singer, H. Bäcker, and P. Stoffers (1982): Hydrothermal serpentine in a Hess Deep sediment core. *Mar. Geol.*, **46**, M17- M26.

Scott, M.R., P.F. Salter, and L.A. Barnard (1979): Chemistry of ridge-crest sediments from the North Atlantic Ocean. *In* Talwani, M., Harrison, C.G., and Hayes, D.E. (eds.): Deep drilling results in the Atlantic Ocean: ocean crust. Amer. Geophys. Union, Washington, D.C., pp. 403-428.

Shau, Y.-H., D. R. Peacor, and E. J. Essene (1990): Corrensite and mixed-layer chlorite/corrensite in metabasalt from northern Taiwan: TEM/AEM, EMPA, XRD, and optical studies. *Contrib. Mineral. Petrol.*, **105**, 123-142.

---, and --- (1992): Phyllosilicates in hydrothermally altered basalts from DSDP Hole 504B, Leg 83 - a TEM and AEM study. *Contrib. Mineral. Petrol.*, **112**, 119-133.

Shearme, S., D.S. Cronan, and P.A. Rona (1983): Geochemistry of sediments from the TAG hydrothermal field, M.A.R. at latitude 26°N. *Mar. Geol.*, **51**, 269-291.

Shimmield, G.B., and N.B. Price (1988): The scavenging of U, ^{230}Th and ^{231}Pa during pulsed hydrothermal activity at 20°S, East Pacific Rise. *Geochim. Cosmochim. Acta*, **52**, 669-677.

---, and S. Mowbray (1991): The inorganic geochemical record of the northwestern Arabian Sea: A history of productivity variation over the last 400 ka from Sites 722 and 724. *In* Prell, W.L., Niitsuma, N., et al., *Proc. ODP, Sci. Results*, **117**: College Station, TX (Ocean Drilling Program), 409-429.

Singer, A., and P. Stoffers (1987): Mineralogy of a hydrothermal sequence in a core from the Atlantis II Deep, Red Sea. *Clay Minerals*, **22**, 251-267.

Sirocko, F., D. Garbe-Schönberg, A. McIntyre, and B. Molfino (1996): Teleconnections between the subtropical monsoons and high-latitude climates during the last deglaciation. *Science*, **272**, 526-529.

Speer, K.G., and P.A. Rona (1989): A model of an Atlantic and Pacific hydrothermal plume. *J. Geophys. Res.*, **94**, C5, 6213-6220.

Spiess, F.N., and RISE Project Group (1980): East Pacific Rise: hot springs and geophysical experiments. *Science*, **207**, 1421-1433.

Stamoudi, C., and C. Mével (1995): High temperature serpentinization of oceanic mantle at the fast spreading East Pacific Rise. *Terra Abstracts*, **7**, Abstr. Suppl. No. 1, 207.

----, ----, P. Agrinier, and A. Gaudichet (1995): Nature et signification des phases serpentineuses dans les péridotites océaniques serpentinisées de Hess Deep et MARK. Journées „Géosciences Marines“, Societé Géologique de France, Livre des Resumés, 66.

Storey, M., J.A. Wolff, M.J. Norry, and G.F. Marriner (1989): Origin of hybrid lavas from Agua de Pau volcano, Sao Miguel, Azores. *In* Saunders, A.D., and M.J. Norry (eds.): Magmatism in the ocean basins, *Geol. Soc. London Spec. Publ.*, **42**, 161-180.

Stuiver, M., and T.F. Braziunas (1993): Modeling atmospheric 14C influences and 14C ages of marine samples to 10,000 BC. *Radiocarbon*, **35**, 137-189.

Stuiver, M., B. Kromer, B. Becker, and C.W. Ferguson (1986): Radiocarbon age calibration back to 13,300 years BP and the ^{14}C age matching of the German oak and US bristlecone pine chronologies. *Radiocarbon*, **28**, 969-979.

---, T.F. Braziunas, B. Becker, and B. Kromer (1991): Climatic, solar, and geomagnetic influences on Late-Glacial and Holocene atmospheric $^{14}C/^{12}C$ change. *Quat. Res.*, **35**, 1-24.

Stumm, W., and J.J. Morgan (1981): Aquatic chemistry. John Wiley and Sons, New York.

Suman, D.O., and M.P. Bacon (1989): Variations in Holocene sedimentation in the North American basin determined from ^{230}Th measurements. *Deep Sea Res.*, **36**, 869-878.

Sun, S.-S., R.W. Nesbitt, and A.Y. Sharaskin (1979): Geochemical characteristics of mid-ocean ridge basalts. *Earth Planet. Sci. Lett.*, **44**, 119-138.

Sveinbjörnsdóttir, A.E. (1992): Composition of geothermal minerals from saline and dilute fluids - Krafla and Reykjanes, Iceland. *Lithos*, **27**, 301-315.

Taylor, S.R., and S.M. McLennan (1985): The continental crust: its composition and evolution. An examination of the geochemical record preserved in sedimentary rocks. Blackwell, London.

Tessier, A., P.G.C. Campbell, and M. Bisson (1979): Sequential extraction procedure for the speciation of particulate trace metals. *Anal. Chem.*, **51**, 844-850.

Thompson, G., S.E. Humphris, B. Schroeder, M. Sulanowska, and P.A. Rona (1988): Active vents and massive sulfides at 26°N (TAG) and 23°N (Snakepit) on the Mid-Atlantic Ridge. *Can. Mineral.*, **26**, 697-711.

Thomson, J., T.R.S. Wilson, F. Culkin, and D.J. Hydes (1984a): Non-steady state diagenetic record in eastern equatorial Atlantic sediments. *Earth Planet. Sci. Lett.*, **71**, 23-30.

---, M.S.N. Carpenter, S. Colley, T.R.S. Wilson, H. Elderfield, and H. Kennedy (1984b): Metal accumulation rates in northwest Atlantic pelagic sediments. *Geochim. Cosmochim. Acta*, **48**, 1935-1948.

---, N.C. Higgs, I. Jarvis, D.J. Hydes, S. Colley, and T.R.S. Wilson (1986): The behaviour of manganese in Atlantic carbonate sediments. *Geochim. Cosmochim. Acta*, **50**, 1807-1818.

---, ---, I. Croudace, S. Colley, and D.J. Hydes (1993): Redox zonation of elements at an oxic/post-oxic boundary in deep-sea sediments. *Geochim. Cosmochim. Acta*, **57**, 579-595.

---, ---, T.R.S. Wilson, I.W. Croudace, G.J. de Lange, and P.J.M. Van Santvoort (1995): Redistribution and geochemical behaviour of redox-sensitive elements around S1, the most recent eastern Mediterranean sapropel. *Geochim. Cosmochim. Acta*, **59**, 3487-3501.

---, ---, and S. Colley (1996): Diagenetic redistributions of redox-sensitive elements in northeast Atlantic glacial/interglacial transition sediments. *Earth Planet. Sci. Lett.*, **139**, 365-377.

Tivey, M.K., S.E. Humphris, G. Thompson, M.D. Hannington, and P.A. Rona (1995): Deducing patterns of fluid flow and mixing within the TAG active hydrothermal mound using mineralogical and geochemical data. *J. Geophys. Res.*, **100**, B7, 12527-12555.

Tómasson, J., and H. Kristmannsdóttir (1972): High temperature alteration minerals and thermal brines, Reykjanes, Iceland. *Contrib. Mineral. Petrol.*, **36**, 123-134.

Torres, M.E., H.J. Brumsack, G. Bohrmann, and K.-C. Emeis (1996): Barite fronts in continental margin sediments: A new look at barium remobilization in the zone of sulfate reduction and formation of heavy barites in diagenetic fronts. *Chem. Geol.*, **127**, 125-139.

Trefry, J.H., and S. Metz (1984): Selective leaching of trace metals from sediments as a function of pH. *Anal. Chem.*, **56**, 745-749.

---, and --- (1989): Role of hydrothermal precipitates in the geochemical cycling of vanadium. *Nature*, **342**, 531-533.

Trocine, R.P., and J.H. Trefry (1988): Distribution and chemistry of suspended particles from an active vent site on the Mid-Atlantic Ridge at 26°N. *Earth Planet. Sci. Lett.*, **88**, 1-15.

Turekian, K.K., and K.H. Wedepohl (1961): Distribution of the elements in some major units of the Earth's crust. *Geol. Soc. Am. Bull.*, **72**, 175-192.

von Breymann, M.T., K.-C. Emeis, and A. Camerlenghi (1990): Geochemistry of sediments from the Peru upwelling area: Results from sites 680, 682, 685, and 688. *In* Suess, E., von Huene, R., et al., *Proc. ODP, Sci. Results*, **112**: College Station, TX (Ocean Drilling Program), 491-503.

---, H. Brumsack, and K.-C. Emeis (1992a): Depositional and diagenetic behavior of barium in the Japan Sea. *In* Pisciotto, K.A., Ingle, J.C. Jr., von Breymann, M.T., Barron, J., et al., *Proc. ODP, Sci. Results*, **127/128**, Pt. 1: College Station, TX (Ocean Drilling Program), 651-665.

---, K.-C. Emeis, and E. Suess (1992b): Water depth and diagenetic constraints on the use of barium as a paleoproductivity indicator. *In* Summerhayes, C.P., Prell, W.L., and Emeis, K.-C. (eds.): Upwelling Systems: Evolution since the Early Miocene. *Geol. Soc. London Spec. Publ.*, **64**, 273-284.

Von Damm, K.L., J.M. Edmond, B. Grant, C.I. Measures, B. Walden, and R.F. Weiss (1985): Chemistry of hydrothermal solutions at 21°N, East Pacific Rise. *Geochim. Cosmochim. Acta*, **49**, 2197-2220.

Walker, S.L., and E.T. Baker (1988): Particle-size distributions within hydrothermal plumes over the Juan de Fuca Ridge. *Mar. Geol.*, **78**, 217-226.

Wallace, H.E., J. Thomson, T.R.S. Wilson, P.P.E. Weaver, N.C. Higgs, and D.J. Hydes (1988): Active diagenetic formation of metal-rich layers in N. E. Atlantic sediments. *Geochim. Cosmochim. Acta*, **52**, 1557-1569.

Walter, P., and P. Stoffers (1985): Chemical characteristics of metalliferous sediments from eight areas on the Galapagos Rift and East Pacific Rise between 2°N and 42°S. *Mar. Geol.*, **65**, 271-287.

Weaver, B.L., J. Tarney, and A.D. Saunders (1985): Geochemistry and mineralogy of basalts recovered from the central North Atlantic. *In* Bougault, H., Cande, S.C., et al., *Init. Rep. DSDP*, **82**: Washington (U.S. Govt. Printing Office), 395-416.

Wedepohl, K.H. (1969): Handbook of Geochemistry. Springer, Berlin.

Weiss, R.F., P. Lonsdale, J.E. Lupton, A.E. Bainbridge, and H. Craig (1977): Hydrothermal plumes in the Galapagos Rift. *Nature*, **267**, 600-603.

White, W.B., M.D.M. Tapia, and J.-G. Schilling (1979): The petrology and geochemistry of the Azores islands. *Contrib. Min. Petrol.*, **69**, 201-213.

Wicks, F.J., and D.S. O'Hanley (1988): Serpentine minerals: structures and petrology. *In* Bailey, S.W. (Ed.): Hydrous phyllosilicates (exclusive of micas). *Reviews in Mineralogy*, **19**, 91-168.

Widom, E., H.-U. Schmincke, and J.-B. Gill (1992): Processes and timescales in the evolution of chemically zoned trachyte; Fogo A, Sao Miguel, Azores. *Contrib. Min. Petrol.*, **111**, 311-328.

Wilson, C., J.-L. Charlou, E. Ludford, G. Klinkhammer, C. Chin, H. Bougault, C. German, K. Speer, and M. Palmer (1996): Hydrothermal anomalies in the Lucky Strike segment on the Mid-Atlantic Ridge (37°17'N). *Earth Planet. Sci. Lett.*, **142**, 467-477.

Wilson, M. (1989): Igneous petrogenesis. A global tectonic approach. Unwin & Hyman, London etc. .

Wilson, T.R.S., J. Thomson, S. Colley, D.J. Hydes, N.C. Higgs, and J. Sørensen (1985): Early organic diagenesis: The significance of progressive subsurface oxidation fronts in pelagic sediments. *Geochim. Cosmochim. Acta*, **49**, 811-822.

---, ---, D.J. Hydes, S. Colley, F. Culkin, and J. Sørensen (1986): Oxidation fronts in pelagic sediments: Diagenetic formation of metal-rich layers. *Science*, **232**, 972-974.

Winn, K., M. Sarnthein, and H. Erlenkeuser (1991): $\delta^{18}O$ stratigraphy and chronology of Kiel sediment cores from the East Atlantic. *Ber.-Rep., Geol.-Paläontolog. Inst. Univ. Kiel*, **46**, 1-99.

Wood, D.A., J. Tarney, J. Varet, A.D. Saunders, H. Bougault, J.L. Joron, M. Treuil, and J.R. Cann (1979): Geochemistry of basalts drilled in the North Atlantic by IPOD Leg 49: Implications for mantle heterogeneity. *Earth Planet. Sci. Lett.*, **42**: 77-97.

Zahn, R., K. Winn, and M. Sarnthein (1986): Benthic foraminiferal $\delta^{13}C$ and accumulation rates of organic carbon: *Uvigerina peregrina* group and *Cibicidoides wuellerstorfi*.. *Paleoceanogr.*, **1**, 27-42.

Acknowledgements

I would like to thank my Ph.D. advisor, Prof. Dr. E. Suess, not only for his scientific advice but especially for his confidence in me and for the liberty he gave me with this study.

Prof. Dr. M. Sarnthein supervised the stratigraphic part of this thesis, and was very competent and helpful in the interpretation of oxygen isotopic and AMS age data.

Dr. Gérard Auffret (IFREMER Brest, France) invited me to participate in the GEOFAR cruise. I am also thankful for his consistent interest in this work, and last but not least for his hospitality during several short stays in Brest.

I gratefully acknowledge discussions on foraminifera, oxygen isotopes and paleoceanography with Dr. U. Pflaumann, Dr. M. Trauth, T. Kiefer, Dr. M. Weinelt and Dr. K. Winn. Dr. H. Erlenkeuser and Dr. M. Joachimski (University of Erlangen) were responsible for the oxygen isotope measurements on foraminifera. AMS age dating was supervised by Prof. Dr. P.M. Grootes, whom I also thank for discussion of results.

Dr. I. König proposed and arranged the measurements by Mössbauer spectroscopy run by M. Drodt (Institute of Nuclear Physics, Med. University of Lübeck), I thank both for explanations on the method and discussion of results.

The serpentine chapter benefitted from discussions with Prof. Dr. P. Stoffers and Prof. Dr. H. Dick (Woods Hole), and from reviews of an early manuscript by Dr. H. Lange and Dr. D. Bideau (Brest). Prof. Dr. M. Czank operated the transmission electron microscope (TEM) at the Mineralogical Institute, University of Kiel.

I thank Dr. G. Bohrmann and Dr. K. Lackschewitz for discussions on various aspects of this work.

B. Domeyer, A. Bleyer, A. Lunau (carbonate and selective leaching), J. Heinze (X-ray diffractometry), K. Wolff, A. Merkau (X-ray fluorescence), K. Kißling and M. Stahlberg (sample preparation for $\delta^{18}O$ analysis) provided help and technical assistance on various analytical methods. Dr. B. Gehrke introduced me to clay mineralogical sample preparation, and T. Nähr explained the gravity separation method.

I thank the GEOFAR Scientific Party and the captain and crew of RV Le Noroit for the pleasant atmosphere on bord. Among my French colleagues, I would like to mention the following persons for communicating unpublished data: C. Rabouille (Gif-sur Yvette), E. Deloule (Nancy) and J.-F. Gaillard (Northwestern Univ., USA) (pore water data), C. Müller (Reuil-sur Malmaison) (calcareous nannoplankton) and A. Boelaert (IFREMER Brest) (carbonate). I am most thankful to H.D. Needham for permission to use his bathymetry data in order to establish the structural setting of the study area. I continuously exchanged ideas with B. Dennielou (IFREMER Brest) over the last three years.

A Ph.D. scholarship of the *Graduiertenkolleg Dynamik globaler Kreisläufe im System Erde* by the*Deutsche Forschungsgemeinschaft* is gratefully acknowledged. Finally I thank he former and present colleagues of the *Graduiertenkolleg* for the working atmosphere and for moral support during the tense final months.

Appendix 1: Selected core logs

GEOFAR KF13

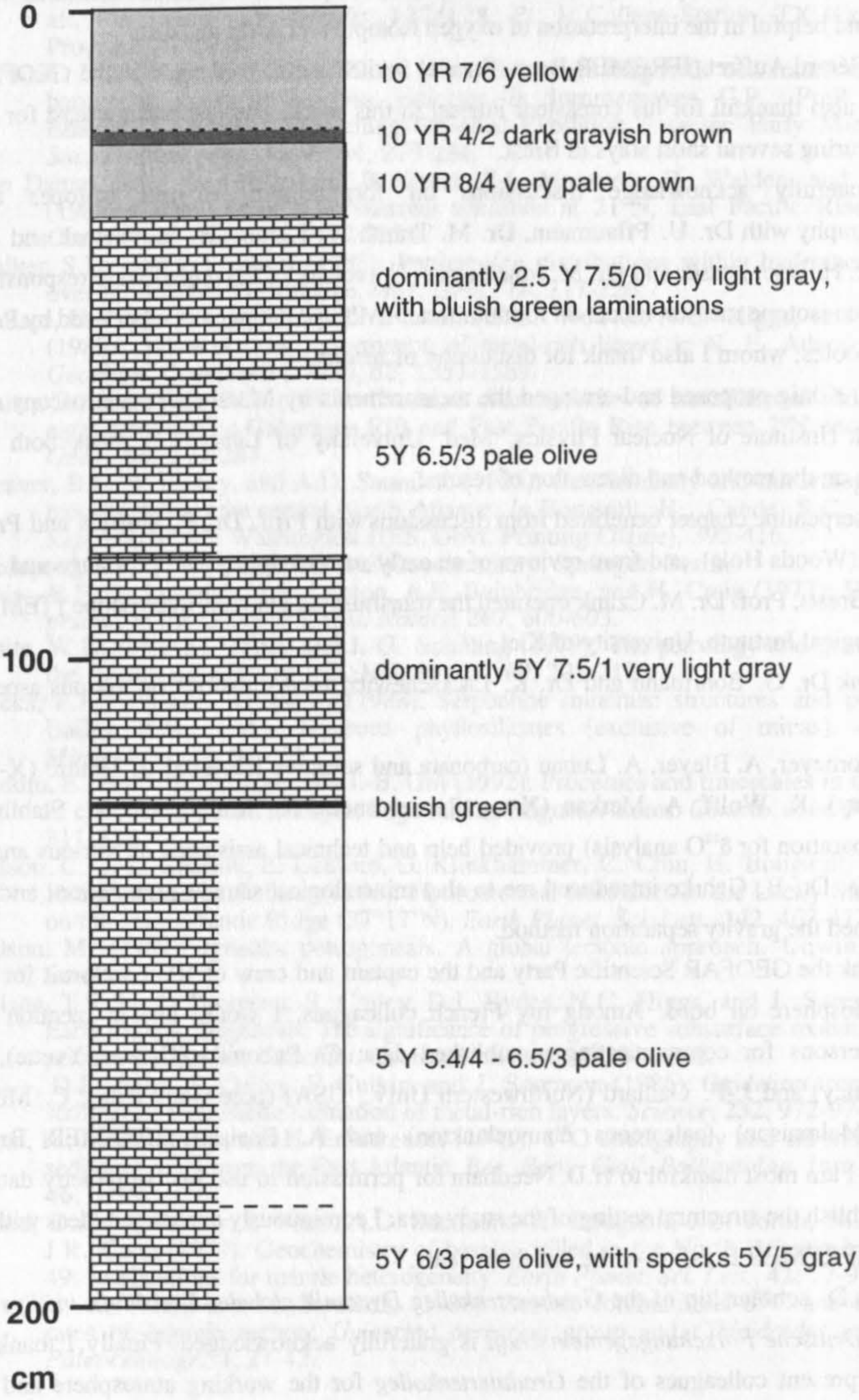
0
10 YR 7/6 yellow
10 YR 4/2 dark grayish brown
10 YR 8/4 very pale brown
dominantly 2.5 Y 7.5/0 very light gray, with bluish green laminations
5Y 6.5/3 pale olive
100
dominantly 5Y 7.5/1 very light gray
bluish green
5 Y 5.4/4 - 6.5/3 pale olive
5Y 6/3 pale olive, with specks 5Y/5 gray
200
cm

Appendix 1: Selected core logs

GEOFAR KF13

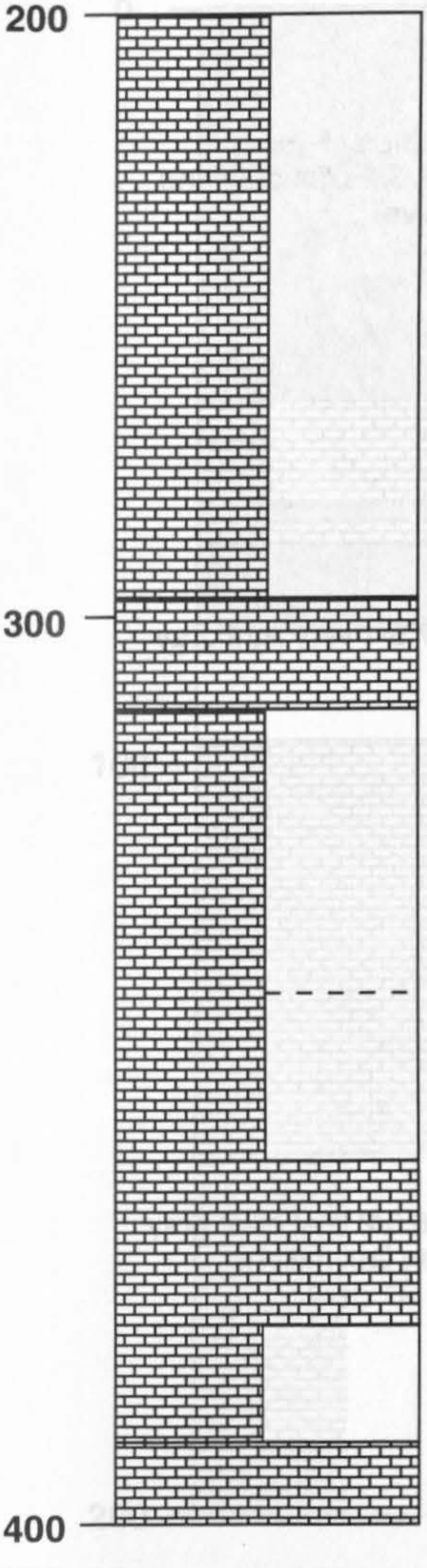

dominantly 5Y 6/3 pale olive
with frequent specks 5Y 5/1 gray

dominantly 5Y 7.5/1 very light gray
with bluish green and gray specks

dominantly 5Y 6.5/3 pale olive
with specks 5Y 5/1 gray and bluish green

dominantly 5Y 6.5/3 pale olive

dominantly 5Y 8/1 white

5Y 6/3 pale olive

dominantly 5Y 8/2 white

Appendix 1: Selected core logs

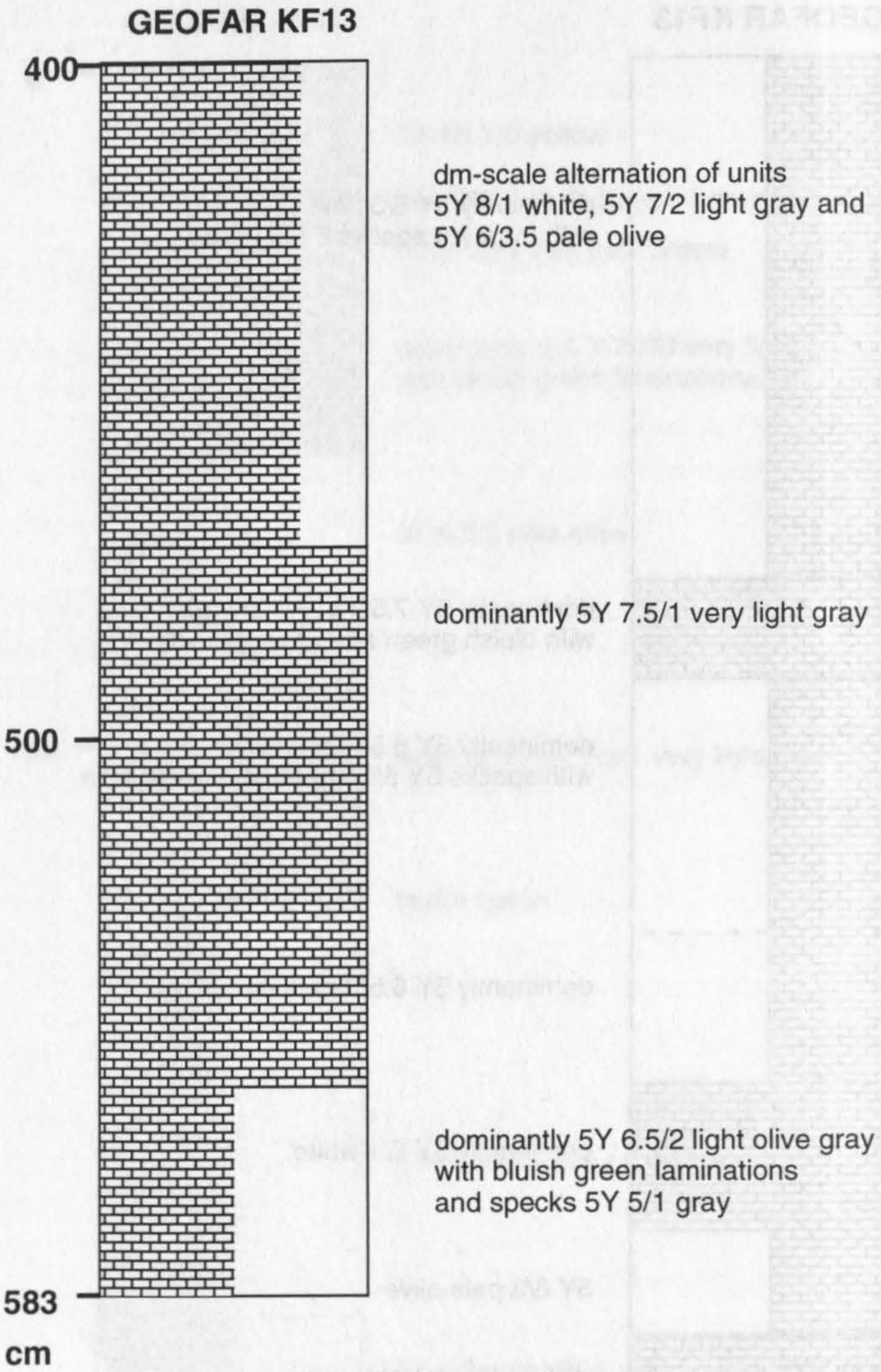
GEOFAR KF13
400
500
583
cm
dm-scale alternation of units
5Y 8/1 white, 5Y 7/2 light gray and
5Y 6/3.5 pale olive
dominantly 5Y 7.5/1 very light gray
dominantly 5Y 6.5/2 light olive gray
with bluish green laminations
and specks 5Y 5/1 gray

Appendix 1: Selected core logs

GEOFAR KF16

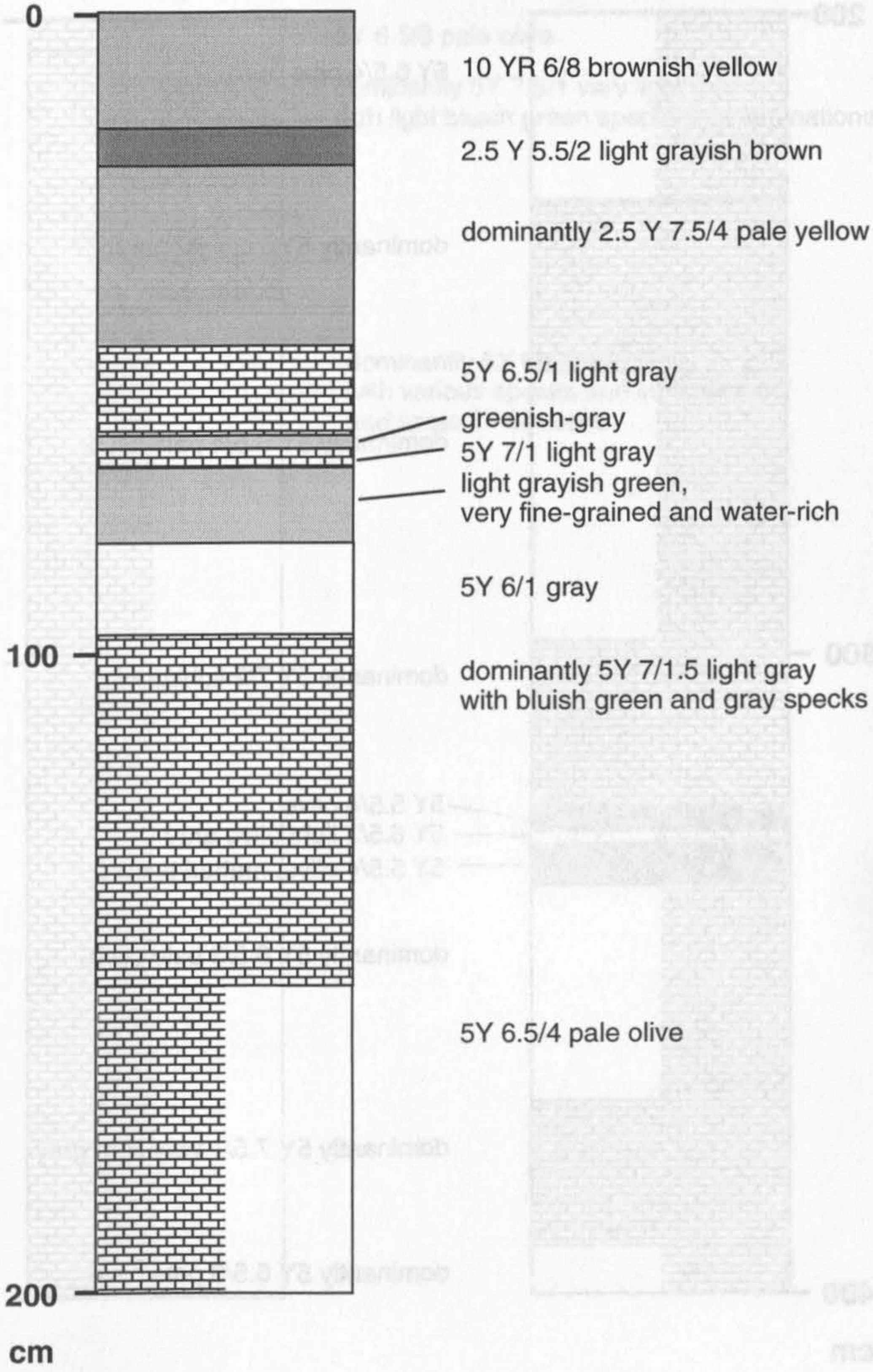
0
10 YR 6/8 brownish yellow
2.5 Y 5.5/2 light grayish brown
dominantly 2.5 Y 7.5/4 pale yellow
5Y 6.5/1 light gray
greenish-gray
5Y 7/1 light gray
light grayish green,
very fine-grained and water-rich
5Y 6/1 gray
100
dominantly 5Y 7/1.5 light gray
with bluish green and gray specks
5Y 6.5/4 pale olive
200
cm

Appendix 1: Selected core logs

GEOFAR KF16

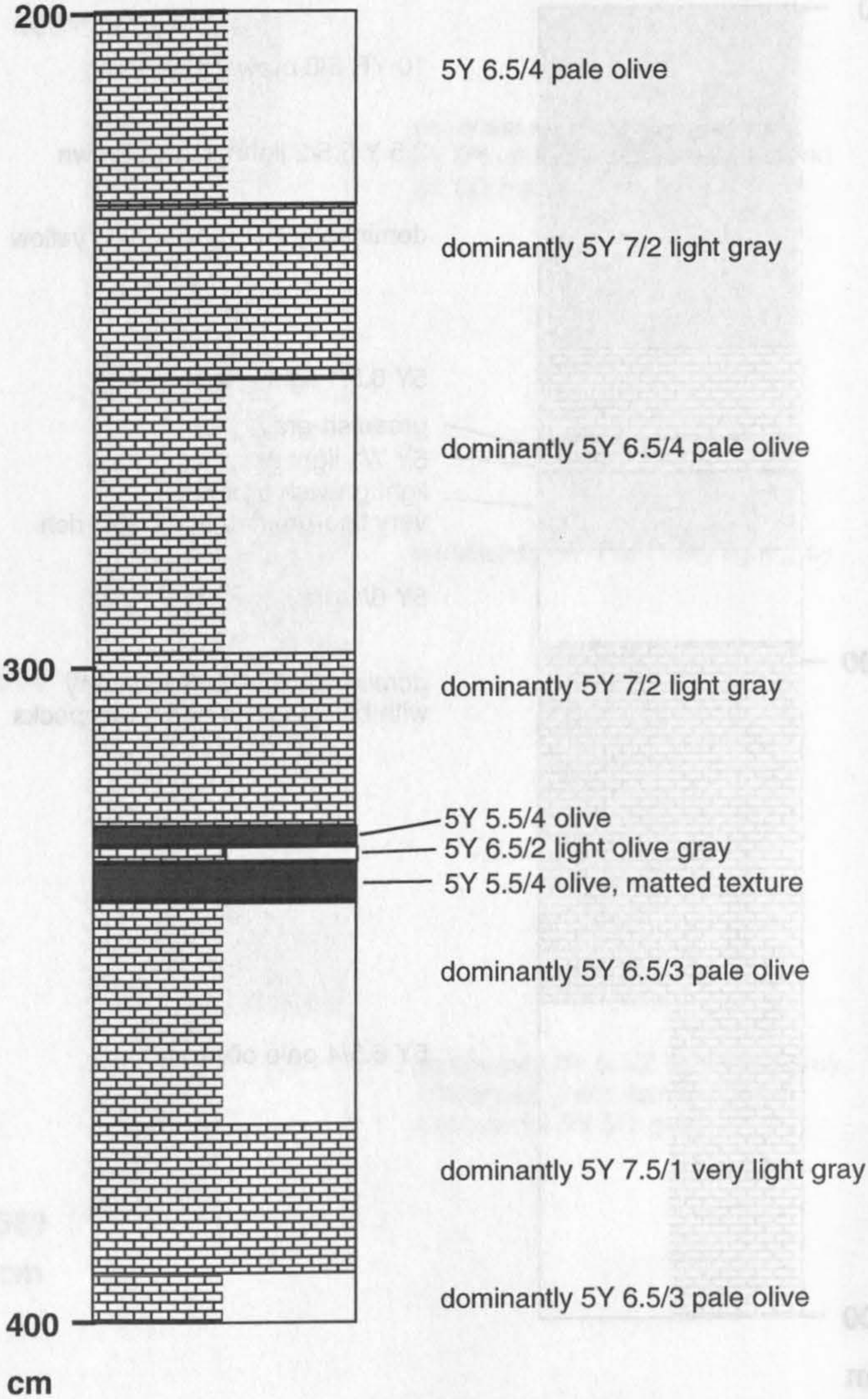
200
300
400
cm
5Y 6.5/4 pale olive
dominantly 5Y 7/2 light gray
dominantly 5Y 6.5/4 pale olive
dominantly 5Y 7/2 light gray
5Y 5.5/4 olive
5Y 6.5/2 light olive gray
5Y 5.5/4 olive, matted texture
dominantly 5Y 6.5/3 pale olive
dominantly 5Y 7.5/1 very light gray
dominantly 5Y 6.5/3 pale olive

Appendix 1: Selected core logs

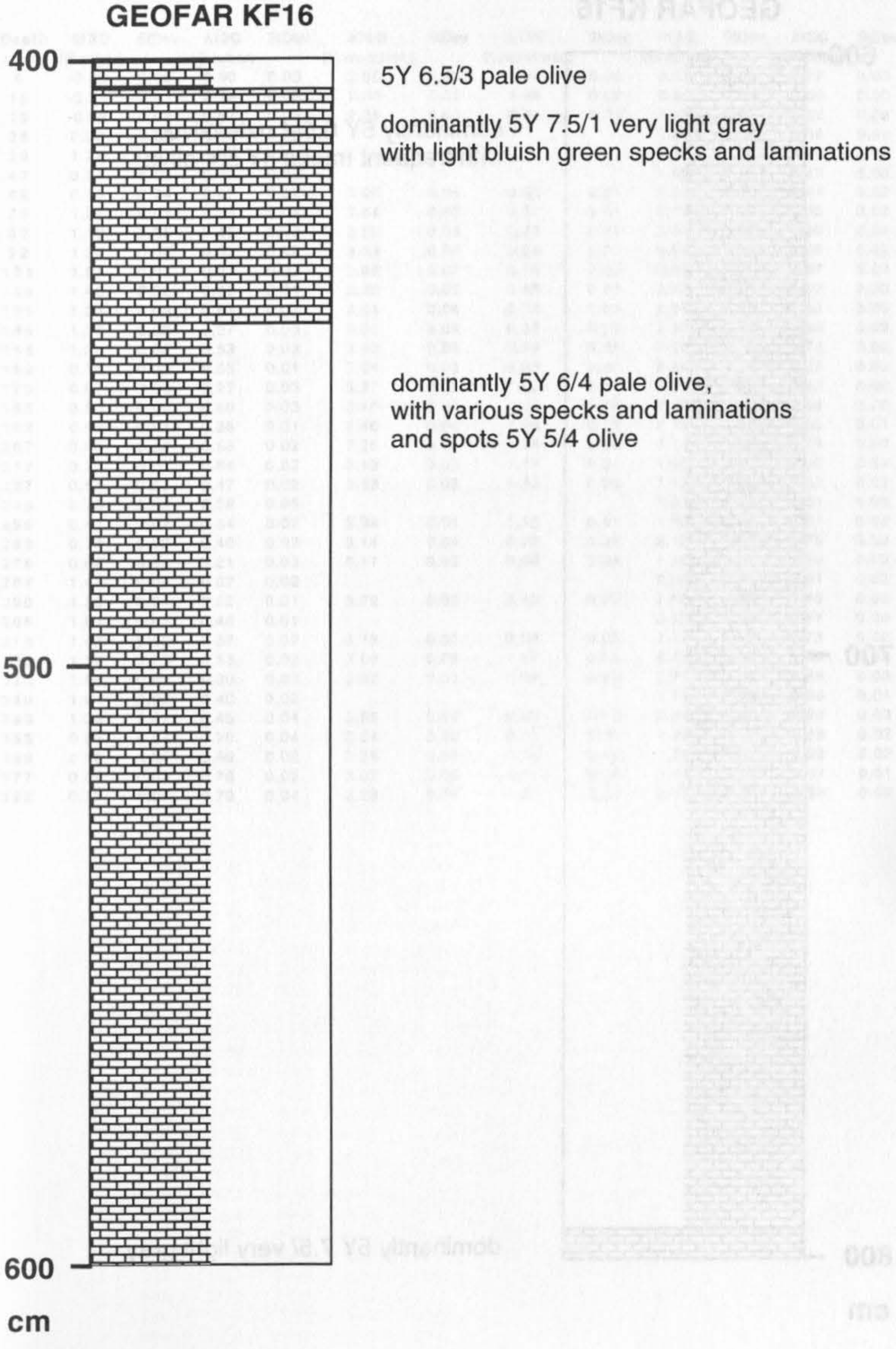
GEOFAR KF16
400
500
600
cm
5Y 6.5/3 pale olive
dominantly 5Y 7.5/1 very light gray
with light bluish green specks and laminations
dominantly 5Y 6/4 pale olive,
with various specks and laminations
and spots 5Y 5/4 olive

Appendix 1: Selected core logs

GEOFAR KF16

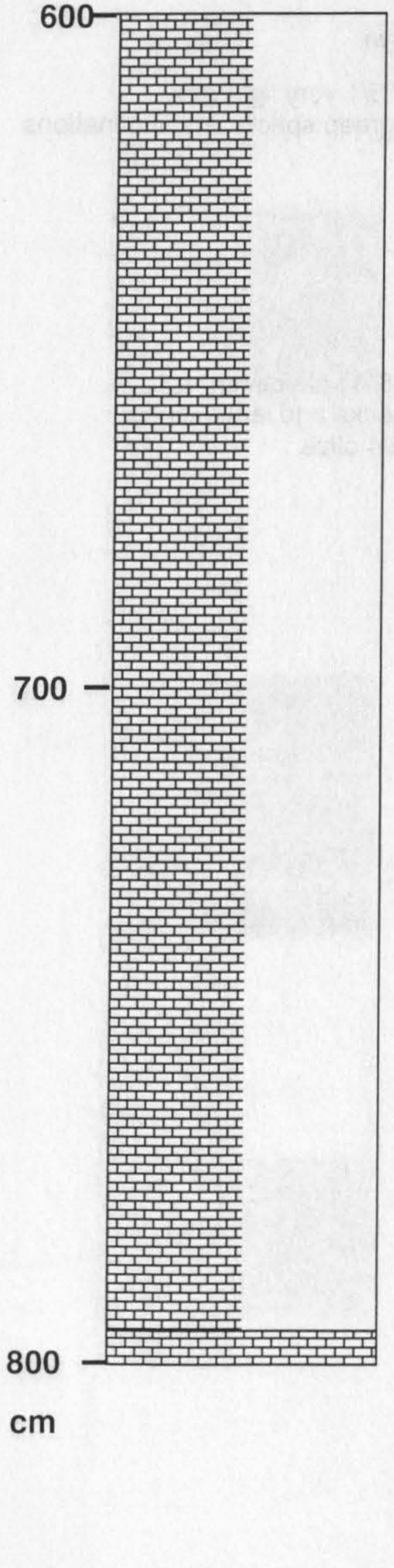

dominantly 5Y 6.5/4 pale olive, with frequent traces 5Y 5/4 olive

dominantly 5Y 7.5/ very light gray

Appendix 2: Stable isotope data

Ac.91KS04 (EPSHOM) (38°05N 30°36W / 2184 m water depth)

Depth (cm)	δ18O (G.ruber)	StDev	δ13C (G.ruber)	StDev	δ18O (C.wuellerst.)	StDev	δ13C (C.wuellerst.)	StDev	δ18O (G.inflata)	StDev	δ13C (G.inflata)	StDev
4	-0.35	0.02	0.90	0.03	2.06	0.05	1.07	0.05	0.92	0.02	0.77	0.03
15	-0.21	0.03	0.39	0.03	2.30	0.02	1.05	0.02	0.95	0.03	0.68	0.03
19	-0.02	0.03	0.57	0.02	2.38	0.03	0.91	0.02	1.15	0.02	0.52	0.02
26	0.33	0.05	0.51	0.03					1.60	0.02	0.66	0.02
36	1.27	0.01	0.50	0.01					1.96	0.05	0.70	0.02
47	0.91	0.03	0.40	0.02					1.69	0.02	0.47	0.03
62	0.59	0.04	0.47	0.02	3.05	0.04	0.85	0.01	2.04	0.04	0.51	0.02
72	1.21	0.03	0.39	0.02	3.54	0.03	0.37	0.01	2.44	0.02	0.62	0.02
82	1.13	0.05	0.45	0.03	3.89	0.03	0.20	0.01	2.53	0.02	0.49	0.02
92	1.34	0.03	0.33	0.02	3.69	0.03	0.65	0.03	2.69	0.03	0.66	0.02
101	1.57	0.03	0.37	0.02	3.89	0.07	0.78	0.05	2.50	0.05	0.57	0.03
115	1.46	0.02	0.47	0.01	3.28	0.03	0.65	0.01	2.47	0.04	0.62	0.03
131	1.33	0.03	0.61	0.03	3.65	0.04	0.78	0.03	2.24	0.03	0.53	0.03
146	1.36	0.03	0.27	0.03	3.63	0.03	0.82	0.02	1.18	0.03	0.18	0.02
154	1.27	0.02	0.53	0.03	3.62	0.03	1.29	0.02	2.16	0.02	0.74	0.02
159	0.74	0.03	0.58	0.01	3.54	0.03	0.82	0.02	2.16	0.04	0.62	0.02
175	0.67	0.03	0.27	0.03	3.27	0.02	1.00	0.02	2.23	0.03	0.93	0.00
185	0.80	0.03	0.60	0.03	3.50	0.02	1.04	0.02	2.15	0.03	0.64	0.02
192	0.88	0.04	0.36	0.01	3.40	0.04	1.09	0.03	2.10	0.04	0.65	0.01
207	0.96	0.02	0.58	0.02	3.25	0.03	1.08	0.04	2.13	0.03	0.78	0.02
217	0.77	0.02	0.64	0.02	3.43	0.03	1.17	0.01	1.95	0.02	0.80	0.02
227	0.87	0.03	0.47	0.02	3.33	0.03	1.23	0.06	1.73	0.02	0.52	0.01
245	0.75	0.05	0.39	0.05					1.91	0.02	0.61	0.03
256	0.47	0.02	0.54	0.02	3.34	0.01	1.12	0.01	1.80	0.02	0.67	0.02
263	0.73	0.02	0.46	0.02	3.14	0.04	0.99	0.03	2.12	0.03	0.75	0.02
278	0.66	0.03	0.21	0.03	3.17	0.03	0.86	0.02	1.78	0.02	0.29	0.02
287	1.43	0.04	0.07	0.02					2.59	0.01	0.61	0.02
290	1.26	0.04	0.22	0.01	3.22	0.05	0.43	0.03	2.60	0.03	0.46	0.02
305	1.61	0.03	0.46	0.01					2.53	0.06	0.47	0.04
315	1.42	0.02	0.57	0.02	3.73	0.02	0.98	0.02	2.47	0.02	0.73	0.02
320	1.12	0.03	0.53	0.02	3.60	0.06	1.37	0.05	2.43	0.03	0.88	0.02
334	1.95	0.02	0.30	0.03	3.92	0.01	1.04	0.02	2.71	0.02	0.89	0.03
340	1.61	0.02	0.40	0.02					2.74	0.04	0.88	0.01
353	1.39	0.02	0.45	0.04	3.65	0.04	0.92	0.02	2.34	0.02	0.80	0.03
358	0.83	0.04	0.20	0.04	3.24	0.22	0.15	0.19	1.98	0.03	0.66	0.02
369	0.58	0.04	0.60	0.02	3.35	0.03	0.88	0.02	1.78	0.02	0.92	0.02
377	0.62	0.03	0.76	0.02	3.07	0.06	0.91	0.04	1.74	0.02	0.97	0.01
392	0.77	0.07	0.70	0.04	3.28	0.04	1.27	0.02	2.07	0.04	0.99	0.02

Appendix 2: Stable isotope data

GEOFAR KF09 (37°07N 32°17 W / 2655 m water depth)

Depth (cm)	δ18O (G.ruber)	StDev	δ13C (G.ruber)	StDev	δ18O (C.wuellerst.)	StDev	δ13C (C.wuellerst.)	StDev
5	-0.30	0.02	0.71	0.03	2.19	0.05	1.08	0.02
10	-0.26	0.03	0.99	0.01	2.24	0.04	1.16	0.02
15	-0.11	0.02	0.81	0.01	2.35	0.03	1.14	0.01
30	-0.41	0.06	0.55	0.02	2.32	0.03	0.65	0.03
40	-0.44	0.03	0.36	0.02	2.26	0.04	0.99	0.02
50	-0.24	0.06	0.57	0.04	2.42	0.04	0.79	0.02
60	-0.15	0.06	0.56	0.02				
70	-0.18	0.05	0.67	0.03				
80	-0.13	0.04	0.55	0.03				
90	0.16	0.03	0.65	0.01				
100	0.29	0.03	0.52	0.02				
110	0.43	0.04	0.59	0.02				
120	0.38	0.03	0.70	0.01	2.73	0.03	0.55	0.01
130	0.63	0.05	0.68	0.02				
140	0.35	0.05	0.34	0.01	2.69	0.07		
150	0.31	0.04	0.44	0.04	2.84	0.02	0.67	0.02
160	0.48	0.04	0.44	0.03				
170	0.25	0.05	0.62	0.02				
180	0.41	0.03	0.47	0.02	3.30	0.02	1.02	0.02
191	0.49	0.03	0.42	0.01	3.07	0.05	0.85	0.02
200	0.39	0.04	0.45	0.01				
210	1.04	0.02	0.42	0.02				
220	1.27	0.03	0.41	0.03				
230	1.33	0.02	0.39	0.04				
240	1.23	0.03	0.47	0.01				
250	1.25	0.04	0.35	0.02				
260	1.07	0.04	0.56	0.02				
270	1.33	0.05	0.52	0.03				
280	1.34	0.07	0.51	0.02				
290	1.12	0.03	0.46	0.02				
300	1.15	0.03	0.58	0.01				
310	1.24	0.04	0.36	0.02				
320	1.31	0.02	0.40	0.01				
330	1.10	0.03	0.54	0.03				
350	1.48	0.05	0.55	0.02				
360	1.42	0.04	0.59	0.02				
370	1.32	0.02	0.56	0.02				
380	1.40	0.01	0.42	0.02				
400	1.11	0.07	0.36	0.02				
420	1.14	0.04	0.48	0.01				
430	1.23	0.05	0.29	0.01				
441	1.13	0.02	0.51	0.01				
451	1.38	0.02	0.58	0.02				
460	1.17	0.04	0.40	0.02	3.83	0.03	1.25	0.01
469	1.30	0.02	0.73	0.02	3.44	0.03	0.52	0.03

Appendix 2: Stable isotope data

GEOFAR KF13 (37°35N 31°51 W / 2690 m water depth)

Depth (cm)	**δ18O** (G.ruber)	StDev	**δ13C** (G.ruber)	StDev	**δ18O** (C.wuellerst.)	StDev	**δ13C** (C.wuellerst.)	StDev
5	-0.28	0.03	1.03	0.01	2.34	0.02	1.17	0.01
10	-0.21	0.03	0.88	0.02	2.38	0.03	1.11	0.02
15	-0.27	0.03	0.87	0.04	2.48	0.04	0.79	0.01
22	0.36	0.03	0.55	0.02	2.68	0.04	1.07	0.02
26	-0.32	0.04	0.72	0.03	2.29	0.06	1.12	0.03
30	-0.22	0.03	0.41	0.02	2.35	0.02	1.04	0.02
35	-0.20	0.04	0.50	0.02	2.54	0.06	1.05	0.01
40	-0.19	0.02	0.59	0.01	2.50	0.06	0.94	0.03
50	-0.04	0.02	0.48	0.04	2.69	0.03	1.07	0.01
55	-0.04	0.02	0.56	0.01				
60	0.74	0.06	0.62	0.02				
65	0.68	0.03	0.19	0.02	2.58	0.05	0.65	0.04
73	0.46	0.05	0.48	0.02	3.02	0.03	1.10	0.02
82	0.53	0.03	0.36	0.02	3.19	0.07	1.09	0.02
90	0.57	0.04	0.44	0.02				
100	0.67	0.02	0.49	0.02	3.22	0.04	0.91	0.01
110	1.13	0.03	0.48	0.02				
120	1.30	0.04	0.27	0.02				
130	1.36	0.02	0.46	0.02	3.81	0.04	0.53	0.04
140	1.15	0.05	0.32	0.02				
150	1.43	0.03	0.51	0.02	4.27	0.03	1.16	0.01
160	1.22	0.03	0.56	0.01				
170	0.98	0.04	0.42	0.02	4.03	0.03	0.92	0.02
180	1.33	0.04	0.48	0.02				
190	1.25	0.03	0.51	0.02				
200	1.47	0.04	0.44	0.03				
210	1.31	0.02	0.50	0.01				
220	1.33	0.06	0.37	0.05				
230	1.39	0.04	0.56	0.02				
240	1.52	0.04	0.38	0.02				
250	1.11	0.01	0.38	0.01				
260	0.95	0.04	0.60	0.02	3.62	0.04	0.46	0.01
271	1.60	0.02	0.61	0.02				
280	0.90	0.04	0.68	0.03				
290	1.25	0.02	0.46	0.02	3.72	0.05	1.14	0.04
300	1.13	0.04	0.58	0.01				
310	1.14	0.03	0.42	0.02				
320	1.19	0.04	0.50	0.03	3.60	0.44	0.16	0.43
330	0.76	0.06	0.22	0.05				
340	0.61	0.04	0.15	0.02				
350	1.11	0.03	0.41	0.02				
360	0.74	0.03	0.58	0.02				
370	0.44	0.02	0.45	0.02	3.95	0.12	1.73	0.12
380	0.99	0.02	0.61	0.02				
390	1.10	0.03	0.62	0.02	3.46	0.26	1.57	0.2
401	0.88	0.03	0.44	0.03	3.87	0.05	1.34	0.02
410	0.62	0.03	0.50	0.02				
420	0.60	0.04	0.36	0.01	3.81	0.03	1.34	0.02
430	0.47	0.02	0.53	0.03	3.25	0.03	1.30	0.03
440	0.59	0.03	0.58	0.02	3.55	0.02	1.33	0.01
450	0.53	0.02	0.58	0.03	3.46	0.03	1.28	0.01
460	1.29	0.04	0.48	0.02				
470	0.70	0.03	0.51	0.01	3.75	0.07	1.42	0.01
479	0.73	0.02	0.50	0.01				
490	0.77	0.02	0.61	0.01				
500	0.48	0.03	0.43	0.02				
510	0.38	0.03	0.54	0.02	3.55	0.03	1.05	0.02
520	1.35	0.03	0.66	0.02	3.29	0.05	0.75	0.01
529	0.51	0.02	0.49	0.02				
540	0.82	0.03	0.40	0.02	3.47	0.02	0.63	0.02
550	1.19	0.03	0.13	0.02				
560	1.65	0.03	0.43	0.02				
570	1.30	0.03	0.37	0.01				
578	1.21	0.03	0.23	0.05				

Appendix 2: Stable isotope data

GEOFAR KF16 (37°60N 31°08W / 3050 m water depth)

Depth (cm)	**δ18O** (G.ruber)	StDev	**δ13C** (G.ruber)	StDev	**δ18O** (G.inflata)	StDev	**δ13C** (G.inflata)	StDev	**δ18O** (C.wuellerst.)	StDev	**δ13C** (C.wuellerst.)	StDev
5	-0.21	0.04	0.88	0.04	0.94	0.02	0.79	0.02	2.16	0.03	1.13	0.02
10	-0.16	0.03	0.95	0.02	0.94	0.04	0.80	0.01				
15	-0.12	0.03	0.90	0.02	0.94	0.03	0.84	0.02	2.22	0.02	1.14	0.03
25	-0.32	0.04	0.82	0.01	1.03	0.02	0.89	0.03	2.27	0.02	1.20	0.01
35					1.10	0.03	1.00	0.01	2.32	0.04	1.16	0.01
45	-0.31	0.01	0.83	0.02	1.12	0.04	1.08	0.01				
57	-0.43	0.06	0.72	0.05	1.02	0.03	0.75	0.01	2.26	0.03	1.20	0.02
67	-0.56	0.03	0.33	0.02	0.87	0.03	0.62	0.02	2.34	0.02	1.07	0.01
89	-0.19	0.04	0.75	0.03	0.95	0.04	0.46	0.02	2.25	0.03	0.90	0.01
95	-0.09	0.03	0.60	0.03	0.95	0.03	0.49	0.02	2.36	0.02	0.69	0.01
100	-0.02	0.03	0.47	0.02	1.10	0.03	0.54	0.02	2.30	0.04	0.91	0.02
110	-0.28	0.03	0.59	0.02	0.94	0.04	0.46	0.02	2.38	0.02	0.61	0.01
120	-0.01	0.03	0.41	0.03	0.94	0.03	0.46	0.01				
130	0.13	0.06	0.42	0.02	1.10	0.03	0.48	0.01	2.38	0.02	0.49	0.04
140	-0.15	0.05	0.44	0.02	1.28	0.03	0.48	0.02				
150	-0.06	0.04	0.49	0.03	1.38	0.04	0.70	0.02				
155	-0.04	0.05	0.57	0.02	1.43	0.03	0.56	0.02				
160	0.09	0.04	0.50	0.02	1.41	0.03	0.64	0.04				
170	0.26	0.03	0.37	0.02	1.45	0.03	0.57	0.03				
180	0.23	0.03	0.40	0.02	1.38	0.03	0.53	0.02				
190	0.33	0.03	0.49	0.03	1.58	0.03	0.47	0.01				
200	0.16	0.03	0.49	0.03	1.35	0.03	0.40	0.02				
210	0.15	0.02	0.57	0.03	1.51	0.02	0.42	0.03				
220	0.19	0.04	0.57	0.03	1.61	0.03	0.59	0.02				
230	0.84	0.02	0.30	0.01	1.96	0.03	0.82	0.01				
240					1.86	0.04	0.59	0.01				
250					2.04	0.02	0.77	0.03				
261					2.03	0.05	0.80	0.03				
270					1.78	0.03	0.56	0.01				
280					1.95	0.03	0.58	0.03				
290					1.95	0.03	0.64	0.02				
300					1.94	0.03	0.63	0.02				
310					1.82	0.03	0.58	0.02				
318					1.88	0.03	0.59	0.01				
325					1.84	0.04	0.47	0.02				
335					2.02	0.03	0.73	0.02				
340					1.97	0.03	0.60	0.02				
350					1.97	0.04	0.55	0.03				
360					1.91	0.04	0.58	0.02				
370	0.38	0.02	0.19	0.02	1.65	0.04	0.31	0.04				
380	0.39	0.05	0.26	0.03	1.78	0.05	0.36	0.02	2.69	0.03	1.13	0.03
390	0.34	0.03	0.30	0.01	1.55	0.04	0.40	0.01				
400	0.29	0.06	0.32	0.05	1.57	0.03	0.26	0.03				
410	0.69	0.02	0.47	0.03	1.79	0.03	0.40	0.03	2.96	0.02	0.89	0.02
420	0.51	0.03	0.46	0.03	1.94	0.01	0.37	0.02	3.08	0.02	0.71	0.01
430	0.70	0.04	0.50	0.01	2.02	0.03	0.35	0.01				
440	1.20	0.05	0.04	0.05	2.39	0.03	0.31	0.02				
450	1.17	0.02	0.47	0.01	2.01	0.02	0.47	0.02				
460	1.66	0.03	0.27	0.01	2.50	0.02	0.50	0.02				
470	1.13	0.06	0.21	0.05	2.38	0.03	0.45	0.03				
480	1.44	0.04	0.38	0.02	2.40	0.03	0.45	0.01				
490	2.04	0.03	0.10	0.01	2.79	0.03	0.59	0.02				
500					2.79	0.03	0.67	0.02				
510	1.08	0.04	0.20	0.03	2.50	0.04	0.58	0.04				
520					2.70	0.03	0.65	0.02				
530	1.22	0.04	0.13	0.02	2.73	0.03	0.64	0.03				
540					2.79	0.03	0.57	0.02				
550					2.95	0.03	0.65	0.02				
560	2.08	0.04	0.65	0.04	2.92	0.03	0.61	0.02				
570	1.40	0.05	0.43	0.03	2.83	0.02	0.53	0.02				

Appendix 2: Stable isotope data

GEOFAR KF16 (37°60N 31°08W / 3050 m water depth)

Depth (cm)	δ18O (G.ruber)	StDev	δ13C (G.ruber)	StDev	δ18O (G.inflata)	StDev	δ13C (G.inflata)	StDev
580	1.75	0.06	0.40	0.04	2.71	0.03	0.56	0.02
590	1.13	0.03	0.64	0.03	2.66	0.03	0.57	0.03
600				0.01	2.72	0.02	0.74	0.02
610				0.03	2.51	0.04	0.64	0.03
620	1.68	0.02	0.66	0.02				
630				0.03	2.72	0.05	0.43	0.01
640	1.77	0.03	0.56	0.01	2.77	0.03	0.69	0.03
650	1.32	0.05	-0.03	0.04	2.61	0.03	0.75	0.03
660	1.72	0.03	0.46	0.02	2.66	0.03	0.65	0.01
670	1.31	0.03	0.26	0.02	2.72	0.03	0.63	0.02
680	1.20	0.04	-0.05	0.05	2.77	0.03	0.61	0.02
690	1.82	0.03	0.41	0.02	2.66	0.03	0.50	0.02
700	1.14	0.02	0.37	0.02	2.61	0.06	0.53	0.06
710	1.15	0.06	0.19	0.03	2.76	0.04	0.66	0.02
720	1.26	0.03	0.40	0.02	2.67	0.03	0.55	0.02
730	1.30	0.03	0.15	0.03	2.44	0.06	0.44	0.02
740	1.17	0.04	0.10	0.01	2.43	0.04	0.49	0.01
750	1.67	0.03	0.53	0.02	2.56	0.03	0.63	0.02
760	1.49	0.04	0.60	0.03	2.64	0.03	0.73	0.02
770	1.51	0.04	0.32	0.01	2.61	0.02	0.47	0.02
780	1.49	0.02	0.52	0.02	2.60	0.03	0.61	0.02
790	1.60	0.03	0.52	0.03	2.69	0.02	0.58	0.01
796	1.60	0.03	0.55	0.02	2.58	0.03	0.60	0.03

Appendix 3: X-ray fluorescence data

major oxides

Ac.KS04	SiO2 (%)	TiO2 (%)	Al2O3 (%)	Fe2O3 (%)	MnO (%)	MgO (%)	CaO (%)	Na2O (%)	K2O (%)	P2O5 (%)	L.O.I. (%)	Sum (%)
Surface	7.02	0.28	2.29	1.77	0.18	0.76	45.47	0.90	0.13	0.16	39.46	98.42
6	8.02	0.38	2.76	2.13	0.25	0.88	45.05	0.77	0.10	0.16	39.07	99.57
10	9.69	0.47	3.29	2.40	0.29	0.98	43.37	0.65	0.08	0.17	37.90	99.29
13	11.19	0.50	3.46	2.75	0.14	1.09	41.83	0.59	0.10	0.17	37.23	99.05
16	10.99	0.45	3.21	2.25	0.10	1.06	42.95	0.78	0.12	0.14	37.02	99.07
22	10.59	0.38	2.98	2.04	0.09	1.09	41.97	0.98	0.13	0.15	38.62	99.02
61	12.19	0.27	3.25	1.72	0.10	1.04	41.27	0.73	0.08	0.12	38.16	98.93
80	11.68	0.15	2.47	1.32	0.07	0.86	40.57	0.71	0.05	0.08	39.77	97.73
93	12.58	0.17	2.70	1.26	0.07	0.95	40.57	0.78	0.06	0.08	39.54	98.76
109	12.98	0.17	2.74	1.49	0.09	0.95	40.01	0.80	0.07	0.09	38.62	98.01
123	13.88	0.22	3.21	1.60	0.10	0.95	40.15	0.67	0.08	0.25	38.09	99.20
138	9.78	0.18	2.15	1.23	0.09	0.75	44.35	0.57	0.06	0.09	40.28	99.53
155	9.78	0.18	2.30	1.50	0.10	0.91	43.93	0.71	0.06	0.10	40.03	99.60
184	8.32	0.17	1.98	1.14	0.09	0.76	45.05	0.70	0.06	0.10	40.83	99.20
200	8.92	0.18	2.34	1.36	0.11	0.81	44.77	1.04	0.08	0.11	40.14	99.86
238	44.49	1.43	14.28	8.71	0.20	6.48	15.67	2.14	0.60	0.27	4.25	98.52
239	44.92	1.45	14.39	8.89	0.20	6.57	15.53	2.40	0.63	0.25	3.69	98.92
249	22.25	0.67	6.61	4.69	0.15	3.13	32.74	1.21	0.20	0.17	27.27	99.09
255	8.53	0.20	2.32	1.19	0.12	0.73	45.19	0.53	0.07	0.13	40.19	99.20
271	10.29	0.25	2.78	1.59	0.13	0.85	43.51	0.50	0.07	0.13	39.20	99.30
280	31.66	0.93	9.27	6.06	0.16	3.63	24.34	1.73	0.37	0.19	20.61	98.95
283	22.67	0.53	5.91	4.78	0.14	2.06	30.92	1.13	0.22	0.13	30.05	98.54
295	18.89	0.42	5.01	2.69	0.11	1.36	35.67	0.89	0.14	0.12	33.79	99.09
310	42.35	1.35	13.58	8.65	0.20	5.37	16.93	2.20	0.54	0.22	7.28	98.67
323	13.99	0.25	3.55	1.79	0.14	1.01	39.87	0.61	0.07	0.10	37.59	98.97
330	17.39	0.35	4.42	3.80	0.13	1.62	35.95	0.96	0.12	0.12	33.97	98.83
342	17.48	0.47	4.99	3.58	0.14	1.87	36.93	0.73	0.12	0.13	32.34	98.78
353	34.87	1.17	10.99	7.49	0.18	4.69	22.24	2.12	0.42	0.24	14.35	98.76
358	8.64	0.20	2.57	1.27	0.13	0.76	44.63	0.70	0.05	0.11	40.33	99.39
366	6.33	0.15	1.53	2.02	0.14	0.63	46.45	0.39	0.04	0.12	41.39	99.19
381	10.99	0.23	3.04	2.03	0.11	0.91	42.67	0.66	0.06	0.11	38.80	99.61

Appendix 3: X-ray fluorescence data

major oxides

GEOFAR	SiO2 (%)	TiO2 (%)	Al2O3 (%)	Fe2O3 (%)	MnO (%)	MgO (%)	CaO (%)	Na2O (%)	K2O (%)	P2O5 (%)	SO3 (%)	CO2 (%)	H2O (%)	L.O.I. (%)	Sum (%)
KF09-															
5	3.47	0.13	1.23	3.96	0.170	0.41	49.10	0.05	0.14	0.296	0.071	37.96	1.76	39.72	98.75
10	3.81	0.15	1.32	4.30	0.183	0.46	48.13	0.26	0.16	0.302	<0.05	37.76	1.92	39.68	98.76
15	4.13	0.17	1.40	4.50	0.210	0.50	48.13	0.26	0.17	0.300	0.071	37.59	1.93	39.51	99.36
18	4.58	0.18	1.47	4.50	0.458	0.55	46.31	0.89	0.20	0.279	<0.05	36.85	2.41	39.26	98.68
20	4.60	0.20	1.64	4.62	0.871	0.51	46.82	0.18	0.18	0.286	<0.05	37.17	2.18	39.35	99.26
22	5.07	0.22	1.64	4.53	0.973	0.53	46.47	0.32	0.19	0.295	<0.05	37.05	2.23	39.28	99.52
25	5.48	0.23	1.79	4.33	0.222	0.23	47.15	0.28	0.20	0.280	<0.05	36.81	1.83	38.64	98.83
30	6.89	0.32	2.27	3.16	0.098	0.32	47.43	0.28	0.27	0.225	<0.05	36.74	1.64	38.38	99.64
35	7.53	0.33	2.42	2.52	0.571	0.65	46.52	0.28	0.30	0.204	<0.05	36.90	0.98	37.87	99.21
37	8.11	0.33	2.46	2.62	0.102	0.61	46.03	0.30	0.33	0.198	<0.05	36.75	1.08	37.83	98.92
43	8.43	0.33	2.44	2.55	0.100	0.70	45.80	0.53	0.36	0.170	0.075	35.92	1.62	37.54	99.03
50	8.73	0.33	2.44	2.04	0.089	0.70	46.07	0.40	0.36	0.151	0.109	36.46	0.92	37.38	98.80
90	9.92	0.28	2.49	1.64	0.097	0.75	44.87	0.97	0.42	0.167	0.187	34.82	1.81	36.63	98.42
150	9.60	0.22	2.44	1.54	0.119	0.70	44.85	0.82	0.46	0.141	0.133	35.08	1.90	36.99	98.00
210	14.57	0.22	3.42	2.45	0.112	0.93	40.32	0.49	0.74	0.134	0.145	32.10	2.78	34.88	98.41
240	15.19	0.17	3.08	2.10	0.094	0.88	40.52	0.62	0.65	0.119	0.182	31.36	2.87	34.22	97.84
300	12.26	0.12	2.40	1.19	0.095	0.63	43.70	0.40	0.48	0.120	0.133	34.08	2.53	36.61	98.14
340	18.69	0.18	3.49	2.45	0.136	0.90	37.68	0.38	0.71	0.116	0.101	32.25	2.82	35.07	99.90
370	14.31	0.15	2.76	1.39	0.106	0.73	41.35	0.61	0.57	0.121	<0.05	32.38	1.74	34.12	96.22
403	15.79	0.15	2.83	1.69	0.109	0.73	40.79	0.35	0.55	0.119	0.170	31.64	2.88	34.53	97.80
445	9.80	0.13	2.19	0.93	0.102	0.56	45.82	0.40	0.45	0.119	0.187	36.44	1.17	37.62	98.30
465	8.66	0.13	1.85	1.30	0.094	0.48	46.59	0.22	0.37	0.122	0.436	36.69	1.18	37.87	98.12
KF13-															
5	4.11	0.18	1.47	2.85	0.186	0.45	48.91	0.13	0.18	0.237	0.073	38.23	1.52	39.76	98.53
10	4.19	0.18	1.49	2.83	0.189	0.58	46.78	1.68	0.25	0.215	0.181	36.61	1.52	38.13	96.70
19	5.28	0.20	1.72	2.60	1.690	0.53	47.36	0.44	0.24	0.190	0.105	37.92	1.70	39.62	99.98
22	5.90	0.25	1.93	3.33	0.093	0.55	47.79	0.44	0.25	0.222	0.107	35.95	2.02	37.97	98.83
33	8.86	0.32	2.57	2.07	0.104	0.65	46.13	0.46	0.37	0.173	<0.05	36.19	1.73	37.91	99.62
50	8.68	0.32	2.47	1.54	0.077	0.73	44.63	1.83	0.43	0.178	0.265	34.72	0.98	35.70	96.85
69	11.51	0.22	2.32	2.22	0.119	0.70	43.63	0.74	0.45	0.143	0.172	34.25	2.39	36.64	98.87
80	8.34	0.22	2.17	1.27	0.088	0.53	47.30	0.47	0.39	0.147	0.240	37.15	1.65	38.79	99.96
120	17.60	0.27	4.02	2.65	0.088	1.01	38.23	0.50	0.83	0.127	0.123	30.38	3.23	33.61	99.06
150	13.24	0.17	2.76	1.67	0.086	0.75	42.80	0.36	0.48	0.108	0.359	33.32	2.75	36.07	98.85
180	12.11	0.13	2.27	2.37	0.073	0.41	43.49	0.30	0.45	0.116	2.199	33.47	2.74	36.21	100.13
200	12.06	0.12	2.64	1.16	0.072	0.66	41.06	2.22	0.54	0.105	0.472	33.28	2.93	36.21	97.32
240	12.75	0.13	2.36	1.30	0.072	0.53	43.77	0.27	0.45	0.105	0.447	33.89	2.48	36.37	98.56
271	12.88	0.17	2.72	1.89	0.113	0.61	43.29	0.34	0.55	0.117	0.433	33.57	2.38	35.95	99.07
310	8.09	0.12	1.64	0.86	0.080	0.56	45.52	1.85	0.39	0.115	0.297	36.70	1.99	38.69	98.21
350	9.15	0.15	2.08	0.92	0.086	0.43	46.75	0.27	0.39	0.210	0.372	36.61	2.03	38.64	99.44
370	7.10	0.13	1.76	0.92	0.103	0.53	46.63	1.59	0.40	0.144	0.123	36.52	1.75	38.27	97.70
390	9.11	0.15	2.12	1.16	0.087	0.60	43.70	2.01	0.49	0.108	0.363	34.97	2.06	37.03	96.93
445	5.97	0.13	1.59	0.79	0.117	0.50	47.54	1.54	0.35	0.151	0.123	37.14	1.54	38.68	97.48
475	5.35	0.12	1.38	0.64	0.106	0.45	48.21	1.43	0.33	0.122	0.159	39.09	1.22	40.31	98.61
503	6.07	0.13	1.57	0.77	0.123	0.41	49.33	0.43	0.30	0.146	0.085	39.47	1.27	40.74	100.10
533	7.64	0.17	2.08	1.04	0.126	0.46	47.90	0.36	0.39	0.142	0.255	37.93	1.61	40.74	100.11
KF16-															
2	5.56	0.23	1.93	2.03	0.190	0.51	47.90	0.70	0.25	0.190	0.090	37.77	1.85	39.62	99.20
5	5.26	0.23	1.81	1.92	0.181	0.68	45.26	1.59	0.29	0.181	0.060	38.95	1.69	40.64	98.10
17	6.27	0.30	2.17	2.35	0.380	0.61	47.93	0.30	0.28	0.206	<0.05	37.44	1.60	39.04	99.84
18	6.40	0.30	2.27	2.33	0.669	0.71	47.03	0.51	0.29	0.204	<0.05	36.61	1.66	38.27	98.98
20	6.61	0.32	2.27	2.45	0.880	0.78	47.23	0.44	0.29	0.213	0.100	37.68	1.54	39.22	100.80
22	6.61	0.30	2.25	2.60	0.247	0.80	47.09	0.50	0.28	0.238	<0.05	36.72	1.77	38.49	99.41
35	7.27	0.32	2.29	2.45	0.110	1.26	44.61	1.87	0.35	0.204	0.200	35.47	1.77	37.24	98.17
49	15.19	0.37	3.72	2.40	0.135	1.48	41.51	0.51	0.52	0.169	0.060	32.92	2.02	34.94	101.00
62	10.35	0.48	3.36	2.45	0.123	1.11	43.94	1.00	0.42	0.206	<0.05	33.72	1.58	35.29	98.74
67	10.99	0.48	3.21	2.83	0.110	1.38	43.36	0.74	0.43	0.188	<0.05	33.36	2.17	35.52	99.25
69	12.77	0.47	3.19	2.67	0.112	3.47	41.06	0.69	0.41	0.185	0.050	31.45	2.54	33.99	99.07
72	15.12	0.38	2.87	3.16	0.124	6.33	37.73	0.57	0.37	0.158	<0.05	28.82	3.36	32.18	98.99
76	16.09	0.37	3.02	3.47	0.127	6.60	36.49	0.61	0.39	0.156	<0.05	27.95	3.60	31.55	98.87
78	17.15	0.32	2.83	3.80	0.137	7.94	34.58	0.55	0.39	0.144	0.050	26.50	4.22	30.72	98.61
82	16.64	0.32	2.53	3.98	0.127	8.11	32.58	2.43	0.47	0.135	0.260	24.47	1.62	26.09	93.67
85	18.46	0.32	2.59	4.69	0.138	8.87	33.07	0.46	0.41	0.140	<0.05	25.42	4.76	30.17	99.33
89	9.88	0.42	2.91	1.82	0.099	1.48	42.25	1.89	0.43	0.174	0.170	33.56	2.08	35.64	97.16
110	10.35	0.43	3.00	1.92	0.103	0.90	43.10	1.89	0.47	0.181	0.210	34.62	1.59	36.21	98.76
130	12.19	0.37	3.08	2.13	0.129	0.78	43.03	0.71	0.48	0.169	0.810	33.26	1.96	35.21	99.09
170	13.88	0.27	2.64	2.65	0.213	4.28	40.07	0.51	0.40	0.144	1.090	31.44	2.89	34.33	100.47
210	12.58	0.32	2.87	1.92	0.139	0.76	42.75	0.75	0.47	0.157	0.890	33.03	2.41	35.44	99.04

Appendix 3: X-ray fluorescence data

major oxides

	SiO2	TiO2	Al2O3	Fe2O3	MnO	MgO	CaO	Na2O	K2O	P2O5	SO3	CO2	H2O	L.O.I.	Sum
KF16-	(%)	(%)	(%)	(%)	(%)	(%)	(%)	(%)	(%)	(%)	(%)	(%)	(%)	(%)	(%)
256	14.33	0.27	2.80	1.69	0.121	0.80	41.41	0.96	0.51	0.140	0.330	32.96	3.00	35.96	99.32
307	13.84	0.28	2.93	1.57	0.139	0.80	42.18	0.65	0.54	0.144	<0.05	33.79	2.75	36.54	99.61
332	48.06	0.13	1.78	1.67	0.067	0.60	20.59	1.60	0.35	0.080	0.630	16.35	5.10	21.45	97.01
340	12.71	0.27	2.83	2.10	0.225	0.80	42.50	0.66	0.51	0.139	1.200	33.38	2.51	35.89	99.84
370	13.82	0.27	2.64	2.60	0.212	4.29	39.91	0.53	0.40	0.142	0.160	31.22	3.02	34.24	99.21
420	10.74	0.23	2.81	1.67	0.125	0.75	44.38	0.43	0.53	0.138	0.220	34.77	2.13	36.90	98.92
470	18.63	0.27	4.29	2.36	0.072	0.86	37.19	0.71	0.88	0.121	0.240	30.56	3.84	34.40	100.02
520	15.57	0.15	2.57	1.43	0.103	0.63	39.86	1.15	0.51	0.110	0.120	30.75	3.73	34.48	96.68
570	18.27	0.15	2.72	1.49	0.133	0.58	38.57	0.61	0.51	0.112	0.190	34.36	4.50	35.86	102.20
580	16.02	0.13	2.49	1.32	0.119	0.83	36.99	2.88	0.57	0.108	0.460	32.53	4.04	36.57	98.49
590	20.58	0.15	2.55	1.33	0.148	0.63	37.80	0.44	0.49	0.108	0.240	30.64	3.98	34.61	99.09
620	17.71	0.13	2.63	1.29	0.148	0.58	38.64	0.97	0.52	0.112	0.080	30.18	4.16	34.34	97.15
666	20.79	0.13	2.78	1.29	0.127	0.53	37.07	0.47	0.49	0.112	1.220	28.59	3.71	32.30	97.31
740	14.63	0.15	2.49	1.22	0.108	0.56	41.48	0.66	0.49	0.121	0.200	33.11	3.76	36.87	98.98
796	14.72	0.15	2.51	1.36	0.139	0.60	40.98	1.02	0.51	0.117	0.270	32.48	3.48	35.96	98.34
KF7-S	16.41	0.40	5.70	3.65	0.135	2.39	38.52	1.27	0.23	0.169	0.053	27.61	1.83	29.45	98.37
KF10-S	19.57	0.38	6.67	4.05	0.154	3.27	36.39	1.13	0.20	0.183	0.061	24.84	1.66	26.5	98.56
KF10-66	6.89	0.18	2.17	1.46	0.051	0.90	47.66	0.82	0.22	0.098	<0.05	33.61	0.29	33.9	94.35
KG18-S	16.63	0.45	6.08	4.63	0.155	2.86	36.10	1.96	0.22	0.216	0.227	24.92	1.77	26.69	96.22
KG18-13	48.34	1.13	17.28	8.28	0.140	8.02	9.30	2.44	0.35	0.343	0.198	0.27	0.77	1.04	96.86
92KS04-															
115	32.06	1.08	9.97	7.72	0.114	4.16	24.57	1.42	0.65	0.208	<0.05	14.99	2.71	17.70	99.65
122	46.17	1.48	15.02	9.72	0.160	6.00	14.83	2.21	0.60	0.250	0.127	2.75	0.66	20.27	99.98
180	48.90	1.67	15.41	10.93	0.175	6.47	12.33	2.39	0.64	0.276	<0.05	0.53	0.61	11.73	100.33
237	31.36	1.25	9.39	8.42	0.119	3.71	24.43	1.70	0.77	0.245	0.156	18.48	1.79	3.42	101.82
254	38.05	1.58	11.45	9.32	0.144	4.24	19.07	2.14	0.86	0.300	0.152	9.63	2.10	1.14	99.04
265	52.58	1.87	14.56	11.20	0.179	5.75	11.77	3.28	0.90	0.327	0.195	1.10	0.72	1.81	104.43
KF01-															
5	3.72	0.15	1.30	1.97	0.151	0.50	48.20	1.46	0.22	0.180	0.192	39.19	1.21	40.40	98.44
35	6.40	0.27	1.98	1.46	0.241	0.66	46.84	1.51	0.33	0.118	0.165	36.26	0.90	37.16	97.13
46	6.35	0.22	1.78	1.24	0.036	0.65	47.31	1.63	0.35	0.099	0.167	36.75	1.20	37.95	97.78
85	12.60	0.17	3.00	1.52	0.036	0.98	39.89	2.62	0.71	0.117	0.347	32.48	2.49	34.97	96.96
KF12-															
5	4.09	0.15	1.45	2.80	0.196	0.66	46.25	1.78	0.25	0.231	0.172	36.71	2.52	39.23	97.26
35	4.73	0.22	1.70	3.42	0.821	0.71	45.37	1.79	0.27	0.222	0.095	36.32	1.84	38.16	97.51
50	6.25	0.28	2.12	3.69	0.364	0.78	44.24	1.79	0.33	0.224	0.200	35.72	2.42	38.14	98.41
95	8.49	0.32	2.47	1.42	0.089	0.76	44.82	1.85	0.42	0.157	0.193	36.16	1.24	37.40	98.39
KS03-															
6	9.01	0.22	3.25	2.33	0.161	0.91	44.92	0.28	0.48	0.132	0.066	35.44	2.36	37.80	99.56
32	21.65	0.50	7.10	4.50	0.167	2.16	32.15	1.05	0.84	0.117	0.192	24.66	4.25	28.91	99.34
42	35.76	0.92	11.86	9.48	0.138	6.08	17.92	1.94	0.65	0.148	0.219	10.96	4.27	15.23	100.35
63	14.99	0.38	5.33	3.43	0.173	1.59	39.54	0.30	0.66	0.118	0.122	30.59	2.44	33.03	99.66
85	42.67	1.05	14.09	10.22	0.166	7.44	12.03	2.21	0.57	0.164	0.126	5.35	5.20	10.55	101.29
115	14.87	0.37	5.46	3.40	0.190	1.43	35.95	2.24	0.83	0.100	0.193	27.71	3.98	31.69	96.72
186	18.25	0.37	5.99	3.52	0.205	1.13	37.02	0.38	0.95	0.099	0.086	29.13	2.83	31.96	99.96
260	13.82	0.30	4.85	2.97	0.184	1.26	38.93	1.35	0.80	0.106	0.174	29.86	3.45	33.31	98.05
341	6.89	0.15	2.47	1.64	0.120	0.61	46.32	1.05	0.41	0.092	0.224	35.47	1.76	37.23	97.21
390	11.36	0.27	4.25	2.42	0.119	0.86	41.52	1.31	0.61	0.089	0.122	33.00	2.24	35.24	98.17
410	6.89	0.17	2.36	1.52	0.080	0.60	47.24	0.96	0.40	0.064	0.153	36.10	1.48	37.58	98.02
450	16.49	0.37	5.70	3.46	0.183	1.24	35.27	1.95	0.96	0.091	0.252	27.03	3.08	30.11	96.08

Appendix 3: X-ray fluorescence data

major elements

Ac.KS04	Si (%)	Ti (%)	Al (%)	Fe (%)	Mn (ppm)	Mg (%)	Ca (%)	Na (%)	K (%)	P (ppm)	L.O.I. (%)
0	3.28	0.17	1.21	1.24	1382	0.46	32.50	0.67	0.11	680	39.46
6	3.75	0.23	1.46	1.49	1948	0.53	32.20	0.57	0.08	680	39.07
10	4.53	0.28	1.74	1.68	2215	0.59	31.00	0.48	0.07	740	37.90
13	5.23	0.30	1.83	1.92	1080	0.66	29.90	0.44	0.08	740	37.23
16	5.14	0.27	1.70	1.57	751	0.64	30.70	0.58	0.10	600	37.02
22	4.95	0.23	1.58	1.43	684	0.66	30.00	0.73	0.11	670	38.62
61	5.70	0.16	1.72	1.20	736	0.63	29.50	0.54	0.07	530	38.16
80	5.46	0.09	1.31	0.92	574	0.52	29.00	0.53	0.04	330	39.77
93	5.88	0.10	1.43	0.88	571	0.57	29.00	0.58	0.05	360	39.54
109	6.07	0.10	1.45	1.04	712	0.57	28.60	0.59	0.06	380	38.62
123	6.49	0.13	1.70	1.12	747	0.57	28.70	0.50	0.07	1110	38.09
138	4.57	0.11	1.14	0.86	671	0.45	31.70	0.42	0.05	400	40.28
155	4.57	0.11	1.22	1.05	745	0.55	31.40	0.53	0.05	440	40.03
184	3.89	0.10	1.05	0.80	714	0.46	32.20	0.52	0.05	430	40.83
200	4.17	0.11	1.24	0.95	819	0.49	32.00	0.77	0.07	480	40.14
238	20.80	0.86	7.56	6.09	1528	3.91	11.20	1.59	0.50	1180	4.25
239	21.00	0.87	7.62	6.22	1542	3.96	11.10	1.78	0.52	1090	3.69
249	10.40	0.40	3.50	3.28	1162	1.89	23.40	0.90	0.17	730	27.27
255	3.99	0.12	1.23	0.83	958	0.44	32.30	0.39	0.06	550	40.19
271	4.81	0.15	1.47	1.11	1010	0.51	31.10	0.37	0.06	580	39.20
280	14.80	0.56	4.91	4.24	1277	2.19	17.40	1.28	0.31	830	20.61
283	10.60	0.32	3.13	3.34	1090	1.24	22.10	0.84	0.18	550	30.05
295	8.83	0.25	2.65	1.88	867	0.82	25.50	0.66	0.12	510	33.79
310	19.80	0.81	7.19	6.05	1532	3.24	12.10	1.63	0.45	980	7.28
323	6.54	0.15	1.88	1.25	1063	0.61	28.50	0.45	0.06	430	37.59
330	8.13	0.21	2.34	2.66	995	0.98	25.70	0.71	0.10	530	33.97
342	8.17	0.28	2.64	2.50	1054	1.13	26.40	0.54	0.10	580	32.34
353	16.30	0.70	5.82	5.24	1412	2.83	15.90	1.57	0.35	1050	14.35
358	4.04	0.12	1.36	0.89	986	0.46	31.90	0.52	0.04	490	40.33
366	2.96	0.09	0.81	1.41	1070	0.38	33.20	0.29	0.03	530	41.39
381	5.14	0.14	1.61	1.42	842	0.55	30.50	0.49	0.05	480	38.80

Appendix 3: X-ray fluorescence data

major elements

GEOFAR	Si (%)	Ti (%)	Al (%)	Fe (%)	Mn (ppm)	Mg (%)	Ca (%)	Na (%)	K (%)	P (ppm)	SO3 (%)	CO2 (%)	H2O (%)	L.O.I. (%)
KF09-														
5	1.62	0.08	0.65	2.77	1317	0.25	35.10	0.04	0.12	1293	0.071	37.96	1.76	39.72
10	1.78	0.09	0.70	3.01	1418	0.28	34.40	0.19	0.13	1319	<0.05	37.76	1.92	39.68
15	1.93	0.10	0.74	3.15	1627	0.30	34.40	0.19	0.14	1310	0.071	37.59	1.93	39.51
18	2.14	0.11	0.78	3.15	3550	0.33	33.10	0.66	0.17	1218	<0.05	36.85	2.41	39.26
20	2.15	0.12	0.87	3.23	6750	0.31	33.47	0.13	0.15	1249	<0.05	37.17	2.18	39.35
22	2.37	0.13	0.87	3.17	7540	0.32	33.22	0.24	0.16	1288	<0.05	37.05	2.23	39.28
25	2.56	0.14	0.95	3.03	1720	0.14	33.70	0.21	0.17	1223	<0.05	36.81	1.83	38.64
30	3.22	0.19	1.20	2.21	759	0.19	33.90	0.21	0.22	983	<0.05	36.74	1.64	38.38
35	3.52	0.20	1.28	1.76	4420	0.39	33.25	0.21	0.25	891	<0.05	36.90	0.98	37.87
37	3.79	0.20	1.30	1.83	790	0.37	32.90	0.22	0.27	865	<0.05	36.75	1.08	37.83
43	3.94	0.20	1.29	1.78	775	0.42	32.74	0.39	0.30	742	0.075	35.92	1.62	37.54
50	4.08	0.20	1.29	1.43	689	0.42	32.93	0.30	0.30	659	0.109	36.46	0.92	37.38
90	4.64	0.17	1.32	1.15	750	0.45	32.07	0.72	0.35	729	0.187	34.82	1.81	36.63
150	4.49	0.13	1.29	1.08	922	0.42	32.06	0.61	0.38	616	0.133	35.08	1.90	36.99
210	6.81	0.13	1.81	1.71	868	0.56	28.82	0.36	0.61	585	0.145	32.10	2.78	34.88
240	7.10	0.10	1.63	1.47	728	0.53	28.96	0.46	0.54	520	0.182	31.36	2.87	34.22
300	5.73	0.07	1.27	0.83	736	0.38	31.24	0.30	0.40	524	0.133	34.08	2.53	36.61
340	8.74	0.11	1.85	1.71	1053	0.54	26.93	0.28	0.59	507	0.101	32.25	2.82	35.07
370	6.69	0.09	1.46	0.97	821	0.44	29.56	0.45	0.47	528	<0.05	32.38	1.74	34.12
403	7.38	0.09	1.50	1.18	844	0.44	29.16	0.26	0.46	520	0.170	31.64	2.88	34.53
445	4.58	0.08	1.16	0.65	790	0.34	32.75	0.30	0.37	520	0.187	36.44	1.17	37.62
465	4.05	0.08	0.98	0.91	728	0.29	33.30	0.16	0.31	533	0.436	36.69	1.18	37.87
92KS04-														
115	14.99	0.65	5.28	5.40	883	2.51	17.56	1.05	0.54	908	<0.05	14.99	2.71	17.70
122	22.27	0.89	7.95	6.80	1240	3.62	10.60	1.64	0.50	1090	0.127	18.48	1.79	20.27
180	22.86	1.00	8.16	7.64	1356	3.90	8.81	1.77	0.53	1205	<0.05	9.63	2.10	11.73
237	14.66	0.75	4.97	5.89	922	2.24	17.46	1.26	0.64	1070	0.156	2.75	0.66	3.42
254	17.79	0.95	6.06	6.52	1115	2.56	13.63	1.59	0.71	1310	0.152	0.53	0.61	1.14
265	24.58	1.12	7.71	7.83	1387	3.47	8.41	2.43	0.75	1430	0.195	1.10	0.72	1.81
KF16-														
2	2.60	0.14	1.02	1.42	1470	0.31	34.24	0.52	0.21	830	0.090	37.77	1.85	39.62
5	2.46	0.14	0.96	1.34	1400	0.41	32.35	1.18	0.24	790	0.060	38.95	1.69	40.64
17	2.93	0.18	1.15	1.64	2940	0.37	34.26	0.22	0.23	900	<0.05	37.44	1.60	39.04
18	2.99	0.18	1.20	1.63	5180	0.43	33.62	0.38	0.24	890	<0.05	36.61	1.66	38.27
20	3.09	0.19	1.20	1.71	6820	0.47	33.76	0.33	0.24	930	0.100	37.68	1.54	39.22
22	3.09	0.18	1.19	1.82	1910	0.48	33.66	0.37	0.23	1040	<0.05	36.72	1.77	38.49
35	3.40	0.19	1.21	1.71	850	0.76	31.89	1.39	0.29	890	0.200	35.47	1.77	37.24
49	7.10	0.22	1.97	1.68	1045	0.89	29.67	0.38	0.43	740	0.060	32.92	2.02	34.94
62	4.84	0.29	1.78	1.71	950	0.67	31.41	0.74	0.35	900	<0.05	33.72	1.58	35.29
67	5.14	0.29	1.70	1.98	850	0.83	30.99	0.55	0.36	820	<0.05	33.36	2.17	35.52
69	5.97	0.28	1.69	1.87	870	2.09	29.35	0.51	0.34	810	0.050	31.45	2.54	33.99
72	7.07	0.23	1.52	2.21	960	3.82	26.97	0.42	0.31	690	<0.05	28.82	3.36	32.18
76	7.52	0.22	1.60	2.43	980	3.98	26.08	0.45	0.32	680	<0.05	27.95	3.60	31.55
78	8.02	0.19	1.50	2.66	1060	4.79	24.72	0.41	0.32	630	0.050	26.50	4.22	30.72
82	7.78	0.19	1.34	2.78	980	4.89	23.29	1.80	0.39	590	0.260	24.47	1.62	26.09
85	8.63	0.19	1.37	3.28	1070	5.35	23.64	0.34	0.34	610	<0.05	25.42	4.76	30.17
89	4.62	0.25	1.54	1.27	770	0.89	30.20	1.40	0.36	760	0.170	33.56	2.08	35.64
110	4.84	0.26	1.59	1.34	800	0.54	30.81	1.40	0.39	790	0.210	34.62	1.59	36.21
130	5.70	0.22	1.63	1.49	1000	0.47	30.76	0.53	0.40	738	0.810	33.26	1.96	35.21
170	6.49	0.16	1.40	1.85	1650	2.58	28.64	0.38	0.33	629	1.090	31.44	2.89	34.33
210	5.88	0.19	1.52	1.34	1080	0.46	30.56	0.56	0.39	686	0.890	33.03	2.41	35.44
256	6.70	0.16	1.48	1.18	940	0.48	29.60	0.71	0.42	610	0.330	32.96	3.00	35.96
307	6.47	0.17	1.55	1.10	1080	0.48	30.15	0.48	0.45	630	<0.05	33.79	2.75	36.54
332	22.47	0.08	0.94	1.17	520	0.36	14.72	1.19	0.29	350	0.630	16.35	5.10	21.45
340	5.94	0.16	1.50	1.47	1740	0.48	30.38	0.49	0.42	607	1.200	33.38	2.51	35.89
370	6.46	0.16	1.40	1.82	1640	2.59	28.53	0.39	0.33	620	0.160	31.22	3.02	34.24
420	5.02	0.14	1.49	1.17	968	0.45	31.72	0.32	0.44	603	0.220	34.77	2.13	36.90
470	8.71	0.16	2.27	1.65	560	0.52	26.58	0.53	0.73	530	0.240	30.56	3.84	34.40
520	7.28	0.09	1.36	1.00	800	0.38	28.49	0.85	0.42	480	0.120	30.75	3.73	34.48
570	8.54	0.09	1.44	1.04	1030	0.35	27.57	0.45	0.42	490	0.190	34.36	4.50	35.86
580	7.49	0.08	1.32	0.92	920	0.50	26.44	2.14	0.47	470	0.460	32.53	4.04	36.57
590	9.62	0.09	1.35	0.93	1150	0.38	27.02	0.33	0.41	470	0.240	30.64	3.98	34.61

Appendix 3: X-ray fluorescence data

major elements

GEOFAR	Si	Ti	Al	Fe	Mn	Mg	Ca	Na	K	P	SO3	CO2	H2O	L.O.I.
KF16-	(%)	(%)	(%)	(%)	(ppm)	(%)	(%)	(%)	(%)	(ppm)	(%)	(%)	(%)	(%)
620	8.28	0.08	1.39	0.90	1150	0.35	27.62	0.72	0.43	490	0.080	30.18	4.16	34.34
666	9.72	0.08	1.47	0.90	980	0.32	26.50	0.35	0.41	489	1.220	28.59	3.71	32.30
740	6.84	0.09	1.32	0.85	835	0.34	29.65	0.49	0.41	530	0.200	33.11	3.76	36.87
796	6.88	0.09	1.33	0.95	1080	0.36	29.29	0.76	0.42	510	0.270	32.48	3.48	35.96
KF13-														
5	1.92	0.11	0.78	1.99	1441	0.27	34.96	0.10	0.15	1035	0.073	38.23	1.52	39.76
10	1.96	0.11	0.79	1.98	1464	0.35	33.44	1.25	0.21	937	0.181	36.61	1.52	38.13
19	2.47	0.12	0.91	1.82	13090	0.32	33.85	0.33	0.20	828	0.105	37.92	1.70	39.62
22	2.76	0.15	1.02	2.33	720	0.33	34.16	0.33	0.21	968	0.107	35.95	2.02	37.97
33	4.14	0.19	1.36	1.45	806	0.39	32.97	0.34	0.31	755	<0.05	36.19	1.73	37.91
50	4.06	0.19	1.31	1.08	596	0.44	31.90	1.36	0.36	776	0.265	34.72	0.98	35.70
69	5.38	0.13	1.23	1.55	922	0.42	31.19	0.55	0.37	624	0.172	34.25	2.39	36.64
80	3.90	0.13	1.15	0.89	682	0.32	33.81	0.35	0.32	642	0.240	37.15	1.65	38.79
120	8.23	0.16	2.13	1.85	682	0.61	27.33	0.37	0.69	555	0.123	30.38	3.23	33.61
150	6.19	0.10	1.46	1.17	666	0.45	30.59	0.27	0.40	472	0.359	33.32	2.75	36.07
180	5.66	0.08	1.20	1.66	565	0.25	31.09	0.22	0.37	507	2.199	33.47	2.74	36.21
200	5.64	0.07	1.40	0.81	558	0.40	29.35	1.65	0.45	458	0.472	33.28	2.93	36.21
240	5.96	0.08	1.25	0.91	558	0.32	31.29	0.20	0.37	459	0.447	33.89	2.48	36.37
271	6.02	0.10	1.44	1.32	875	0.37	30.94	0.25	0.46	511	0.433	33.57	2.38	35.95
310	3.78	0.07	0.87	0.60	620	0.34	32.54	1.37	0.32	501	0.297	36.70	1.99	38.69
350	4.28	0.09	1.10	0.64	666	0.26	33.42	0.20	0.32	917	0.372	36.61	2.03	38.64
370	3.32	0.08	0.93	0.64	798	0.32	33.33	1.18	0.33	628	0.123	36.52	1.75	38.27
390	4.26	0.09	1.12	0.81	674	0.36	31.24	1.49	0.41	471	0.363	34.97	2.06	37.03
445	2.79	0.08	0.84	0.55	906	0.30	33.98	1.14	0.29	658	0.123	37.14	1.54	38.68
475	2.50	0.07	0.73	0.45	821	0.27	34.46	1.06	0.27	532	0.159	39.09	1.22	40.31
503	2.84	0.08	0.83	0.54	953	0.25	35.26	0.32	0.25	638	0.085	39.47	1.27	40.74
533	3.57	0.10	1.10	0.73	976	0.28	34.24	0.27	0.32	620	0.255	37.93	1.61	40.74
KF7-S	7.67	0.24	3.02	2.55	1046	1.44	38.52	0.94	0.19	740	0.053	27.61	1.83	29.5
KF10-S	9.15	0.23	3.53	2.83	1193	1.97	36.39	0.84	0.17	800	0.061	24.84	1.66	26.5
KF10-66	3.22	0.11	1.15	1.02	395	0.54	47.66	0.61	0.18	430	<0.05	33.61	0.29	33.9
KG18-S	17.89	0.62	7.41	7.46	1200	3.96	25.78	1.45	0.37	3200	0.227	24.92	1.77	26.7
KG18-13	22.60	0.68	9.15	5.79	1084	4.84	9.30	1.81	0.29	1500	0.198	0.27	0.77	1.04
KF01-														
5	1.74	0.09	0.69	1.38	1170	0.30	34.45	1.08	0.18	785	0.192	39.19	1.21	40.4
35	2.99	0.16	1.05	1.02	1870	0.40	33.48	1.12	0.27	514	0.165	36.26	0.90	37.2
46	2.97	0.13	0.94	0.87	278	0.39	33.82	1.21	0.29	432	0.167	36.75	1.20	38
85	5.89	0.10	1.59	1.06	279	0.59	28.51	1.94	0.59	510	0.347	32.48	2.49	35
KF12-														
5	1.91	0.09	0.77	1.96	1520	0.40	33.06	1.32	0.21	1007	0.172	36.71	2.52	39.2
35	2.21	0.13	0.90	2.39	6360	0.43	32.43	1.33	0.22	968	0.095	36.32	1.84	38.2
50	2.92	0.17	1.12	2.58	2820	0.47	31.62	1.33	0.27	977	0.200	35.72	2.42	38.1
95	3.97	0.19	1.31	0.99	690	0.46	32.04	1.37	0.35	685	0.193	36.16	1.24	37.4
KS03-														
6	4.21	0.13	1.72	1.63	1250	0.55	32.11	0.21	0.40	576	0.066	35.44	2.36	37.8
32	10.12	0.30	3.76	3.15	1290	1.30	22.98	0.78	0.70	510	0.192	24.66	4.25	28.9
42	16.72	0.55	6.28	6.63	1070	3.67	12.81	1.44	0.54	645	0.219	10.96	4.27	15.2
63	7.01	0.23	2.82	2.40	1340	0.96	28.26	0.22	0.55	514	0.122	30.59	2.44	33
85	19.95	0.63	7.46	7.15	1285	4.49	8.60	1.64	0.47	715	0.126	5.35	5.20	10.6
115	6.95	0.22	2.89	2.38	1470	0.86	25.70	1.66	0.69	436	0.193	27.71	3.98	31.7
186	8.53	0.22	3.17	2.46	1590	0.68	26.46	0.28	0.79	432	0.086	29.13	2.83	32
260	6.46	0.18	2.57	2.08	1425	0.76	27.83	1.00	0.66	462	0.174	29.86	3.45	33.3
341	3.22	0.09	1.31	1.15	930	0.37	33.11	0.78	0.34	401	0.224	35.47	1.76	37.2
390	5.31	0.16	2.25	1.69	922	0.52	29.68	0.97	0.51	388	0.122	33.00	2.24	35.2
410	3.22	0.10	1.25	1.06	620	0.36	33.77	0.71	0.33	279	0.153	36.10	1.48	37.6
450	7.71	0.22	3.02	2.42	1420	0.75	25.21	1.45	0.80	397	0.252	27.03	3.08	30.1

Appendix 3: X-ray fluorescence data

major elements (carbonate-free basis)

GEOFAR	Si (%)	Ti (%)	Al (%)	Fe (%)	Mn (%)	Mg (%)	K (%)	P (%)
KF09-								
5	12.89	0.64	5.17	22.04	1.05	1.99	0.95	1.03
10	12.40	0.63	4.88	20.98	0.99	1.95	0.91	0.92
15	13.45	0.70	5.16	21.95	1.13	2.09	0.98	0.91
18	12.12	0.62	4.42	17.85	2.01	1.87	0.96	0.69
20	12.87	0.72	5.21	19.33	4.04	1.86	0.90	0.75
22	13.66	0.75	5.01	18.27	4.35	1.84	0.92	0.74
25	15.87	0.87	5.89	18.78	1.07	0.87	1.05	0.76
30	20.61	1.22	7.68	14.15	0.49	1.22	1.41	0.63
35	20.38	1.16	7.41	10.19	2.56	2.26	1.45	0.52
37	20.87	1.10	7.16	10.08	0.44	2.04	1.49	0.48
43	21.22	1.08	6.95	9.59	0.42	2.26	1.62	0.40
50	22.55	1.11	7.13	7.90	0.38	2.32	1.66	0.36
90	22.89	0.84	6.51	5.67	0.37	2.22	1.73	0.36
150	22.12	0.64	6.35	5.32	0.45	2.07	1.87	0.30
210	23.86	0.46	6.34	5.99	0.30	1.96	2.14	0.20
240	25.19	0.35	5.78	5.21	0.26	1.88	1.92	0.18
300	25.59	0.31	5.67	3.71	0.33	1.70	1.79	0.23
340	26.21	0.33	5.55	5.13	0.32	1.62	1.77	0.15
370	25.09	0.34	5.48	3.64	0.31	1.65	1.76	0.20
403	26.66	0.33	5.42	4.26	0.30	1.59	1.66	0.19
445	24.70	0.43	6.26	3.51	0.43	1.83	2.00	0.28
465	23.62	0.47	5.71	5.31	0.42	1.69	1.81	0.31
KF13-								
5	14.52	0.83	5.90	15.05	1.09	2.04	0.78	0.78
10	10.54	0.59	4.25	10.65	0.78	1.88	0.42	0.50
19	15.68	0.76	5.78	11.56	8.31	2.03	0.28	0.53
22	18.45	1.00	6.82	15.57	0.48	2.21	0.41	0.65
33	23.18	1.06	7.61	8.12	0.45	2.18	0.18	0.42
50	18.04	0.84	5.82	4.80	0.26	1.96	0.19	0.34
69	24.18	0.58	5.53	6.97	0.41	1.89	0.21	0.28
80	24.87	0.83	7.33	5.68	0.43	2.04	0.20	0.41
120	26.52	0.52	6.86	5.96	0.22	1.97	0.21	0.18
150	25.41	0.41	5.99	4.80	0.27	1.85	0.54	0.19
180	23.56	0.33	5.00	6.91	0.24	1.04	0.61	0.21
200	19.27	0.24	4.78	2.77	0.19	1.37	0.45	0.16
240	25.84	0.35	5.42	3.94	0.24	1.39	0.50	0.20
271	25.31	0.42	6.05	5.55	0.37	1.56	0.53	0.21
310	18.03	0.33	4.15	2.86	0.30	1.62	0.65	0.24
350	25.33	0.53	6.51	3.79	0.39	1.54	0.34	0.54
370	17.58	0.42	4.93	3.39	0.42	1.69	0.16	0.33
390	17.52	0.37	4.61	3.33	0.28	1.48	0.24	0.19
445	16.18	0.46	4.87	3.19	0.53	1.74	0.33	0.38
475	15.69	0.44	4.58	2.82	0.52	1.69	0.19	0.33
503	27.27	0.77	7.97	5.19	0.92	2.40	0.38	0.61
533	25.69	0.72	7.91	5.25	0.70	2.01	0.33	0.45
KF16-								
2	15.32	0.82	6.01	8.37	0.87	1.83	1.24	0.49
5	16.22	0.92	6.33	8.83	0.92	2.70	1.58	0.52
17	19.52	1.20	7.66	10.93	1.96	2.47	1.53	0.60
18	16.94	1.02	6.80	9.24	2.93	2.44	1.36	0.50
20	17.77	1.09	6.90	9.83	3.92	2.70	1.38	0.53
22	17.63	1.03	6.79	10.38	1.09	2.74	1.31	0.59
35	18.66	1.04	6.64	9.39	0.47	4.17	1.59	0.49
49	25.78	0.80	7.15	6.10	0.38	3.23	1.56	0.27
62	21.86	1.31	8.04	7.72	0.43	3.03	1.58	0.41
67	21.44	1.21	7.09	8.26	0.35	3.46	1.50	0.34
69	21.85	1.02	6.19	6.84	0.32	7.65	1.24	0.30
72	20.01	0.65	4.30	6.25	0.27	10.81	0.88	0.20
76	20.49	0.60	4.36	6.62	0.27	10.84	0.87	0.19
78	20.51	0.49	3.84	6.80	0.27	12.25	0.82	0.16
82	20.11	0.49	3.46	7.19	0.25	12.64	1.01	0.15
85	20.30	0.45	3.22	7.71	0.23	12.58	0.80	0.13
89	22.38	1.21	7.46	6.15	0.37	4.31	1.74	0.37
110	24.20	1.30	7.95	6.70	0.40	2.70	1.95	0.40
130	23.26	0.90	6.65	6.08	0.41	1.92	1.63	0.30
170	22.69	0.56	4.89	6.47	0.58	9.02	1.15	0.22
210	23.50	0.76	6.07	5.36	0.43	1.84	1.56	0.27
256	23.66	0.56	5.23	4.17	0.33	1.69	1.48	0.22
307	25.84	0.68	6.19	4.39	0.43	1.92	1.80	0.25
332	36.06	0.13	1.51	1.88	0.08	0.58	0.47	0.06
340	24.53	0.66	6.19	6.07	0.72	1.98	1.73	0.25
370	22.18	0.55	4.81	6.25	0.56	8.89	1.13	0.21
420	23.83	0.66	7.07	5.55	0.46	2.14	2.09	0.29
470	25.82	0.47	6.73	4.89	0.17	1.54	2.16	0.16
KF16-								
520	23.12	0.29	4.32	3.18	0.25	1.21	1.33	0.15
570	28.84	0.30	4.86	3.51	0.35	1.18	1.42	0.17
580	25.55	0.27	4.50	3.14	0.31	1.71	1.60	0.16
590	31.16	0.29	4.37	3.01	0.37	1.23	1.33	0.15
620	27.95	0.27	4.69	3.04	0.39	1.18	1.45	0.17
666	27.69	0.23	4.19	2.56	0.28	0.91	1.17	0.14
740	25.97	0.34	5.01	3.23	0.32	1.29	1.56	0.20
796	26.34	0.34	5.09	3.64	0.41	1.38	1.61	0.20
KF 7-S	24.05	0.75	9.47	8.00	0.33	4.52	0.60	0.20
KF10-S	25.59	0.64	9.87	7.91	0.33	5.51	0.48	0.19
KF10-66	21.06	0.72	7.52	6.67	0.26	3.53	1.18	0.27
KG18-S	17.89	0.62	7.41	7.46	0.28	3.96	0.37	0.23
KG18-13	22.60	0.68	9.15	5.79	0.11	4.84	0.29	0.10
KF01-								
5	12.16	0.63	4.82	9.64	0.84	2.10	1.31	0.56
35	17.82	0.95	6.26	6.08	1.13	2.38	1.60	0.32
46	18.66	0.82	5.90	5.46	0.19	2.45	1.84	0.29
85	20.02	0.34	5.40	3.60	0.10	2.01	1.99	0.18
KF12-								
5	10.70	0.50	4.31	10.98	0.84	2.24	1.18	0.56
35	11.36	0.67	4.63	12.29	3.29	2.21	1.15	0.51
50	13.58	0.79	5.21	11.99	1.31	2.19	1.36	0.22
95	19.42	0.93	6.41	4.84	0.34	2.25	1.72	0.32
KS03-								
6	20.77	0.64	8.49	8.04	0.64	2.71	1.96	0.29
32	23.28	0.69	8.65	7.24	0.30	2.99	1.61	0.12
42	22.26	0.73	8.36	8.83	0.15	4.89	0.71	0.09
63	23.32	0.77	9.38	7.98	0.43	3.19	1.82	0.18
85	22.71	0.72	8.49	8.14	0.15	5.11	0.54	0.09
115	19.00	0.60	7.90	6.51	0.41	2.35	1.88	0.13
186	24.62	0.64	9.15	7.10	0.46	1.96	2.26	0.13
260	20.74	0.58	8.25	6.68	0.45	2.44	2.10	0.15
341	18.17	0.51	7.39	6.49	0.51	2.09	1.92	0.22
390	20.08	0.60	8.51	6.39	0.34	1.97	1.91	0.15
410	20.07	0.62	7.79	6.61	0.37	2.24	2.05	0.17
450	20.39	0.58	7.99	6.40	0.37	1.98	2.10	0.11
92KS04-								
115	22.42	0.97	7.90	8.08	0.13	3.75	0.81	0.14
237	22.41	1.15	7.60	9.00	0.14	3.42	0.98	0.16
254	22.62	1.21	7.71	8.29	0.14	3.26	0.90	0.17
91KS04-								
Surface	17.20	0.91	6.34	6.49	0.72	2.39	0.57	0.15
6	18.70	1.14	7.28	7.43	0.97	2.62	0.38	0.15
10	22.60	1.39	8.67	8.37	1.10	2.94	0.35	0.16
13	20.20	1.16	7.05	7.40	0.42	2.54	0.29	0.13
16	21.50	1.11	7.11	6.56	0.31	2.67	0.43	0.11
22	19.30	0.89	6.15	5.57	0.27	2.57	0.43	0.11
61	21.10	0.58	6.38	4.45	0.27	2.32	0.27	0.09
80	19.30	0.32	4.62	3.25	0.20	1.84	0.14	0.05
93	20.80	0.36	5.06	3.11	0.29	2.01	0.17	0.06
109	20.70	0.35	4.94	3.54	0.24	1.94	0.19	0.06
123	22.40	0.44	5.86	3.86	0.26	1.95	0.23	0.17
138	21.30	0.49	5.32	4.01	0.31	2.10	0.21	0.08
155	20.60	0.52	5.51	4.74	0.34	2.48	0.22	0.09
184	19.40	0.51	5.23	4.00	0.36	2.28	0.24	0.10
200	20.20	0.53	6.00	4.55	0.40	2.37	0.32	0.10
238	23.00	0.95	8.37	6.74	0.18	4.33	0.56	0.06
239	23.00	0.95	8.34	6.80	0.18	4.33	0.57	0.05
249	20.70	0.80	6.97	6.53	0.25	3.76	0.34	0.07
255	20.20	0.62	6.21	4.19	0.48	2.22	0.28	0.12
271	21.00	0.66	6.42	4.85	0.44	2.23	0.25	0.11
280	25.60	0.97	8.51	7.35	0.22	3.79	0.54	0.06
283	23.10	0.69	6.83	7.29	0.24	2.71	0.39	0.05
295	23.70	0.67	7.12	5.05	0.23	2.20	0.32	0.06
310	23.70	0.97	8.61	7.25	0.20	3.88	0.54	0.05
323	22.10	0.50	6.35	4.22	0.36	2.06	0.21	0.07
342	23.40	0.79	7.57	7.17	0.30	3.24	0.28	0.07
353	23.60	1.01	8.43	7.59	0.21	4.10	0.51	0.07
358	19.40	0.59	6.53	4.27	0.47	2.19	0.20	0.10
366	16.90	0.49	4.62	8.03	0.61	2.15	0.15	0.13
381	21.00	0.57	6.57	5.80	0.34	2.25	0.22	0.09

Appendix 3: X-ray fluorescence data
trace elements

GEOFAR	Sc	V	Cr	Co	Ni	Cu	Zn	As	Rb	Sr	Y	Nb	Ba	Pb
	(ppm)	(ppm)	(ppm)	(ppm)	(ppm)	(ppm)	(ppm)	(ppm)	(ppm)	(ppm)	(ppm)	(ppm)	(ppm)	(ppm)
KF09-														
5	<1	156	<18	7	24	82	30	75	<4	1775	18	5	188	17
10	<1	170	19	9	23	57	30	41	<4	1835	21	7	268	6
15	<1	164	<18	31	31	80	31	73	<4	1824	22	8	209	10
18	<1	146	21	11	35	63	39	40	<4	1739	23	8	244	11
20	<1	157	<18	33	44	58	37	50	<4	1748	21	7	268	17
22	5	127	18	53	55	81	38	68	<4	1744	22	12	249	11
25	<1	124	19	21	28	83	30	34	<4	1728	23	7	281	9
30	2	72	<18	<4	21	53	26	33	<4	1758	22	15	357	17
35	1	40	19	49	53	43	24	16	<4	1750	20	12	376	11
37	2	37	24	24	29	45	23	<12	<4	1708	22	10	369	10
43	<1	59	21	35	24	70	26	<12	<4	1685	20	11	385	12
50	7	56	22	18	19	71	24	16	<4	1710	20	12	366	<4
90	7	28	20	<4	36	46	38	29	<4	1580	23	8	549	10
150	<1	34	25	16	31	40	33	<12	6	1588	24	13	661	11
210	<1	49	26	<4	26	42	41	17	19	1449	28	9	1710	18
240	4	43	25	23	36	58	51	12	15	1469	25	5	1162	15
300	5	28	<18	13	26	37	40	<12	6	1721	22	10	808	11
340	8	48	24	22	35	40	47	<12	17	1404	23	7	1133	17
370	13	31	22	36	26	34	44	18	14	1621	19	<2	993	14
403	1	35	<18	33	35	39	45	18	10	1551	26	4	1046	16
445	2	29	<18	<4	27	43	36	15	9	1699	22	4	774	11
465	3	31	<18	<4	23	46	24	<12	5	1708	22	<2	593	15
KF13-														
5	7	99	<18	10	19	40	49	17	<4	1806	21	11	182	20
10	5	89	<18	<4	19	43	29	31	<4	1784	20	8	180	17
19	5	61	<18	91	48	65	37	23	<4	1638	22	11	286	13
22	2	88	<18	<4	18	59	39	26	<4	1737	22	15	220	18
33	9	43	21	<4	21	19	30	14	<4	1677	22	4	392	14
50	9	36	18	10	19	36	33	26	4	1576	21	14	413	17
69	7	33	23	17	45	54	37	<12	4	1550	24	9	519	11
80	10	30	19	15	32	38	32	<12	<4	1643	21	5	489	13
120	8	41	36	5	32	54	55	19	23	1389	28	6	1830	15
150	<1	39	25	25	32	56	46	<12	5	1489	21	5	850	10
180	5	31	21	14	47	40	35	20	4	1613	22	3	677	19
200	9	34	23	13	23	37	41	25	8	1552	22	2	753	19
240	<1	22	18	<4	26	39	41	<12	6	1487	24	3	879	5
271	5	30	<18	38	36	57	43	21	10	1588	25	4	1004	20
310	12	17	<18	<4	16	34	35	<12	<4	1641	22	10	490	14
350	2	17	18	26	32	44	31	27	<4	1634	23	<2	599	11
370	9	25	<18	15	8	19	38	<12	<4	1683	25	9	523	22
390	2	25	18	7	20	41	36	<12	6	1610	23	10	620	20
445	8	21	<18	29	6	23	26	<12	<4	1829	25	8	402	17
475	5	17	<18	8	15	24	32	29	<4	2001	19	11	295	19
503	3	14	20	25	19	17	22	<12	<4	1907	18	3	318	7
533	6	20	18	14	29	38	29	13	<4	1832	22	4	402	14
KF16-														
2	<1	57	<18	11	20	34	23	<12	<4	1811	15	5	176	12
5	9	57	<18	30	12	26	28	45	<4	1744	20	17	180	114
17	5	45	<18	<4	28	34	19	<12	<4	1801	20	11	193	8
18	<1	58	<18	12	41	35	27	<12	<4	1778	20	8	197	6
20	11	59	<18	63	47	42	52	49	<4	1789	21	18	212	26
22	<1	49	19	18	37	57	29	19	<4	1746	21	8	188	4
35	8	57	27	12	35	40	31	17	<4	1698	24	18	196	21
49	13	74	25	18	26	36	43	<12	10	1461	25	16	521	16
62	<1	54	24	15	33	39	38	<12	<4	1648	18	10	296	5
67	<1	66	58	41	62	36	38	<12	<4	1665	18	15	293	7
69	<1	52	91	20	149	44	34	<12	<4	1643	18	11	311	11
72	6	47	151	<4	331	43	33	13	<4	1560	16	12	281	10
76	1	46	142	20	352	83	39	<12	<4	1478	19	8	283	10
78	4	52	171	41	431	57	36	<12	<4	1443	15	10	293	11
82	12	51	168	51	429	34	37	<12	6	1357	18	14	273	19
85	6	58	192	14	488	56	29	<12	5	1378	13	7	273	<4
89	5	45	32	21	53	41	35	18	<4	1600	21	17	331	21
110	6	52	19	39	30	36	43	<12	4	1639	23	19	382	16
130	<1	22	18	<4	26	39	41	<12	6	1487	24	3	507	5
170	5	39	97	16	227	46	35	<12	5	1547	22	7	485	9
210	5	38	18	14	41	48	41	<12	5	1540	23	15	559	6
256	<1	41	30	<4	43	39	47	<12	8	1461	20	4	755	5
307	3	26	29	18	17	30	43	<12	7	1501	22	10	754	20
332	8	17	<18	6	29	36	45	<12	7	771	16	9	569	101
340	<1	29	28	18	44	52	39	<12	10	1509	22	5	726	8
370	4	42	98	19	207	29	36	23	4	1528	22	10	522	12
420	<1	25	24	14	34	39	32	<12	12	1599	23	12	951	15
470	<1	37	22	34	40	42	58	21	22	1387	26	10	1286	16
520	<1	23	<18	27	23	40	42	<12	8	1501	17	3	777	9
570	<1	20	<18	38	48	36	41	<12	8	1489	20	<2	815	8
580	<1	25	<18	36	28	70	44	17	8	1422	22	11	764	20

Appendix 3: X-ray fluorescence data
trace elements

GEOFAR	Sc	V	Cr	Co	Ni	Cu	Zn	As	Rb	Sr	Y	Nb	Ba	Pb
KF16-	(ppm)	(ppm)	(ppm)	(ppm)	(ppm)	(ppm)	(ppm)	(ppm)	(ppm)	(ppm)	(ppm)	(ppm)	(ppm)	(ppm)
590	<1	16	<18	18	30	44	39	<12	9	1481	18	2	745	14
620	<1	26	<18	28	36	37	40	18	9	1502	18	<2	818	18
666	3	26	<18	10	45	58	43	14	8	1421	19	6	836	6
740	7	22	<18	13	23	36	37	<12	6	1648	19	<2	747	8
796	<1	21	<18	30	32	57	42	<12	9	1578	18	8	722	<4
KF7-S	10	90	122	28	39	79	54	<12	<4	1209	14	<2	380	<4
KF10-S	13	104	338	33	66	81	46	<12	<4	1168	17	6	268	<4
KF10-66	3	29	35	41	19	37	36	<12	<4	1380	13	<2	487	7
KG18-S	16	113	183	52	45	266	92	27	<4	1135	18	9	769	23
KG18-13	32	224	510	59	125	95	73	15	10	222	22	19	143	14
KF01-														
5	<1	58	<18	8	8	43	28	<12	<4	1838	18	8	203	10
35	4	18	173	30	39	36	33	24	<4	1561	19	11	333	19
46	5	27	64	16	34	31	55	<12	<4	1489	17	7	394	15
85	8	38	<18	27	21	42	45	16	16	1386	24	6	1336	17
KF12-														
5	9	93	<18	15	16	49	38	25	<4	1740	20	9	170	25
35	8	110	<18	38	27	70	35	42	<4	1690	23	10	195	24
50	14	98	<18	22	19	54	35	47	<4	1625	23	11	199	15
95	8	59	32	23	25	52	46	<12	27	1286	30	10	235	22
KS03-														
6	2	52	24	10	15	30	37	17	7	2125	24	9	126	19
32	16	82	56	37	32	56	58	<12	18	1614	29	10	311	33
42	20	163	143	80	63	144	105	18	14	612	30	8	123	29
63	12	61	37	29	30	59	50	13	13	1955	27	8	123	23
85	22	180	159	39	74	134	106	<12	17	325	32	12	70	6
115	14	70	92	42	58	57	49	15	20	1336	27	5	152	26
186	6	66	29	42	32	60	66	18	31	1326	35	10	321	26
260	6	63	26	11	29	55	45	31	23	1247	33	13	199	21
341	8	32	<18	24	17	39	27	18	7	1536	27	10	112	20
390	10	47	<18	20	16	28	36	18	16	1429	24	11	119	22
410	8	29	20	29	12	26	30	<12	5	1695	26	3	300	20
450	8	59	32	23	25	52	46	<12	27	1286	30	10	235	22
92KS04-														
115	21	166	104	23	54	67	68	<12	15	814	26	22	313	6
122	28	282	92	17	46	49	80	<12	21	361	27	32	251	<4
180	35	281	191	12	63	53	77	<12	14	305	25	24	231	<4
237	20	172	70	32	59	72	62	<12	17	829	21	27	252	<4
254	18	206	64	48	40	64	78	<12	18	653	30	33	389	6
265	28	282	92	17	46	49	80	<12	21	361	27	32	296	<4
91KS04-														
Surface	22	55	16	19	18	34	32	9	7	1600	12	9	220	11
6	24	62	18	20	22	33	30	11	8	1540	14	12	260	6
10	21	61	22	24	22	36	34	9	8	1500	15	15	350	6
13	20	63	27	18	21	42	35	8	10	1410	15	15	370	7
16	25	59	24	17	18	29	35	n.d.	11	1380	14	14	330	6
22	23	54	26	20	21	35	36	4	10	1310	14	12	350	8
61	25	50	24	22	27	45	44	4	18	1340	19	8	1010	8
80	22	42	17	25	33	34	41	5	14	1320	12	5	670	7
93	21	46	23	28	42	45	46	3	16	1320	16	4	880	13
109	18	46	20	25	36	47	45	6	15	1350	18	5	850	15
123	24	51	25	18	24	46	47	3	19	1320	20	6	1080	17
138	18	38	21	19	24	31	35	3	10	1380	15	5	490	7
155	22	42	21	18	20	25	33	6	11	1420	17	5	480	11
184	23	39	18	17	20	31	32	3	9	1520	16	5	380	5
200	23	43	25	17	20	24	30	2	11	1570	17	6	380	6
238	37	245	258	39	81	71	70	1	15	430	22	30	210	2
239	39	245	251	40	80	72	72	2	15	430	21	31	210	2
249	26	120	94	29	44	44	46	4	12	1120	17	15	290	6
255	20	44	21	15	15	24	29	2	11	1620	15	6	330	6
271	27	49	21	17	17	27	34	3	12	1540	16	7	370	25
280	27	145	77	30	40	60	59	2	21	790	22	21	600	5
283	20	90	41	28	35	42	47	6	25	1030	23	14	790	8
295	23	75	34	20	26	51	51	8	22	1240	22	11	750	9
310	32	240	160	38	61	91	72	4	15	480	21	28	230	4
323	23	53	28	17	21	34	35	8	17	1360	18	7	510	7
342	27	96	57	23	29	30	37	9	13	1230	16	10	290	5
353	31	200	126	33	52	66	64	2	13	670	20	23	220	2
358	27	47	21	17	21	36	37	4	14	1480	17	6	290	26
366	23	42	16	22	18	18	22	7	9	1510	14	5	240	5
381	21	49	21	18	20	33	31	4	17	1440	18	8	330	7

Appendix 3: X-ray fluorescence data

trace elements (carbonate-free basis)

GEOFAR	Sc	V	Cr	Co	Ni	Cu	Zn	As	Rb	Y	Nb	Ba	Pb
	(ppm)	(ppm)	(ppm)	(ppm)	(ppm)	(ppm)	(ppm)	(ppm)	(ppm)	(ppm)	(ppm)	(ppm)	(ppm)
KF09-													
5	<8	1241	<140	56	191	652	239	597	<32	143	40	1500	135
10	<7	1185	132	63	160	397	209	286	<28	146	49	1870	42
15	<7	1143	<125	216	216	557	216	509	<28	153	56	1460	70
18	<6	827	119	62	198	357	221	227	<23	130	45	1380	62
20	<6	940	<108	197	263	347	221	299	<24	126	42	1600	102
22	29	732	104	305	317	467	219	392	<23	127	69	1435	63
25	<6	769	118	130	174	515	186	211	<25	143	43	1740	56
30	13	461	<115	<26	134	339	166	211	<26	141	96	2290	109
35	6	232	110	284	307	249	139	93	<23	116	69	2180	64
37	11	204	132	132	160	248	127	<66	<22	121	55	2030	55
43	<5	318	113	188	129	377	140	<65	<22	108	59	2070	65
50	39	310	122	100	105	392	133	88	<22	111	66	2020	<22
90	35	138	99	<20	178	227	187	143	<20	113	39	271	49
150	<5	167	123	79	153	197	163	<60	30	118	64	3260	54
210	<4	172	91	<14	91	147	144	60	67	98	32	5990	63
240	14	153	89	82	128	206	181	43	53	89	18	4120	53
300	22	125	<80	58	116	165	179	<54	27	98	45	3610	49
340	24	144	72	66	105	120	141	<36	51	69	21	3400	51
370	49	116	83	135	98	128	165	68	53	71	<8	3725	53
403	4	126	<65	119	126	141	163	65	36	94	14	3780	58
445	11	156	<97	<22	146	232	194	81	49	119	22	4175	59
465	17	181	<105	<23	134	268	140	<70	29	128	<12	3460	87
KF13-													
5	53	750	<136	76	144	303	371	129	<30	159	83	1377	151
10	34	602	<120	<22	129	291	196	210	<22	135	54	1218	115
19	35	422	<120	629	332	450	256	159	<25	152	76	1978	90
22	10	438	<90	<27	90	294	194	130	<27	110	75	1096	90
33	50	241	118	<22	118	106	168	78	<22	123	22	2200	78
50	49	195	98	54	103	195	179	141	22	114	76	2240	92
69	31	148	103	76	202	243	166	<54	18	108	40	2330	49
80	64	191	121	96	204	242	204	<77	<26	134	32	3120	83
120	26	132	116	16	103	174	177	61	74	90	19	5900	48
150	<4	160	103	<16	131	230	189	<49	21	86	21	3490	41
180	21	129	87	58	196	167	143	83	17	92	12	2820	79
200	42	160	108	61	108	174	193	117	38	103	9	3537	89
240	<4	92	78	<17	113	169	178	<52	26	104	13	3810	22
271	21	126	<76	<17	151	240	181	88	42	105	17	4220	84
310	73	103	<110	<19	97	206	212	<70	<19	133	60	2964	85
350	12	101	107	<24	189	260	183	160	<24	136	<12	3540	65
370	63	174	<125	105	56	132	265	<84	<21	174	63	3647	153
390	11	139	100	39	111	228	200	<67	33	128	56	3454	111
445	58	153	<130	211	44	168	190	<87	<23	182	58	2930	124
475	35	121	<130	57	106	170	227	206	<25	135	78	2092	135
503	29	134	192	<38	183	163	211	<115	<38	173	29	3060	67
533	43	144	129	<29	209	273	209	94	<29	158	29	2890	101
KF16-													
2	<6	336	<106	65	118	200	136	<71	<24	88	29	1037	71
5	59	376	<119	198	79	171	185	297	<21	132	112	1187	751
17	33	300	<120	<27	187	227	127	<80	<27	133	73	1286	53
18	<6	329	<102	68	*232*	198	153	<68	<23	113	45	1116	34
20	63	339	<104	362	*270*	242	299	282	<23	121	104	1219	150
22	<6	280	108	103	*211*	325	165	108	<23	120	46	1072	23
35	44	313	148	66	192	220	170	93	<18	132	99	1076	115
49	47	269	91	65	94	131	156	44	36	91	58	1892	58
62	<5	244	108	68	149	176	172	54	<18	81	45	1337	23
67	<4	275	242	171	259	150	159	50	<17	75	63	1222	29
69	<4	190	333	73	545	161	124	44	<15	66	40	1138	40
72	17	133	427	<11	937	122	93	37	<11	45	34	795	28
76	3	125	387	54	959	226	106	<33	<11	52	22	771	27
78	10	133	437	105	1102	146	92	<31	<10	38	26	749	28
82	31	132	434	132	1109	88	96	<31	16	47	36	706	49
85	14	136	452	33	1148	132	68	<28	12	31	16	642	<9
89	24	218	155	102	257	199	170	87	<17	102	82	1604	102
110	30	260	95	195	150	180	215	<60	20	115	95	1910	80
130	<4	97	79	<18	115	172	180	<50	26	106	13	2236	22
170	16	128	320	53	747	151	115	<40	16	72	23	1597	30
210	25	186	88	69	201	236	201	<60	25	113	74	2743	29
256	<4	145	106	<14	152	138	166	<42	28	71	14	2666	18
307	12	104	116	72	68	120	172	<48	28	88	40	3011	80
332	13	27	<29	10	47	58	72	<19	11	26	14	913	162
340	<5	142	137	88	215	254	190	<60	49	108	24	3550	39
370	14	150	351	68	742	104	129	82	14	79	36	1872	43
420	<5	119	114	66	161	185	152	<60	57	109	57	4514	71
470	<3	110	65	101	119	125	172	62	65	77	30	3813	47
520	<3	73	<57	86	73	127	133	<38	25	54	10	2467	29

Appendix 3: X-ray fluorescence data

trace elements (carbonate-free basis)

GEOFAR	Sc	V	Cr	Co	Ni	Cu	Zn	As	Rb	Y	Nb	Ba	Pb
KF16-	(ppm)	(ppm)	(ppm)	(ppm)	(ppm)	(ppm)	(ppm)	(ppm)	(ppm)	(ppm)	(ppm)	(ppm)	(ppm)
570	<3	68	<61	158	162	122	138	<41	27	68		2752	27
580	<3	85	<61	153	96	239	150	58	27	75	38	2607	68
590	<3	52	<58	58	97	143	126	<39	29	58	6	2413	45
620	<3	88	<61	95	122	125	135	61	30	61		2762	61
666	10	90	<63	35	157	202	150	49	28	66	21	2908	21
740	27	84	<68	49	87	137	140	<46	23	72		2836	30
796	<4	80	<69	115	123	218	161	<46	34	69	31	2764	77
KF7-S	27	244	331	76	106	214	146	<32	<10	38	<5	1030	<10
KF10-S	30	241	782	76	153	187	106	<28	<9	39	14	620	<9
KF10-66	19	183	220	258	120	233	227	<75	<25	82	<12	3065	44
KG18-S	37	260	420	120	104	610	212	62	<10	41	21	1875	53
KG 18-13	32	225	510	59	126	96	73	15	10	22	19	144	14
KF01-													
5	<7	405	<125	56	56	300	196	<84	<20	126	56	1420	70
35	24	107	1030	179	232	215	197	143	<20	113	66	1980	143
46	31	170	402	100	214	195	345	<75	<20	107	44	2475	94
85	27	129	<61	92	71	142	153	54	54	82	20	4540	58
KF12-													
5	50	520	<100	84	90	275	213	140	<20	112	50	950	140
35	41	565	<93	195	139	360	180	216	<20	118	51	1000	123
50	65	455	<84	102	88	251	163	219	<20	107	51	925	70
95	39	289	157	113	122	254	225	<59	132	147	49	1150	108
KS03-													
6	9	237	109	46	68	137	168	77	32	109	41	570	86
32	35	181	124	82	71	124	128	<27	40	64	22	690	73
42	27	222	195	109	86	196	143	25	19	41	11	168	39
63	38	192	116	91	94	186	157	41	41	85	25	387	72
85	25	205	181	44	84	153	121	<14	19	36	14	80	7
115	38	191	252	115	159	156	134	41	55	74	14	416	71
186	17	182	80	116	88	165	182	50	85	96	28	880	72
260	19	202	83	35	93	177	144	100	74	106	42	640	67
341	45	181	<100	135	96	220	152	102	40	152	56	630	113
390	38	178	<68	76	60	106	136	68	60	91	42	450	83
410	50	181	125	181	75	162	187	<75	31	162	19	1870	125
450	21	156	85	61	66	137	122	<32	71	79	26	620	58
92KS04-													
115	31	251	158	34	82	101	103	<20	22	39	33	473	16
237	32	270	110	50	92	113	97	<20	27	33	42	395	<6
254	23	258	80	60	50	80	97	<15	23	37	41	487	8
91KS04-													
Surface	114	289	83	97	93	176	165	52	38	65	50	1141	120
6	121	311	90	100	108	165	152	55	38	68	60	1307	30
10	103	304	112	120	111	181	167	45	41	72	73	1723	30
13	76	243	103	69	80	161	134	31	37	57	59	1407	27
16	105	245	102	73	77	121	148	n.d.	45	58	57	1392	25
22	90	210	99	78	83	136	139	14	41	54	48	1366	31
61	93	187	88	82	100	168	163	13	68	70	30	3744	30
80	77	149	59	89	116	121	144	18	50	50	18	2358	25
93	74	161	81	100	148	157	162	11	57	55	15	3114	46
109	61	156	69	85	123	160	152	21	52	61	16	2900	51
123	83	175	88	61	83	160	163	9	64	68	21	3722	56
138	84	177	99	90	112	146	165	14	49	71	21	2274	33
155	100	190	95	80	90	113	150	27	51	76	23	2176	50
184	113	193	91	85	101	156	159	15	47	78	25	1867	25
200	110	208	121	83	95	115	145	12	54	81	30	1820	29
238	40	271	286	44	90	79	78	1	17	24	34	229	2
239	43	268	274	44	87	79	78	2	17	23	34	233	2
249	56	260	200	62	95	94	100	9	25	35	32	626	13
255	102	222	108	76	75	122	146	9	54	77	32	1682	28
271	117	215	90	74	74	119	147	15	52	69	30	1604	109
280	47	251	133	52	69	104	103	4	36	39	36	1040	9
283	44	196	89	61	76	91	102	13	55	49	31	1724	17
295	62	200	90	53	71	137	137	21	58	59	28	2006	23
310	40	300	206	48	77	115	91	5	19	27	35	288	5
323	77	179	95	56	70	114	119	25	58	59	23	1707	24
342	77	276	163	65	84	85	106	26	36	46	28	826	14
353	46	291	183	48	75	96	93	3	18	29	34	323	3
358	128	226	102	83	98	173	176	19	65	84	28	1373	125
366	131	236	88	125	103	100	125	42	50	80	27	1362	26
381	86	200	87	73	80	136	126	16	69	72	31	1356	27

Appendix 3: X-ray fluorescence data

Standard rocks: major oxides

Sample		SiO2	TiO2	Al2O3	Fe2O3	MnO	MgO	CaO	Na2O	K2O	P2O5
		(%)	(%)	(%)	(%)	(%)	(%)	(%)	(%)	(%)	(%)
QLO-1	Quartz	65.55	0.624	16.18	4.35	0.093	1.00	3.17	4.20	3.60	0.254
(12/94)	Latite	67.00	0.62	16.49	4.34	0.096	1.02	3.22	4.56	3.70	0.256
(4/96)		65.77	0.61	16.15	4.17	0.094	1.00	3.17	3.88	3.63	0.257
SCO-1	Cody Shale	62.78	0.628	13.67	5.14	0.053	2.72	2.62	0.90	2.77	0.206
(12/94)		64.86	0.59	13.59	5.15	0.050	2.66	2.70	1.18	2.72	0.206
(4/96)		63.74	0.58	13.29	5.16	0.050	2.71	2.67	0.74	2.70	0.198
KH-3	Limestone	8.59	0.13	2.40	0.87	0.080	0.65	47.60	0.10	0.43	0.117
		8.63	0.13	2.22	0.82	0.087	0.61	47.75	0.13	0.44	0.126
BM-ZGI	Basalt	49.51	1.14	16.25	9.68	0.140	7.47	6.47	4.65	0.20	0.106
(12/94)		50.16	1.16	16.20	9.69	0.148	7.30	6.28	4.97	0.17	0.108
(4/96)		49.38	1.14	15.83	9.50	0.146	7.27	6.23	4.53	0.16	0.110
SY-3	Syenite	59.68	0.150	11.76	6.49	0.320	2.67	8.25	4.12	4.23	0.54
		59.79	0.150	11.57	6.31	0.326	2.52	8.14	4.28	4.21	0.523
SY-2	Syenite	60.11	0.15	12.04	6.31	0.320	2.69	7.96	4.31	4.45	0.43
(12/94)		60.61	0.140	12.06	6.42	0.327	2.62	7.92	4.47	4.55	0.421
(9/94)		61.66	0.140	12.40	6.41	0.330	2.69	8.08	4.31	4.57	0.426
NIM-S	Syenite	63.63	0.044	17.34	1.40	0.01	0.46	0.68	0.43	15.35	0.12
		64.01	0.040	17.19	1.38	0.008	0.40	0.67	0.52	15.51	0.114
UB-N	Serpentine	39.43	0.110	2.90	8.34	0.120	35.21	1.20	0.10	0.02	0.04
		39.76	0.100	2.88	8.41	0.125	35.66	1.18	0.27	<0.02	0.009
RGM-1	Rhyolite	73.45	0.267	13.72	1.91	0.036	0.275	1.15	4.07	4.30	*0.048*
(12/94)		74.87	0.270	14.04	1.80	0.036	0.26	1.21	4.27	4.41	0.043
(4/96)		73.45	0.270	13.67	1.83	0.037	0.24	1.19	3.83	4.35	0.044
BHVO-1	Basalt	49.94	2.710	13.80	12.23	0.168	7.23	11.40	2.26	0.52	0.273
(12/94)		50.98	2.840	13.95	12.54	0.176	7.13	11.39	2.53	0.54	0.278
(4/96)		49.79	2.770	13.41	12.22	0.172	7.18	11.24	2.03	0.52	0.265
PCC-1	Peridotite	41.71	*0.01*	0.68	8.25	0.120	43.43	0.52	*0.03*	*0.007*	*0.002*
		42.55	<0.02	0.66	8.56	0.122	44.39	0.55	<0.04	<0.02	<0.006
W-1	Diabase	52.51	1.07	15.01	11.12	0.170	6.62	10.99	2.16	0.64	0.130
		53.01	1.11	14.99	11.36	0.179	6.63	10.93	2.15	0.64	0.126
SDC-1	Mica Schist	65.85	1.01	15.75	6.90	0.114	1.69	1.40	2.05	3.28	0.158
		65.55	0.99	15.65	6.95	0.114	1.68	1.40	1.79	3.27	0.141
SGR-1	Oil Shale	28.24	0.264	6.52	3.03	0.034	4.44	8.38	2.99	1.66	*0.328*
		28.27	0.250	6.41	3.08	0.032	4.40	8.32	2.81	1.61	0.275
STM-1	Nepheline	59.64	0.135	18.39	5.22	0.220	0.10	1.09	8.94	4.28	0.158
	Syenite	59.46	0.130	18.22	5.30	0.224	0.05	1.13	8.50	4.24	0.154

Appendix 3: X-ray fluorescence data

Standard rocks: trace elements

Sample	Sc	V	Cr	Co	Ni	Cu	Zn	As	Rb	Sr	Y	Nb	Ba	Nd	Pb
	(ppm)	(ppm)	(ppm)	(ppm)	(ppm)	(ppm)	(ppm)	(ppm)	(ppm)	(ppm)	(ppm)	(ppm)	(ppm)	(ppm)	(ppm)
QLO-1	*8.9*	54	*3.2*	7.2	*5.8*	29	61	*3.5*	74	336	24	10.3	1370	*26*	20.4
(12/94)	7	62	<18	<4	4	17	63	<12	72	335	25	8	1396	16	28
(4/96)	12	41	<18	<4	<2	30	58	<12	68	327	23	7	1376	12	22
SCO-1	10.8	131	68	10.5	27	11.6	103	12.4	112	174	26	*11*	570	26	31
(12/94)	14	126	67	18	34	37	103	14	112	163	22	9	563	20	31
(4/96)	12	133	69	<4	44	58	98	<12	106	161	24	9	572	24	29
KH-3										2368					
										2583					
BM-ZGI	34	190	121	36	57	43	120	13	10	220	27		250	15	13
(12/94)	28	187	130	41	68	81	127	14	5	223	29	3	261	<7	12
(4/96)	28	193	133	33	69	93	116	<12	4	217	28	<2	264	<7	13
SY-3	*6.8*	*50*	*11*	*8.8*	*11*	*17*	244	*18.8*	206	302	718	*148*	*450*	*670*	133
	5	41	<18	19	<2	13	240	<12	216	296	686	145	408	661	148
SY-2	7.0	*50*	*9.5*	8.6	*9.9*	*5.2*	248	17.3	217	271	128	*29*	460	*73*	85
(12/94)	3	38	<18	22	43	18	271	25	230	268	125	17	443	77	96
(9/94)	9	48	<18	8	15	24	261	27	241	280	131	24	478	72	103
NIM-S	*4*	10	12	*3*	*7*	19	*10*		530	62	*20*	*4*	2400	*6*	*5*
	<1	<12	<18	8	11	18	<15	<12	549	62	<2	<2	30	<7	10
UB-N	*13*	75	2300	100	2000	28	85	10	4	9	2.5	0.05	27	0.6	13
	7	64	2343	99	2080	464	87	55	4	9	3	<2	30	<7	10
RGM-1	4.4	13	*3.7*	2.0	*4.4*	11.6	*32*	3.0	149	108	*25*	8.9	807	19	24
(12/94)	2	14	<18	<4	<2	5	37	<12	150	101	22	5	830	21	24
(4/96)	8	<12	<18	<4	<2	38	32	<12	145	100	23	5	823	12	26
BHVO-1	32	317	289	45	121	136	105	*0.4*	11	403	27.6	19	139	25.2	*2.6*
(12/94)	25	311	283	69	125	112	110	<12	8	399	26	13	128	18	<4
(4/96)	30	275	291	13	125	93	99	<12	7	402	24	13	144	16	<4
PCC-1	8.4	31	2730	112	2380	*10*	*42*	*0.056*	0.066	0.4	*0.1*	1	1.2	0.042	10
	8	39	2855	122	2431	25	53	<12	<4	<4	6	6	<8	<7	20
W-1	35	257	119	47	75	113	84	2.2	21.4	186	26	9.9	162	14.6	*7.5*
	40	269	124	73	83	93	95	<12	23	195	26	13	169	11	15
SDC-1	17	102	64	17.9	*38*	30	103	0.22	127	183	40	*18*	630	40	25
	16	90	58	17	42	50	101	<12	119	171	39	16	657	32	18
SGR-1	4.6	128	30	11.8	*29*	66	74	67	83	420	*13*	*5.2*	290	15.5	38
	8	136	30	<4	33	53	99	31	74	365	11	3	300	12	37
STM-1	0.61	*8.7*	*4.3*	*0.9*	*3*	*4.6*	235	*4.6*	118	700	46	268	560	79	17.7
	2	<12	<18	<4	11	34	242	<12	110	683	41	232	550	76	13

Appendix 4:
Carbonate and organic carbon

Sample	CaCO3 (%)	C org. (%)	Method
KF09-			
5	88.77	0.248	LECO
10	88.05	0.235	"
15	85.16	0.231	"
18	83.47	0.134	"
20	84.60	0.148	"
22	86.73	0.143	"
25	86.48	0.122	"
30	84.21	0.145	"
35	83.53	0.127	"
37	83.32	0.152	"
43	80.43	0.139	"
50	85.14	0.183	"
150	81.66	0.301	"
210	75.12	0.246	"
240	71.79	0.480	"
300	79.50	0.405	"
340	77.70	0.446	"
390	68.13	0.510	"
403	76.04	0.546	"
445	83.33	0.351	"
465	85.55	0.284	"
KF13-			
5	88.78	0.197	LECO
10	82.23	0.339	Carlo Erba
19	81.84	0.302	LECO
22	79.63	0.334	Carlo Erba
33	81.63	0.164	LECO
50	78.33	0.255	Carlo Erba
69	80.56	0.253	LECO
74	80.94	0.347	Carlo Erba
80	83.33	0.250	LECO
90	81.36	0.335	Carlo Erba
120	68.87	0.246	LECO
150	76.54	0.385	"
180	77.85	0.513	"
200	74.67	0.540	Carlo Erba
240	78.78	0.377	LECO
271	78.30	0.184	"
310	79.97	0.520	Carlo Erba
350	87.05	0.254	LECO
370	81.88	0.295	Carlo Erba
390	77.80	0.403	"
445	86.16	0.209	"
475	85.91	0.206	"
503	89.71	0.085	LECO
533	86.87	0.075	"
KF16-			
2	83.03	0.372	Carlo Erba
5	80.58	0.491	"
17	84.82	0.122	"
18	82.35	0.263	LECO
20	82.61	0.289	Carlo Erba
22	82.47	0.381	"
35	77.45	0.240	"
49	72.46	0.282	"
62	77.86	0.176	"
67	76.03	0.248	"
69	72.68	0.192	"
72	64.66	0.271	"
76	63.30	0.207	"
KF16-			
78	60.90	0.172	Carlo Erba
82	56.77	0.170	"
85	53.78	0.161	"
89	76.03	0.296	"
110	76.57	0.284	"
130	77.33	0.341	LECO
170	69.63	0.319	"
210	79.62	0.422	"
256	71.68	0.804	Carlo Erba
307	74.96	0.512	"
332	33.17	0.852	"
340	79.55	0.319	LECO
370	72.11	0.212	"
420	82.42	0.169	"
470	66.27	0.736	Carlo Erba
520	68.51	0.994	"
570	70.39	1.200	"
580	64.77	1.182	"
590	69.13	1.163	"
620	70.38	1.119	"
666	71.25	1.200	LECO
740	73.66	0.969	Carlo Erba
796	73.88	0.771	"
KF7-S	63.25	0.261	Carlo Erba
KF10-S	56.56	0.313	"
KF10-66	82.16	0.231	"
KG18-S	58.66	0.359	"
KG18-13	0.40	0.072	"
KF01-			
5	82.93	0.369	Carlo Erba
35	80.73	0.220	"
46	84.55	0.207	"
85	73.78	0.465	"
KF12-			
5	79.65	0.380	Carlo Erba
35	79.88	0.380	"
50	78.47	0.350	"
95	76.87	0.350	"
KS03-			
6	81.06	0.282	Carlo Erba
32	55.87	0.228	"
42	22.63	0.232	"
63	67.91	0.235	"
85	10.47	0.209	"
115	64.16	0.160	"
186	64.63	0.197	"
260	69.27	0.165	"
341	83.05	0.133	"
390	71.31	0.217	"
410	83.16	0.231	"
450	63.15	0.137	"
92KS04-			
115	33.14	0.195	Carlo Erba
237	34.57	0.112	"
254	21.36	0.121	"

Appendix 5: Selective leaching data

Sample	**Leach I** (carbonate) (% weight loss)	**Leach II** (organic) (% weight loss)	**Leach III** (oxyhydroxide) (% weight loss)	**Residue** (% of total)	**Leach II** (% of Residue after L I)	**Leach III** (% of Residue after L I)	**Residue** (% of Residue after L I)
KF1-5	92.34	0.65	1.06	5.95	8.49	13.84	77.68
KF12-5	90.07	2.11	1.89	5.93	21.25	19.03	59.72
KF16-5	88.7	0.66	2.61	8.03	5.84	23.1	71.06
KF13-10	89.12	0	4.84	6.04	0	44.49	55.51
KF13-20	86.36	0	5.54	8.1	0	40.62	59.38
KF16-20	89.16	0	3.41	7.43	0	31.46	68.54
KF12-50	84.71	1.28	3.56	10.45	8.37	23.28	68.35
KF16-35	84.41	0	1.63	13.96	0	10.46	89.54
KF1-35	88.9	1.43	0.36	9.31	12.88	3.24	83.87
KG18-S	62.44	0	2.5	35.06	0	6.66	93.34
KS03-6	83.93	0	3.39	12.68	0	21.1	78.9
KF12-95	86.27	1.74	0.22	11.77	12.67	1.6	85.72
KF16-110	81.29	0.33	3.5	14.88	1.76	18.71	79.53
KF13-200	83.29	2.78	0.23	13.7	16.64	1.38	81.99
KF13-475	89.16	0.73	0.15	9.96	6.73	1.39	91.88
KF16-580	77.87	4.89	1.05	16.19	22.1	4.74	73.16
KF16-620	77.54	5.66	0.98	15.82	25.2	4.36	70.44
KS03-85	37.5	0	1.68	60.82	0	2.69	97.31
KS03-186	67.1	0	2.79	30.11	0	8.48	91.52
KG18-13	4.45	0	1	94.55	0	1.05	98.95
KF1-46	89.93	1.3	0	8.77	12.91	0	87.09
KF1-85	80.52	3.37	0.69	15.42	17.3	3.54	79.16
	Fe in L I (% of total Fe)	**Fe in L III** (% of total Fe)	**Fe in Residue** (% of total Fe)	**Mn in L I** (% of total Mn)	**Mn in L III** (% of total Mn)	**Mn in Residue** (% of total Mn)	**Cl-** (% of total)
KF1-5	5.4±0.08	25±0.30	69.6	22±0.4	50±2.0	28	n.a.
KF12-5	6.1±0.34	26±0	67.9	25±0.5	75±0	0	n.a.
KF16-5	2.5±0.07	37±0.13	60.5	12.5±1.0	42±1.0	45.5	3.84
KF13-10	1.5±0.02	30±0.10	68.5	28±1.0	66±2.0	6	3.83
KF13-20	0.3±0.03	33±0.05	66.7	4.6±0	91±0.4	4.4	3.46
KF16-20	0.5±0.04	33±0.06	66.5	8±0.4	64±1.0	28	3.82
KF12-50	2.0±0.17	35±0.24	63	17±1.3	61±0.6	22	n.a.
KF1-35	n.d.	16±0.4	84	11±0.6	80±6.0	9	4.15
KG18-S	n.d.	16±0.06	84	9±0.5	56±2.2	35	n.a.
KS03-6	0.2±0.01	21±0.19	78.8	37±0.2	62±9.0	1	3.93
KS03-85	n.d.	4.8±0.11	95.2	14±1.2	52±1.0	34	3.94
KS03-186	n.d.	7.8±0.25	92.2	n.d.	80±2.0	20	n.a.
KF16-35	2±0.10	11±0.026	86.4	65±0.8	n.d.	35	4.36
KF12-95	n.d.	8.9±0.10	91.1	88±3.0	n.d.	12	4.67
KF16-110	0.9±0.01	5.1±0.07	94	70±6.0	11±2.7	19	3.82
KF13-200	n.d.	n.d.	100	93.5±0	n.d.	6.5	4.89
KF13-475xys	3.1±0.30	16±2.7	80.9	98±3.0	n.d.	2	n.a.
KF16-580	2.5±0.20	3.7±0.10	93.8	90±0	n.d.	10	4.48
KF16-620	3.1±0.41	4.7±0	92.2	91.5±0.1	n.d.	8.5	3.29
KG18-13	0.8±0.04	2±0.05	97.2	10.5±4.3	n.d.	89.5	4.01
KF1-46	n.d.	n.d.	100	73±14	n.d.	27	n.a.
KF1-85	n.d.	n.d.	100	65±0	n.d.	35	n.a.

Appendix 6:
Metal accumulation rates

GEOFAR KF09

Depth (cm)	Age (ky cal.)	dry bulk density (g/cm^3)	Bulk accumulation (g/cm^2•ky)	Fe (mg/cm^2•ky)	Mn (mg/cm^2•ky)	Cu (µg/cm^2•ky)	Zn (µg/cm^2•ky)	Ni (µg/cm^2•ky)	Mn hydrothermal (% normative)
5	0.61	0.64	5.22	145	6.87	428	157	125	74.8
10	1.23	0.71	5.80	175	8.22	331	174	133	77.6
15	1.84	0.75	6.12	193	9.96	490	190	190	80.8
18	2.21	0.75	6.16	194	21.87	388	240	216	91.0
20	2.45	0.75	6.16	199	41.58	357	228	271	95.1
22	2.70	0.75	6.16	195	46.45	499	234	339	95.6
25	3.07	0.75	6.16	187	10.60	511	185	172	79.9
30	3.68	0.76	6.20	137	4.71	329	161	130	49.4
35	4.34	0.76	6.16	108	27.23	265	148	326	91.0
37	4.68	0.76	6.16	113	4.87	277	142	179	49.2
43	5.27	0.72	5.97	106	4.63	418	155	143	47.2
50	6.13	0.69	5.63	81	3.88	400	135	107	39.3
90	10.32	0.64	12.29	141	9.22	565	467	442	57.7
150	13.74	0.65	9.69	105	8.93	388	320	300	63.1
210	17.50	0.58	14.50	248	12.59	609	595	377	56.3
240	18.64	0.53	13.70	201	9.97	795	699	493	51.1
310	21.06	0.57	14.73	122	10.84	545	589	383	60.4
340	22.42	0.54	13.96	239	14.70	558	656	489	63.1
370	23.94	0.52	13.44	130	11.03	457	591	349	59.8
403	25.23	0.50	12.93	153	10.91	504	582	453	59.7
445	27.19	0.50	11.84	77	9.35	509	426	320	62.6
465	28.58	0.50	13.73	125	10.00	632	330	316	65.5

GEOFAR KF13

Depth (cm)	Age (ky cal.)	dry bulk density (g/cm^3)	Bulk accumulation (g/cm^2•ky)	Fe (mg/cm^2•ky)	Mn (mg/cm^2•ky)	Cu (µg/cm^2•ky)	Zn (µg/cm^2•ky)	Ni (µg/cm^2•ky)	Mn hydrothermal (% normative)
5	5.16	0.69	4.55	91	6.56	182	223	86	71.5
10	6.16	0.75	4.95	98	7.25	213	144	94	73.4
19	7.33	0.77	5.08	92	66.5	330	188	244	96.9
22	7.72	0.75	4.95	115	3.56	292	193	89	40.9
33	9.04	0.72	7.34	106	5.92	139	220	154	51.0
50	11.06	0.75	5.78	62	3.44	208	191	110	27.1
69	13.65	0.72	5.18	80	4.78	280	192	233	51.4
80	14.41	0.73	25.35	226	17.29	963	811	811	65.5
120	17.21	0.50	15.65	290	10.67	845	861	501	37.8
150	18.30	0.57	17.84	209	11.88	999	821	571	54.0
180	20.50	0.59	7.02	117	3.97	281	246	330	33.2
200	22.19	0.59	7.02	57	3.92	260	288	161	26.7
240	25.30	0.58	7.60	69	4.24	296	312	198	33.5
271	26.93	0.60	12.84	169	11.23	732	552	462	62.1
310	28.98	0.70	14.98	90	9.29	509	524	240	63.6
350	32.77	0.70	6.09	39	4.06	268	189	195	41.5
370	34.95	0.76	6.61	42	5.27	126	251	53	56.7
390	37.13	0.71	6.18	50	4.17	253	222	124	42.2
445	43.11	0.74	6.44	35	5.83	148	167	39	62.9
475	46.38	0.79	6.87	31	5.64	165	220	103	62.7
503	49.44	0.80	6.96	38	6.63	118	153	132	66.5
533	54.89	0.77	3.77	28	3.68	143	109	109	46.6

Appendix 6:
Metal accumulation rates

GEOFAR KF16

Depth (cm)	Age (ky cal.)	dry bulk density (g/cm³)	Bulk accumulation (g/cm²•ky)	Fe (mg/cm²•ky)	Mn (mg/cm²•ky)	Cu (µg/cm²•ky)	Zn (µg/cm²•ky)	Ni (µg/cm²•ky)	Mn hydrothermal (% normative)
2	0.11	0.64	11.97	170	17.6	407	275	239	81.5
5	0.27	0.68	12.72	170	17.8	331	356	153	81.7
17	0.91	0.70	13.17	216	38.7	448	250	369	90.4
18	0.96	0.70	13.11	214	67.9	459	354	538	94.4
20	1.07	0.68	13.00	222	88.7	546	676	611	95.7
22	1.18	0.68	12.89	235	24.6	735	374	477	84.8
35	1.87	0.65	12.16	208	10.3	486	377	426	64.7
49	2.62	0.69	12.81	215	13.4	461	551	333	60.1
62	3.31	0.67	12.44	213	11.8	485	473	411	59.0
67	3.58	0.67	12.53	248	10.7	451	476	777	55.8
89	3.85	0.76	14.21	180	10.9	583	497	753	56.1
110	4.97	0.81	15.15	203	12.1	545	651	454	57.5
130	6.04	0.68	12.72	190	12.7	496	522	331	63.7
170	8.18	0.61	11.41	211	18.8	525	399	2590	79.5
210	10.32	0.61	11.71	157	12.6	562	480	480	67.2
256	12.57	0.60	21.36	252	20.1	833	1004	918	68.3
307	13.97	0.63	21.36	235	23.1	641	918	363	71.4
332	14.66	0.59	21.36	250	11.1	769	961	619	59.4
340	14.89	0.58	21.00	309	36.5	1092	819	924	82.7
370	15.72	0.67	24.25	441	39.8	703	873	5020	83.1
420	17.10	0.68	24.62	288	23.8	960	788	837	69.9
470	17.95	0.51	29.73	491	16.6	1249	1724	1189	27.3
520	19.38	0.50	14.30	143	11.4	572	601	329	76.1
570	21.19	0.42	12.01	125	12.4	432	492	576	79.6
580	21.55	0.48	13.73	126	12.6	961	604	384	79.4
590	21.91	0.39	11.15	104	12.8	491	435	335	82.1
620	23.00	0.41	11.73	106	13.5	434	469	422	82.0
666	24.66	0.43	12.44	112	12.2	722	535	560	65.3
740	27.33	0.52	14.87	126	12.4	535	550	342	77.8
796	29.50	0.52	14.87	141	16.1	848	625	476	82.8

Ac.91KS04 (EPSHOM)

Depth (cm)	Age (ky cal.)	dry bulk density (g/cm³)	Bulk accumulation (g/cm²•ky)	Fe (mg/cm²•ky)	Mn (mg/cm²•ky)	Cu (µg/cm²•ky)	Zn (µg/cm²•ky)	Ni (µg/cm²•ky)	Mn hydrothermal (% normative)
0	9.40	0.97	8.92	111	12.33	303	285	161	75.4
6	10.00	0.96	8.83	132	17.20	291	265	194	80.5
10	10.50	0.96	8.83	148	19.56	318	300	194	80.8
13	10.80	0.96	8.83	170	9.54	371	309	185	59.3
16	11.10	0.89	8.19	129	6.15	238	287	147	42.6
22	11.80	0.85	7.82	112	5.35	274	282	164	38.7
62	16.10	0.79	7.27	87	5.35	327	320	196	38.3
80	18.10	0.73	6.72	62	3.86	228	276	222	29.8
92	19.50	0.70	5.81	51	3.32	261	267	244	20.7
109	21.60	0.66	5.48	57	3.90	258	247	197	34.1
123	23.20	0.64	5.31	59	3.97	244	250	127	30.8
138	25.00	0.74	6.14	53	4.12	190	215	147	41.3
154	27.00	0.93	7.72	81	5.75	193	255	154	51.2
185	32.10	0.67	2.55	20	1.82	79	82	51	5.1
200	36.10	0.86	3.27	31	2.68	78	98	65	27.2
256	47.90	0.82	3.12	26	2.99	75	90	47	36
271	53.10	0.94	2.63	29	2.66	71	89	45	27.8
295	59.10	0.68	3.54	67	3.07	181	181	92	8.7
323	63.60	0.67	3.48	43	3.70	118	122	73	36.6
340	67.70	0.62	1.49	37	1.57	45	55	43	*(-22.9)*
358	70.60	0.93	2.23	20	2.20	80	83	47	18.8
366	74.80	0.91	2.18	31	2.33	39	48	39	32.2
381	80.90	0.78	1.87	27	1.57	62	58	37	*(-13.2)*